THE UNIVERSITY
of ADELAIDE

SOOT EVOLUTION IN TURBULENT NON-PREMIXED BLUFF-BODY FLAMES

AMIR ROWHANI

School of Mechanical Engineering

The University of Adelaide

Australia

A thesis submitted in fulfilment of the requirements

for the degree of Doctor of Philosophy

May 22, 2022

This thesis is dedicated to the memory of my father who would have been very proud of this work. It is also dedicated to my beloved mother, and to my lovely wife, Banafsheh, without her support, the completion of this work would not have been achievable.

[This page is intentionally left blank]

Thesis Abstract

Most practical combustion systems, including; boilers, furnaces and jet engines work under turbulent flow conditions, where recirculating flows play a significant role in flame stabilisation, pollutants' emission mitigation and enhanced mixing. Our current understanding of soot evolution in turbulent circulating reacting flows is still limited, due to the complex flow dynamics, mixing characteristics and wide range of strain rates. Axi-symmetric bluff-body turbulent non-premixed flames have been used to study such flows in the past, because they feature a strong recirculation zone at the base of the flames. They are also relevant to practical applications, simple in design, have well defined boundary and initial conditions and are optically accessible. Their use has contributed to our understanding of the impact of mixing, strain rate and kinetics on soot evolution, transport and oxidation.

The current thesis reports an investigation of soot evolution in a series of turbulent non-premixed bluff-body flames, with a focus on the nexus between soot and flow field features in these flames. Two different fuels were utilised in this study: ethylene blended with nitrogen (4:1, by volume), and pure methane. Three bluff-body burners were used in the experiments, comprising the same 4.6 mm diameter central tube (D_J), but with a different outer bluff-body diameter; 38, 50, and 64 mm. All burners were mounted centrally in a contraction delivering the co-flow air. All other specifications and features of the burners were identical. The mean residence time within the recirculation zone of each flame were estimated computationally using a validated CFD model, whilst the soot volume fraction (f_v) and flow field features were simultaneously measured employing planar laser-induced incandescence (P-LII) and 2D polarised particle image velocimetry (2D-P-PIV), respectively. For all studied cases, the time-averaged and instantaneous scalars including soot volume fraction, axial and radial velocity components, strain rate, and turbulence intensity are presented.

The impact of the bluff body diameter on the structure of the ethylene/nitrogen flames (ENB series) with a constant Reynold number of 15,000, was investigated experimentally and computationally. It was found that, the temperature and the mixture fraction non-dimensional distribution, within the flames, particularly in the recirculation zone, remains the same irrespective of the bluff body diameter. However, as the bluff-body dimeter increases from 38mm to 64mm, the residence

time within the recirculation zone increases by a factor of two to three, and the length of the flame decreases accordingly, by ~20%. The effect on soot, however, was pronounced with the total integrated soot in the flame increasing by 35% when using a larger-diameter burner, and by a factor of four within the recirculation zone. Also, low local strain rates, below 1000 s^{-1}, were measured at different regions within the recirculation zone which favours the inception of soot in all three flames. Analyses of the mean and instantaneous soot volume fraction and strain rate images, within the recirculation zone, reveal that soot is formed in the low-strain high residence time inner vortex and transported to the outer vortex where it peaks closer to the outer shear layer. In the neck zone, relatively small amount of soot, less than 30 ppb, was observed which is deduced from the instantaneous images as having been transported from the recirculation zone, mostly from the inner vortex, closest to the fuel jet. In the recirculation zone, the most probable soot is found in the high-strain region (up to 6000 s^{-1}), and believed to have been transported to this zone from the low strain rate region. The strain rate associated with the most probable soot in the neck zone and jet-propagation region is found to be around 1000 s^{-1} and 500 s^{-1}, respectively. The strain rate in the jet region is not found to be significantly correlated with the axial or radial location. However, the strain rate of 500 s^{-1} in the jet region of the bluff-body flames is found to be consistent with those reported previously for turbulent simple jet flames (600 s^{-1} to 700 s^{-1}). Joint statistical analysis of the local instantaneous soot and strain rate reveals that there is no clear trend to link these two parameters since the instantaneous results of local soot volume fraction and strain rate are not well-correlated. Quantitatively, the correlation of coefficient, R^2, between the local instantaneous SVF and the inverse of the strain rate (1/S) in the recirculation zone and the jet region, indicates a low to weak correlation, where $0.3 < R^2 < 0.6$, which is consistent with the calculated joint PDFs. This provides further evidence that the time scales for SVF are much longer than those for local strain rate. In other word, the variations induced by previous times or locations, dominate over the influence of the values of the local strain rate.

The effect of fuel type was investigated by contrasting the ethylene/nitrogen flames with those burning pure methane as the fuel. Three flames (MB-1, MB-2 and MB-3) with different operating conditions have been investigated. Flames MB-1 and MB-2 have a coflow velocity of 14.1 m/s and Reynolds numbers of 8000 and 15000, respectively. Flame MB-3 has a Reynolds number of 15000 and a coflow velocity of 20 m/s. A strong dependence between the SVF and the momentum flux ratio (fuel to coflow air) in the recirculation zone of these flames was observed. Increasing the momentum flux ratio shifts the location of the mean stoichiometric mixture fraction

to the rich inner vortex which substantially increases the SVF in the recirculation zone. The impact of the momentum flux ratio is evident on soot formation, transport and oxidation within the RZ, and that also impacts on soot in the rest of the flame. Furthermore, the calculated mean mixture fraction profiles show a clear intersection with the mean stoichiometric mixture value, in the vicinity of the jet in MB-2 flames, resulting in a narrower reaction zone. Conversely, in the other two flames, MB-1 and MB-3, the mixture fraction profiles are broadly distributed in the outer vortex, and close to the coflowing air side. As a result, less soot is found in the recirculation zones of the MB-1 and MB-3 flames in comparison to MB-2 flame, mostly due to more favourable oxidation conditions.

The interdependency of the soot, strain rate and turbulence intensity exhibit similarities between methane and ethylene/nitrogen flames. Nonetheless, an almost one order of magnitude lower soot concentration is found in methane flames, when compared with the ethylene/nitrogen flame operated under the same conditions. This reduction is primarily attributed to the differences in molecular structure between methane and the ethylene fuels and its propensity to generate the precursors for soot formation.

The improved understandings and key findings of the current thesis have been configured in the format of four journal articles, presenting results from a combination of experimental and computational studies. The experimental dataset is available on the International Sooting Flame Workshop (ISF) website for model validation purposes.

Thesis Declaration

I certify that this work contains no material which has been accepted for the award of any other degree or diploma in my name, in any university or other tertiary institution and, to the best of my knowledge and belief, contains no material previously published or written by another person, except where due reference has been made in the text. In addition, I certify that no part of this work will, in the future, be used in a submission in my name, for any other degree or diploma in any university or other tertiary institution without the prior approval of the University of Adelaide and where applicable, any partner institution responsible for the joint-award of this degree.

The author acknowledges that copyright of published works contained within the thesis resides with the copyright holder(s) of those works.

I also give permission for the digital version of my thesis to be made available on the web, via the University's digital research repository, the Library Search and also through web search engines, unless permission has been granted by the University to restrict access for a period of time.

I acknowledge the support I have received for my research through the provision of an Australian Government Research Training Program Scholarship.

Amir Rowhani

Acknowledgments

I would like to acknowledge the efforts of all the people who helped along the journey of my PhD study culminating in this thesis. I would cherish the memories of all of them for the rest of my life.

Firstly, I would like to express my endless thanks to my wonderful supervisors and mentors Prof. Bassam Dally, Prof. Gus Nathan, and A/Prof. Paul Medwell for their great guidance, insightful inputs, encouragement, support and friendship. I could not possibly wish for a better supervisory board. I would also like to give thanks to Dr Zhiwei Sun, Dr Alfonso Chinicci and Dr Michael Evans for their support at different stages of this project.

I would also like to add my thanks to my wonderful friends, colleagues, and officemates Navid Freidoonimehr, Mahyar Silakhori, Nima Sedaghati Zadeh, and many more who made my PhD journey joyful and helped me through the dark moments of my candidature.

I am also indebted to the Electrical and Mechanical workshops of the ECMS faculty at the University of Adelaide, especially Jason Peak and Philip Schmidt. I gratefully acknowledge the "Phoenix HPC team" for all their help with technical support for in using the high-performance computing system.

Lastly, I wish to extend my heartfelt thanks to my family who has been so understanding throughout my studies and always encouraged me to pursue my dreams. I am thankful to their unconditional love and support of all my undertakings; academic and otherwise.

Acronyms

CCD	charge-coupled device
CW	continuous wave
DPSS	diode-pumped-solid-state laser
ENB	ethylene nitrogen bluff-body flame
ENH	ethylene nitrogen hydrogen jet flame
FWHM	full width at half maximum
HAB	height above the burner
HHV	Higher heating value
ICCD	intensified charge-coupled device
IML	inner mixing layer
ISF	International Sooting Flame workshop
ISL	inner shear layer
IV	Inner vortex
JZ	jet zone
LRZ	length of recirculation zone
LHS	left-hand side
LII	Laser Induced Incandescence
MB	methane bluff-body flame
NZ	neck zone
OSL	outer shear layer
OV	outer vortex
PAH	polyaromatic hydrocarbon
PDF	probability density function
PIV	Particle Image Velocimetry
ppm	part per million
ppb	part per billion
RHS	right-hand side

RMS	root mean square
RZ	recirculation zone
SP	stagnation point
SVF	soot volume fraction

Contents

List of Figures

List of Tables

Chapter 1 Introduction

1.1 Combustion and Energy

The combustion of flammable material is traced back to the Stone Age where the early humans used the energy from biomass for their primary needs such as heating, cooking, and lighting [1]. Over time and with advances in technology and industry, combustion has been employed in an industrial scale for applications such as power generation, manufacturing, chemicals' production, automotive, and aviation. The evolution of combustion technology was coincident with the replacement of the traditional biomass-based fuels such as charcoal, wood, and dried crops with fossil based fuels due to their higher energy density, abundance and low production cost [2]. Fossil fuels, amongst all energy resources, have dominated energy generation in all sectors and throughout the globe. While alternative energy sources have been developed and utilized such as biofuels, nuclear energy, and renewable sources, fossil fuels and in particular coal, oil and natural gas, still supply the highest share in the global energy generation [3, 4]. The World Energy Council (WEC) and the international energy outlook report (2019) have predicted that the combustion of fossil fuels will still provide around 50-70% of the world energy supply by the end of 2050. Figure 1.1 depicts the projected global energy consumption to 2050, per energy resources type, which shows that combustion of fossil fuels will remain a major source of the world energy demand for decades to come [5].

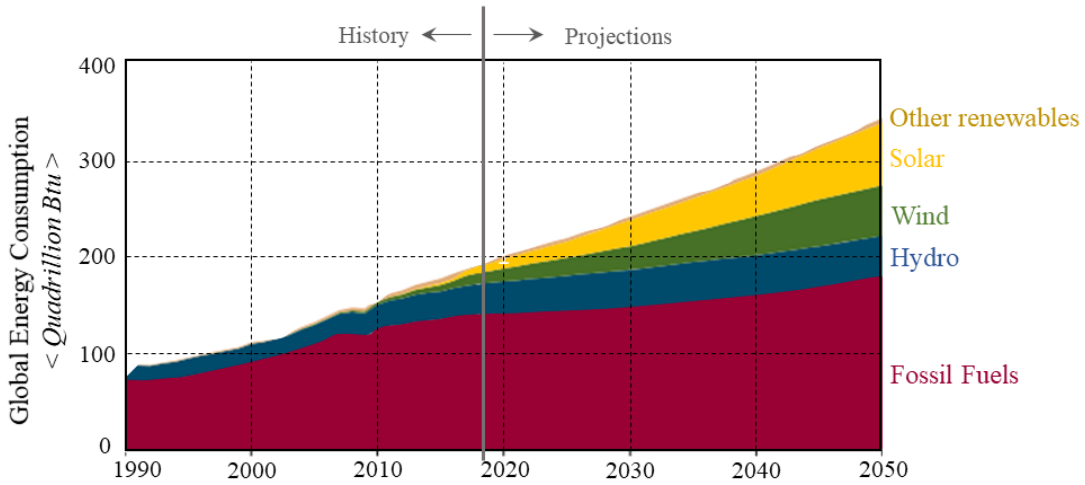

Figure 1.1: Global energy production by fuel type and its projection to 2050. Data is taken from [5].

The combustion of fossil fuel, while has been instrumental for the industrial revolution and in advancing human development, it is also known to produce undesired by-products such as carbon oxides (CO and CO_2), nitrogen oxides (NO_x), unburnt hydrocarbons (UHC), sulphur oxides (SO_x) and solid particles (including soot). Carbon dioxide (CO_2), which is one of the main greenhouse gases, is always emitted into the atmosphere as a result of burning hydrocarbon fuels. In 2019, the global CO_2 emissions from hydrocarbon fuels reached a high of 30.5 Gt, driven by population growth and industrialisation of new economies [5-7].

Abatement techniques have been proposed over the years to mitigate the harmful impact of these pollutants on the atmosphere and the environment. For example, CO_2 reduction may be in the form of increased energy generation and utilization efficiency, using less carbon intensive fuels, or CO_2 capture, use or storage. Carbon monoxide (CO), which is a toxic gas, is produced when partial oxidation of the fuel happens due to poor mixing, deficient supply of oxygen or short residence time. Notably, the CO equilibrium concentration is substantially dependent on the burned gas temperature in such a manner that at temperatures ranged up to 2300 K, the CO production is greater than 1% [8]. The oxides of nitrogen, known as NO_x, are amongst the worst air polluting combustion products. The main constituents of NO_x are the nitrogen oxide, NO, which is known to form through different mechanisms and in most flames, and the nitrogen dioxide, NO_2; a by-product that forms at particular temperatures in the range of 700-800K [9]. These products adversely affect the environment and contribute to photochemical smog and acid rain. Aside from the nitrogen oxides chemistry, the oxide of sulphur (SO_x) could have worse effects on the environment when the fuel contains sulphur such as coal and oils. During the devolatilization and char oxidation process, the sulphur content is released, mostly in the form of SO_2 (more than 99%) and the rest is converted to SO_3 when the temperature is quite high (above 1150K). SO_3 then could be converted to sulfuric acid (H_2SO_4) at lower temperature (below 700K). The condensate of the sulfuric acid as well as the sulphur salt are extremely corrosive products and can damage the combustion system and cause serious environmental effects. In addition to NO_x and SO_x, the incomplete combustion of hydrocarbon fuels can result in soot production [10, 11]. Soot particles are black carbonaceous particulate matters which are produced by the pyrolysis and combustion of hydrocarbon fuels at high temperature and fuel-rich conditions. These fine particles, when emitted to the environment, can be the source of a variety of pulmonary and cardiovascular diseases as well as negative environmental impacts. Nonetheless, the presence of soot particles

in flames has the added benefit of increasing the radiation heat transfer from flames and as long as it burns before exiting the combustion chamber it is highly desirables in applications such as steam boilers and industrial furnaces because it enhances the thermal radiation from the flame. An added benefit of soot in flames is the use as a commodity, known as carbon black, in the manufacturing of tires, plastics and filters. Hence, the understanding and control of soot evolution in flames has been a topic of research for many decades [12] due to its environmental impact when released to the atmosphere and its beneficial quality to enhance heat transfer and production of high value commodity. Soot formation, growth and oxidation in flames are very complex processes. It involves multiple and simultaneous chemical and physical processes with many interdependent parameters that affect it; such as temperature, pressure, mixing rate, strain rate, and fuel type. This thesis reports on a study that is concerned with deepening our understanding of soot and these dependencies under turbulent recirculating non-premixed flame conditions.

1.2 Motivations of soot studies

In the combustion process of hydrocarbon fuels, condensed-phase nanoparticle substances are formed and suspended in combustion gases of industrial systems such as in internal combustion engines, cement kilns, furnaces, boilers, and jet engines. One of the main nanoparticle materials is soot which is important for a variety of reasons. Soot particles are generated under high-temperature fuel-rich conditions, and the presence of a large amount of soot in a combustion device can indicate poor fuel–oxidiser mixing, leading to rich fuel pockets that favours the formation of soot particulates. Soot particulates with less than 2.5 µm diameter (PM2.5), where PM refers to particulate matter, are classified as fine particles. In some applications, the particle size is found to be less than 100 nm. This category of particles is defined as ultra-fine particles. Exposure to these particles is extremely hazardous for humans' health and could cause various diseases among which the pulmonary diseases and cardiovascular illnesses are of the main cause for morbidity and early deaths [6, 7, 13-15]. Moreover, soot emission can adversely affect the earth's climate by absorbing solar radiation and can contribute to the heating of the Earth's surface [16]. On the environmental effects, soot particles affect the Earth's climate system by absorbing sunlight and consequently reduces the radiation which is reflected to space. This phenomenon is known as direct radiative forcing. Additionally, soot emission to the environment could modify the properties of the ice clouds and liquid by changing

the number of ice particles and the cloud extend. Finally, soot deposition on ice, which is known as positive climate forcing, could warm the earth by affecting the troposphere and cryosphere [16, 17]. Due to health and environmental concerns, many countries have placed restricting regulations on particulate emissions, including the Australian government [18].

Noteworthy is that some of the produced soot in practical combustion devices is oxidized and consequently not emitted to the atmosphere. Consequently, the presence of soot in the flames is known to have advantages in enhancing thermal radiation heat transfer especially in boilers, cement kilns, and furnaces. The high emissivity of the solid soot particles helps to enhance the thermal efficiency and reduce the flame gaseous temperature which has positive effects on reducing thermal NOx from flames [9].

1.3 Overview of soot particles

Soot is a black carbonaceous solid material and is composed of carbon particles with various sizes and fractal dimensions. In the literature, a unique definition of soot cannot be found as its composition and morphology vary with the type of fuel and the combustion process. Soot is mainly comprised of carbon, and around 10% by mole [19] or 1% of the weight of this compound is hydrogen [20]. Soot particles initially contain more hydrogen, but through the soot formation process, this hydrogen is abstracted and replaced by a carbon atom. This process is called Hydrogen Abstraction Carbon Addition (HACA) [21] and is detailed in Chapter 2. Soot particles are almost spherical in shape and is composed of several hundred individual sphere-like particles known as nascent (primary) soot particles. The size (diameter) of the primary soot particles fall in the range of 10 nm to 80 nm that most of which range between 10 to 50 nm [22-25]. Nascent soot particles are ultra-fine particles, based on their sizes, and through agglomeration, they grow larger to form mature soot particles [26, 27]. Figure 1.2 shows a scanning electron microscopy image of soot particles with their size.

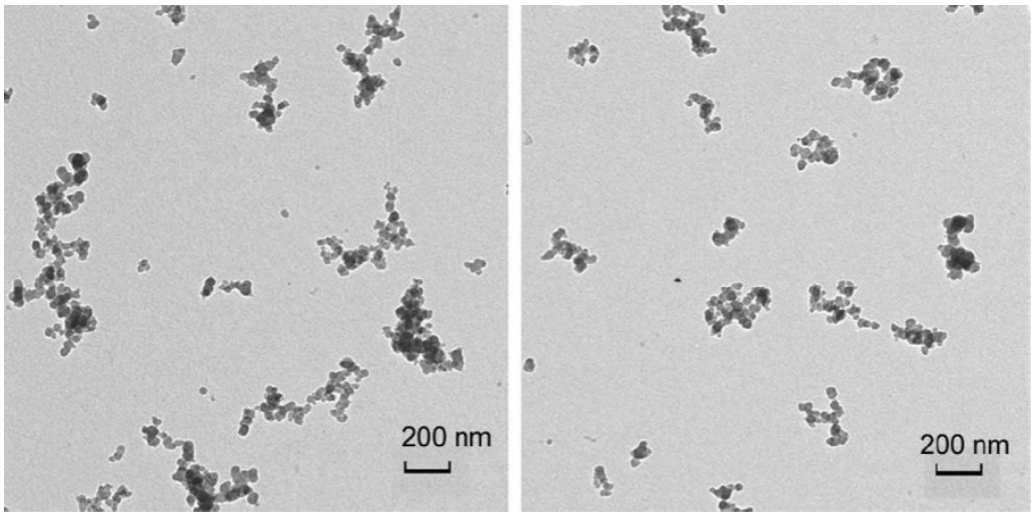

Figure 1.2: Spherical shaped soot particles adapted from [28].

1.4 Diagnostic techniques

Advances in laser diagnostic techniques have provided unrivalled new insights into soot in flames that were not possible through the use of intrusive measurement techniques such as soot probing [29, 30], chemiluminescence and soot luminosity [31], shadowgraph [32, 33], and acoustic sensors [34, 35]. Laser based techniques have offered numerous advantages over the intrusive techniques such as spatial and temporal resolution, spectral selectivity, and the most important of which the capability of simultaneous measurements of several scalars in the flames. Laser techniques have aided the measurement of innumerable parameters including but not limited to flow field features (velocity, strain rate, turbulence length and time scales, and turbulence intensity, etc.), scalar field (temperature, species concentration, mixture fraction, heat release rate, etc.), and particulates (particle size, volume fraction, number density, etc.). A summary of the various combustion diagnostic techniques is presented in Figure 1.3. The major diagnostic techniques that are broadly employed in both reacting and non-reacting flows are laser Doppler anemometry [36, 37] (LDA), particle image velocimetry (PIV) [38-41], and particle tracking velocimetry (PTV) for gas velocity measurements [42-44], laser absorption spectroscopy (LAS) [45-47], laser-induced fluorescence (LIF) [48-51], laser Rayleigh scattering (LRS) [52, 53], spontaneous Raman scattering (SRS) [54, 55], and coherent anti-Stokes Raman spectroscopy (CARS) for gas temperature and species measurements [56-61], laser scattering/absorption, and laser-induced incandescence (LII) for soot measurements [62-65], and phase Doppler anemometry (PDA) [66-68],

tracer LIF [69], structured laser illumination planar imaging (SLIPI) [70, 71], and ballistic imaging and X-ray imaging for droplet and spray measurements [72, 73].

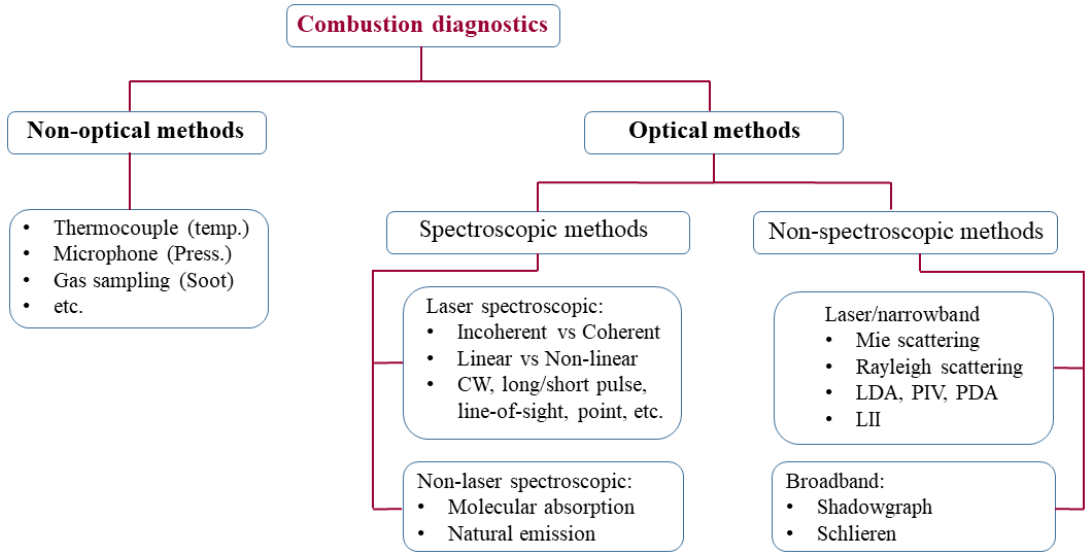

Figure 1.3: Classification of the combustion diagnostic techniques [28-35].

While previous studies into turbulent simple jet flames provided important insight onto the interaction between soot and the dynamics of the flow, given the importance of the recirculating flow on flame stabilisation in practical combustors, axisymmetric bluff-body flames are used to explicitly identify the effect of recirculating flow on soot formation, oxidation, and transport. Moreover, there is a clear need for a robust experimental dataset for model validation purposes for these flames. This thesis will therefore analyse the soot formation and flow field in turbulent bluff-body flames in order to deepen our current understanding of the interactions between soot and flowfield characteristics in turbulent bluff-body flames and to provide experimental data to support model development and verification.

1.5 Thesis outline

This thesis is formatted as a collection of four manuscripts, two of which have been published and two are under review in peer-reviewed journals. These papers form the basis of this thesis and constitute its chapters which sequentially show the progress of the current study. These papers include data analyses of the soot and the flowfield in order to explore the effects of residence time on soot formation and to develop qualitative and quantitative correlations between the soot and flowfield features in turbulent non-premixed bluff-body flames.

Chapter 2 contains background literature that is relevant to soot measurement in turbulent flames, and the existing correlations between soot and flowfield characteristics such as mean and instantaneous velocities, strain rate, turbulence kinetic energy, and turbulence intensity. The chapter concludes by identifying the research gap and formulating the scientific aim and objectives.

Chapter 3-6 present results from a systematic study of the effect of residence time on soot formation and oxidation, and the correlations between soot and flowfield features such as residence time, velocity, and strain rate in a series of turbulent non-premixed bluff-body flames of ethylene/nitrogen (80:20 by Vol.), as well as pure methane.

Chapter 3 investigates the effect of bluff-body diameter on the flow field characteristics of reacting and non-reacting flows. This chapter particularly assesses the feasibility of conducting particle image velocimetry (PIV) technique for flow visualisation in turbulent flames containing high soot loadings. The influence of increased bluff-body diameter on the residence time distribution of simulated particles in the recirculation zone of these flames was also estimated computationally. The contents of this chapter have been published in the journal of "Combustion Science and Technology".

Chapter 4 presents the experimental finding of the simultaneous measurements of soot and flowfield features in the recirculation zone and the neck zone of the bluff-body flames. Time-averaged and instantaneous velocity, strain rate, and soot volume fraction together with the underlying correlations between these scalars are discussed. The results and discussion were published in the "38$^{\text{th}}$ Proceeding of the Combustion Institute".

Chapter 5 expands the information in Chapter 4 to further explore the nexus between the instantaneous soot and strain rate and to enhance our understanding of the formation and oxidation of soot throughout the flame length. This chapter closely looks at the relationship between the inception of soot in the jet flames and its

transport and oxidation in the neck region. The results and discussion have been submitted to the “Combustion and Flame” journal and is currently under review.
Chapter 6 investigates the sensitivity of soot propensity, formation, and oxidation to the fuel type in a series of turbulent methane flames. Using the 64 mm diameter bluff body burner, the soot volume fraction was measured and compared with those of ethylene-based fuels burning under similar operating flame conditions. Also presented in this chapter is the effect of varying the fuel jet and co-flow velocities which impacts on the mixture strength within the recirculation zone and soot formation and oxidation. The findings of this chapter have been submitted to the journal of "Combustion and Flame" and the paper is currently under review.
Chapter 7 summarises the findings of this study and provides overall conclusions to the thesis by addressing the scientific research questions paused. The chapter ends with suggested directions for future work.

1.6 References

[1] N. Clark and K. Yusoff, "Combustion and Society: A Fire-Centred History of Energy Use", Theory, Culture, and Society, vol. 31, no. 8, pp. 203-226, 2014.

[2] V. Smil, "21st century energy: some sobering thoughts", OECD Observer, vol. 258-259, pp. 22, 2006.

[3] M. Ryle, "Economics of alternative energy sources", Nature, 267, pp. 111-117, 1977.

[4] L. Schlapbach and A. Züttel, "Hydrogen-storage materials for mobile applications", Materials for Sustainable Energy, pp. 265-270, 2010.

[5] "International Energy Outlook 2019", U.S. Energy Information Administration, November 2019.

[6] K. Donaldson, D. Brown, A. Clouter, R. Duffin, W. MacNee, L. Renwick, L. Tran, and V. Stone, "The Pulmonary Toxicology of Ultrafine Particles", Journal of Aerosol Medicine, vol. 15, no. 2, pp. 213-220, 2002.

[7] K. Donaldson, L. Tran, L. A. Jimenez, R. Duffin, D. E. Newby, N. Mills, W. MacNee, and V. Stone, "Combustion-derived nanoparticles: a review of their toxicology following inhalation exposure", Particle and fibre toxicology, vol. 2, no. 10, pp. 1-14, 2005.

[8] U. Asghar, S. Rafiq, A. Anwar, T. Iqbal, A. Ahmed, F. Jamil, M. S. Khurram, M. M. Akbar, A. Farooq, N. S. Shah, and Y-K. Park, "Review of the Progress in Emission Control Technologies for the Abatement of CO2, SOx and NOx from Fuel Combustion", Journal of Environmental Chemical Engineering, 2021, https://doi.org/10.1016/j.jece.2021.106064.

[9] G. J. Nathan, P. A. M. Kalt, Z. T. Alwahabi, B. B. Dally, P. R. Medwell, and Q. N. Chan, "Recent advances in the measurement of strongly radiating, turbulent reacting flows", Progress in Energy and Combustion Science, vol. 38, no. 1, pp. 41-61, 2012.

[10] A. Levy, "Unresolved problems in SOx, NOx, soot control in combustion", Proceedings of the Combustion Institute, vol. 19, no. 1, pp. 1223-1242, 1982.

[11] S. Li, T. Xu, P. Sun, Q. Zhou, H. Tan, S. Hui, “NOx and SOx emissions of a high sulfur self-retention coal during air-staged combustion”, Fuel, vol. 87, no. 6, pp.723-731, 2008.

[12] "International Sooting Flame (ISF) Workshop." http://www.adelaide.edu.au/cet/isfworkshop/ (accessed July 23, 2016., 2016).

[13] G. B. Hamra, N. Guha, A. Cohen, F. Laden, O. Raaschou-Nielsen, J. M. Samet, P. Vineis, F. Forastiere, P. Saldiva, T. Yorifuji, and D. Loomis,, "Outdoor particulate matter exposure and lung cancer: A systematic review and metaanalysis”, Environmental Health Perspectives, vol. 122, no. 9, pp. 906-911, 2014.

[14] A. Sydbom, A. Blomberg, S. Parnia, N. Stenfors, T. Sandstorm, and S-E. Dahlen, "Health efects of diesel exhaust emissions”, European Respiratory Journal, vol. 17, pp. 733-746, 2001.

[15] L. L. McCrain and W. L. Roberts, "Measurements of the soot volume field in laminar diffusion flames at elevated pressures”, Combustion and Flame, vol. 140, no. 1-2, pp. 60-69, 2005.

[16] V. Ramanathan, C. Chung, D. Kim, T. Bettge, L. Buja, J. T. Kiehl, W. M. Washington, Q. Fu, D. R. Sikka, and M. Wild, "Atmospheric brown clouds- Impacts on South Asian climate and hydrological Cycle”, Proceedings of the National Academy of Sciences of the United States of America PNAS, Proceedings of the National Academy of Sciences, vol. 102, no. 15, pp. 5326-5333, 2005.

[17] J. Fan, Y. Wang, D. Rosenfeld, and X. Liu, "Review of Aerosol–Cloud Interactions: Mechanisms, Significance, and Challenges”, Journal of the Atmospheric Sciences, vol. 73, no. 11, pp. 4221-4252, 2016.

[18] "Australia's 2030 Emission Reduction Target." www.pmc.gov.au. (October 30, 2019).

[19] B. S. Haynes and H. Gg. Wagner, "Soot Formation”, Proceedings of the Combustion Institute, vol. 7, no. 4, pp. 229-273,1981.

[20] I. Glassman, “Soot fprmation in combution processes”, Proceedings of the Combustion Institute, vol. 22, no. 1, pp. 295-311,1989.

[21] M. Frenklach, "Reaction mechanism of soot formation in flames”, Physical Chemistry Chemical Physics, vol. 4, no. 11, pp. 2028-2037, 2002.

[22] R. C. Flagan and J. H. Seinfeld, Fundamentals of air pollution engineering. Courier Corporation, 2012.

[23] C. M. Megaridis and R. A. Dobbins, "Morphological Description of Flame-Generated Materials", Combustion Science and Technology, vol. 71, no. 1-3, pp. 95-109, 1990.

[24] R. Puri, T. F. Richardson, R. J. Santoro, and R. A. Dobbins., "Aerosol dynamic processes of soot Aggregates in a laminar ethene diffusion flame", Combustion and Flame, vol. 92, no. 3, pp. 320-333, 1993.

[25] H. Wang, "Formation of nascent soot and other condensed-phase materials in flames", Proceedings of the Combustion Institute, vol. 33, no. 1, pp. 41-67, 2011.

[26] M. Kholghy, M. Saffaripour, C. Yip, and M. J. Thomson, "The evolution of soot morphology in a laminar coflow diffusion flame of a surrogate for Jet A-1", Combustion and Flame, vol. 160, no. 10, pp. 2119-2130, 2013.

[27] S. Chatterjee and Ö. L. Gülder, "Soot concentration and primary particle size in swirl-stabilized non-premixed turbulent flames of ethylene and air", Experimental Thermal and Fluid Science, vol. 95, pp. 73-80, 2018.

[28] k. Tian, K. A. Thomson, F. Liu, D. R. Snelling, G. J. Smallwood and D. Wang, " Determination of the morphology of soot aggregates using the relative optical density method for the analysis of TEM images", Combustion and Flame, vol. 144, no. 4, pp. 782-791, 2006.

[29] H. Bladh, N-E. Olofsson, T. Mouton, J. Simonsson, X. Mercier, A. Faccinetto, P-E. Bengtsson, and P. Desgroux, "Probing the smallest soot particles in low-sooting premixed flames using laser-induced incandescence", Proceedings of the Combustion Institute, vol. 35, no. 2, pp. 1843-1850, 2015.

[30] H. A. Michelsen, "Probing soot formation, chemical and physical evolution, and oxidation: A review of in situ diagnostic techniques and needs", Proceedings of the Combustion Institute, vol. 36, no. 1, pp. 717-735, 2017.

[31] S. Karnani and D. Dunn-Rankin, "Visualizing CH* chemiluminescence in sooting flames", Combustion and Flame, vol. 160, no. 10, pp. 2275-278, 2013.

[32] F. Parsinejad, J. C. Keck, and H. Metghalchi, "On the location of flame edge in Shadowgraph pictures of spherical flames: a theoretical and experimental study", Experiments in Fluids, vol. 43, pp. 887-894, 2007.

[33] S. Rasenat, G. Hartung, B. L. Winkler, and I. Rehberg, "The shadowgraph method in convection experiments", Experiments in Fluids, vol. 7, pp. 412-420, 1989.

[34] S. Prakash, T. Muruganandam, Y. Neumeier, T. Lieuwen, J. Seitzman, and B. Zinn, "Acoustic Sensing and Mitigation of Lean Blow Out in Premixed Flames", presented at the 43rd AIAA Aerospace Sciences Meeting and Exhibit, Reno, Nevada, 2005.

[35] T. Muruganandam, S. Nair, Y. Neumeier, T. Lieuwen, and Jerry Seitzman, "Optical and Acoustic Sensing of Lean Blowout Precursors", presented at the 38th AIAA/ASME/SAE/ASEE Joint Propulsion Conference and Exhibit, Indianapolis, Indiana, 2002.

[36] C. Tropea, "Laser Doppler anemometry: recent developments and future challenges", Measurement Science and Technology, vol. 6, pp. 605, 1995.

[37] N. L. Walker and J. B. Moss, "Laser Doppler Anemometry Measurement in and around a Turbulent Buoyant Flame", Combustion Science and Technology, vol. 41, pp. 43-53, 1984.

[38] I. Grant, "Particle image velocimetry: A review", Proceedings of the Institution of Mechanical Engineers, Part C: Journal of Mechanical Engineering Science, vol. 211, no. 1, pp. 55-76, 1997.

[39] A. Melling, "Tracer particles and seeding for particle image velocimetry", Measurement Science and Technology, vol. 8, pp. 1406, 1997.

[40] A. Stella, G. Guj, J. Kompenhans, M. Raffel, and H. Richard, "Application of particle image velocimetry to combusting flows: design considerations and uncertainty assessment", Experiments in Fluids, vol. 30, pp. 167-180, 2001.

[41] C. Fang and L. I. U. Hong, "Particle image velocimetry for combustion measurements: Applications and developments", Chinese Journal of Aeronautics, vol. 31, no. 7, pp. 1407-1427, 2018.

[42] H.-J. Neußer, L. Spiegel, and J. Ganser, "Particle Tracking Velocimetry - A Powerful Tool to Shape the In-Cylinder Flow of Modern Multi-Valve Engine Conceptss.", SAE Transactions, vol. 104, pp. 242–256, 1995.

[43] A. Alpers, P. Gritzmann, D. Moseev, and M. Salewski, "3D particle tracking velocimetry using dynamic discrete tomography", Computer Physics Communications, vol. 187, pp. 130-136, 2015.

[44] K. Liu and D. Liu, "Particle tracking velocimetry and flame front detection techniques on commercial aircraft debris striking events", Journal of Visualization, vol. 22, pp. 783-794, 2019.

[45] L. Xu, C. Liu, W. Jing, Z. Cao, X. Xue, and Y. Lin, "Tunable diode laser absorption spectroscopy-based tomography system for on-line monitoring of two-dimensional distributions of temperature and H_2O mole fraction", Review of Scientific Instruments vol. 87, pp. 013101-013111, 2016.

[46] M. Soo, S. Goroshin, N. Glumac, K. Kumashiro, J. Vickery, D. L.Frost, and J. M. Bergthorson, "Emission and laser absorption spectroscopy of flat flames in aluminum suspensions", Combustion and Flame, vol. 290, pp. 230-238, 2017.

[47] C. Liu and L. Xu, "Laser absorption spectroscopy for combustion diagnosis in reactive flows: A review", Applied Spectroscopy Reviews, vol. 54, no. 1, pp. 1-44, 2018.

[48] D. R. Crosley and G. P. Smith, "Laser-Induced Fluorescence Spectroscopy For Combustion Diagnostics", Optical Engineering, vol. 22, no. 5, pp. 225545, 1983.

[49] K. McManus, B. Yip, and S. Candel, "Emission and laser-induced fluorescence imaging methods in experimental combustion", Experimental Thermal and Fluid Science, vol. 10, no. 4, pp. 486-502, 1995.

[50] J. W. Daily, "Laser induced fluorescence spectroscopy in flames", Progress in Energy and Combustion Science, vol. 23, no. 2, pp. 133-199, 1997.

[51] P. H. Paul and H. N. Najm, "Planar laser-induced fluorescence imaging of flame heat release rate", Proceedings of the Combustion Institute, vol. 27, no. 1, pp. 43-50, 1998.

[52] F. Q. Zhao and H. Hiroyasu, "The applications of laser Rayleigh scattering to combustion diagnostics", Progress in Energy and Combustion Science, vol. 19, no. 6, pp. 447-485, 1993.

[53] F. Caldas, D. Duarte, P. Ferräo, M. V. Heitor, and C. Poppe, "On the Use of Laser Rayleigh Scattering to Study the Aerothermochemistry of Recirculating Premixed Flames", Developments in Laser Techniques and Fluid Mechanics, pp. 439-453, 1997.

[54] R. W. Dibble, A. R. Masri, R. W. Bilger, "The spontaneous raman scattering technique applied to nonpremixed flames of methane", Combustion and Flame, vol. 67, no. 3, pp. 189-206, 1987.

[55] H. Ajrouche, A. Lo, P. Vervisch, and A. Cessou, "Assessment of a fast electro-optical shutter for 1D spontaneous Raman scattering in flames", Measurement Science and Technology, vol. 26, pp. 075501, 2015.

[56] W. R. Lempert and I. V. Adamovich, "Coherent anti-Stokes Raman scattering and spontaneous Raman scattering diagnostics of nonequilibrium plasmas and flows", Journal of Physics D: Applied Physics, vol. 47, pp. 433001, 2014.

[57] A. B. Harvey and J. W. Nibler, "Coherent Anti-Stokes Raman Spectroscopy of Gases", Applied Spectroscopy Reviews, vol. 14, no. 1, pp. 101-143, 1978.

[58] J. W. Nibler and G. V. Knighten, "Coherent Anti-Stokes Raman Spectroscopy", Raman Spectroscopy of Gases and Liquids. Topics in Current Physics, vol. 11, pp. 253-299, 1979.

[59] F. El-Diasty, "Coherent anti-Stokes Raman scattering: Spectroscopy and microscopy", Vibrational Spectroscopy, vol. 55, no. 1, pp. 1-37, 2011.

[60] S. Roy, J. R. Gord, and A. K. Patnaik, "Recent advances in coherent anti-Stokes Raman scattering spectroscopy: Fundamental developments and applications in reacting flows", Progress in Energy and Combustion Science, vol. 36, no. 2, pp. 280-306, 2010.

[61] W. M. Tolles, J. W. Nibler, J. R. McDonald, and A. B. Harvey, "A Review of the Theory and Application of Coherent Anti-Stokes Raman Spectroscopy (CARS)", Applied Spectroscopy, vol. 31, no. 4, pp. 253-271, 1977.

[62] C. Schulz, B. F. Kock, M. Hofmann, H. Michelsen, S. Will, B. Bougie, R. Suntz, and G. Smallwood, "Laser-induced incandescence: recent trends and current questions", Applied Physics B, vol. 83, pp. 336-354, 2006.

[63] R. L. Vander Wal, "Laser-induced incandescence: excitation and detection conditions, material transformations and calibration", Applied Physics B, vol. 96, pp. 601-611, 2009.

[64] C. Lou, C. Chen, Y. P. Sun, and H. C. Zhou, "Review of soot measurement in hydrocarbon-air flames", Science China Technological Sciences, vol. 53, pp. 2129-2141, 2010.

[65] H. A. Michelsen, C. Schulz. G .J . Smallwood, and S. Will, "Laser-induced incandescence: Particulate diagnostics for combustion, atmospheric, and industrial applications", Progress in Energy and Combustion Science, vol. 51, pp. 2-48, 2015.

[66] C.F. Edwards and R. C. Rudoff, "Structure of a swirl-stabilized spray flame by imaging, laser doppler velocimetry, and phase doppler anemometry", Proceedings of the Combustion Institute, vol. 23, no. 1, pp. 1353-1359, 1991.

[67] F. Israel, A. M. K. P. Taylor, and J. H. Whitelaw, "Simultaneous measurement of droplet velocity and size and flame mantle temperature by phase Doppler anemometry and two-colour pyrometry", Measurement Science and Technology, vol. 6, pp. 727, 1995.

[68] E. Kristensson, A. Ehn, J. Bood, and M. Aldén, "Advancements in Rayleigh scattering thermometry by means of structured illumination", Proceedings of the Combustion Institute, vol. 35, no. 3, pp. 3689-3696, 2015.

[69] C. Schulz and V. Sick, "Tracer-LIF diagnostics: quantitative measurement of fuel concentration, temperature and fuel/air ratio in practical combustion systems", Progress in Energy and Combustion Science, vol. 31, no. 1, pp. 75-121, 2005.

[70] E. Berrocal, E. Kristensson, M. Richter, M. Linne, and M. Aldén, "Application of structured illumination for multiple scattering suppression in planar laser imaging of dense sprays", Optics Express, vol. 16, no. 22, pp. 17870-17881, 2008.

[71] F. Zentgraf, M. Stephan, E. Berrocal, B. Albert, B. Böhm, and A. Dreizler "Application of structured illumination to gas phase thermometry using thermographic phosphor particles: a study for averaged imaging", Experiments in Fluids, vol. 58, pp. 58-82, 2017.

[72] N. Hansen, R. S. Tranter, K. Moshammer, J. B. Randazzo, J. P. A. Lockhart, P. G. Fugazzi, T.Tao, and A. L.Kastengrene, "2D-imaging of sampling-probe perturbations in laminar premixed flames using Kr X-ray fluorescence", Combustion and Flame, vol. 181, pp. 214-224, 2017.

[73] M. A. Linne, M. Paciaroni, E. Berrocal, and D. Sedarsky, "Ballistic imaging of liquid breakup processes in dense sprays", Proceedings of the Combustion Institute, vol. 32, no. 2, pp. 2147-2161, 2009.

Chapter 2 Background Literature

2.1 Soot formation and oxidation mechanism

The processes of soot formation and destruction in flames are intricate phenomena that despite the enormous research contributions in the past few decades, the detailed understanding of these complex processes have remained rather limited. The interests in exploring the underlying physical and chemical processes driving the formation and evolution of these ultra-fine carbonaceous particles have inspired a wide spectrum of research to discover the interdependency of the soot controlling parameters in flames. The importance and role of these parameters on the evolution of soot will be detailed in this chapter, focusing on different types of flames including the laminar flames [1-7], acoustically-forced laminar flames [8-12], turbulent simple jet flames [13-20], bluff-body flames [17, 21, 22], swirling flames [23-26], and spray flames [27-29]. While various pathways have been proposed to best describe the evolution of soot particles in flames, the prevailing consensus is that the overall process comprises four main steps: soot inception (nucleation), surface growth, coagulation, and agglomeration in conjunction with soot oxidation [30]. A schematic of the soot formation and oxidation mechanism in a laminar flame is depicted in Figure 2.1. The different steps are briefly discussed in the following subsections.

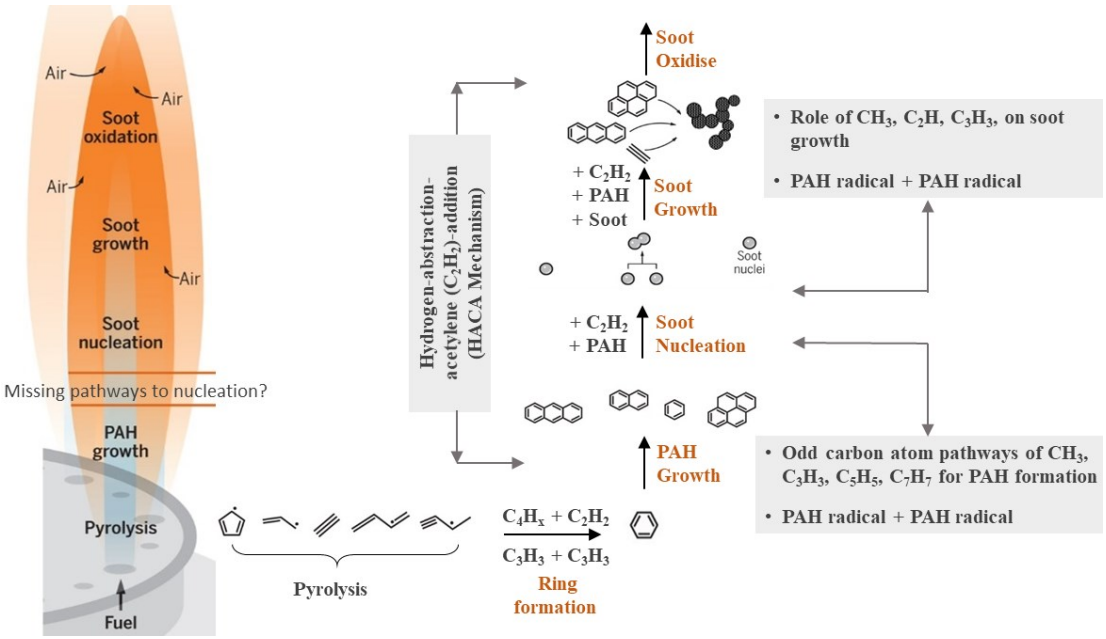

Figure 2.1: A schematic of soot formation in a co-flow laminar diffusion flame adopted from [31].

2.1.1 Formation of Aromatics

Different pivotal species responsible for soot inception have been proposed in the literature including polyacetylenes [32], ionic species [33], or polycyclic aromatic hydrocarbons (PAH) [34]. Nonetheless, the majority of experimental and numerical research concur on the importance of PAH species as the main precursors that drive soot particles to form. Hence, a profound understanding of gas-phase kinetics of the PAH and their formation following fuel pyrolysis and within the flame is critically important. The formation of the PAH as the most plausible soot precursor is initiated from the formation of the first aromatic rings, such as phenyl and benzene, by the pyrolysis of the hydrocarbon fuels. It is perceived by many researchers that the potential roots for the formation of the aromatic rings involve the addition of the small aliphatic, such as acetylene (C_2H_2), to the even-atom-carbon molecules such as poly-butadienyl (n-C_4H_3) and poly- cyclopropylmethylene (n-C_4H_5) to form phenyl and benzene, respectively [35-38].

$$\text{n-}C_4H_3 + C_2H_2 \rightarrow \quad \text{phenyl}$$

$$\text{n-}C_4H_5 + C_2H_2 \rightarrow \text{benzene} + H$$

Others argue that due to the rapid transformation of n-C_4H_3 and n-C_4H_5 to their corresponding resonantly stabilised isomer, iso-C_4H_3 and iso-C_4H_5, the concentration of n-C_4H_3 and n-C_4H_5 are insufficient [39-42]. Instead, they suggested an odd-carbon-atom pathway via a combination of propargyl radicals:

$$C_3H_3 + C_3H_3 \rightarrow \text{benzene or phenyl} + H$$

The propargyl radicals is a stable hydrocarbon radical, and its impact on aromatics formation is extensively supported [38, 43]. It is noteworthy that the formation of the single aromatic ring is not the rate-limiting step [2] and the PAH growth can be initiated by the multi-ring PAH formation.

Another possible pathway, which supports the aromatic ring formation route, is the formation of the cyclopentadienyl radical as a result of the reaction between propargyl and acetylene [38]:

$$C_3H_3 + C_2H_2 \rightarrow c\text{-}C_5H_5$$

This reaction consists of the most abundant building block of the aromatic formation, acetylene, and the aforementioned highly stable radial, propargyl. Once

this reaction happens, the naphthalene is formed from a pair of cyclopentadienyl radicals [38, 44-46]. A detailed explanation of the role of these radicals in the aromatic formation can be found in [47]. The chemical structures of the species referred to in this section are depicted in Figure 2.2. The next step involves the growth of these aromatic rings to larger compounds and eventually soot particles. The soot growth mechanism is detailed in section 2.1.4.

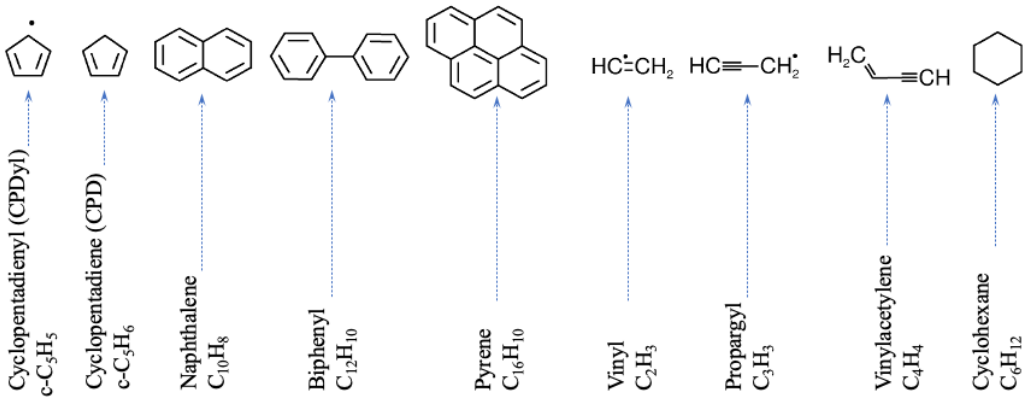

Figure 2.2: Structure of the chemical species adopted from [48]. The dot on the species represents the radical.

2.1.2 Growth of Aromatics

Different pathways for the growth of the PAH have been proposed and those primarily include; (a) the hydrogen-abstraction-acetylene-addition (HACA) mechanism; (b) the addition of radicals such as methyl (CH_3), vinyl (C_2H_3), and propargyl (C_3H_3); (c) and the addition of PAH/PAH radicals over each other and the forming of biaryls. In all the aforementioned pathways, the mitigation of H atoms on the PAH edge, and shifting the positions of the radicals, plays a crucial role in the growth of the aromatics. Amongst all the mechanisms listed above, it is broadly accepted that the HACA mechanism described by Frenklach et al., is the most accepted and has been extensively used in explaining the soot growth mechanism [35-38, 43, 47]. Please note that the letter C in the HACA acronym is used interchangeably to mean acetylene and carbon. The term "HACA" which is used as an acronym for "Hydrogen-abstraction-acetylene-addition" mechanism involves two principal stages: (a) a gaseous hydrogen atom abstracts a hydrogen atom from a reacting hydrocarbon in the reaction (A_i + H → A_i- + H_2), where the A_i is the

aromatic molecule. This reaction willingly continues to grow aiding acetylene and forms larger PAH. This reaction is followed by (b) the addition of gaseous acetylene molecule to the radical (A_i- + C_2H_2 → products), where the A_i- is the aromatic radical. This reaction needs another hydrogen abstraction to become a radical first, and further grow with acetylene. It is worth mentioning that acetylene is not the only species driving the PAH growth, and several studies have suggested that methyl, propargyl, and cyclopentadienyl are also involved in this process [49-54]. The PAH growth mechanism is affected by flame characteristics such as temperature and the concentration of hydrogen and acetylene which are influenced by the fuel type. While, dependent on the fuel type and the experimental conditions, the formation of the aromatic rings may proceed through different reactions, and these initial pathways turn to the acetylene-addition path [35, 38].

2.1.3 Soot nucleation (Inception)

The transition of PAH to soot particles is a poorly-understood step of the soot formation mechanism albeit a large number of studies have been carried out to explore the soot evolution in various flames over the last few decades. Two main pathways have been presented in the literature which describe the soot inception: chemical growth and physical coagulation. The chemical growth of soot was explained in the experimental investigation of a low-sooting flame [50]. The transmission electron microscopy (TEM) images of soot particles demonstrate the two-dimensional PAH growth into a curved-liked structure, which suggests the physical growth process of soot particles. In the coagulation process, the moderate-sized PAHs grow into stacked-clustered, and in turn, the PAH coagulate into cross-linked three-dimensional structures. Quite a large number of studies argue that the PAH coagulation process does not play a major role in their reaction mechanism which could largely be attributed to the low coagulation efficiencies assumed for radicals larger than pyrene ($C_{16}H_{10}$). The investigation of the soot models, on the other side, showed that with the shift in collision quality, substantial variance in the expected particulate volume fraction can be obtained and is thus an important factor for the theoretical analysis of soot nucleation. The details of the soot inception process can be found in recent work performed by D'Anna [55].

2.1.4 Soot growth

The growth pathways of soot particles are related to those found for the PAH namely: (a) chemical growth pathways by either acetylene (C_2H_2) or PAH; (b) PAH condensation; and (c) soot particle coagulation. The first two pathways are involved in increasing the soot mass while the ultimate size of the soot particles is determined by the coagulation of the particulates which form their chain-like structure. Simulations revealed that more than 60% of the carbon present in the PAH comes from the addition of acetylene (C_2H_2), irrespective of the fuel type, and the rest comes from the PAH [47, 56, 57]. It has been experimentally shown that the rate of soot surface growth is directly proportional to the hydrogen atom concentration in the reaction zone [47]. Noting too that the coagulation of soot particles is described by coalescence and agglomeration processes. Coalescence occurs when small molecules collide with other particles. The smaller particles will be embedded inside the bigger particles and maintain their spherical shape. The collision of bigger particles with the species aggregates into chain-like structures, which maintain their shape because the surface growth rate is too small to reshape the structures. The next step involves the reaction of soot mass with oxidants in the reaction environment.

2.1.5 Soot oxidation

The oxygen molecule (O_2) and the hydroxyl radical (OH) are the primary oxidants that are responsible for soot surface oxidation. Other possible species such as CO_2, H_2O, and O radical are considered as soot oxidants [58-64]. Soot formation and growth of the particles are competing processes with the oxidation process, in the reaction zone. When the soot particles are formed, depending on the combustion chamber conditions, they can be either oxidized or converted to graphite-like material. The latter usually happens at high temperatures and low oxygen conditions when the residence time is long enough, while in the fuel-lean conditions, surface oxidation of soot particles happens by either the OH radical or the O_2 molecule. In fuel-lean conditions, OH contributes the most to the oxidation whilst O_2 contributes to the oxidation in fuel-rich combustion conditions [65]. Xu et al. [66] also found that in the temperature range of 1570 K to 1870 K, and O_2 mole fraction range of 10^{-5} to 3×10^{-2}, the OH radical is the primary oxidant of soot particles and its precursors. A small part of the soot which is not oxidized in the combustion system is emitted to the environment [57]. Although both OH radical and O_2 can oxidise both the aromatics and soot particles, in the case of aromatic rings and before soot

nucleation, as deduced from the numerical simulations of laminar premixed flames [37], the O_2 oxidation of the aromatics is more dominant rather than the OH. The oxidation of the aromatics affects largely their growth due to the rapidly decreasing O_2 concentration, which is consistent with the depletion of O_2 during the HACA progression. This also justifies why the soot inception occurs in the vicinity of the reaction zone with rich hydrogen atoms and insufficient O_2 molecules. The role of OH in the oxidation of aromatic rings is not very well understood. During the soot oxidation under the fuel-lean condition, the aggregated soot particles break apart into small fragments which is known as soot fragmentation. The soot fragmentation process is a consequence of the combined effect of internal burning in soot by O_2 and surface regression due to external oxidation [67]. However, it was proposed that internal burning is dependent on particle size and is possible for particles larger than 10 nm. Also, the fragmentation extent is inversely proportional to the peak temperature, since soot burnout occurs rapidly at higher flame temperatures [68, 69].

2.2 Parameters affecting soot in flames

The challenges in understanding soot formation and oxidation primarily arise from the complex multi-scale and multi-phase chemical and physical interactions which are largely controlled by temperature, strain rate, pressure, mixture fraction, residence time, and fuel type. When turbulence exists, these dependencies are non-linearly coupled, since the mixing and the soot formation are of the same time scales, and this makes the soot evolution process further complicated. Nonetheless, past research has focused on both laminar and turbulent flames to understand how the relevant parameters influence the soot evolution process. The following sub-sections, briefly discuss and identify the gaps in knowledge of the effects of pressure, temperature, mixing, and fuel type on the evolution of soot in laminar and turbulent flames.

2.2.1 Pressure

A large number of practical combustion systems operate at elevated pressure, up to more than 200 bar, in some applications to increase the device efficiency. In gas turbines and diesel engines, for instance, the pressure increases up to 60 bar and 225 bar, respectively. Therefore, a detailed investigation of soot-pressure coupling is

essential to enable controlling the soot production in high-pressure combustors. To investigate the pressure effect, a large body of the literature has excluded the effects of turbulence and focused on the pressure effects on soot formation in diffusion-controlled flames in the laminar regime [70-73]. Presumably, the investigation of Smith et al. [74] was among the first pieces of evidence suggesting that elevated pressure results in increasing the soot yield in a laminar counterflow flame fuelled with ethylene and ethylene/hydrogen blends. Even in ethylene-lean non-sooting flames, increasing the pressure caused soot to be formed after reaching a specific pressure. Noteworthy is that the soot formation mechanism at high pressures may be different from that at atmospheric pressure. That is, soot removal by oxidation decreases while the soot formation is enhanced at elevated pressures. Although the sophistication of soot evolution at elevated pressure is still elusive, it is agreed that at increased pressure the reaction rate would be changed as a result of higher flame temperatures and sharper concentration gradients which lead to the formation of more soot under high-pressure conditions [70]. The dependence of the soot yield (%) on the pressure (atm) is presented in Fig. 2.3. To correlate the soot volume fraction (f_v) with the ambient pressure, a power-law function, $f_v \sim P^a$, was proposed, where a is a scaling factor, typically in the range 1 to 3. The scaling factor is dependent on the fuel type since different fuels exhibit different sensitivity to pressure, and hence, the power-law functions show different scaling factors. The larger scaling factor was commonly used in the literature to characterise a lower pressure. Comprehensive reviews of the effect of elevated pressure on the formation and oxidation of soot in laminar flames can be found in the review papers written by McArragher and Tan [70] as well as Gülder et al. [72]. In the turbulent regime, a mostly linear relationship between the rate of soot formation and pressure was reported in a series of turbulent non-premixed jet flames burning kerosene [75]. In contrast, a study of turbulent methane flames with pressures ranging from 1 bar to 3 bar, revealed larger dependency, more than one order of magnitude, of soot volume fraction on pressure [76]. The effect of increased pressure up to 20 bar was also experimentally investigated using the DLR swirl burner operated on kerosene as the fuel. Due to the complex configuration of the DLR gas turbine model combustor and the differences in the equivalence ratio of the flames, it was difficult to isolate the pressure effects in the turbulent regime [24, 26, 77]. Boyette et al. [78] experimentally investigated a series of turbulent non-premixed C_2H_4/N_2 (65%/35% by volume) flames (KEN flames) with Reynolds number between 10,000 to 50,000 and pressures of 1, 3 and 5 bar. It was observed that for the constant Reynolds number series of flames, consistent with laminar diffusion flames, the peak mean soot volume fraction and volume-integrated mean soot volume fraction scale with the pressure as $P^{2.2}$.

While for the constant velocity series of flames, the peak mean soot volume fraction experiences the same pressure sensitivity as in the other series and the volume-integrated mean soot volume fraction on a per fuel mass basis scales with the pressure as $P^{1.5}$ [78]. The current thesis is focused on soot evolution in flames at atmospheric pressure and will not consider the effect of pressure.

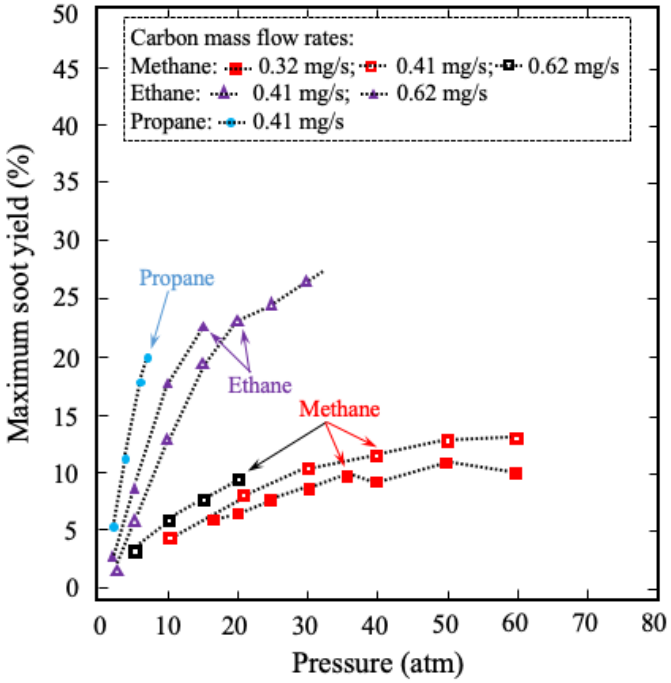

Figure 2.3: Maximum soot yield in a series of co-flow laminar flames of methane, ethane, and propane as a function of pressure at different mass flow rates adopted from [72].

2.2.2 Temperature

There is an established interdependence between soot concentration and the flame temperature in various flames, hence, it is essential to examine the temperature effect and its correlations with soot volume fraction. Soot, when formed in flames, can significantly increase the radiative heat transfer due to the fourth power dependency on the flame temperature. Increasing the soot loading can relatively enhance the radiation and in turn, 'cool' the flame. On the other side, temperature characterises the enthalpy of the reaction which controls many chemical and physical processes within the flame and consequently influences soot concentration. The chemical reaction rate, K, which affects soot formation in flames is exponentially

dependent on the flame temperature, which indicates the smallest change in the temperature would substantially affect the soot yield. The exponential correlation, known as the Arrhenius equation, is expressed as

$$K(T) = A.T^{n}.e^{-E_a/R_u.T} \tag{2.1}$$

where A is the pre-exponential factor, E_a is the activation energy, R_u is the universal gas constant equal to 8.314 J/mol.K, and n is the rate constant which is between $-1 < n < 1$. Noting that the reaction rate for soot nucleation and soot mass growth is estimated by:

$$r_n = 2k_1(T)[C_2H_2]M_s + 6k_2(T)[C_6H_6]M_s \tag{2.2}$$

$$r_g = 2k_3(T)f(A_s)[C_2H_2]M_s \tag{2.3}$$

where r_n is nucleation rate, r_g is growth rate, and M_s is soot molar mass, taken to be 12.011 kg/kmol. The chemical reaction rates (K_i, $i=1:3$) which are dependent on the activation energy for soot formation and oxidation is taken to be between 3.6 $\times 10^{-1}$ to 0.75 $\times 10^{5}$ (kg.mol/m^3.s) [79].

Hence, a thorough understanding of the soot evolution in flames involves the systematic investigating of soot-temperature interaction in both laminar and turbulent regimes. The temperature dependence of soot differs significantly in premixed and diffusion flames. In premixed flames, the C/O ratio plays a vital role in soot formation [34, 56, 80, 81]. The C/O ratio, which is highly dependent on the flame temperature, should be less than unity, except for the detonation case, for soot formation to begins. At a constant C/O ratio, it was shown that soot formation is governed by the chemical kinetics and occurs under oxidation conditions. When the flame temperature decreases in the lower-temperature region of the flames, below 1350 K – 1400 K, the value of the C/O is increased, which results in enhancing the soot volume fraction. Ciajolo et al. [82] also showed that at the low-temperature threshold, on one hand, PAH and other pyrolytic species are largely formed, but on the other side, the low temperature, below 1520 K, inhibits the PAH coagulation, and in turn, soot does not form. At higher temperature regions, due to the high oxidation rate and destroying the PAH, the soot inception is decreased. While in non-premixed flames, the flame temperature is inversely correlated with the soot volume fraction, whereby the lower temperature promotes soot to form [83]. At regions where the temperature is around 1300 K, early soot inception is identified, which then is transported to the higher-temperature zones where surface growth is maintained. Noticeably, at higher temperature regions, the soot oxidation is

enhanced. Figure 2.4 represents the dependence of the flame temperature (K) on the soot yield (%) obtained during the pyrolysis of hydrocarbons including acetylene, allene, and 1,3-butadiene. It shows that the peaks of the temperature profiles are dependent by the observation time and the extinction mode even though the local position of the peak soot yields are dissimilar.

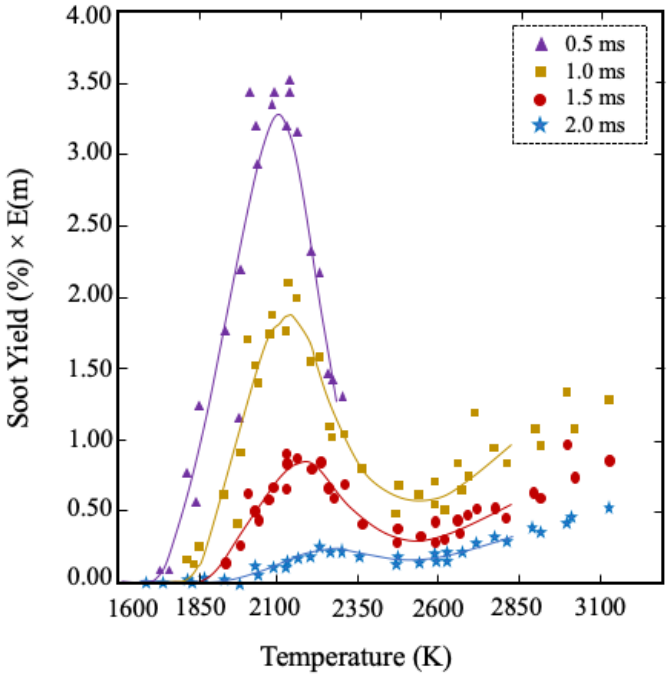

Figure 2.4: Soot yield versus temperature in acetylene pyrolysis adopted from [43].

To measure the flame temperature, several laser-based thermometry techniques have been developed and employed in flames, however, some are limited to a clean combustion environment. A summary of various thermometry techniques is presented in Table 2.1. Some of these techniques rely on elastic and none-elastic scatter from the molecules and others work on fluorescence signal from species, radicals or dopants seeded into the flame.

Rayleigh scattering, for instance, which is a relatively simple thermometry technique, is a form of elastic scattering of light from molecules that allows the flame temperature to be deduced from the ideal gas law by measuring the total molecule number density [84-86]. This method is highly vulnerable to the Mie scattering, elastic-scattered of light from the particles, therefore unfit to be applicable in sooting flames. To overcome the interference of the elastic Mie scattering in the Rayleigh scattering technique, Miles et al. [87] utilised a narrowband filter at the centre-frequency of a single-mode laser to allow thermometry in the presence of strong

elastic scattering, and reject the interference of the scatted light from the particles in the flame which are identical to the incident beam. This technique, known as Filtered Rayleigh scattering (FRS), was broadly employed in the thermography of flames [85, 88-91], however, the variation in Rayleigh cross-section across the reaction zone, remains an obstacle in turbulent flame measurements. Moreover, the FSR is not applicable in sooting flames due to the degradation of the molecular filter performance with pulsed-lasers [92, 93].

Table 2.1: Thermometry techniques applicable in reacting environment [94-126].

Method	Minimum Temp. (^{o}C)	Maximum Temp. (^{o}C)	Response	Accuracy	Ref.
Thermocouple	-270	2300	Very fast	$\pm$0.5 – 2 ^{o}C	[94-99]
Thermographic phosphors	-250	2000	Very fast	0.1 – 5 ^{o}C	[100-102]
Infrared thermometer	-40	2000	Very fast	$\pm$2 ^{o}C	[103, 104]
Shadowgraph	0	2000	Fast	N/A	[105, 106]
Absorption spectroscopy	20	2500	Very fast	15%	[107-109]
Emission spectroscopy	20	2700	Very fast	15%	[110-112]
Rayleigh scattering	20	2500	Very fast	1%	[113-115]
Raman scattering	20	2227	Very fast	7%	[116, 117]
CARS	20	2000	Fast	5%	[118, 119]
LIF	0	2700	Very fast	10%	[120-122]
TLAF	530*	2530	Very fast	5%	[123-126]

**This temperature range is achieved using indium for seeding the flame.*

Another approach that has been developed to get around the problems stemmed from the elastic scattering interference in the Rayleigh scattering technique is the Raman scattering [127]. Unlike Rayleigh scattering, the Raman technique is an inelastic-scattered of light that can shift the frequency to either longer or shorter wavelengths: i.e. Stokes and anti-Stokes. The Stoke to anti-Stoke ratio method requires the measurement of the Stokes to anti-Stokes signal strength, and then deduce the temperature utilising the Boltzman occupation factor for the lines in question [128]. However, the inherently-low signal intensity is insufficient for planar thermometry and is merely limited to point or line measurements [116, 129]. Notable too that the Raman scattering technique is capable to measure the flame temperature approximately in the range of 293 K to 2500 K with 7% accuracy [130].

The aforementioned techniques are not applicable in particle-laden flows and harsh combustion environments such as sooting flames in turbulent regimes. Other approaches such as Coherent Anti-Stokes Raman Spectroscopy (CARS) and Two-

Line Atomic Fluorescence (TLAF) are also used for thermography and do not suffer from particles or droplets interferences [131, 132]. CARS is proven to be a useful non-invasive tool for thermometry as well as the measurement of major-species concentration in reacting flows. This technique utilises two collinear laser beams to induce Raman coherence in the target molecule, which produces a coherent laser-like signal at a blue-shifted wavelength in the phase-matching direction when measured by a third laser. The temperature then is identified from the spectral shape obtained from scanning the Stokes beam across the Raman transitions of the molecules [118]. CARS has several advantages over the other thermography techniques such as spectral selectivity, laser-like directional signal, low absorption, and excellent spatial resolution. Conversely, CARS also suffer from some disadvantages, when employed in turbulent flames, the most important of which is the lack of high spatial fidelity which limits the technique to single-point measurement, rather than planar. Ultimately, CARS is prone to beam steering and attenuation, in sooting flames in particular, due to its reliance on the three laser beams. In addition, the nitrogen molecule has been used in almost all of the CARS measurements and hence its presence in the flame is essential for this technique to work. The accuracy of this method is reported to be approximately 5% and is capable of measuring the temperature in the range of 293 K to 2273 k [103, 133]. Shifted vibrational coherent anti-Stoke Raman spectroscopy (SC-CARS) was employed by Köhler et al. [18] for the measurement of temperature in a lifted turbulent jet flame. Although single-point measurements provided valuable data, the simultaneous planar measurement of the soot and the temperature is desired due to the three-dimensional nature of the turbulent flames.

Another thermometry technique that is not affected by molecular collisions, and therefore is suitable for sooty and spray flames, especially where the planar measurement is desired, is two-line atomic fluorescence (TLAF). The fundamentals of the TLAF technique follow the other two-line fluorescence techniques, whereby the atomic species, such as indium and gallium, utilised in TLAF inhibits sophistication relative to the rotational-vibrational structure of the molecular spectra. Chan et al. [134], for the very first time, *simultaneously* measured the soot concentration and temperature in premixed and non-premixed laminar and wrinkled flames with a view towards its application in turbulent flames. Despite the limited operating range in this technique ($T > 800$ K), the temperature range was found to be sufficient in the regions where soot exist.

Simultaneous measurement of temperature and soot volume fraction, SVF, in turbulent non-premixed jet flames was also conducted by Mahmoud et al. [15]. They employed a non-linear excitation regime two-line atomic fluorescence (NTLAF) and LII for temperature and SVF measurement, respectively. The NTLAF technique, which was developed by Medwell et al. [125], provides stronger signals and higher precision in comparison to the TLAF technique. The details of the NTLAF can be found in [125]. The strong influence of temperature on SVF, which was consistent with the previous understanding of the soot-temperature interaction, was reported. Although Mahmoud's recent work [15] has simultaneously measured the soot-temperature interaction in a series of well-characterised turbulent flames, there is still a need to assess the nexus between temperature and soot in flames where recirculating flows exist, such as bluff-body and swirl flames.

2.2.3 Mixing

The process of mixing the base fuel and the oxidiser is one of the primary governing mechanisms that affects the flame structure, temperature, residence time, as well as soot evolution. Enormous efforts have been undertaken to realise and quantify the effects of mixing on soot in different flames such as steady/un-steady laminar flames and turbulent flames [8-12, 14, 16-19]. In laminar flames, mixing is dominant by convection and diffusion on a molecular level, while in turbulent flames, mixing is largely influenced by the dynamics of the flow. Mixing can be characterised by the residence time and consequently the strain rate. These two parameters, which are dependent to each other, are widely approached in the field. In the following sub-sections, an overview of these two parameters is presented and the relevance of strain rate and residence time to soot are discussed.

2.2.3.1 Strain rate

Strain rate is defined as the local deformation rate of the fluid elements in the presence of velocity gradient. It affects the mixture distribution (mixing) in the flames, and consequently influences the flame temperature and soot formation. The strain rate is calculated from the velocity derivatives obtained from the flow field measurements, i.e. axial and radial velocity components as shown in Equation 2.4.

$$|S_{xy}| = \frac{1}{2}\left|\left(\frac{\partial U}{\partial y} + \frac{\partial V}{\partial x}\right)\right| \quad (2.4)$$

where U and V are the axial and radial velocity components, respectively. In the non-reacting/reacting flow fields, the velocity components (U, V, W) and the velocity fluctuations (u',v',w') can be obtained through both invasive and non-intrusive techniques. The most well-established and commonly-used techniques are laser doppler velocimetry (LDV) [135-138], and particle imaging velocimetry (PIV) [138-141]. LDV is a well-investigated and commercially available measurement technique that determines the spatially and temporally resolved velocity components and higher moments in flames on a point-wise basis. In this method, small particles (usually less than 10 microns) such as Al_2O_3, MgO, TiO_2, and SiO_2 seeded into and passed through the flame [142, 143]. In this technique, a monochromatic laser beam is sent toward a target and collects a reflected radiation. The two beams meet and create a pattern called Doppler shift. As the particles pass through this pattern, they emit light at different frequencies. This frequency depends on the pattern and hence, the velocity of the target can be evaluated. The error associated with this technique is reported to be 3% for mean velocity and 6% for the fluctuations [144]. In reacting environments, Dally et al. [145, 146] used the LDV in a series of turbulent non-premixed bluff-body non-sooting flames fuelled with H_2/CNG and provided invaluable information relevant to the mixing in the recirculation zone in their flames. Although the LDV can effectively measure all velocity components in three-dimensional space, it is only applied for a point (small volume) measurement and is not capable of measuring velocity gradients and large-scale flow structures. It is also unsuitable for flow environments with high spatial velocity gradients and has limited spatial resolutions. This has led to the emergence of other techniques to be applied for 2D and 3D planar measurements such as; PIV and tomographic-PIV [135, 147, 148]. PIV is a non-intrusive laser diagnostic technique that visualises the fluid flow by providing a quantitative measurement of the instantaneous velocity distribution across the flow field. Additionally, PIV offers the advantages of visualisation in a 2D or 3D (tomographic PIV) field over the single point LDV. As with the LDV, the flow is seeded with sufficiently small particles, and illuminated with two consecutive laser beams, usually fired at 532 nm, and separated with a delay depending on the flow condition. The Mie scattering light from the particles seeded to the flow is captured by a CCD camera. Post-processing the image pair provides the velocity components in the field of view. The main source of error in the PIV measurements arises from the regions with high-velocity gradients, where there is a need for interrogation windows. Although the PIV measurements are found to overestimate the true values of the velocity, it is as accurate as 2% of the maximum flow velocity

[139]. PIV has been extensively used in flow visualisation, particularly in clean flames, however, the presence of high concentration of soot makes the application of the PIV technique challenging, due to soot interference on the Mie scattering from the seed particles. Hence, in the current thesis, a novel optical arrangement has been developed and employed in the sooting flame which enables the minimisation of the interference from soot on the PIV signal in flames with high soot loading.

2.2.3.2 Residence time

The residence time of the fuel and fuel-pyrolysed species in the combustion zone, which is defined as the time duration that these fuel parcels spent inside a particular region, can significantly affect the soot formation in various flames. However, measuring the distribution of the particles in a specified zone of a reacting environment and the residence time is quite complex. A few attempts have been made by researchers to evaluate the residence time distribution (RTD) in non-reacting and reacting environments. The residence time distribution (RTD) measurement in reacting flows is challenging due to the high temperature under a reacting environment, thermophoresis effects, and the presence of soot particles. To reduce such complexity, some researchers investigated the RTD in non-reacting flows [6-9]. The RTDs have been evaluated by the measurement of the concentration of a tracer that can be solid or gaseous, employing a technique like laser-induced fluorescence (LIF) or gas analysis methods. For instance, Cheng et al. [149] measured the residence time using a time-resolved planar laser-induced fluorescence (P-LIF) combined with particle image velocimetry (PIV) technique to evaluate the fuel concentration-response to a sudden cut-off in the injection of the fuel stream. They used this system for the residence time measurement in a single-phase isothermal flow, although this technique can also be adapted to a reacting environment. A relatively costly method of radioactive gaseous tracers was developed and used for the solid particles injected in flames [150, 151]. It is important to note that it is unlikely to measure the residence time of soot particles in a flame since they are regularly and quickly formed and destroyed within the flames. In other words, these particles are not conserved within the flame, and hence only the gaseous flow residence time is attempted. Due to complexities and uncertainties found in the literature when attempting the RTD measurements of the reacting flows containing soot particles, in this thesis, the distribution of the particles and the residence time were estimated using validated numerical models.

2.2.4 Fuel type

Molecular structure of the fuel is a major contribution to the soot evolution in flames [152-154]. Calcote and Manos [155] introduced the rational threshold soot index (TSI) and found that the molecular structure plays a major and significant role in the onset of soot formation and is independent of the experimental setup: i.e. premixed or non-premixed mode of combustion. Table 2.2 summarises a series of fuel and the correspondent soot yield in both premixed and non-premixed regimes.

Table 2.2: Summary of the mean soot threshold index measured for different hydrocarbon fuels in both non-premixed and premixed regimes adopted form [155].

Fuel	Formula	Mol. Wt.	C/H	Mean soot index	
				Premixed	Non-premixed
Methane	CH_4	16	0.250	-	-
Ethane	C_2H_6	30	0.333	35 ± 7	0 ± 1.2
Propane	C_3H_8	44	0.375	50 ± 2	0.6 ± 0.7
n-Butane	C_4H_{10}	58	0.400	57 ± 4	1.4 ± 0.2
n-Pentane	C_5H_{12}	72	0.417	-	1.3 ± 0.2
Isopentane	C_5H_{12}	72	0.417	-	-
n-Hexane	C_6H_{14}	86	0.429	64 ± 1	2.5 ± 0.2
2-Methyl pentane	C_6H_{14}	86	0.429	-	2.9 ± 0.0
Cyclohexane	C_6H_{12}	84	0.500	56 ± 3	3.2 ± 0.1
n-Octane	C_8H_{18}	114	0.444	62 ± 10	3.2 ± 0.0
Isooctane	C_8H_{18}	114	0.444	-	-
Decalin	$C_{10}H_{18}$	138	0.556	-	13 ± 0.5
Isododecane	$C_{12}H_{26}$	170	0.462	-	-
n-Cetane	$C_{16}H_{34}$	226	0.471	-	-
Ethylene	C_2H_4	28	0.500	30 ± 6	1.3 ± 0.0
Propylene	C_3H_6	42	0.500	40 ± 3	4.8 ± 2.2
n-Butene	C_4H_8	56	0.500	50 ± 4	-
Isobutene	C_4H_8	56	0.500	65 ± 3	-
n-Pentene	C_5H_{10}	70	0.500	-	-
n-Heptene	C_7H_{14}	98	0.500	60 ± 5	2.7 ± 0.2
1,3-Butadiene	C_4H_6	54	0.667	-	25 ± 1.0
Acetylene	C_2H_2	26	1.00	0.00 ± 1.5	3.7 ± 1.0
Benzene	C_6H_6	78	1.00	80 ± 9	31 ± 0.5
Toluene	C_7H_8	92	0.875	83 ± 7	50 ± 2.0
Xylenes	C_8H_{10}	106	0.800	91 ± 5	51 ± 8.0
Cumene	C_9H_{12}	120	0.750	80 ± 4	-
Dicyclopentadiene	$C_{10}H_{10}$	130	1.00	86 ± 0	-
Tetralin	$C_{10}H_{12}$	132	0.833	98 ± 7	-
1-Methylnaphthalene	$C_{11}H_{10}$	142	1.10	100 ± 9	89 ± 0.0

It was noted that the sooting tendency is strongly affected by the C/H ratio in both pre-mixed and non-premixed flames. Increasing the number of carbon atoms in aromatic compounds leads to the production of more soot, than alkanes and alkenes. Based on these measurements, the tendency of soot in premixed flames is found to follow the order of:

Acetylene < Alkenes < Isoalkanes < *n*-alkanes < Aromatic hydrocarbons < Naphtalenes

This behaviour is applicable for both alkane and alkene fuels in non-premixed flames, which means alkenes produce more soot than alkanes. Moreover, the soot tendency in aromatic fuels is greater than the alkanes and alkenes with single and double C-H bonds. In multi-ring structures, including saturated rings, the soot tendency is higher in comparison to other aromatics. Therefore, in this thesis, two different types of fuels are used; ethylene, categorised as Alkenes, and methane, categorised as Alkanes, and the sooting tendency under turbulent conditions with increased residence time are investigated.

2.2.5 Soot-flowfield interaction

The nexus between the flowfield features and soot formation, oxidation, and transport in various laminar and turbulent flames have been investigated by few researchers in the past, and correlations were established between residence time, strain rate, and soot volume fraction [13, 17, 26]. Laminar counter-flow diffusion flames have been utilised in the investigation of diverse combustion phenomena owing to their unique features, namely: one-dimensional stable flames with well-defined initial and boundary conditions that produce shorter residence time, compared to laminar simple jet flames, and exhibit closer characteristics to turbulent non-premixed jet flames. In an early work, Glassman et al. [154, 156] discovered an inverse relationship between the residence time and the strain rate in a counter-flow flame. They reported that at elevated strain rate regions, the reaction zone is compressed, and consequently, the residence time is reduced which leads to suppression of the soot formation. Decroix and Roberts [157] assessed the effects of fuel type by using natural gas (NG) and propane in a counterflow burner configuration and confirmed that the inverse correlation between the strain rate and the soot volume fraction, irrespective of the fuel composition. Similar correlations

between the local instantaneous soot volume fraction and strain rate were also reported in other counter-flow diffusion flames' studies [158, 159].

Laminar flames have been further utilised to investigate the formation and oxidation of soot mostly because they are better controlled and characterised, and they lend themselves to the use of laser diagnostic techniques to measure soot volume fraction, particle size distribution, number densities, and morphology in laminar configurations. Santoro et al. [3, 160, 161] conducted an extensive investigation of the effects of different parameters such as temperature and flow dynamics on soot formation and oxidation in laminar flames. They used an Argon Ion dual-beam laser velocimetry technique to obtain the axial and radial velocity components and observed an ascending trend in soot concentration against increasing the residence time in their flames similar to counter-flow flames. The outcomes of the investigations in laminar flames all agreed that increasing the flame strain rate resulted in a decrease in both the soot volume fraction and the soot zone thickness [157-159, 162].

Turbulent flames, on the other hand, are the building blocks of combustion studies because they resemble those flames found in practical combustion systems. The latest advancements in non-intrusive measurement techniques have motivated much of the latest work to understand the soot-turbulence interaction in highly-turbulent flames. Kent and Bastin [163] performed a pioneering parametric study of sooting turbulent acetylene diffusion flame, using a laser extinction method for soot measurement, and revealed an inverse relationship between the strain rate and soot volume fraction, consistent with laminar flames. It was noted that soot formation is controlled by fuel-air mixing at low strain rates, while at regions with high strain rates, the formation of soot is dominated by finite-rate chemistry. It was also found that there was a slight decrease in the peak soot concentrations at low strain rate values, whilst at high strain values, a sharp drop in the peak soot was observed. The relationship between the soot volume fraction, particle size, and distribution in a turbulent ethylene flame was measured by Geitlinger et al. [164] and Bockhorn et al. [165], and a wide range of similarities was observed with the trends in laminar sooting flames. Kent and Honnery [166] showed that at low strain rates, the mean soot volume fraction is only a function of the mixture fraction, while at high strains, the soot volume fraction is influenced by both the mixture fraction and the bulk strain rate. These studies confirmed that the inverse correlation which exists between the soot and strain rate in turbulent flames is consistent with observations in the earlier investigations in the laminar flames.

Research in turbulent flames with high soot loading was limited to the investigation of the correlations and trends of global scalars, rather than local, due to the barriers that existed in the diagnostic techniques. The effect of global mixing rate, defined as the ratio of axial jet velocity and jet nozzle diameter (U/D_J), on soot volume fractions was investigated in three different turbulent non-premixed flames including simple jet flames, precessing jet flames, and bluff-body flames with variable global mixing rates [16, 17]. Despite the discrepancies in the mixing characteristics in these flames, an inverse relationship between the total soot and the global mixing, inverse of the global residence time, in the three turbulent flames was reported. This work, however, suffers from the lack of direct comparability owing to the different burner configurations and flow patterns. Additionally, the utilisation of industrial liquefied petroleum gas, LPG (mostly propane) as fuel, is another drawback of this work since the kinetics of the LPG under sooting conditions was unfamiliar for the modellers. Köhler et al. [18-20] investigated the soot-turbulence interaction in a series of turbulent lifted jet flames. In these flames, soot formation is inhibited due to the partial premixing in the lift off region at the base of the flame. Also, such flames are difficult to model due to the premixing induced at the flames base and its effect of soot inception. To solve this issue, Lee et al. [167] used a piloted turbulent non-premixed jet flame and studied the effect of the exit Reynolds number on SVF. These measurements revealed that in turbulent jet flames, while soot volume fraction scales inversely with the global strain rate, which is broadly consistent with previous findings [168], the volume-integrated SVF, scales as an inverse exponential function of the global strain rate. Although they simultaneously measured the SVF, OH radical, and polycyclic aromatic hydrocarbons (PAH) concentrations, they did not isolate the effect of the Reynolds number from strain rate changes. To address this gap, Mahmoud et al. [13-15], in a comprehensive parametric investigation, isolated the effects of global strain rate and Reynolds number and provided detailed insight into the soot-turbulence interactions in well-characterised turbulent non-premixed simple jet flames fuelled with a mixture of $C_2H_4/H_2/N_2$ (40:41:19 by vol.). They confirmed the existence of the inverse relationship between the soot volume fraction and the global exit strain rate. The total soot yield linearly scaled with both the jet diameter and the fuel flow rate and was found to be a function of the exit strain rate and the flame volume. Additionally, they assessed the effects of the Reynolds number while keeping the exit strain rate unchanged. Measurements of the mean, instantaneous and integrated soot volume fraction revealed a weak inverse dependence on the exit Reynolds number.

These studies, despite their significance, are mostly limited to the global values rather than local instantaneous correlations. On an instantaneous local basis, soot

and velocity fields were simultaneously measured in the soot inception region of a series of simple jet flames, and the correlations between the instantaneous soot, axial velocity, and strain rate have been extracted [169]. It was observed that increasing the Reynolds number resulted in higher soot intermittency. Furthermore, at higher strain rates, soot was found to form closer to the reaction zone than previously thought. Deduced from the joint statistical calculations, a preferred velocity of 3 m/s and the strain rate of 700 s^{-1} were reported as the most favourable for soot formation. Nonetheless, their findings were only confined to the soot inception region close to the flame base, which cannot be extended to all regions of the flame.

The above-mentioned investigations conducted in turbulent simple, attached and lifted, jet flames represent parabolic flows where no recirculating flows exist. The complex recirculating flows which can be produced by means of swirlers or bluff-bodies are broadly used in practical combustion applications. To bridge this gap, few investigations have been carried out in modelled gas turbines to study soot and flowfield interactions in flames with recirculating flows. It was shown that the recirculating flows can significantly increase the residence time and create regions of enhanced soot formation and transport [170]. Meyer et al. [171] carried out simultaneous soot and OH radical measurements utilising LII and OH-PLIF in swirl-stabilised flames. They found spotty, irregular, and intermittent soot pockets formed in the inner cone region between the inner recirculation zone (IRZ) and the conical spray, and then transported to the outside of the spray region. However, no velocity measurements were conducted, and these findings were deduced only based on the soot data. The gas turbine model combustor fuelled with ethylene was extensively investigated by Geigle et al. [23-26], and soot volume fraction, temperature, velocity, and OH radicals have been measured using LII, CARS, tomographic PIV, and OH-PLIF diagnostic techniques to further expand the knowledge of the soot formation, oxidation, and transport in these flames. They noted that soot is not detected in the high velocity and high strain rate regions, and was mainly found in the inner recirculation zone where the strain rate is relatively low (below 1000 s^{-1}). Stöhr et al. [172] utilised joint high-speed measurements and large eddy simulation (LES) and found that soot is formed where the rich burned gas succeeded in the inner recirculation zone (IRZ) with low flow velocity and strain rate. Also, they noted that the soot intermittency in these flames was mainly driven by the intermittent flow field of lean burned gas in the IRZ. Although gas turbine model combustors can be useful to study many turbulent phenomena in a flame, laboratory-scale bluff-body flames, on the other side, can easily emulate the recirculating flows which are broadly employed for flame stabilization. Additionally, bluff-body flames have better defined

initial and boundary conditions when compared with swirl-stabilised flames, which are highly-desired by modellers. The stabilisation mechanism and recirculation of a hot mixture of reactants and products to the exit plane allows for increasing the Reynolds number to very high values (above 50,000) which are not easily achievable in other burner configurations. Mueller et al. [22] used a joint experimental and computational investigation to further assess the soot formation and oxidation in Adelaide bluff-body ISF workshop target flame 4 [172]. Experimentally, using the LII technique, to measure soot volume fraction, they found out that soot formation in the jet-propagation region of the bluff-body flames is similar to that of turbulent simple jet flames, however, in the recirculation zone, the residence time plays a dominant role in the amount of soot which is formed in this region. In the neck zone, where the recirculation zone is connected to the jet-like region, only a small amount of soot is found in the neck zone which has survived from the recirculation zone and is transported to the neck, since the high strain rate in the neck zone inhibits soot formation in this region. Computationally, using an advanced LES model, they found a unique feature of the soot formation and growth mechanism in non-premixed bluff-body flames. Unlike the simple jet flames in which the PAH-based growth (nucleation and oxidation) is dominant over the surface growth, in bluff-body flames, the mixture fraction cannot support the PAH-based model and hence, the acetylene-based surface growth was found to be the dominant surface process by a factor of more than five. Figure 2.5 compares the two different growth mechanisms together with a typical soot volume fraction contour for a bluff-body flame [22]. The bi-modal soot structure in the recirculation zone shows the inner peak was due to the soot inception, while the second maxima represent the acetylene-based surface growth.

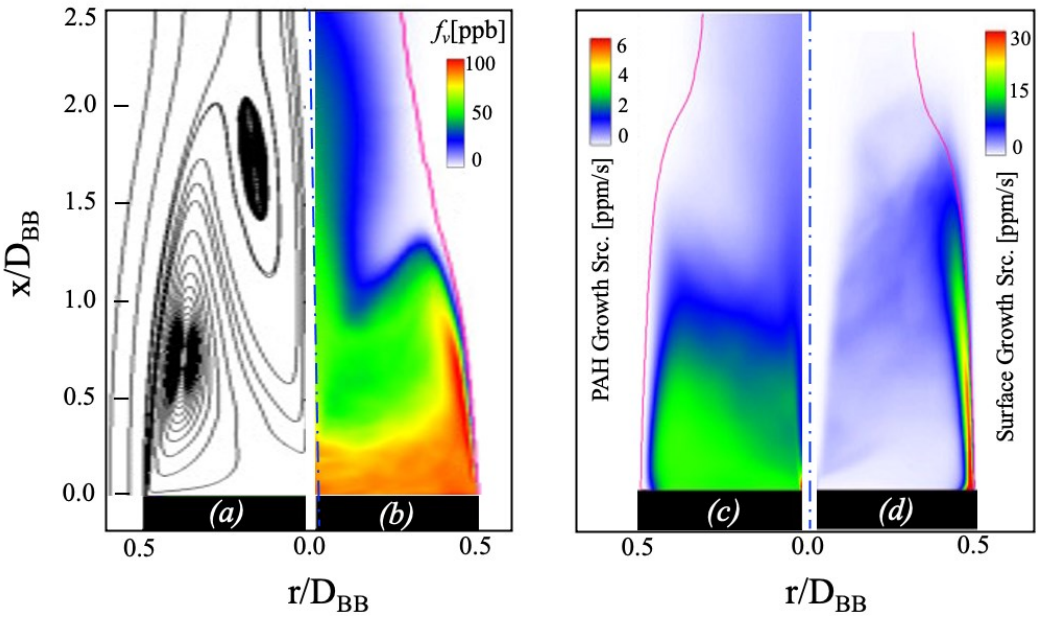

Figure 2.5: (a) Time-averaged stream lines; (b) time-averaged soot volume fraction; (c) PAH-based source includes nucleation and condensation; and (d) the acetylene-based source includes surface growth only in the recirculation zone obtained from the LES adopted from [22].

While aforesaid studies provide important insight into the interaction between soot and flowfield features in turbulent flames, there are structural differences in the soot formation and growth mechanism in the flames where recirculating flows are employed as a flame stabilisation mechanism. In these flames, the soot formation and destruction is significantly affected by the increased residence time created as a result of the recirculating flows in the combustion domain. Due to the extensive application of such flames, including bluff-body flames and swirl-stabilised flames in practical combusting devices, and lack of sufficient dataset to validate computational models, there remains a necessity to perform a systematic study on the effect of residence time on soot evolution in turbulent flames in order to improve the understanding of the soot formation, oxidation, and transport mechanism in these flames.

2.3 Aim and objectives of the thesis

Substantial progress has been made, over many decades, to improve the understanding of the complex process of soot formation and oxidation in both laminar and turbulent flames. Many of these studies employed simplified boundary conditions such as simple jet flames. Limited number of studies reporting on flames with more complex fluid dynamics while isolating one or more of controlling parameters. The reviewed literature, in the previous section, revealed that very few available studies divulge structural differences in the soot inception and growth mechanism in flames with strong recirculating flows. Although efforts have been devoted to understanding the soot-turbulence interactions in model gas turbines, the following gaps have been identified in the literature and are yet to be answered:

1. The effects of increased residence time and the mixture strength on soot inception and growth in the turbulent flames with recirculating flows have not been systematically investigated.

2. Simultaneous measurements of flow field and soot volume fraction under high soot loading is not available for flames with strong recirculating flows. From the literature it is clear that the flow field measurement in turbulent flames with high soot loading has been a challenge for quite some time. The complexity primarily arises from the interference of soot particles at the PIV excitation wavelength, e.g. 532 nm. Previous flow field measurements were confined to either the upstream region of the simple jet flames, where instantaneous soot volume fraction was reported to be less than 60 ppb [169] or model gas turbines with relatively low soot load (below 10 ppb) [23, 24, 57]. In order to eliminate this obstacle in the simultaneous measurement of the soot-flow field in flames with a high soot concentration and high soot intermittency, there is a pressing need to develop the current flow field measurement techniques to allow measurements of the flow-field across the entire flame length, as well as the regions with relatively high residence time and soot volume fraction.

3. The statistical data relevant to the flow field features such as axial and radial velocity components as well as the strain rate, and also the soot volume fraction in the turbulent bluff-body flames is scarcely found in the literature for turbulent flames with high soot load. Additionally, there is a lack of sufficient joint statistical analyses in the literature to understand the correlations between local instantaneous soot volume fraction and turbulence field in different regions of the bluff-body flames.

4. Soot evolution differs for different fuels under the same operating conditions mainly due to the molecular structure of the chemical compounds. It is yet to be investigated how soot evolution differs for different fuels under increased residence time conditions in the recirculation zone and further evolution in the jet-propagation region in bluff-body flames. Most of the past research has mainly focused on ethylene because of its simple well-known chemistry, as well as its high soot yield. However, more practical fuels, such as methane due to its broad application in industry, particularly in gas turbines, are of crucial importance. Hence, there is a necessity to resolve the sensitivity of the fuel type to the soot volume fraction in turbulent recirculating flames.

Based on the aforementioned gaps in the context of soot formation, the current study aims to develop a new understanding of the interaction between flow-field features (velocity, strain rate, residence time) and soot evolution in turbulent flames with complex fluid dynamics (Bluff body flames), and advance the understanding of the sensitivity of soot evolution to the fuel composition under turbulent conditions.

To achieve this aim, the objectives of the thesis are as follows:

- To understand the flowfield characteristics, using non-intrusive advanced PIV technique, in highly-sooting flames by measuring the mean and instantaneous axial and radial components of the velocity, and calculating the strain rate in various zones of the non-premixed bluff-body flames;

- To isolate the effect of residence time via increasing the bluff-body diameter while keeping other dimensions and operating conditions the same, on soot volume fraction and flow field features;

- To realize the soot evolution sensitivity to the fuel type through using two different fuel compositions: ethylene/nitrogen (80:20 by Vol.) and pure methane;

- To investigate the correlations between the mean and instantaneous soot volume fraction and the strain rate for various operating conditions and fuels.

2.4 References

[1] M. Kholghy, M. Saffaripour, C. Yip, and M. J. Thomson, "The evolution of soot morphology in a laminar coflow diffusion flame of a surrogate for Jet A-1", Combustion and Flame, vol. 160, no. 10, pp. 2119-2130, 2013.

[2] P. Markatou, H. Wang, and M. Frenklach, "A computational study of sooting limits in laminar premixed flames of ethane, ethylene, and acetylene", Combustion and Flame, vol. 93, no. 4, pp. 467-482, 1993.

[3] R. J. Santoro, T. T. Yeh, J. J. Horvath, and H. G. Semerjian, "The Transport and Growth of Soot Particles in Laminar Diffusion Flames", Combustion Science and Technology, vol. 53, no. 2-3, pp. 89-115, 1987.

[4] C. R. Shaddix and T. C. Williams, "Measurements of the velocity field in laminar ethylene inverse jet diffusion flames", Combustion and Flame, vol. 156, no. 4, pp. 942-945, 2009.

[5] M. Smooke, M. Long, B. Connelly, M. Colket, and R. Hall, "Soot formation in laminar diffusion flames", Combustion and Flame, vol. 143, no. 4, pp. 613-628, 2005.

[6] Z.W. Sun, B.B. Dally, G.J. Nathan, and Z. T.Alwahabi, "Effects of hydrogen and nitrogen on soot volume fraction, primary particle diameter and temperature in laminar ethylene/air diffusion flames", Combustion and Flame, vol. 175, pp. 270-282, 2017.

[7] Z. Xu, H. Zhao, X. Chen, and C. Lou, "Multi-parameter measurements of laminar sooting flames using thermophoretic sampling technique", Combustion and Flame, vol. 180, pp. 158-166, 2017.

[8] K. K. Foo, P. R. Medwell, Z. T. Alwahabi, G. J. Nathan, and B. B. Dally, "Influence of nozzle diameter on soot evolution in acoustically forced laminar non-premixed flames", Combustion and Flame, vol. 194, pp. 376-386, 2018.

[9] A. Jocher, K. K. Foo, Z. W. Sun, B. B Dally, H. Pitsch, Z. T. Alwahabi, and G. J. Nathan, "Impact of acoustic forcing on soot evolution and temperature in ethylene-air flames", Proceedings of the Combustion Institute, vol. 36, no. 1, pp. 781-788, 2017.

[10] K. K. Foo, M. J. Evans, Z. W. Sun, P. R. Medwell, Z. T. Alwahabi, G. J. Nathan, and B. B Dally, "Calculated concentration distributions and time histories

of key species in an acoustically forced laminar flame", Combustion and Flame, vol. 204, pp. 189-203, 2019.

[11] K. K. Foo, Z. W. Sun, P. R. Medwell, Z. T. Alwahabi, G. J. Nathan, and B. B. Dally, "Experimental investigation of acoustic forcing on temperature, soot volume fraction and primary particle diameter in non-premixed laminar flames", Combustion and Flame, vol. 181, pp. 270-282, 2017.

[12] K. K. Foo, Z. W. Sun, P. R. Medwell, Z. T. Alwahabi, G. J. Nathan, and B. B. Dally, "Soot evolution and flame response to acoustic forcing of laminar non-premixed jet flames at varying amplitudes", Combustion and Flame, vol. 198, pp. 249-259, 2018.

[13] S. M. Mahmoud, G. J. Nathan, Z. T. Alwahabi, Z. W. Sun, P. R. Medwell, and B. B. Dally, "The effect of exit strain rate on soot volume fraction in turbulent non-premixed jet flames", Proceedings of the Combustion Institute, vol. 36, no. 1, pp. 889-897, 2017.

[14] S. M. Mahmoud, G. J. Nathan, Z. T. Alwahabi, Z. W. Sun, P. R. Medwell, and B. B. Dally, "The effect of exit Reynolds number on soot volume fraction in turbulent non-premixed jet flames", Combustion and Flame, vol. 187, pp. 42-51, 2018.

[15] S. M. Mahmoud, G. J. Nathan, P. R. Medwell, B. B. Dally, and Z. T. Alwahabi, "Simultaneous planar measurements of temperature and soot volume fraction in a turbulent non-premixed jet flame", Proceedings of the Combustion Institute, vol. 35, no. 2, pp. 1931-1938, 2015.

[16] N. H. Qamar, Z. T. Alwahabi, Q. N. Chan, G. J. Nathan, D. Roekaerts, and K. D. King, "Soot volume fraction in a piloted turbulent jet non-premixed flame of natural gas", Combustion and Flame, vol. 156, no. 7, pp. 1339-1347, 2009.

[17] N. H. Qamar, G. J. Nathan, Z. T. Alwahabi, and K. D. King, "The effect of global mixing on soot volume fraction: measurements in simple jet, precessing jet, and bluff body flames", Proceedings of the Combustion Institute, vol. 30, no. 1, pp. 1493-1500, 2005.

[18] M. Köhler, I. Boxx, K. -P. Geigle, and W. Meier, "Simultaneous planar measurements of soot structure and velocity fields in a turbulent lifted jet flame at 3 kHz", Applied Physics B, vol. 103, no. 2, pp. 271-279, 2011.

[19] M. Köhler, K.-P. Geigle, T. Blacha, P. Gerlinger, and W. Meier, "Experimental characterization and numerical simulation of a sooting lifted turbulent jet diffusion flame", Combustion and Flame, vol. 159, no. 8, pp. 2620-2635, 2012.

[20] M. Köhler, K. -P. Geigle, W. Meier, B. M. Crosland, K. A. Thomson, and G. J. Smallwood, "Sooting turbulent jet flame: characterization and quantitative soot measurements", Applied Physics B, vol. 104, no. 2, pp. 409-425, 2011.

[21] S. Deng, M. E. Mueller, Q. N. Chan, N. H. Qamar, B. B. Dally, Z. T. Alwahabi, and G. J. Nathan, "Hydrodynamic and chemical effects of hydrogen addition on soot evolution in turbulent nonpremixed bluff body ethylene flames", Proceedings of the Combustion Institute, vol. 36, no. 1, pp. 807-814, 2017.

[22] M. E. Mueller, Q. N. Chan, N. H. Qamar, B. B. Dally, H. Pisch, Z. T. Alwahabi, and G. J. Nathan., "Experimental and computational study of soot evolution in a turbulent nonpremixed bluff body ethylene flame", Combustion and Flame, vol. 160, no. 7, pp. 1298-1309, 2013.

[23] K. -P. Geigle, R. Hadef, M. Stöhr, and W. Meier, "Flow field characterization of pressurized sooting swirl flames and relation to soot distributions", Proceedings of the Combustion Institute, vol. 36, no. 3, pp. 3917-3924, 2017.

[24] K. -P. Geigle, M. Köhler, W. O'Loughlin, and W. Meier, "Investigation of soot formation in pressurized swirl flames by laser measurements of temperature, flame structures and soot concentrations", Proceedings of the Combustion Institute, vol. 35, no. 3, pp. 3373-3380, 2015.

[25] M. Grader, Z. Yin, K. -P. Geigle, and P. Gerlinger, "Influence of flow field dynamics on soot evolution in an aero-engine model combustor", Proceedings of the Combustion Institute, vol. 38, no. 4, pp. 6421-6429, 2020.

[26] K. -P. Geigle , R. Hadef, and W. Meier, "Soot formation and flame characterization of an aero-engine model combustor burning ethylene at elevated pressure", Journal of Engineering for Gas Turbines and Power, vol. 136, no. 2, pp. 021505, 2014.

[27] L.-Y. Wang, C. K. Bauer, and Ö. L. Gülder, "Soot and flow field in turbulent swirl-stabilized spray flames of Jet A-1 in a model combustor", Proceedings of the Combustion Institute, vol. 37, no. 4, pp. 5437-5444, 2019.

[28] M. J. Evans, P. R. Medwell, Z. W. Sun, A. Chinnici, J. Ye, Q. N. Chan, and B. B. Dally, "Downstream Evolution of n-Heptane/Toluene Flames in Hot and Vitiated Coflows", Combustion and Flame, vol. 202, pp. 78–89, 2019.

[29] J. Ye, P. R. Medwell, B. B. Dally, and M. J. Evans, "The transition of ethanol flames from conventional to MILD combustion", Combustion and Flame, vol. 171, pp. 173-184, 2016.

[30] M. Frenklach, "Reaction mechanism of soot formation in flames", Physical chemistry chemical Physics, vol. 4, pp. 2028-2037, 2002.

[31] M. Thomson and T. Mitra, "A radical approach to soot formation", Science (American Association for the Advancement of Science), vol. 36, no. 6406, pp. 978-979, 2018.

[32] K. H. Homann and H. G. Wagner, "Some new aspects of the mechanism of carbon formation in premixed flames", Proceedings of the Combustion Institute, vol. 11, pp. 371, 1967.

[33] H. F. Calcote, "Mechanisms of soot nucleation in flames—a critical review", Combustion and Flame, vol. 42, pp. 215, 1981.

[34] B. S. Haynes and H. G. Wagner, "Soot Formation", Progress in Energy and Combustion Science, vol. 7, no. 4, pp. 229-273, 1981.

[35] M. Frenklach, D. W. Clary, W. C. Gardiner, and S. E. Stein, "Effect of fuel structure on pathways to soot", Proceedings of the Combustion Institute, vol. 21, pp. 1067, 1986.

[36] M. Frenklach, W. C. Gardiner, S. E. Stein, D. W. Clary, and T. Yuan, "Mechanism of soot formation in acetylene-oxygen mixtures", Combustion Science and Technology, vol. 50, pp. 79, 1986.

[37] M. Frenklach and J. Warnatz, "Detailed modeling of PAH profiles in a sooting low-pressure acetylene flame", Combustion Science and Technology, vol. 51, pp. 265, 1987.

[38] M. Frenklach, T. Yuan, and M. K. Ramachandra, "Soot formation in binary hydrocarbon mixtures", Energy and Fuels, vol. 2, pp. 462, 1988.

[39] J. A. Miller and C. F. Melius, "Kinetic and thermodynamic issues in the formation of aromatic compounds in flames of aliphatic fuels", Combustion and Flame, vol. 91, no. 1, pp. 21-39, 1992.

[40] R. D. Kern and K. Xie, "Shock tube studies of gas phase reactions preceding the soot formation process", Progress in Energy and Combustion Science, vol. 17, pp. 191-210, 1991.

[41] S. E. Stein, J. A. Walker, M. M. Suryan, and A. Fahr, "A new path to benzene in flames", Proceedings of the Combustion Institute, vol. 23, no. 1, pp. 85-90, 1991.

[42] U. Alkemade and K. H. Homann"Formation of C6H6 Isomers by Recombination of Propynyl in the System Sodium Vapour/Propynylhalide", Physical Chemistry Chemical Physics, vol. 161, pp. 19-26, 1989.

[43] M. Frenklach, S. Taki, M. B. Durgaprasad, and R. A. Matula, "Soot formation in shock-tube pyrolysis of acetylene, allene, and 1,3-butadiene", Combustion and Flame, vol. 54, no. 1-3, pp. 81-101, 1983.

[44] C. F. Melius, M. E. Colvin, N. M. Marinov, W. J. Pitz, and S. M. Senkan, "Reaction mechanisms in aromatic hydrocarbon formation involving the C5H5 cyclopentadienyl moiety", Proceedings of the Combustion Institute, vol. 26, no. 1, pp. 685-692, 1996.

[45] N. M. Marinov, W. J. Pitz, C. K. Westbrook, M. J. Castaldi, and S. M. Senkan, "Modeling of aromatic and polycyclic aromatic hydrocarbon formation in premixed methane and ethane ames", Combustion Science and Technology, vol. 116, no. 1-6, pp. 211-287, 1996.

[46] E. Ikeda, R. S. Tranter, J. H. Kiefer, R. D. Kern, H. J. Singh, and Q. Zhang, "The pyrolysis of methylcyclopentadiene: Isomerization and formation of aromatics", Proceedings of the Combustion Institute, vol. 28, no. 2, pp. 1725-1732, 2000.

[47] M. Frenklach, "Reaction mechanism of soot formation in flames", Physical Chemistry Chemical Physics, 10.1039/B110045A vol. 4, no. 11, pp. 2028-2037, 2002.

[48] A. Raj, "Formation, growth and oxidation of soot: a numerical study", PhD Thesis, University of Cambridge, 2010.

[49] M. B. Colket and D.J. Seery, "Reaction mechanisms for toluene pyrolysis", Proceedings of the Combustion Institute, vol. 25, no. 1, pp. 883-891, 1994.

[50] A. D'Anna and A. Violi, "A kinetic model for the formation of aromatic hydrocarbons in premixed laminar flames", proceedings of the Combustion Institute, vol. 27, no. 1, pp. 425-433, 1998.

[51] A. D'anna, A. D'Alessio, and J. Kent, "A computational study of hydrocarbon growth and the formation of aromatics in coflowing laminar diffusion flames of ethylene", Combustion and Flame, vol. 125, no. 3, pp. 1196-1206, 2001.

[52] C. S. McEnally and L. D. Pfefferle, "The use of carbon-13-labeled fuel dopants for identifying naphthalene formation pathways in non-premixed flames", Proceedings of the Combustion Institute, vol. 28, no. 2, pp. 2569-2576, 2000.

[53] C. J. Pope and J. A. Miller, "Exploring old and new benzene formation pathways in low-pressure premixed flames of aliphatic fuels", Proceedings of the Combustion Institute, vol. 28, no. 1, pp. 1519-1527, 2000.

[54] J. A. Mulholland, M. Lu, D. H. Kim, "Pyrolytic growth of polycyclic aromatic hydrocarbons by cyclopentadienyl moieties", Proceedings of the Combustion Institute, vol. 28, no. 2, pp. 2593-2599, 2000.

[55] A. D'Anna, "Combustion-formed nanoparticles", Proceedings of the Combustion Institute, vol. 32, no. 1, pp. 593-613, 2009.

[56] Z. A. Mansurov, "Soot Formation in Combustion Processes (Review)", Combustion, Explosion, and Shock Waves, vol. 41, no. 6, pp. 727-744, 2005.

[57] H. Wang, "Formation of nascent soot and other condensed-phase materials in flames", Proceedings of the Combustion Institute, vol. 33, no. 1, pp. 41-67, 2011.

[58] S. B. Dworkin, Q. Zhang, M. J. Thomson, N. A. Slavinskaya, and U. Riede, "Application of an enhanced PAH growth model to soot formation in a laminar coflow ethylene/air diffusion flame", Combustion and Flame, vol. 158, no. 9, pp. 1682-1695, 2011.

[59] U. O. Koylu and G. M. Faeth, "Structure of overfire soot in buoyant turbulent diffusion flames at long residence times", Combustion and Flame, vol. 89, no. 2, pp. 140-156, 1992.

[60] U. O. Koylu and G. M. Faeth, "Optical properties of overfire soot in buoyant turbulent diffusion flames at long residence times", Journal of Heat Transfer, vol. 116, no. 1, pp. 152-159, 1994.

[61] P. Roth, O. Brandt, and S. V. Gersum, "High temperature oxidation of suspended soot particles verified by CO and CO2 measurements", Proceedings of the Combustion Institute, vol. 23, no. 1, pp. 1485-1491, 1991.

[62] A. Garo, G. Prado, and J. Lahaye, "Chemical aspects of soot particles oxidation in a laminar methane-air diffusion flame", Combustion and Flame, vol. 79, no. 3-4, pp. 226-233, 1990.

[63] F. Liu, H. Guo, G. J. Smallwood, and Ö. L. Gülder, "Numerical modelling of soot formation and oxidation in laminar coflow non-smoking and smoking ethylene diffusion flames", Combustion Theory and Modelling, vol. 7, no. 2, pp. 301-315, 2003.

[64] N. A. Eaves, A. Veshkini, C. Riese, Q. Zhang, S. B. Dworkin, and M. J. Thomson, "numerical study of high pressure, laminar, sooting, ethane-air coflow diffusion flames", Combustion and Flame, vol. 159, no. 10, pp. 3179-3190, 2012.

[65] H. Richter and J. B. Howard, "Formation of polycyclic aromatic hydrocarbons and their growth to soot-a review of chemical reaction pathways", Progress in Energy and Combustion Science, vol. 26, no. 4-6, pp. 565-608, 2000.

[66] F. Xu, A. M. El-Leathy, C. H. Kim, and G. M. Faeth., "Soot surface oxidation in hydrocarbon/air diffusion flames at atmospheric pressure", Combustion and Flame, vol. 132, no. 1-2, pp. 43-57, 2003.

[67] K. G. Neoh, J. B. Howard, and A. F. Sarofim, "Effect of oxidation on the physical structure of soot", Proceedings of the Combustion Institute, vol. 20, no. 1, pp. 951-957, 1985.

[68] H. Ghiassi, I. C. Jaramillo, P. Toth, and J. S. Lighty, "Soot oxidation-induced fragmentation: Part 2: Experimental investigation of the mechanism of fragmentation"‟, Combustion and Flame, vol. 163, pp. 170-178, 2016.

[69] H. Ghiassi, P. Toth, I. C. Jaramillo, and J. S. Lighty, "Soot oxidation-induced fragmentation: Part 1: The relationship between soot nanostructure and oxidationinduced fragmentation", Combustion and Flame, vol. 163, pp. 179-187, 2016.

[70] J. S. McArragher and K. J. Tan, "Soot formation at high pressures: A literature review", Combustion Science and Technology, vol. 5, no. 1, pp. 257-261, 1972.

[71] H. I. Joo and Ö. L. Gülder, "Experimental study of soot and temperature field structure of laminar co-flow ethylene–air diffusion flames with nitrogen dilution at elevated pressures", Combustion and Flame, vol. 158, no. 3, pp. 416-422, 2011.

[72] A. E. Karataş and Ö. L. Gülder, "Soot formation in high pressure laminar diffusion flames", Progress in Energy and Combustion Science, vol. 38, no. 6, pp. 818-845, 2012.

[73] L. L. McCrain and W. L. Roberts, "Measurements of the soot volume field in laminar diffusion flames at elevated pressures", Combustion and Flame, vol. 140, no. 1-2, pp. 60-69, 2005.

[74] E. C. W. Smith, "The emission spectrum of hydrocarbonflames", Proceedings of the Royal Society, vol. 174, pp. 110-125, 1940.

[75] K. J. Young, C. D. Stewart, and J. B. Moss, "Soot formation in turbulent nonpremixed kerosine-air flames burning at elevated pressure: experimental measurements", Proceedings of the Combustion Institute, vol. 25, no. 4, pp. 609-617, 1994.

[76] S.J. Brookes and J. B. Moss, "Measurements of soot production and thermal radiation from confined turbulent jet diffusion flames of methane", Combustion Science and Technology, vol. 116, no. 1-2, pp. 49-61, 1999.

[77] M. Stöhr, K. P. Geigle, R. Hadef, I. Boxx, C. D. Carter, M. Grader, and P. Gerlinger, "Time-resolved study of transient soot formation in an aero-engine model combustor at elevated pressure", Proceedings of the Combustion Institute, vol. 37, no. 4, pp. 5421-5428, 2019.

[78] W. R. Boyette, A. M. Bennett, E. Cenkar, T. F. Guiberti, and W. L. Roberts, "Effects of pressure on soot production in piloted turbulent non-premixed jet flames", Combustion and Flame, vol. 227, pp. 271-282, 2021.

[79] R.M. Woolley and M. Fairweather, "Conditional moment closure prediction of soot formation in turbulent, nonpremixed ethylene flames", Combustion and Flame, vol. 152, no. 3, pp. 360-376, 2008.

[80] M. Alfè, B. Apicella, J. N. Rouzaud, A. Tregrossi, and A. Ciajolo, "The effect of temperature on soot properties in premixed methane flames", Combustion and Flame, vol. 157, no. 10, pp. 1959-1965, 2010.

[81] B. Apicella, A. Tregrossi, A. Ciajolo, J. Abrahamson, R.L. Vander Wal, and C. Russo, "The Effect of Temperature on Soot Properties in Premixed Ethylene Flames", Combustion Science and Technology, vol. 191, no. 9, 2019.

[82] A. Ciajolo, A. D'Anna, R. Barbella, A. Tregrossi, and A. Violli, "The effect of temperature on soot inception in premixed ethylene flames", Proceedings of the Combustion Institute, vol. 26, pp. 2327-2333, 1996.

[83] L. J. Weng, "Distribution Characteristics of Gas Temperature and Soot Fraction Volume in Ethylene/air Inverse Diffusion Flame", Acta Chimica Sinica, vol. 69, pp. 1011-1016, 2011.

[84] R. W. Dibble and R. E. Hollenbach, "Laser Rayleigh thermometry in turbulent flames", Proceedings of the Combustion Institute, vol. 18, pp. 27515, 1981.

[85] D. Hoffman, K. U. Münch, andA. Leipertz, "Two-dimensional temperature determination in sooting flames by filtered Rayleigh scattering", Optics Letters, vol. 21, no. 7, pp. 525-527, 1996.

[86] R. B Miles, W. R. Lempert, and J. N. Forkey, "Laser Rayleigh scattering", Measurement Science and Technology, vol. 12, no. 5, pp. 33-51, 2001.

[87] R. Miles, J. Forkey, and W. R. Lempert, "Filtered Rayleigh scattering measurements in supersonic/hypersonic facilities", presented at the AIAA 17th Aerospace Ground Testing Conference, Nashville, USA, 1992.

[88] G. S. Elliott, N. Glumac, and C. D. Carter, "Molecular filtered Rayleigh scattering applied to combustion", Measurement Science and Technology, vol. 12, pp. 452-466, 2001.

[89] S. P. Kearney, R. W. Schefer, S. J. Beresh, and T. W. Grasser, "Temperature imaging in non-premixed flames by joint Rayleigh and Raman scattering", Applied Optics, vol. 44, pp. 1546-1558, 2005.

[90] R. B. Miles, A. P. Yalin, Z. Tang, S. H. Zaidi, and J. N. Forkey, "Flow field imaging through sharp-edged atomic and molecular 'notch' filters", Measurement Science and Technology, vol. 12, pp. 442-451, 2001.

[91] A. P. Yalin and R. B. Milles, "Ultraviolet filtered Rayleigh scattering temperature measurements with a mercury filter", Optics Letters, vol. 24, pp. 590-592, 1999.

[92] G. S. Elliott and T. J. Beutner, "Molecular filter based planar doppler velocimetry", Progress in Aerospace Science, vol. 35, pp. 799-845, 1999.

[93] S. J. Beresh, T. W. Grasser, and S. P. Kearney, "Filtered Rayleigh scattering diagnostic for multi-parameter thermal-fluids measurements", in "LDRD final report", Sandia National Laboratories, 2004.

[94] A Ballantyne and J. B. Moss, "Fine wire thermocouple measurements of fluctuating temperature", Combustion Science and Technology, vol. 17, no. 1-2, pp. 63-72, 1977.

[95] L. J. Forney and G. C. Fralick, "Two wire thermocouple: Frequency response in constant flow", Review of Scientific Instruments, vol. 65, pp. 3252-3257, 1994.

[96] P. G. O'Reilly, R. J. Kee, R. Fleck, and P. T. McEntee, "Two-wire thermocouples: A nonlinear state estimation approach to temperature reconstruction", Review of Scientific Instruments, vol. 72, pp. 3449-3457, 2001.

[97] M. Tagawa and Y. Ohta, "Two-thermocouple probe for fluctuating temperature measurement in combustion—Rational estimation of mean and fluctuating time constants", Combustion and Flame, vol. 109, no. 4, pp. 549-560, 1997.

[98] P. A. Santoni, T. Marcelli, E. Leoni, "Measurement of fluctuating temperatures in a continuous flame spreading across a fuel bed using a double thermocouple probe", Combustion and Flame, vol. 131, no. 1-2, pp. 47-58, 2002.

[99] C. R. Shaddix, "Correcting thermocouple measurements for radiation loss: A critical review", Sandia National Labs, Livermore, CA (US), 1999.

[100] S. W. Allison and G. T. Gillies, "Remote thermometry with thermographic phosphors: Instrumentation and applications", Review of Scientific Instruments, vol. 68, pp. 2615 -2650, 1997.

[101] A. Omrane, P. Patersson, M. Aldén, and M. A. Linne "Simultaneous 2D flow velocity and gas temperature measurements using thermographic phosphors", Applied Physics B, vol. 92, pp. 99-102, 2008.

[102] M. Aldén, A. Omrane, M. Richter, G. Särner, "Thermographic phosphors for thermometry: A survey of combustion applications", Progress in Energy and Combustion Science, vol. 37, no. 4, pp. 422-461, 2011.

[103] P. R. N. Childs, J. R. Greenwood, and C. A. Long, "Review of temperature measurement", Review of Scientific Instruments, vol. 71, no. 8, pp. 2959-2978, 2000.

[104] S. Keyvan, R. Rossow, C. Romero, and X. Li, "Comparison between visible and near-IR flame spectra from natural gas-fired furnace for blackbody temperature measurements", Fuel, vol. 83, no. 9, pp. 1175-1181, 2004.

[105] S. Rasenat, G. Hartung, B.L. Winkler, and I. Rehberg, "The shadowgraph method in convection experiments", Experiments in Fluids, vol. 7, pp. 412-420, 1989.

[106] F. Parsinejad, J. C. Keck, H. Metghalchi, "On the location of flame edge in Shadowgraph pictures of spherical flames: a theoretical and experimental study", Experiments in Fluids, vol. 43, pp. 887-894, 2007.

[107] C. Liu and L. Xu, "Laser absorption spectroscopy for combustion diagnosis in reactive flows: A review", Applied Spectroscopy Reviews, vol. 54, no. 1, pp. 1-44, 2018.

[108] L. Xu, C. Liu, W. Jing, Z. Cao, X. Xue, and Y. Lin, "Tunable diode laser absorption spectroscopy-based tomography system for on-line monitoring of two-dimensional distributions of temperature and H2O mole fraction", Review of Scientific Instruments, vol. 87, pp. 013101, 2016.

[109] S. G. Michael Soo, Nick Glumac, Keishi Kumashiro, James Vickery, David L.Frost, Jeffrey M. Bergthorson, "Emission and laser absorption spectroscopy of flat flames in aluminum suspensions", Combustion and Flame, vol. 290, pp. 230-238, 2017.

[110] M. Soo, S. G. Goroshin, A. Higgins, T. Bazyn, N. Glumac, and H. Krier, "Emission spectroscopy of flame fronts in aluminum suspensions", Proceedings of the Combustion Institute, vol. 31, no. 2, pp. 2011-2019, 2007.

[111] T. Parameswaran, R. Hughes, P. Gogolek, and P. Hughes, "Gasification temperature measurement with flame emission spectroscopy", fuel, vol. 134, pp. 579-587, 2014.

[112] C. Hu, Q. Guo, Y. Gong, L. He, and G. Yu, "Alkalis atomic emission spectroscopy and flame temperature measurement of diesel impinging flames in an opposed multi-burner gasifier", Experimental Thermal and Fluid Science, vol. 98, pp. 445-453, 2018.

[113] F. Q. Zhao and H. Hiroyasu, "The applications of laser Rayleigh scattering to combustion Diagnostics", Progress in Energy and Combustion Science, vol. 19, pp. 447-485, 1993.

[114] F. Caldas, D. Duarte, P. Ferräo, M. V. Heitor, and C. Poppe, "On the Use of Laser Rayleigh Scattering to Study the Aerothermochemistry of Recirculating Premixed Flames", Developments in Laser Techniques and Fluid Mechanics, pp. 439-453, 1997.

[115] E. Kristensson, A. Ehn, J. Bood, and M. Aldén, "Advancements in Rayleigh scattering thermometry by means of structured illumination", Proceedings of the Combustion Institute, vol. 35, no. 3, pp. 3689-3696, 2015.

[116] M. C. Drake and G. M. Rosenblatt, "Flame temperatures from Raman scattering", Chemical Physics Letters, vol. 44, no. 2, pp. 313-316, 1976.

[117] D. W. Ball, "Raman Scattering from Flames", Spectroscopy, vol. 15, pp. 28-29, 2001.

[118] L. R. Boedeker and G. M. Dobbs, "CARS Temperature Measurements in Sooting, Laminar Diffusion Flames", Combustion Science and Technology, vol. 46, pp. 301-323, 1985.

[119] W. M. Tolles, J. W. Nibler, J. R. McDonald, and A. B. Harvey, "A Review of the Theory and Application of Coherent Anti-Stokes Raman Spectroscopy (CARS)", Applied Spectroscopy, vol. 31, no. 4, pp. 253-271, 1977.

[120] A. Labergue, V. Deprédurand, A. Delconte, G. Castanet, and F. Lemoine, "New insight into two-color LIF thermometry applied to temperature", presented at the 15th Int Symp on Applications of Laser Techniques to Fluid Mechanics, Lisbon, Portugal, 2010.

[121] C. Schulz and V. Sick, "Tracer-LIF diagnostics: quantitative measurement of fuel concentration, temperature and fuel/air ratio in practical combustion systems", Progress in Energy and Combustion Science, vol. 31, no. 1, pp. 75-121, 2005.

[122] D. Gu, Z. W. Sun, B. B. Dally, P. R. Medwell, Z. T. Alwahabi, and G. J. Nathan, "Simultaneous measurements of gas temperature, soot volume fraction and primary particle diameter in a sooting lifted turbulent ethylene/air non-premixed flame", Combustion and Flame, vol. 179, pp. 33-50, 2017.

[123] D. Gu, Z. W. Sun, G. J. Nathan, P. R. Medwell, Z. T. Alwahabi, and B. B. Dally, "Improvement of precision and accuracy of temperature imaging in sooting flames using two-line atomic fluorescence (TLAF)", Combustion and Flame, vol. 167, pp. 481-493, 2016.

[124] A. Manteghi, Y. Shoshin, N. J. Dam, and L. P. H. de Goey, "Two-line atomic fluorescence thermometry in the saturation regime", Applied Physics B, vol. 118, no. 2, pp. 281-293, 2014.

[125] P. R. Medwell, Q. N. Chan, P. A. M. Kalt, Z. T. Alwahabi, B. B. Dally, and G. J. Nathan, "Development of temperature imaging using two-line atomic fluorescence", Applied Optics, vol. 48, pp. 1237-1248, 2009.

[126] P. R. Medwell, Q. N. Chan, P. A. M. Kalt, Z. T. Alwahabi, B. B. Dally, and G. J. Nathan, "Instantaneous Temperature Imaging of Diffusion Flames Using Two-Line Atomic Fluorescence", Applied Optics, vol. 64, no. 2, pp. 173-176, 2010.

[127] M. Lapp, L. M. Goldman, and C. M. Penney, "Raman Scattering fomr Flames", Science, vol. 175, no. 4026, pp. 1112-1115, 1972.

[128] G. J. Edwards, "Review of the status, traceability and industrial application of gas temperature measurement techniques", in "NPL Report", CBTM S1, 1997.

[129] W. Meier, S. Prucker, M.-H. Cao, and W. Stricker, "Characterization of Turbulent hytVAir Jet Diffusion Flames by Single-Pulse Spontaneous Raman Scattering", Combustion Science and Technology, vol. 118, no. 4-6, pp. 293-312, 1996.

[130] E. J. Burlbaw and R. L. Armstrong, "Rotational Raman Interferometric Measurement of Flame Temperatures", Applied Optics, vol. 22, pp. 2860-2866, 1983.

[131] S. Roya, J. R. Gord, and A. K. Patnaik, "Recent advances in coherent anti-Stokes Raman scattering spectroscopy: Fundamental developments and applications in reacting flows", Progress in Energy and Combustion Science, vol. 36, no. 2, pp. 280-306, 2010.

[132] M. J. Evans and P. R. Medwell, "Understanding and Interpreting Laser Diagnostics in Flames: A Review of Experimental Measurement Techniques", Frontiers in Mechanical Engineering, vol. 5, pp. 1-21, 2019.

[133] Y. R. Sivathanu and G. M. Faeth, "Temperature-soot volume fraction correlations in the fuel-rich region of buoyant turbulent diffusion flames", Combustion and Flame, vol. 81, no. 2, pp. 150-165, 1990.

[134] Q. N. Chan, P. R. Medwell, P. A. M. Kalt, Z. T. Alwahabi, B. B. Dally, and G. J. Nathan, "Simultaneous imaging of temperature and soot volume fraction", Proceedings of the Combustion Institute, vol. 33, no. 1, pp. 791-798, 2011.

[135] C. Tropea, "Laser Doppler anemometry: recent developments and future challenges", Measurement Science and Technology, vol. 6, pp. 605, 1995.

[136] J. W. Czarske, "Laser Doppler velocimetry using powerful solid-state light sources", Measurement Science and Technology, vol. 17, no. 7, pp. R71-R91, 2006.

[137] G. Fruchtel, E. P. Hassel, and J. Janicka, "Turbulent length scales in a swirling flame", Proceedings of the Combustion Institute, vol. 26, pp. 195-202, 1996.

[138] A. Stella, G. Guj, J. Kompenhans, M. Raffel, and H. Richard, "Application of particle image velocimetry to combusting flows: design considerations and uncertainlity assessment", Experiments in Fluids, vol. 30, pp. 167-180, 2001.

[139] J. Westerweel, "Fundamentals of digital particle image velocimetry", Measurement Science and Technology, vol. 8, pp. 1379–1392, 1997.

[140] M. Jahanmiri, "Particle image velocimetry-Fundamentals and its applications", PhD Thesis, Chalmers University of Technology, 2011.

[141] R. J. Adrian, "Twenty years of particle image velocimetry", Experiments in Fluids, vol. 39, no. 2, pp. 159-169, 2005.

[142] F. Durst, A. Melling, and J. H. Whitelaw, Principles and Practice of Laser-Doppler Anemometry, London : Academic Press, 1981.

[143] H. Forker and J. Janicka, "Large eddy simulation of a turbulent hydrogen diffusion flame", presented at the 1st Int. Symposium on Turbulence and Shear Flow Phenomena, Santa Barbara, CA, 1999.

[144] E. P. Hassel and S. Linow, "Laser diagnostics for studies of turbulent combustion", Measurement Science and Technology, vol. 11, pp. 37-57, 2000.

[145] B. B. Dally, D. F. Fletcher, and A. R. Masri, "Flow and mixing fields of turbulent bluff-body jets and flames", Combustion Theory and Modelling, vol. 2, no. 2, pp. 193-219, 1998.

[146] B. B. Dally, A. R. Masri, R. S. Barlow, and G. J. Fiechtner, "Instantaneous and Mean Compositional Structure of BluffBody Stabilized Nonpremixed flames", Combustion and Flame, vol. 114, no. 1-2, pp. 119-148, 1998.

[147] F. Schneider and J. Janicka, "The Reynolds-stress tensor in diffusion flames: an experimental and theoretical investigation", Combustion and Flame, vol. 81, pp. 1-12, 1990.

[148] T. Landenfeld, A. Kremer, E. P. Hassel, and J. Janicka, "Comparison of Reynolds stress closures for strongly swirling combusting jets", presented at the 11th Symposium on Turbulent Shear Flows, Grenoble, 1997.

[149] L. Cheng and A. Spencer, "Residence time measurement of an isothermal combustor flow field", Experiments in Fluids, vol. 52, no. 3, pp. 647-661, 2011.

[150] J.S. Rao, N. V. S. Ramani, H. J. Pant, and D. N. Reddy, "Measurement of residence time distributions of coal particles in a pressurized fluidized bed gasifier (PFBG) using radio tracer technique.", Indian Journal of Science and Technology, vol. 5, no. 12, pp. 3746-3752, 2012.

[151] K. Göckeler, S. Terhaar, and C. O. Paschereit, "Residence Time Distribution in a Swirling Flow at Nonreacting, Reacting, and Steam-Diluted Conditions", Journal of Engineering for Gas Turbines and Power, vol. 136, no. 4, pp. 1-9, 2014.

[152] D. W. Naegeil and C. A. moses, "Effect of Fuel Molecular Structure on Soot Formation in Gas Turbine Engines", presented at the American Society of Mechanical Engineering, New Orleans, Louisiana, USA, 1980.

[153] K. P. Schug, Y. Manheimer-Timnat, P. Yaccarino, and I. Glassman, "Sooting Behavior of Gaseous Hydrocarbon Diffusion Flames and the Influence of Additives", Combustion Science and Technology, vol. 22, no. 5-6, pp. 235-250, 1980.

[154] I. Glassman, "Soot formation in combustion processes", Proceedings of the Combustion Institute, vol. 22, no. 1, pp. 295-311, 1989.

[155] H. F. Calcote and D. M. Manos, "Effect of Molecular Structure on Incipient Soot Formation", Combustion and Flame, vol. 49, pp. 289-304, 1983.

[156] A. Gomez and I. Glassman, "Quantitative comparison of fuel soot formation rates in laminar diffusion flames", Proceedings of the Combustion Institute, vol. 21, no. 1, pp. 1087-1095, 1986.

[157] M. E. Decroix and W. L. Roberts, "Transient Flow Field Effects on Soot Volume Fraction in Diffusion Flames", Combustion Science and Technology, vol. 160, no. 1, pp. 165-189, 2000.

[158] U. Vandsburger, I.M. Kennedy, and I. Glassman, "Sooting counter-flow diffusion flames with varying velocity gradients", Proceedings of the Combustion Institute, vol. 20, no. 1, pp. 1105-1112, 1985.

[159] A. Beltrame, P. Porshnev, W. Merchan-merchan, A. Saveliev, A. Fridman, and L. A. Kennedy, "Soot and NO formation in methane–oxygen enriched diffusion flames", Combustion and Flame, vol. 124, no. 1-2, pp. 295-310, 2001.

[160] R.J. Santoro, H. G. Semerjian, and R. A. Dobbins, "Soot particle measurmeent in diffusion flames", Combustion and Flame, vol. 51, pp. 203-218, 1983.

[161] R.J. Santoro and H. G. Semerjian “,Soot formation in diffusion flames- flow rate fuel species and temperature efects”, Proceedings of the Combustion Institute, vol. 20, pp. 997-1006, 1984.

[162] H. Wang, D. X. Du, C. J. Sung, and C. K. Law, "Experiments and numerical simulation on soot formation in opposed-jet ethylene diffusion flames”, Proceedings of the Combustion Institute, vol. 26, no. 2, pp. 2359-2368, 1996.

[163] J. H. Kent and S. J. Bastin, "Parametric effects on sooting in turbulent acetylene diffusion flames”, Combustion and Flame, vol. 56, no. 1, pp. 29-42, 1984.

[164] H. Geitlinger, Th. Streibel, R. Suntz, and H. Bockhorn, "Two-dimensional imaging of soot volume fractions, particle number densities, and particle radii in laminar and turbulent diffusion flames”, Proceedings of the Combustion Institute, vol. 27, no. 1, pp. 1613-1621, 1998.

[165] H. Bockhorn, H. Geitlinger, B. Jungfleisch, Th. Lehre, A. Schön, Th. Streibel, and R. Suntz, "Progress in characterization of soot formation by optical methodsPresented at the Bunsen Discussion on Formation and Degradation of Hydrocarbons in High-Temperature Reactions, " Physical Chemistry Chemical Physics, vol. 4, no. 15, pp. 3780-3793, 2002.

[166] J. H. Kent and D. Honnery, "Soot and Mixture Fraction in Turbulent Diffusion Flames”, Combustion Science and Technology, vol. 54, no. 1-6, pp. 383-398, 1987.

[167] S.-Y. Lee, S. R. Turns, and R. J. Santoro, "Measurements of soot, OH, and PAH concentrations in turbulent ethylene/air jet flames”, Combustion and Flame, vol. 156, no. 12, pp. 2264-2275, 2009.

[168] A. Rowhani, Z. W. Sun, P. R. Medwell, G. J. Nathan, and B. B. Dally, "Soot-flowfield interactions in turbulent non-premixed bluff-body flames of ethylene/nitrogen”, Proceedings of the Combustion Institute, vol. 38, no. 1, pp. 1125-1132, 2021.

[169] V. Narayanaswamy and N. T. Clemens, "Simultaneous LII and PIV measurements in the soot formation region of turbulent non-premixed jet flames”, Proceedings of the Combustion Institute, vol. 34, no. 1, pp. 1455-1463, 2013.

[170] R. D. Brum and G. S. Samuelsen, "Two-component laser anemometry measurements of non-reacting and reacting complex ows in a swirl-stabilized model combustor”, Experiments in Fluids, vol. 5, no. 2, pp. 95-102, 1987.

[171] T. R. Meyer, S. Roy, V. M. Belovich, E. Corporan, and J. R. Gord, "Simultaneous planar laser-induced incandescence, OH planar laser-induced fluorescence, and droplet Mie scattering in swirl-stabilized spray flames", Applied Optics, vol. 44, no. 3, pp. 445-454, 2005.

[172] International Sooting Flame (ISF) Workshop. Available: http://www.adelaide.edu.au/cet/isfworkshop/, (July 23, 2016).

Chapter 3 Effect of Bluff Body Diameter

Statement of Authorship

Title of Paper	Effects of the bluff-body diameter on the flow-field characteristics of non-premixed turbulent highly-sooting Flames
Publication Status	☑ Published ☐ Accepted for Publication ☐ Submitted for Publication ☐ Unpublished and Unsubmitted work written in manuscript style
Publication Details	Amir Rowhani, Zhiwei Sun, Paul. R. Medwell, Zeyad. T. Alwahabi, Graham. J. Nathan, Bassam. B. Dally, "Effects of the Bluff-Body Diameter on the Flow-Field Characteristics of Non-Premixed Turbulent Highly-Sooting Flames", Combustion Science and Technology, vol. 194 (2), 378-396, 2022.

Principal Author

Name of Principal Author (Candidate)	Amir Rowhani		
Contribution to the Paper	Based on a thorough literature review conducted by me, and meetings and discussions between my supervisors and I, several operating parameters were selected for experimental and numerical investigations. I decided different experimental cases with my supervisors. I set up a numerical model using ANSYS and performed several simulations on the selected flames. I set up experiments with co-authors, Paul R. Medwell and Zhiwei Sun, to measure the flame radiation and flowfield in the three flames. I performed the radiation measurements as well as the flowfield measurements in the flames. I processed experimental and numerical data and analysed the results and presented the in text or figures. I integrated all the analysis and drafted the manuscript. Also, I acted as the corresponding author and took primary responsibility for responding the reviewers.		
Overall percentage (%)	65%		
Certification:	This paper reports on original research I conducted during the period of my Higher Degree by Research candidature and is not subject to any obligations or contractual agreements with a third party that would constrain its inclusion in this thesis. I am the primary author of this paper.		
Signature		Date	07-10-2021

Co-Author Contributions

By signing the Statement of Authorship, each author certifies that:

i. the candidate's stated contribution to the publication is accurate (as detailed above);

ii. permission is granted for the candidate in include the publication in the thesis; and

iii. the sum of all co-author contributions is equal to 100% less the candidate's stated contribution.

Name of Co-Author	Dr. Zhiwei Sun		
Contribution to the Paper	This co-author co-designed the experimental setup and helped to conduct experiments.		
Signature		Date	08-10-2021

Name of Co-Author	Associate Professor Paul R. Medwell		
Contribution to the Paper	This co-author helped with the experimental setup and with editing and revising the manuscript.		
Signature		Date	08-OCT-2021

Name of Co-Author	Associate Professor Zeyad T. Alwahabi		
Contribution to the Paper	This co-author provided suggestions with developing ideas.		
Signature		Date	

Name of Co-Author	Professor Graham J. Nathan		
Contribution to the Paper	This co-author co-supervised the development of the work. He also assisted to evaluate and edit the manuscript.		
Signature		Date	14-10-21

Name of Co-Author	Professor Bassam B. Dally		
Contribution to the Paper	This co-author co-supervised the development of the work. He also helped plan and structure the manuscript. He also provided assistance with rebutting reviewers' comments and with revising the manuscript.		
Signature		Date	07-10-2021

Effects of the bluff-body diameter on the flow-field characteristics of non-premixed turbulent highly-sooting Flames

This chapter consists of the published journal article:

Amir Rowhani, Zhiwei Sun, Paul. R. Medwell, Zeyad. T. Alwahabi, Graham. J. Nathan, Bassam. B. Dally, "Effects of the Bluff-Body Diameter on the Flow-Field Characteristics of Non-Premixed Turbulent Highly-Sooting Flames", *Combustion Science and Technology*, vol. 194 (2), 378-396, 2022.

The article is identical to its submitted format with the following exceptions:

1. The typesetting and referencing styles have been altered to maintain a consistent appearance within the thesis.

2. The numbering of tables, figures, and equations has been changed to include the number of the chapter.

The article in its published format is available at:
https://doi.org/10.1080/00102202.2019.1680508

3.1 Abstract

This paper presents a joint experimental and computational study on the effect of the bluff-body diameter on the flow field and residence time distribution (RTD) in a set of turbulent non-premixed ethylene/nitrogen flames with a high soot load. A novel optical design to undertake the PIV measurements successfully in highly-sooting turbulent flames has been developed, using polarizing filters. The mean velocity components and turbulent intensity are reported for three bluff-body burners with different bluff-body diameters (38, 50, and 64 mm), but which are otherwise identical in all other dimensions. The central jet diameter of 4.6 mm was supplied with a mixture of ethylene and nitrogen (4:1, by volume) to achieve a bulk Reynolds number of 15,000 for the reacting cases. Isothermal cases were also investigated to isolate the effect of heat release on the flow field. Pure nitrogen was utilized in the isothermal cases where the Reynolds number was kept the same as the reacting cases. The annular bulk velocity of the co-flowing air was kept constant at 20 m/s for all experiments. Computationally, a 2-D RANS model was developed, validated against the experimental data, and was mainly used to investigate the effect of the bluff body diameter on the residence time in the recirculation zone. The flow structure for both isothermal and reacting cases was found to be consistent with the literature, exhibiting similar vortical structures of the recirculating zone and mixture fraction distribution, for similar momentum flux ratios. The flame length and volume decreased by 20% and 9%, respectively, as the bluff diameter increased from 38mm to 64mm. The length of the recirculation zone for the isothermal cases was found to be ~1.2 $D_{BB,}$ while for the reacting cases it was ~1.5-1.75 $D_{BB.}$ A stochastic tracking model was employed to estimate the pseudo-particles' residence time distribution in the recirculation region. The model revealed that an increase in the bluff body diameter from 38mm to 64 mm leads to tripling of the mean residence time within the recirculation zone. Thermal radiation measurements from the recirculation zone show a 35% increase as the bluff body diameter is increased from 38 mm to 64 mm, whilst the total radiation from the whole flame drops by 15%, believed to be mainly due to the decrease in flame volume. The effect of these differences on soot propensity and transport are described briefly and will be the subject of future investigations.

Keywords: Bluff-body flame; Particle Image Velocimetry (PIV); Residence time; soot; recirculation zone

3.2 Introduction

Turbulent non-premixed flames with recirculating flows are used in many industrial combustors such as gas turbines, afterburners, and industrial furnaces. They are typically generated by means of either bluff-bodies or swirlers to enhance the mixing of the fuel and the oxidizer, as well as to stabilize the flame by recirculating the reactants and hot products to the exit plane and providing a continuous ignition source [1-3]. A recirculation zone also creates a homogeneous hot mixture close to the exit plane, which contributes to increased flame stability, reduced strain rate, and, at some conditions, rich fuel mixtures, which lead to the formation of soot. This is undesirable in gas turbines and propulsion devices but can be desirable in furnaces and boilers where radiation heat transfer is important. Hence, a better understanding of the formation and destruction of soot in non-premixed flames with more complex fluid dynamics is of great importance in order to design high-performance and low-emission combustion devices. To do so, laboratory-scale bluff-body burners are well suited to studying recirculating flames, since they provide well-characterised recirculation zones that are relevant to those in the more complex environments of practical combustion systems. However, most previous work on bluff-body flames has been performed in non-sooting environments and included both premixed and non-premixed flames. Hence, the aim of this work is to generate new and detailed understanding from high-fidelity measurements of bluff-body flames in a highly-sooting environment.

The aerodynamics of the flows past various bluff-body geometries and the effects of bluff-body configurations have been studied in the past [4-6]. It is well known that the length of the recirculation zone in such flows plays a significant role in the flame stabilization mechanism and the residence time distribution, which can subsequently affect soot and NOx formation in the flame [7]. Different parameters can influence the structure of the flow and consequently the recirculation zone length. Those include the bluff-body shape, position, confinement ratio of the burner and the combustor, and the blockage ratio of the burner or the co-flowing channel. For instance, the effect of the blockage ratio was investigated by Taylor and Whitelaw [8], and it was revealed that the recirculation zone length was increased by increasing the blockage ratio. Furthermore, Schefer et al. [3] demonstrated that changing the confinement ratio—the area that is blocked by the bluff-body from the approaching co-flow stream—did not significantly impact the recirculation zone length or the flame structure. Yang et al. [9] stated that increasing the blockage ratio would shift

the reaction zone to the inner side of the recirculation zone, similar to the effect of increasing the momentum flux ratio of the fuel and air. The dependency of the recirculation zone structure on the jet to co-flow momentum ratio was investigated by Li et al. [10] and Danlos et al. [11]. It was found that increasing the Reynolds number slightly affects the recirculation zone length at a constant blockage ratio. The structure is more dependent on the change in the blockage ratio, while the Reynolds number has little influence on the length of the recirculation zone. The shape and the position of the bluff-body flame holders on the flame structure were also investigated and their effects were reported, for example [12-15].

The flow structure downstream of an unconfined annular bluff-body burner in both isothermal and reacting regimes was investigated extensively by Dally et al. [1, 16]. In their experiments, a bluff-body burner consisting of a central tube with a diameter of 3.6 mm, surrounded by a larger tube with an external diameter of 50 mm, was used. The area between the exit planes of the two tubes was covered with a flat ceramic disc. In bluff-body flames, the momentum flux ratio affects the flame structure, and that most turbulent flames contain three distinct zones, namely; (1) the low-strain recirculation zone, which is the most complex part of the flow, (2) the downstream jet-like region, which behaves in a similar manner to turbulent jet flames, and a (3) the high-strain neck zone, which connects the recirculation zone to the jet zone [1, 16]. There are two shear layers in the recirculation zone: one closer to the region between the co-flow and the outer vortex and one between the central jet and the inner vortex. Increasing the momentum flux ratio (jet to co-flow) decreases the mixture strength in the outer vortex and increase it in the inner vortex. However, the flames investigated by Dally et al. [1, 16] were free of soot and were measured using a single point LDV technique. The effects of momentum flux ratio have major effects on the resulting vortical structure of the recirculation zone, the strength of its semi-uniform mixture, and the appearance of soot particulates [16]. To the authors' best knowledge, no systematic study is available that investigates the effects of bluff-body diameter alone on the structure of the bluff body flames. It is hypothesized that changing the bluff-body diameter only while keeping all other geometrical and operating conditions the same, will result in a similar vortical structure of the recirculation zone, a similar mixture fraction distribution, and a different length and hence residence time. Such a feature will be of interest to the investigation of soot in these complex flames, where the effect of residence time is isolated while all the other parameters are kept almost constant. A few non-intrusive in-situ measurements have been reported on turbulent sooting flames. The majority of these flames are either piloted jet flames, lifted jet flames, or simple jet flames with fuel blends. Such flames are insightful to study soot, except that they provide

additional challenges for modelers due to the complexity of the boundary conditions and the kinetic effects of the blended mixtures. Furthermore, due to the difficulties in measuring the velocity and turbulence in highly-sooting flames, most of the past studies focused on flames with a low soot loading. For instance, Köhler et al. [17, 18] simultaneously measured the flow field and soot concentration in a turbulent ethylene flame. Despite their significance, these measurements were performed for lifted turbulent jet flames, which makes the boundary conditions quite challenging for modelers. In another work [19], simultaneous PIV and LII measurements were undertaken in turbulent attached jet flames. These measurements were carried out solely at the downstream of the jet flame. Mahmoud et al. [20-22] reported systematic measurements of the soot volume fraction in a series of turbulent attached ethylene/nitrogen/hydrogen flames, but no data was provided for the instantaneous velocity and turbulence levels in their flames, and only the global strain rate was investigated. The velocity field of a series of gas turbines' relevant laboratory-scale burners, using ethylene as well as n-heptane as fuels, were also measured in a swirl burner [23, 24]. These measurements, despite their significance, were only performed in a limited set of flames with a specific equivalence ratio in order to ensure feasible and successful PIV measurements due to soot scattering interference with the PIV flow markers. Nathan et al. [25] investigated a wrinkled, pseudo-laminar ethylene diffusion flame at a low Reynolds number. They successfully measured the velocity in the presence of soot in the flame and verified the possibility of undertaking the PIV in a range of flames containing soot. Their investigation was limited to a series of laminar sooting flames but not turbulent flames. To the best of the authors' knowledge, only a limited number of studies are documented in the literature reporting sooting flame velocity data. Such data, in most cases, have been collected for a single flame that suffers from either a lack of comparability or the presence of turbulence. Hence, the main objective of this work is to measure the flow field in a turbulent bluff-body flame with high soot loading. A bluff-body flame has relatively simpler boundary conditions than lifted or piloted jet flames and is also stable for a wider range of co-flow and fuel jet Reynolds numbers.

Residence time, as noted above, is one of the key controlling parameters influencing soot formation, growth and oxidation in flames. The amount of soot that is formed during the combustion process depends strongly on the residence time [26]. Although the method suggested by Turns and Myhr [27] to estimate the global residence time is a useful indicator of the characteristic strain rate in a jet flame, the distribution of the pseudo-particles' residence time is required since the flame spans over an extended range of local strain. A few attempts have been made in the past to

evaluate the residence time distribution (RTD) in different non-reacting/reacting systems [28, 29]. However, no measurement or calculations of RTDs in a turbulent axisymmetric bluff-body flame have been reported before. This gap forms the second objective of the paper, which is to assess the effect of bluff-body diameter on the residence time distribution, particularly for the recirculation zone in each flame.

3.3 Methodology

3.3.1 Bluff-body burner

The schematic diagram of the bluff-body burner used in this work is presented in Figure 3.1. The burner is similar to that of Dally et al. [1, 16], with an inner tube (d_J=4.6 mm) centred within a larger outer tube (D_{BB}) with a length of 1.0 m. Three different burners with different D_{BB} were used, namely 38, 50 and 64 mm. The entire burner is made of brass, except for the top surface that is manufactured from ceramic to be resistant to high temperatures and reduce heat loss. An air contractor with a round shape at the exit plane is used to deliver the co-flow air, as shown in Figure 3.1. The round contractor has an internal diameter of 190 mm and has been selected to avoid the formation of corner vortices. The bluff body burner is mounted 10mm above the height of the contractor in order to allow optical access. The burner, together with the contractor, was vertically traversed through a fixed laser sheet to enable measurements of the entire length of the flame. The distance of the flame tip and the extraction hood was kept unaltered by traversing the hood with the burner in order to minimize any interaction between the exhaust and the unconfined flame.

3.3.2 Flame cases

In this set of experiments, six different cases comprising of three non-reacting as well as three reacting cases with similar bulk Reynolds number of 15,000 have been investigated. For the reacting cases, the fuel stream contained a mixture of high-purity ethylene (99%) and ultra-high purity nitrogen (99.99%) at the volume fraction of 4:1, at ambient temperature and atmospheric pressure. These flames were selected because they were stable on all bluff-body burners with identical fuel and co-flowing air flow rates. Ethylene (C_2H_4) was selected due to its high soot yield, as well as its relatively-simpler chemical kinetics when compared with other hydrocarbon fuels.

The nitrogen (N_2) addition to the fuel stream helped reduce the soot concentration in order to reduce the interference from soot particles on the PIV measurements.

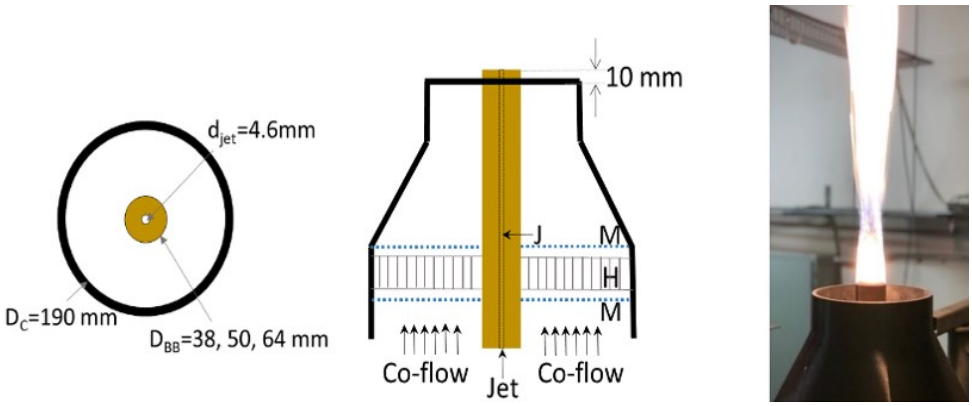

Figure 3.1: Bluff body burner and co-flow air contractor setup: Top view (left), Side view (middle) and Flame photo (right). (BB – Bluff-body tube; J – Fuel jet tube; M – screen mesh; H – Aluminium honeycomb; d_{jet} – Fuel jet diameter; D_{BB} – Bluff-body diameter; DC – Air contractor).

For non-reacting cases, pure nitrogen was used instead of the ethylene/nitrogen mixture. It is worth noting that the density of ethylene and nitrogen is similar, while the viscosity of the C_2H_4/N_2 mixture is 1.21E-5 (kg/m/s) and that of N_2 is 1.81E-5 (kg/m/s). The full details of the experimental conditions are shown in Table 3.1. The photographs of the flames were taken with a standard Nikon D3500 DSLR camera with f/32 and ISO 100 sensitivity and an exposure time of 0.25 seconds and are presented in Figure 3.2.

Table 3.1: Baseline experimental conditions for cold/reacting flows.

Designation	Bluff-body diameter	Fuel jet composition (% by vol.)	Bulk jet exit Velocity (±2%)	Jet exit Reynolds	Bulk fuel flow rate	Bulk co-flow air velocity	Mean flame length* (L_f) (±5%)
	(mm)	-	(m/s)	-	(g/s)	(m/s)	(mm)
NB-1	38	100 N_2	51.8	15,000	0.97	20	-
NB-2	50	100 N_2	51.8	15,000	0.97	20	-
NB-3	64	100 N_2	51.8	15,000	0.97	20	-
ENB-1	38	80 C_2H_4: 20 N_2	32.1	15,000	0.61	20	1215
ENB-2	50	80 C_2H_4: 20 N_2	32.1	15,000	0.61	20	1070
ENB-3	64	80 C_2H_4: 20 N_2	32.1	15,000	0.61	20	972

* The flame length, obtained from averaged of 20 images, is considered as the distance between the burner exit plane up to the most visible flamelet downstream of the flame.

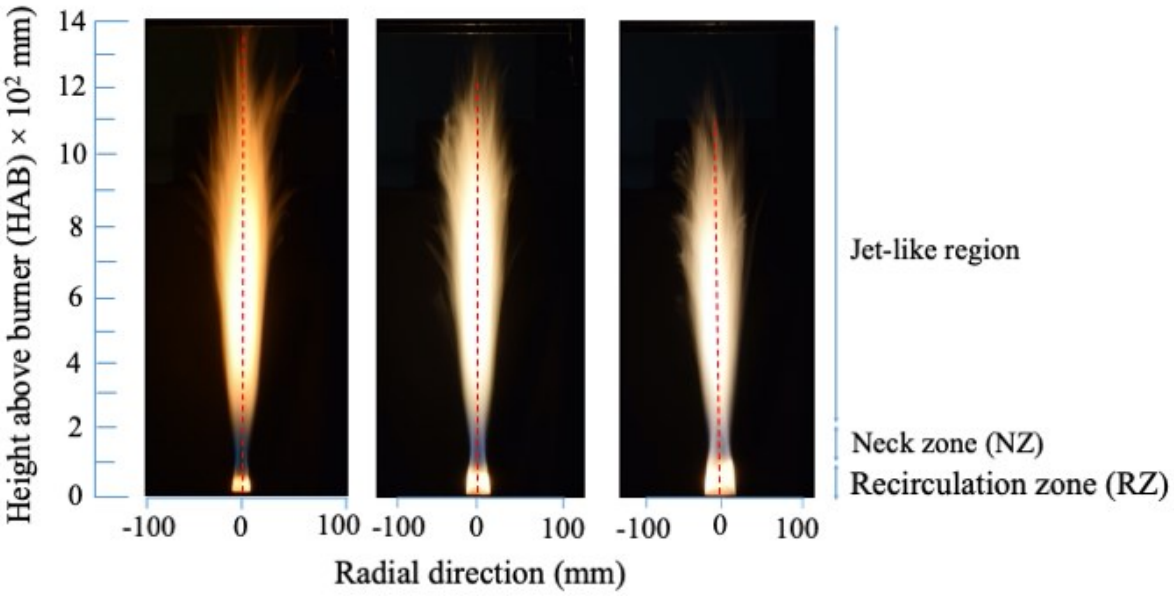

Figure 3.2: Photographs of the ENB-1 (left), ENB-2 (middle), and ENB-3 (right) flames.

3.3.3 Radiant intensity measurement

The total radiation from the bluff-body flames was measured using a Schmidt-Boelter heat flux factory-calibrated sensor. The sensor was placed at a radial distance of 250 mm from the flame axis and traversed vertically with 30 equi-spaced heights. The starting point was at the fuel jet exit similar to the bluff-body surface. For each point, 20,000 samples were collected at 1000Hz, which was found to be sufficient for statistical convergence [30, 31]. The mean values of the radiation heat flux, as well as the radiant fractions for three flames, have been compared. The uncertainties associated with the radiation measurements are attributed to the increment of the equal-spaced sampling points, which are within ±2%. Also, the heat flux gauge has an estimated ±3% error. Hence the total uncertainties of the radiation measurement are estimated to be ±5%.

3.3.4 Velocity measurement: Optical diagnostic setup

Particle image velocimetry (PIV) was performed to measure the flow field. The schematic diagram of the PIV setup is shown in Figure 3.3. The light source for the PIV was a frequency-doubled beam from a dual-head Nd:YAG laser (Quantel BrilliantB/Twins). Two laser pulses at 532 nm, 140 mJ energy per pulse, a pulse

duration of 5ns and a pulse rate of 10 Hz were used. A temporal separation of 15–60 μs between the two pulses was chosen, depending on the local flow conditions. The laser beam passed through a wave-plate and sheet forming optics and finally collimated to a sheet with dimensions of 70 × 1 mm^2. Titanium oxide (TiO_2) particles with a nominal diameter of 1 μm were fed as flow tracers for both the jet and co-flow streams through an in-house built fluidized-bed particle seed generator. The Mie scattering from the TiO_2 particles was captured with a Kodak Megaplus II CCD camera (1920 × 1080 $pixels^2$, 16 bit) equipped with a Sigma lens 105 mm, f-number2.8 and equipped with a 532 nm bandpass filter (Andover) with an FWHM of 1 nm for suppressing both laser-induced and natural incandescence. The novelty of this system comes from the use of two additional polarizing components. A half wave-plate at 29 degrees to the vertical was placed in front of the laser beam to direct the beam horizontally. In addition, a second linear polarizer was attached to the 1 nm bandpass filter to capture vertically-polarized scattering signals. Such an optical arrangement significantly suppresses the scattering signals from soot (which are relatively small) to very low levels but only reduces scattering from PIV particles (which are large) by a factor of approximately two. Thus, soot interference on the PIV images was much reduced when compared with a conventional PIV setup. The field of view was set to a 70 mm × 40 mm window positioned at the centreline of the flame, which gives a resolution of 29.25 pixels per millimetre. XCAP imaging software was used to capture the images. A total of 2000 image pairs were collected with an acquisition rate of 5 Hz. The PIV images were processed by a PIV software package, PIVLab 2.20 [32, 33], and the mean velocity vector fields were calculated. The interrogation window was sequentially reduced to 64×64 pixels and then to 32×32 pixels with a 50% overlap. This leads to a corresponding spatial resolution of 2.56 × 2.56 mm^2 and 1.28 × 1.28 mm^2, respectively. Standard Fast Fourier transform (FFT) was then used to calculate the displacements of the particles in the field.

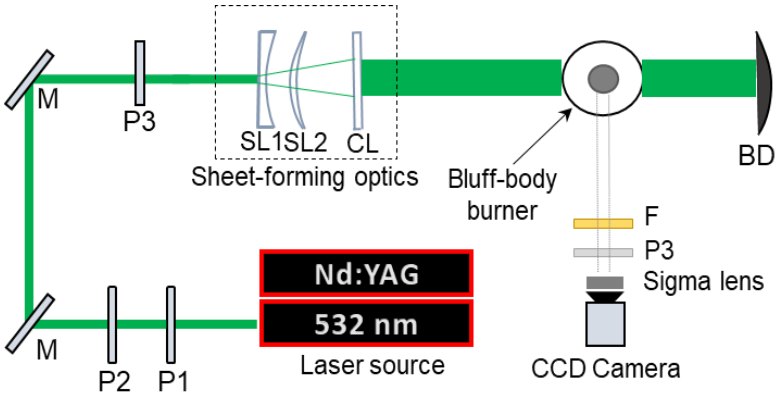

Figure 3.3: PIV experimental layout. (P1 – λ/2 wave plate at 29°; P2 – 532 nm film polarizer @45°; M – Mirror; P3 – Prism; SL#1/#2 – Spherical lenses; CL – Cylindrical lens; BD – Beam dump; F – 532 nm bandpass filter (FWHM) and P3 – Linear polariser).

3.3.4.1 Accuracy of the PIV measurements

The Stokes number (Sk) criterion for particles to follow the flow path is Sk<< 0.1. In these experiments, the Stokes number was calculated for the 1-micron TiO_2 particles and ranged from 10^{-4} to 10^{-3}, which satisfied the Stokes number criterion. This indicates that the particle lagging for the mean velocity is not significant, and for turbulent fluctuations is around 1% of the mean values. A sensitivity analysis was performed to find out an adequate number of pair images, such that the results are statistically independent. A total of 5000 image pairs were taken and processed. It was concluded that the results did not change more than 1% for more than 2000 image pairs. The optics utilized in the current setup prevent the system from suffering from the system-inherent long exposure time of the second frame of the CCD camera. Since the polarizers can substantially reduce the line-of-sight integrated luminosity, both images are almost free of soot scattering. The small amount of scattering caused by the flame brush in the second exposure can be removed in the image pre-processing step. The total error can be determined by the ratio of the nominal correlation peak value, which is 0.1 pixel [34], to the maximum displacement of the particles. The maximum displacement should not be more than one-third of the smallest interrogation window size, which is 32×32 $pixels^2$. Therefore, the accuracy of the velocity component measurement is estimated to be ±0.95 m/s.

3.3.5 Computational method

A 2-D axisymmetric model was generated in Ansys Fluent 19. The dimensions of the model were based on the bluff-body setup used in the experimental section. In order to minimize the effect of the surrounding environment on the flame, the domain was extended to $10D_{BB}$ towards the downstream, and $5D_{BB}$ in the radial direction. Mesh structure plays an important role in obtaining high accuracy and cost-efficient numerical results. A mesh sensitivity study was performed to find out the dependency of the results on the mesh resolution. A comparison of the axial and radial velocity distribution at four specific axial distances for 220,000, 470,000, and 770,000 cells revealed that increasing the number of meshes to 770,000 does not change the results by more than 2% in comparison with the 440,000 case, so the 440,000-cell mesh was selected. The steady, incompressible Reynolds-averaged Navier−Stokes (RANS) equations were used for the turbulent bluff-body flame, and the conservation equations of mass, momentum, and energy were solved numerically. The standard k-ε model was selected owing to its well-known capability for predicting recirculating flows. Dally et al. [35] suggested a modification for the standard k-ε turbulence model in order to improve the prediction of the axial velocity decay rate of a round jet, therefore the c_1 coefficient in the dissipation equation was modified to 1.6. The steady flamelet model, coupled with the DRM-22 reduced kinetic mechanism (22 species and 104 reactions), was used for the combustion model. The DRM-22 has been shown to give a reasonable prediction of a bluff-body flame with fewer computational costs in comparison with other detailed mechanisms. The SIMPLE pressure velocity coupling with a standard pressure scheme was used. All equations were discretized using a second-order upwind scheme. The convergence criteria were set to 1E-6 for all equations. The residence time of the pseudo-particles was estimated by calculating the trajectory of the particles in a Lagrangian frame. This method was recently employed by Chinnici et al. [36] to calculate the particle residence time and trajectories in a solar vortex particle reactor. The trajectory of the pseudo-particles is computed based on the integration of the particle force balance equation. Turbulent dispersion of the particles was calculated using a standard stochastic eddy lifetime tracking model. Inert pseudo-particles with a diameter of 1nm were injected into the domain from the air and fuel inlet boundaries and measured at the exit plane from the recirculation zone, where the axial velocity components are positive. Since, in turbulent flows, the species transport is mainly dominated by turbulent diffusion rather than molecular diffusion, it is possible to track these inert pseudo-particles.

A comparison of the axial and radial velocity components at 15 mm and 65 mm above the burner (HAB) in the axial direction is shown in Figure 3.4. A good agreement is seen in the axial velocity components for both heights at almost all the radial locations (less than 5% difference). A small discrepancy is seen in the outer shear layer, which can be attributed to the high-velocity gradient in the shear layers, which can cause the centre of the recirculation zone (RZ) to vary at any instance. These results can lead to an inaccuracy in the radial velocity components. However, the length of the recirculation zone obtained from the PIV is less than 2% different from the predicted RZ length. This gives confidence that the model can be used to predict the residence time of the pseudo particles in the RZ reliably, since the trajectory of the particles is calculated by integrating the particle force balance equation, which is a function of the relative velocity components. The uncertainties associated with CFD arise from the simplifications in the turbulence model, mesh resolution, and the boundary conditions (B.C.) of the inlets, which assumed Dirichlet (fixed-value) boundary conditions.

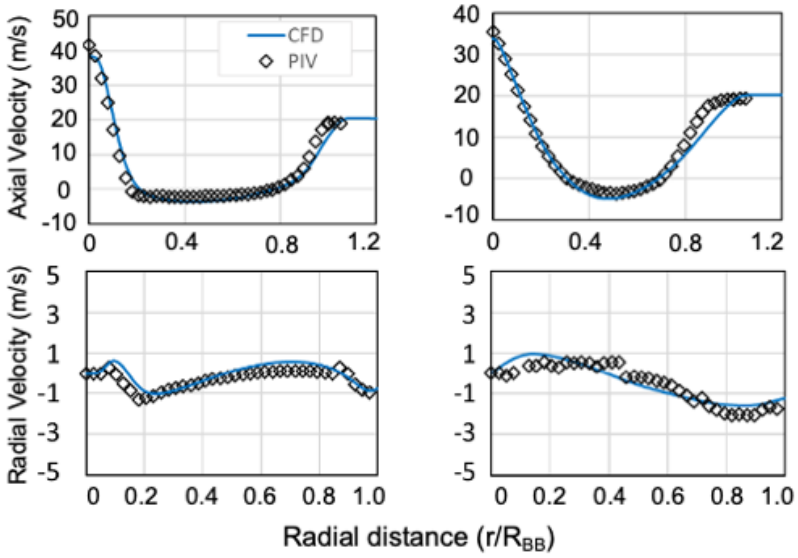

Figure 3.4: Comparison of the axial velocities (top) and radial velocities (bottom) at a height of x/D_{BB}=0.3 (left column) and x/D_{BB}=0.6 (right column) above the burner obtained from the PIV using CFD.

3.4 Results and discussion

3.4.1 Overall flame structure

The structure of the flames, as shown in Figure 3.2, has been found to be similar to those reported previously [37, 38]. These flames are characterized by three distinct regions: a highly-sooting recirculation zone in the upstream, a high-strain neck zone, and a jet-like region downstream of the neck zone. Comparing the photographs of the three flames reveals a few differences, noting that all operating conditions are identical. Firstly, increasing the bluff-body diameter leads to an increase in the recirculation zone length. Secondly, the overall flame length is slightly decreased (20%) by increasing the bluff-body diameter, since more fuel is burnt in the recirculation zone. Finally, it is inferred from the photographs that the soot concentration in the neck zone is considerably increased in the larger burner, while it is observed that the neck zone in the smallest bluff-body is almost free of soot. The flame length, L_f, was obtained from 20 instantaneous images. The flame length is considered as the distance between the bluff-body exit plane up to the most visible flamelet downstream of the flame. The length of the recirculation zone was also measured for the three flames. This length is the distance from the jet exit up to the stagnation point where the mean axial velocity of the flame is zero. Both the flame length and the recirculation zone length have been compared for the three burners on the left side of Figure 3.5. The length of the recirculation zone was measured from the bluff-body surface to the stagnation point. As expected, increasing the bluff-body diameter resulted in an increase in the length of the recirculation zone. The RZ lengths for all three cases are compared on the right side of Figure 3.5. It can be seen that the smallest RZ length, which is 60±1 mm, belongs to the smallest bluff-body (38 mm), while the largest RZ is for the 64-mm burner and is 110±1 mm in length.

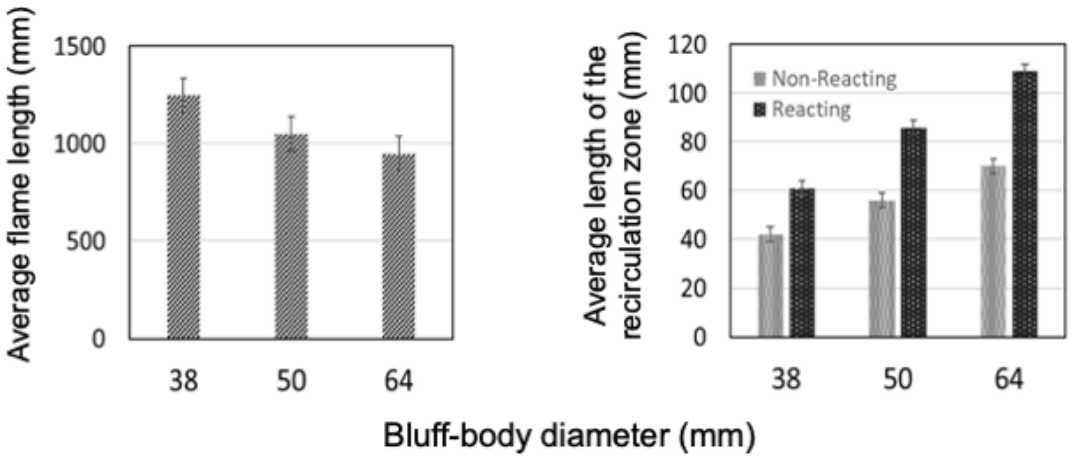

Figure 3.5: Measured average flame length (left) and measured length of the recirculation zone (right) for the three burners.

3.4.2 Radiation heat flux and radiation fraction

Soot formation in the flame affects the radiation heat flux and, as a consequence, the flame temperature and NOx formation [30]. A comparison of the radiation heat flux measurements for the three bluff-body flames is presented in Figure 3.6a. This Figure shows the measured axial radiation distribution at a fixed radial distance of 250 mm from the flame axis. The radiation in the recirculation zone is increased by almost 32% when the bluff-body diameter is increased to 64mm. In this region, since the flame is less strained in the 64-mm burner and has more time to recirculate, more soot is formed, and consequently the radiation is increased. In the jet-like region, the radiation peaks are found at x_p/L_f of 0.43, 0.47, and 0.50 for the 38-mm, 50-mm, and the 64mm burners respectively, which are in the range $0.4 < x_p \,/\, L_f < 0.5$ for all three bluff-body burners. Here, the L_f is the average flame length, and the x_p is the axial distance to the peak heat flux. The radiation peak corresponds to the maximum soot volume fraction in each flame. This trend is consistent with our previous measurements in turbulent jet flames [30]. The radiant heat fraction χ_r is calculated from equation 1 following [39]:

$$\chi_r = \left[\frac{2\pi R . \int_0^\infty q''(\dot{x})dx}{\dot{m_f} \times HHV}\right] \quad (1)$$

where R is the radial distance from the flame axis to the radiation gauge, q" is the measured radiant heat flux, $\dot{m_f}$ is the fuel mass flow rate (kg/s), and HHV is the higher heating value of the fuel. Figure 3.6b shows the radiant heat fraction plotted

as a function of the bluff-body diameter. It can be seen that increasing the bluff-body diameter leads to a linear reduction in the radiation fraction by ~15%, which can be partly related to the increased radiation losses from the RZ to the bluff body burner itself. It can also be related to the decrease in the estimated total volume of the flame stabilized on the larger burner by ~9%.

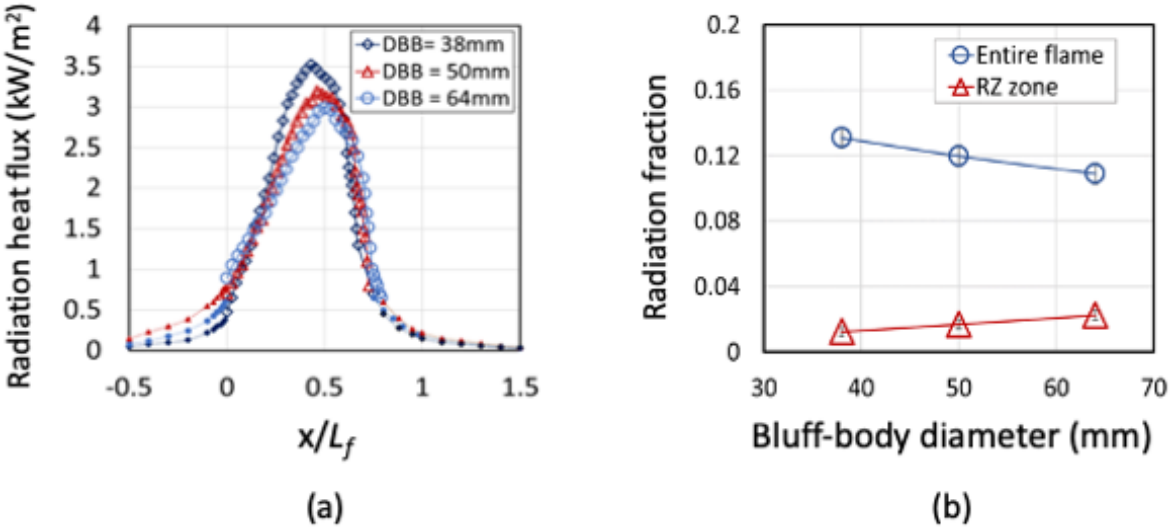

Figure 3.6: a) Radiant heat flux distribution measured along the flame length for three bluff-body flames, and b) radiant fraction as a function of the burner diameter, calculated for the entire flame (blue), as well as the recirculation zone (red).

3.4.3 Mean flow field of non-reacting cases

The non-reacting flow streamline overlaid on the mean velocity contour for half of the domain is visualized in Figure 3.7 for all three cases. Pure nitrogen with an exit jet velocity of 51.8 m/s was issued through the central jet in order to create a similar flow to the reacting case at a Reynolds number of 15,000. The co-flowing air velocity was kept constant at 20 m/s for all cases. All three cases exhibit similar characteristics: the outer vortex (OV), which is adjacent to the co-flowing air, and a pronounced inner vortex (IV), which is sandwiched between the jet and the OV. Increasing the bluff-body diameter from 38mm to 64mm doubled the recirculation zone length. The RZ length for the smallest bluff-body burner is 29±1 mm, while this length is increased to 51±1 mm and 69±1mm for the 50 mm and the 64 mm burners, respectively. As the bluff-body diameter increases, it may also be seen that the centre of the toroidal vortex and the stagnation points are shifted downstream

of the flow. It is clear that the non-reacting flows exhibit much shorter RZ with a length closer to the bluff-body diameter (0.8-1.1), while the reacting cases have much longer RZ and measure (1.5-1.75) for the bluff body diameters. This discrepancy is discussed further in the next section. It is noteworthy that the momentum flux ratio of the jet to the co-flow for the reacting and non-reacting cases is similar. This ratio was found to control the vortical structure and length of the RZ [1, 16].

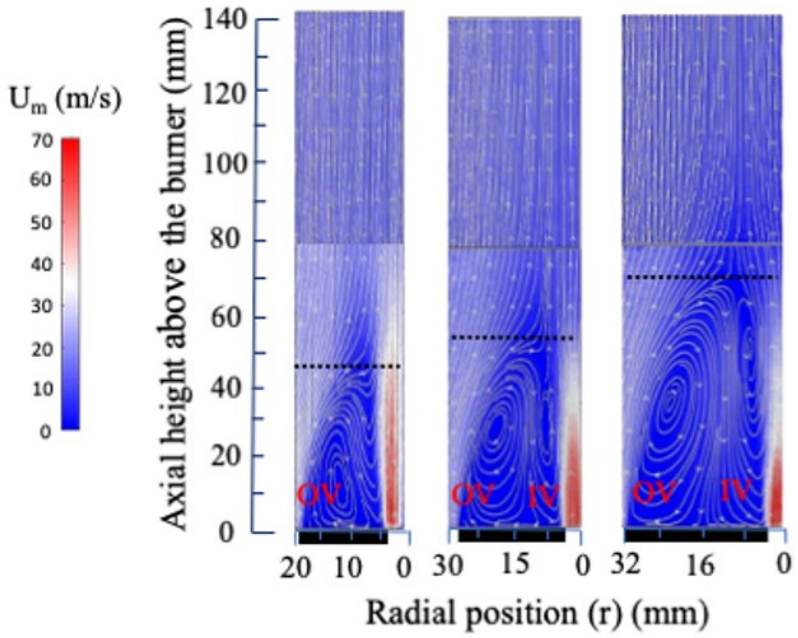

Figure 3.7: Streamline plot overlaid on the mean flow field contour of the isothermal nitrogen flow past the bluff-body burners, D_{BB}=38 (left), D_{BB}=50mm (middle) and D_{BB}=64mm (right). The dashed line indicates the stagnation point and the RZ length.

3.4.4 Mean flow field of reacting cases

The flow characteristics in the reacting cases have been revealed by calculating the time-averaged flow fields from the instantaneous flow features. The same characteristics are observed for all three bluff-body burners, similar to the cold flow conditions. Figure 3.8 shows the mean velocity distribution. The colours denote the velocity magnitude, and the white lines represent the streamlines. The stagnation points, where the flame propagated to the neck and jet region, are shown and the recirculation zone lengths can be compared. The peak velocity occurs at the trailing edges for all three burners at a Reynolds number of 15,000. The maximum co-flow velocity can be seen close to the shear layer. This indicates that both the IV and OV have been surrounded by the high-velocity fuel jet and co-flowing air streams. The OV serves to return the hot products to the inflow and stabilize the flame.

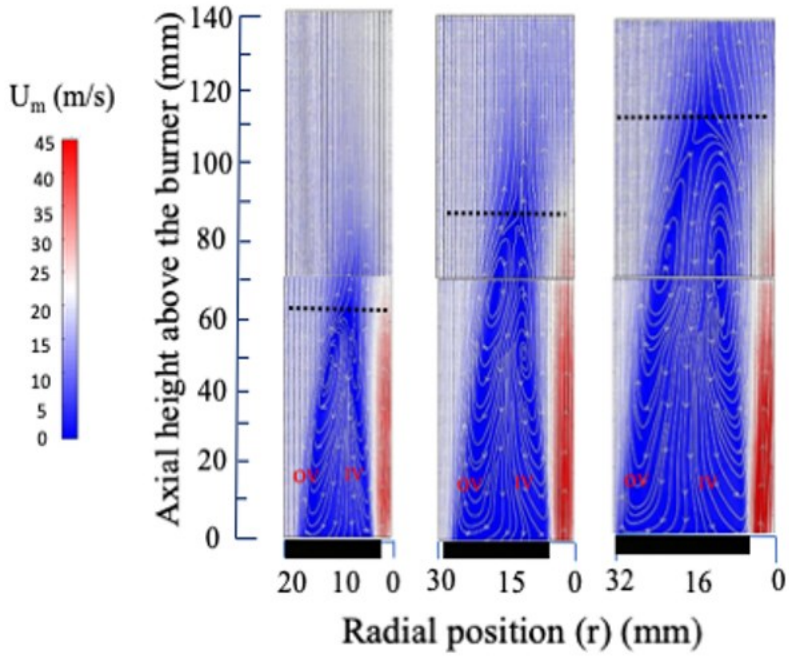

Figure 3.8: Measured streamline plot overlaid on the mean flow field contour of the reacting ethylene/nitrogen flow past the bluff-body burners, D_{BB}=38 (left), D_{BB}=50mm (middle) and D_{BB}=64mm (right).

The flow features of the non-reacting cases are similar to the reacting cases; the highest velocities are found at the centerline of the flame. However, the recirculation zones differ in the non-reacting and reacting flows. The non-reacting case exhibits a narrower inner vortex, as well as a wider outer vortex, regardless of the bluff-body diameter. In reacting cases, since the jet penetrates through a high-temperature low-density medium, the stagnation point is shifted further downstream, and causes the centre of the toroidal vortex to move outwards. This is consistent with previous trends in non-sooting bluff-body flames [1, 2, 16].

Figures 3.9 and 3.10 show the radial profile of the mean and rms of the axial and radial velocity components at three different locations within the recirculation zone and the neck zone for all three flames. The axial locations above the burners have been normalized by the bluff-body diameter (D_{BB}), and represent the flow both in the recirculation zone (X/D_{BB}= 0.3, 0.9) and further upstream in the neck zone (X/D_{BB}=1.8). The maximum velocity gradient and the peak of the fluctuations coincide with the inner and outer shear layers. Overall, the trend of the mean axial velocity and the fluctuations for the current cases are in good agreement with what Dally et al. [1, 16] measured for non-sooting methane/hydrogen flames on the same bluff-body burner. The maximum fluctuation is seen in the inner sheer layers between the outer and inner vortices for all three cases.

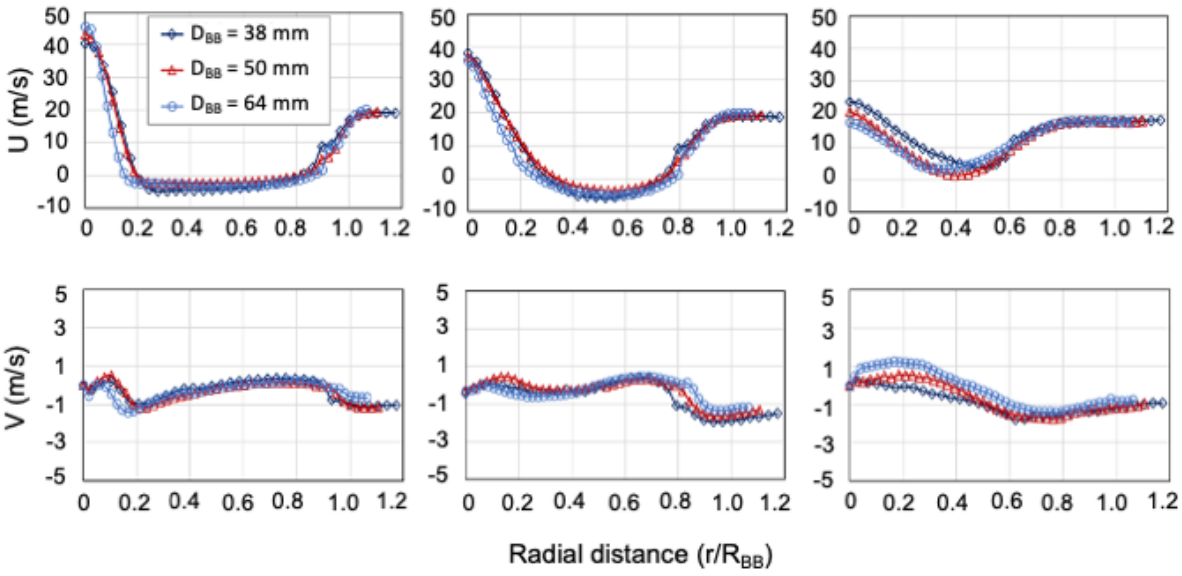

Figure 3.9: Radial profile of the mean axial velocity (first row), and the mean radial velocity (second row) at three heights above the burner; X/D_{BB}=0.3 (left), X/D_{BB}=0.9 (middle), and X/D_{BB}=1.8 (right).

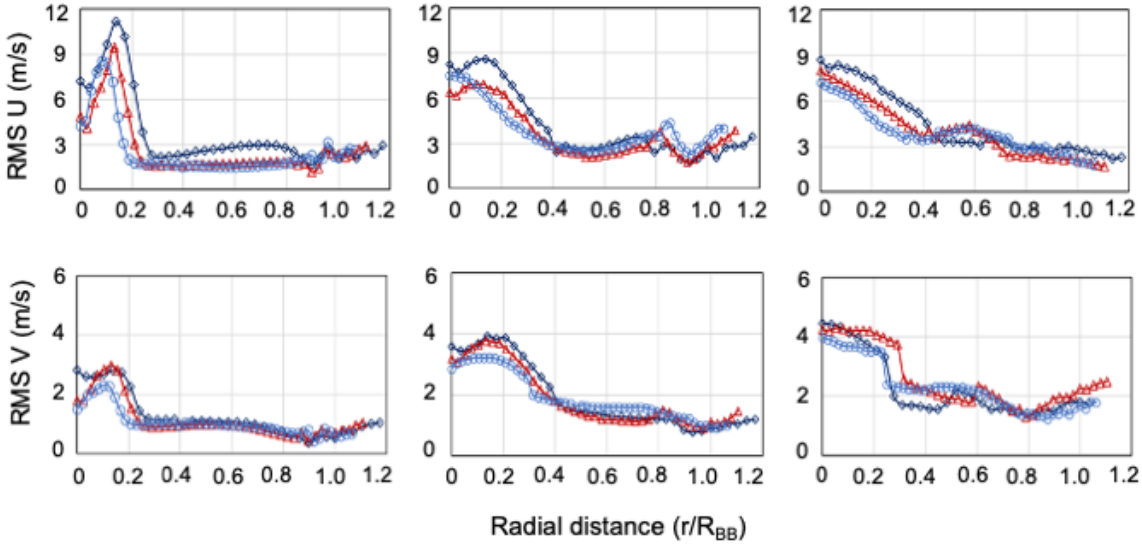

Figure 3.10: Radial profile of the mean axial velocity fluctuations (first row), and the mean radial velocity fluctuations (second row) at three heights above the burner; X/D_{BB}=0.3 (left), X/D_{BB}=0.9 (middle), and X/D_{BB}=1.8 (right).

3.4.5 Residence Time Distribution Prediction

Shown in Figure 3.11 are the calculated streamlines from the recirculation zone of three flames, each with a different bluff-body diameter burner. Also indicated in the Figure is the length of the recirculation zone, defined by the furthest axial profile with a zero-axial velocity. It was observed that, as discussed earlier, increasing the bluff-body diameter resulted in increasing the length of the recirculation zone. This increase is attributed to the level of mixing and interaction between the jet and the co-flow and was found in the past [1] to be governed by the momentum flux ratio and the diameter of the bluff-body burner. Since this ratio of both the jet and the co-flow was kept the same for all three burners, the length is only controlled by the change in the bluff-body diameter. Here, it can be seen that increasing the diameter from 38 mm to 50 mm and 64 mm, resulted in an increase in the recirculation zone length by almost 40% and 85% respectively (from 61 mm to 86.0 and 110.7 mm). Hence, it is expected that this increase in the length of the recirculation zone will increase the residence time in this zone and consequently affect soot formation in this region.

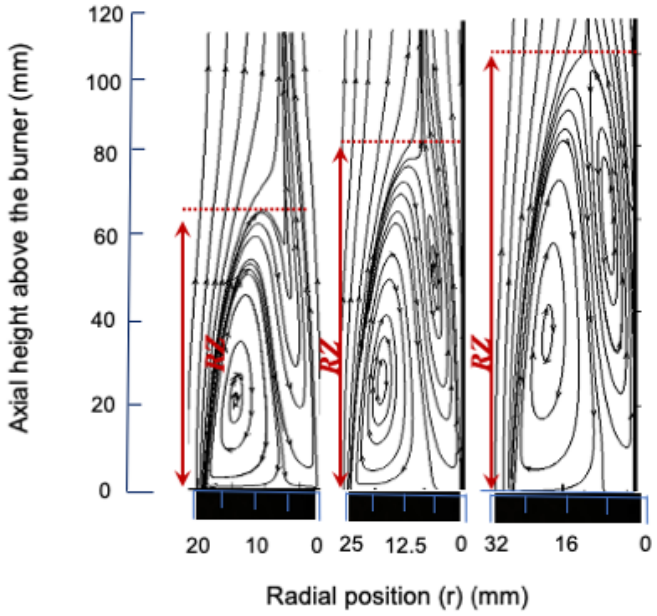

Figure 3.11: Computed flow field for three bluff-body burners: 38 mm (left), 50 mm (middle), and 64 mm (right). Red lines indicate the length of the recirculation zone.

The residence time distribution for the three burners is compared in Figure 3.12. The different distributions indicate that fewer than 10% of the pseudo-particles originating in the fuel jet do not enter the circulating zone and escape out to the neck zone. The distribution of the rest of the pseudo-particles can be observed in this Figure. The mean residence time of the particles is almost doubled when the diameter increases from 38 mm to 64 mm. Since there is an overlap of the timescales between turbulent mixing and soot formation in turbulent flames, which is in the order of few milliseconds to 10 milliseconds, it is inferred that the residence time of the pseudo-particles can affect soot formation in the recirculation zone. A comparison of the mean residence time along with the length of the recirculation zone for three burners is shown in right side of Figure 3.12. It is clear that there is a direct correlation between the recirculation zone length and the average residence time.

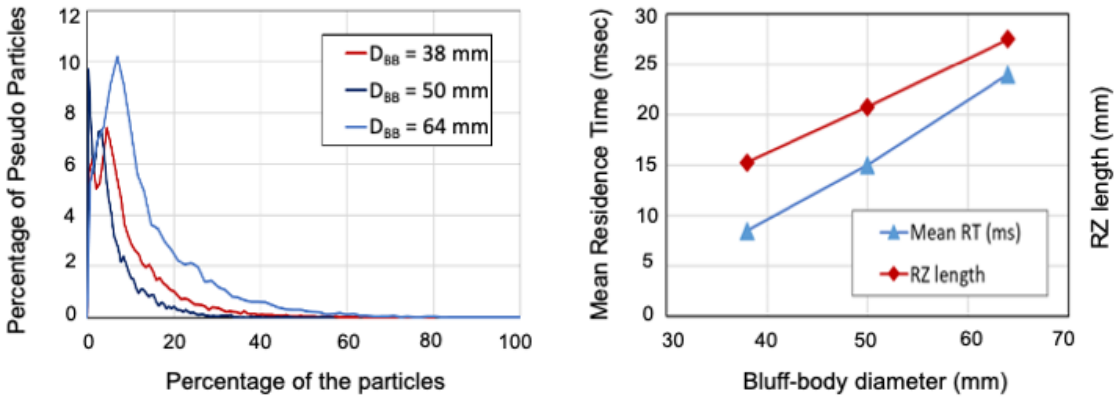

Figure 3.12: Residence Time Distribution (RTD) of the particles in the recirculation zone (left). Calculated mean residence time of the particles inside the recirculation zone, and the length of the zone (right).

The calculated mixture fraction distribution within the recirculation zone, RZ, for all three bluff-body burners and at three axial locations is shown in Figure 3.13. It can be observed that the mixture fraction and location of the reaction zone are almost identical on the outer part of the RZ, irrespective of the bluff-body diameter. Also noticeable is that increasing the bluff-body diameter induces a larger amount of the fuel to enter into the inner part of the RZ, creating richer mixtures that are favourable for soot formation.

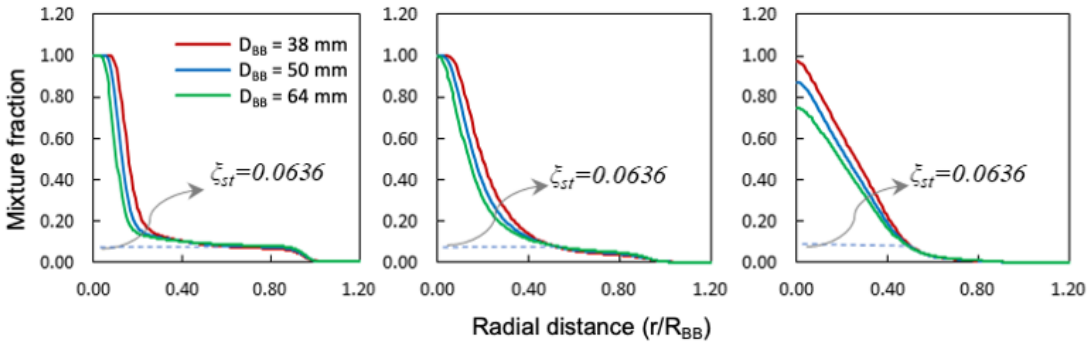

Figure 3.13: Effect of the bluff-body diameter on the mixture fraction distribution at X/D_{BB}=0.3 (top), X/D_{BB}=0.6 (middle), and X/D_{BB}=1.3 (bottom). A stoichiometric mixture fraction of 0.0636 is shown on all the Figures.

3.5 Conclusion

Experimental and computational tools were used to investigate the flow field and residence time distribution (RTD) of the reactants within the recirculation zone in a set of turbulent non-premixed ethylene/nitrogen bluff-body flames. Three identical burners except of the diameter of the bluff-body (38mm, 50mm and 64mm) were considered in this study. Successful PIV in a highly-sooting turbulent environment, as well as the radiation heat flux measurements, have been conducted. A novel optical design was applied to a conventional PIV system to suppress interference from soot, in the recirculation zone of flames with a fuel comprising 80% ethylene and 20% nitrogen by volume, and make the velocity measurement feasible in such flames. Commercial CFD code running a 2-D RANS model, was used to investigate the effect of bluff-body diameter on the recirculation zone characteristics, and to predict the distribution of the residence time of pseudo-particles within the recirculation zones of those flames. The radiation measurements show that increasing the bluff-body diameter would increase the radiation in the recirculation zone by 32%, whilst the total radiation from the flame decrease by 15% believed due to the decrease in flame volume. It was observed that increasing the bluff-body diameter increases the recirculation zone length with measured length of ~1.5-1.75 D_{BB}, while the length of recirculation zone for the non-reacting cases is ~1.2 D_{BB}. This difference is believed to be attributed to the thermal effects. The CFD results have revealed a similar increase in recirculation length in reacting cases with the largest burner showing a length of 1.7 D_{BB}. This increase in the size and length of the recirculation

zone leads to an increase in the residence time of the reactants inside the recirculation zone by a factor of three, which can considerably influence the soot formation in this region. It can also be observed that neither the mixture fraction nor the reaction zone in the recirculation region structure are significantly influenced by increasing the bluff-body diameter. Further research is underway to conduct simultaneous measurements of the soot concentrations and the flow fields of these flames.

3.6 Nomenclature

D_{BB}	Bluff-body diameter
d_J	Jet diameter
HHV	Higher heating value
I	Turbulence intensity
IV	Inner vortex
K	Turbulent kinetic energy
OV	Outer vortex
R	Radius of the bluff-body burner
r	Radial locations
RMS	Root mean square
U_m	Velocity magnitude
U	Axial velocity component
V	Radial velocity component
x	Axial locations
χ_r	Radiant fraction

Subscripts

BB	Bluff-body
C	Contractor
f	Flame
J	Jet
m	Mean

Acknowledgements

The authors gratefully acknowledge the support of the Australian Research Council for their funding through grant DP130100198. The Australian Government for the funding the PhD scholarship is gratefully acknowledged.

3.7 References

[1] B. B. Dally, D. F. Fletcher, and A. R. Masri, "Flow and mixing fields of turbulent bluff-body jets and flames", Combusion Theory and Modelling, vol. 2, pp. 193-219, 1998.

[2] R. W. Schefer, M. Namazian, and J. Kelly, "Velocity Measurements in a Turbulent Nonpremixed Bluff-Body Stabilized Flame", Combustion Science and Technology, vol. 56, pp. 101-138, 1987.

[3] R. W. Schefer, M. Namazian, J. Kelly, and M. Perrin, "Effect of Confinement on Bluff-Body Burner Recirculation Zone Characteristics and Flame Stability", Combustion Science and Technology, vol. 120, pp.185-211, 1996.

[4] R. S. Barlow, M. J. Dunn, M. S. Sweeney, and S. Hochgreb, "Effects of preferential transport in turbulent bluff-body-stabilized lean premixed CH_4/air flames", Combustion and Flame, vol. 159, pp. 2563-2575, 2012.

[5] R. Zhou, S. Balusamy, M. S. Sweeney, R. S. Barlow, and S. Hochgreb, "Flow field measurements of a series of turbulent premixed and stratified methane/air flames", Combustion and Flame, 160, 2017-2028, 2013.

[6] G. Magnotti and R. S. Barlow, "Effects of high shear on the structure and thickness of turbulent premixed methane/air flames stabilized on a bluff-body burner", Combustion and Flame, vol. 162, pp. 100-114, 2015.

[7] A. Rowhani, Z. W. Sun, A. Chinnici, P. R. Medwell, G. J. Nathan, B. B. Dally,"Effect of bluff-body diameter on the flow field and residence time of turbulent ethylene/nitrogen flames". In: Proceeding of the 12th Asia-Pacific Conference on Combustion, Fukuoka, Japan, 2019.

[8] A. M. K. P. Taylor and J. H. Whitelaw, "Velocity characteristics in the turbulent near wakes of confined axisymmetric bluff bodies", Journal of Fluid Mechanics, vol. 139, pp. 391-416, 1984.

[9] H. Tang, D. Yang, T. Zhang, and M. Zhu, "Characteristics of Flame Modes for a Conical Bluff-Body Burner With a Central Fuel Jet", Journal of Engineering and Gas Turbine Power, vol. 135, no. 9, pp. 091507-091516, 2013.

[10] K. Li and R.S. Tankin, "A Study of Cold and Combusting Flow Around Bluff-Body Combustors", Combustion Science and Technology, vol. 52, pp. 173-206, 1987.

[11] A. Danlos, G. Lalizel, and B. Patte-Rouland, "Experimental characterization of the initial zone of an annular jet with a very large diameter ratio", Experiments in Fluids, vol. 54, pp. 1-17, 2013.

[12] R. Perrin, M. Braza, E. Cid, S. Cazin, F. Moradei, and A. Barthet, "Near-Wake Turbulence Properties in the High Reynolds Number Incompressible Flow Around a Circular Cylinder Measured by Two- and Three-Component PIV", Flow, Turbulence and Combustion volume, vol. 77, pp. 185-204, 2006.

[13] M. Ozgoren, "Flow structure in the downstream of square and circular cylinders", Flow Measurement and Instrumentation, vol. 17, pp. 225-235, 2006.

[14] I. Esquiva–Dano, H. T. Nguyen, and D. Escudie, "Influence of a bluff-body's shape on the stabilization regime of non-premixed flames", Combustion and Flame, vol. 127, pp. 2167-2180, 2011.

[15] Y. Tong, X. Liu, S. Chen, Z. Li, and J. Klingmann, "Effects of the position of a bluff-body on the diffusion flames: A combined experimental and numerical study", Applied Thermal Engineering, vol. 131, pp. 507-521, 2018.

[16] A. R. Masri, B. B. Dally, R. S. Barlow, and J. G. Fiechtner, " Instantaneous and Mean Compositional Structure of Bluff-Body Stabilized Nonpremixed flames", Combustion and Flame, vol. 114, pp. 119-148, 1998.

[17] M. Köhler, I. Boxx, K. P. Geigle, and W. Meier, "Simultaneous planar measurements of soot structure and velocity fields in a turbulent lifted jet flame at 3 kHz" Applied Physics B, vol. 103, pp. 271-279, 2011.

[18] M. Köhler, K. P. Geigle, W. Meier, B. M. Crosland, K. A. Thomson, and G. J. Smallwood, "Sooting turbulent jet flame: characterization and quantitative soot measurements" Applied Physics B, vol. 104, pp. 409-425, 2011.

[19] V. Narayanaswamy and N. T. Clemens, "Simultaneous LII and PIV measurements in the soot formation region of turbulent non-premixed jet flames", Proceedings of the Combustion Institute, vol. 34, pp. 1455-1463, 2013.

[20] S. M. Mahmoud, G. J. Nathan, Z. T. Alwahabi, Z. W. Sun, P. R. Medwell, and B. B. Dally,"The effect of exit strain rate on soot volume fraction in turbulent non-premixed jet flames", Proceedings of the Combustion Institute, vol. 36, pp. 889-897, 2017.

[21] S. M. Mahmoud, G. J. Nathan, Z. T. Alwahabi, Z. W. Sun, P. R. Medwell, and B. B. Dally, "The effect of exit Reynolds number on soot volume fraction in

turbulent non-premixed jet flames", Combustion and Flame, vol. 187, pp. 42-51, 2018.

[22] S. M. Mahmoud, G. J. Nathan, P. R. Medwell, B. B. Dally, and Z. T. Alwahabi,"Simultaneous planar measurements of temperature and soot volume fraction in a turbulent non-premixed jet flame", Proceedings of the Combustion Institute, vol. 35, pp. 1931-1938, 2015.

[23] S. Chatterjee and Ö. L. Gülder,"Soot concentration and primary particle size in swirl-stabilized non-premixed turbulent flames of ethylene and air", Experimental Thermal and Fluid Science, vol. 95, pp. 73-80, 2018.

[24] L.-Y. Wang, C. K. Bauer, and Ö. L. Gülder, "Soot and flow field in turbulent swirl-stabilized spray flames of Jet A-1 in a model combustor". Proceedings of the Combustion Instititue, vol. 37, pp. 5437-5444, 2019.

[25] G. J. Nathan, P. A. M. Kalt, Z. T. Alwahabi, B. B. Dally, P. R. Medwell, and Q. N. Chan, "Recent advances in the measurement of strongly radiating, turbulent reacting flows", Progress in Energy and Combustion Science, vol. 38, pp. 41-61, 2012.

[26] H. I. Joo, and Ö. L. Gülder, "Experimental study of soot and temperature field structure of laminar co-flow ethylene–air diffusion flames with nitrogen dilution at elevated pressures", Combustion and Flame, vol. 158, pp. 416-422, 2011.

[27] Turns, S.R., Myhr, F.H. Oxides of nitrogen emissions from turbulent jet flames-Part 1-Fuel effects and flame radiation. Combustion and Flame, 87, 319–335.

[28] S. J. Rao, N. V. S. Ramani, H. J. Pant, and D. N. Reddy, "Measurement of residence time distributions of coal particles in a pressurized fluidized bed gasifier (PFBG) using radio tracer technique", Indian Journal of Science and Technology, vol.5, pp. 3746-3752, 2011.

[29] S. Bürkle, L. G. Becker, M. A. Agizza, A. Dreizler, V. Ebert, and S. Wagner,"In-situ measurement of residence time distributions in a turbulent oxy-fuel gas-flame combustor", Experiments in Fluids, vol. 58, pp. 58-77, 2017.

[30] X. Dong, G. J. Nathan, S. M. Mahmoud, P. J. Ashman, D. Gu, and B. B. Dally, "Global characteristics of non-premixed jet flames of hydrogen–hydrocarbon blended fuels", Combustion and Flame, vol. 162, pp. 1326-1335, 2015.

[31] A. S. Langman, G. J. Nathan, J. Mi, and P. J. Ashman, "The influence of geometric nozzle profile on the global properties of a turbulent diffusion flame" Proceedings of the Combustion Institute, vol. 31, pp. 1599–1607, 2007.

[32] W. Thielicke, "The flapping fligh of birds - analysis and application", Rijksuniversity, Groningen, 2014.

[33] W. Thielicke, E. J. Stamhuis, " PIVlab - Towards User-friendly, Affordable and accurate digital particle image velocimetry",. Journal of Open Research Software, vol. 2, no. 1, 2014.

[34] J. Westerweel, "Fundamentals of digital particle image velocimetry", Measurment Science and Technology, vol. 8, pp. 1379-1392, 1997.

[35] A. R. Masri, B. B. Dally, " Modelling of Bluff-body recirculating flows", In: Proceeding of the 12st Australasian Fluid Mechanics Conference, Sydney, Australia, 1995.

[36] A. Chinnici, M. Arjomandi, Z. F. Tian, Z. Lu, and G. J. Nathan, "A Novel Solar Expanding-Vortex Particle Reactor: Influence of Vortex Structure on Particle Residence Times and Trajectories", Solar Energy, vol. 22, pp. 58-75, 2015.

[37] S. Deng, M. E. Mueller, Q. N. Chan, N. H. Qamar, B. B. Dally, and Z. T. Alwahabi, "Hydrodynamic and chemical effects of hydrogen addition on soot evolution in turbulent nonpremixed bluff body ethylene flames", Proceedings of the Combustion Institute, vol. 36, pp. 807-814, 2017.

[38] M. E. Mueller, Q. N. Chan, N. H. Qamar, B. B. Dally, H. Pitsch, Z. T. Alwahabi, "Experimental and computational study of soot evolution in a turbulent nonpremixed bluff body ethylene flame", Combustion and Flame, vol. 160, pp. 1298–1309, 2013.

[39] A. Katoh, H. Oyama, K. Kitagawa, and A. K. Gupta, "Visualization of OH Radical Distribution in a Methane-Hydrogen Mixture Flame by Isotope Shift/Planar Laser Induced Fluorescence Spectroscopy", Combustion Science and Technology, vol. 178, pp. 2061-2074, 2006.

Chapter 4 Soot-Flowfield Interactions-Mean/Instantaneous Analyses

Statement of Authorship

Title of Paper	Soot-flowfield interactions in turbulent non-premixed bluff-body flames of ethylene/nitrogen.
Publication Status	☑ Published ☐ Accepted for Publication ☐ Submitted for Publication ☐ Unpublished and Unsubmitted work written in manuscript style
Publication Details	Amir Rowhani, Zhiwei Sun, Paul. R. Medwell, Zeyad. Graham. J. Nathan, Bassam. B. Dally, "Soot-flowfield interactions in turbulent non-premixed bluff-body flames of ethylene/nitrogen", Proceeding of the Combustion Institute, 38 (1) 1125-1132, 2021.

Principal Author

Name of Principal Author (Candidate)	Amir Rowhani		
Contribution to the Paper	I planned and proposed the experimental design matrix to the co-authors after a thorough literature review. After several discussions, we decided to experimental cases. I set up the experiments with the assistance of the second co-author, Zhiwei Sun. We collected experimental data. I processed, analysed and interpreted all the experimental data. After discussion with the co-authors regarding the interpretation of the experimental data, I wrote the manuscript. Furthermore, I acted as the corresponding author and responded to the reviewers' comments and recommendations.		
Overall percentage (%)	65%		
Certification:	This paper reports on original research I conducted during the period of my Higher Degree by Research candidature and is not subject to any obligations or contractual agreements with a third party that would constrain its inclusion in this thesis. I am the primary author of this paper.		
Signature		Date	07-10-2021

Co-Author Contributions

By signing the Statement of Authorship, each author certifies that:

i. the candidate's stated contribution to the publication is accurate (as detailed above);

ii. permission is granted for the candidate in include the publication in the thesis; and

iii. the sum of all co-author contributions is equal to 100% less the candidate's stated contribution.

Name of Co-Author	Dr. Zhiwei Sun		
Contribution to the Paper	This co-author provided assistance with the experimental setup and data collection.		
Signature		Date	08-10-2021

Name of Co-Author	Associate Professor Paul R. Medwell		
Contribution to the Paper	This co-author assisted with revising the manuscript and responding the reviewers' comments.		
Signature		Date	08-OCT-2021

Name of Co-Author	Professor Graham J. Nathan		
Contribution to the Paper	This co-author co-supervised the development of the work. He also helped to evaluate and edit the manuscript.		
Signature		Date	14/10/21

Name of Co-Author	Professor Bassam B. Dally		
Contribution to the Paper	This co-author co-supervised the development of the work. He also helped plan and structure the manuscript. He also provided assistance with rebutting reviewers' comments and with revising the manuscript.		
Signature		Date	07-10-2021

Soot-flowfield interactions in turbulent non-premixed bluff-body flames of ethylene/nitrogen

This chapter consists of the published journal article:

Amir Rowhani, Zhiwei Sun, Paul. R. Medwell, G. J. Nathan, Bassam. B. Dally, "Soot-flowfield interactions in turbulent non-premixed bluff-body flames of ethylene/nitrogen", *Proceeding of the Combustion Institute,* Vol. 38 (1), 1125-1132, 2021.

The article is identical to its submitted format with the following exceptions:

1. The typesetting and referencing styles have been altered to maintain a consistent appearance within the thesis.

2. The numbering of tables, figures, and equations has been changed to include the number of the chapter.

The article in its published format is available at:
https://doi.org/10.1016/j.proci.2020.06.148

4.1 Abstract

Simultaneous measurements of soot concentrations and the velocity flowfields are used to better understand soot evolution and its correlation with the strain rate and residence time in a series of turbulent non-premixed bluff-body flames. Laser-induced incandescence (LII) and planar Particle Image Velocimetry (PIV) were applied simultaneously to measure the soot volume fraction (SVF) and the velocity field, respectively. Three flames were stabilised on axisymmetric bluff-body burners with different bluff-body diameters (38, 50, and 64 mm) but which are otherwise identical in dimension. A mixture of ethylene/nitrogen (4:1 by volume) was issued from a 4.6 mm central round jet at a bulk Reynolds number of 15,000. The annular co-flowing air velocity was kept constant at 20 m/s for all cases. In agreement with previous work, the highest SVF was found in the recirculation zone within the outer vortex, adjacent to the co-flowing air. The maximum SVF almost doubled, from 140 ppb to 250 ppb, when using the 64 mm burner, as compared with the 38 mm burner. Relatively small amounts of soot, around 30 ppb, were observed in the highly-strained neck zone. This was deduced from the instantaneous images as having been transported there from the recirculation zone, mostly from the inner vortex. The SVF in the jet region decreased with the increase in bluff-body diameter, which was found to be related to the decrease in the estimated total volume of the flame of almost 9%. The instantaneous images reveal the roller vortices between the co-flow and the recirculation zone suppress soot and cause it to oxidize.

Keywords: Soot, Bluff-body flames, Particle Image Velocimetry (PIV), Laser-induced Incandescence (LII), Turbulence

4.2 Introduction

Research into the impact of gas-phase dynamics on the evolution of soot in turbulent flames has recently been the subject of renewed interest [1]. The new research effort is motivated by the interest in alternative bio-oil fuels [2, 3], advancements in non-intrusive measurement techniques [4-7] and the need for better predictive soot models [8]. The challenges associated with the prediction of turbulent sooting flames, of complex geometries and industrial fuels, are mostly related to the multi-phase, non-linear and localised inter-dependency of many controlling parameters [9]. Those include, but are not limited to, the flame temperature and thermal radiation dependency, turbulence scale, strain rate (S) and residence time, turbulence intensity and mixing, and the type of fuel. Hence, the advancement of soot research under turbulent conditions requires simultaneous and systematic measurements of these parameters to help deepen understanding of their relationship and to provide additional correlations for model validation and development. Studies into turbulent sooting flames stabilised on simple geometries have provided important insights into some of the issues mentioned above, and correlations between soot and the flowfield have been proposed on a global basis. Qamar et al. [10] demonstrated an inverse relationship between the global mixing rate, defined as the inverse of the global residence time, and both the total amount of soot in the flame and local instantaneous soot volume fractions, broadly consistent with trends in laminar flames. However, probability density functions revealed that the relationship between local instantaneous and time-averaged soot volume fractions differ in the lower and upper regions of each flame. Later, Köhler et al. [11] found that the unconditional SVF is a function of both the radial and axial locations of turbulent jet flames. All these measurements, despite their significance, were made in lifted jet flames, which are more challenging to model, leading to delayed soot formation through partial pre-mixing at the base of the flame. Investigated using the Adelaide simple jet flames [1, 12, 13], it was found that while the SVF scales inversely with the global strain, U/D, consistent with [10], the volume-integrated SVF, scales as an inverse exponential function of U/D. On a local basis, simultaneous PIV/LII in jet flames revealed that soot formation happens predominantly at a combination of a flow velocity above 3 m/s and a strain rate of 700 s^{-1} [14]. Geigle et al [15], investigating a model combustor, confirmed the role and significance of residence time and the localised strain condition on soot formation and evolution. Mueller et al. [16, 17] and Deng et al. [18] reported joint experimental and computational work (using LES) of soot evolution in axisymmetric bluff-body stabilised turbulent flames.

Using ethylene as the main fuel, their work revealed that, unlike jet flames, the mechanism of soot evolution in bluff-body stabilized flames is dominated by acetylene-based surface growth processes, whilst in jet flames, the PAH-based growth (nucleation and condensation) dominates over the surface growth. They also found that in bluff-body flames, most of the soot is nucleated near the inner shear layer and a portion of the soot is backed to the bluff-body by the recirculating flows. The growth rate in the recirculation zone (RZ) is low since the mixture fraction in this region does not support either PAH formation or acetylene-based surface growth. Subsequently, the soot particles are transported by the outer vortex, downstream of the flame. While this work has provided important insights, it did not include any measurements of the impact of strain and residence time on soot. It was also not clear about the mechanism of soot oxidation and soot transportation to the neck zone. Given the importance of recirculating flows, axi-symmetric bluff-body flames are considered in the current study as this helps bridge the gap between the simple jet and more practical swirling flames. In our recent work [19], we demonstrated that when the bluff-body diameter changes while all other parameters are identical, the residence time inside the recirculation zone is the only parameter that changes, whereas the mean mixture fraction and the mean temperature are almost unaltered. The calculated temperature and mixture fraction distribution for these flames are compared in the supplementary material (Fig. A.S1). The current study uses the same configuration in [19] with the aim of investigating in depth the flow structure in the recirculation zone and its impact on flame features and soot in ethylene-nitrogen turbulent flames. In particular, the paper examines the impact of flow dynamics within the RZ on soot formation, transport and oxidation through simultaneous measurements of the soot volume fraction and flowfield. The mean and instantaneous results from the three flames, operating under the same conditions, are compared in this study. The relationship between the soot, flow and strain fields are also presented and discussed for all flames.

4.3 Experimental methods

4.3.1 Burner and flames

Three bluff-body burners, similar in geometry to the Sydney bluff-body burner [20], were used in this study. In brief, each burner comprises of the same 4.6 mm diameter (D_J) central tube, from which the fuel stream issues, but with a different diameter of the outer bluff-body: 38, 50 and 64 mm. All other specifications and features of the burners are identical. The burners were made of brass, with a heat-resistant ceramic coating on the bluff-body surface to reduce heat loss to the burner. The burner was surrounded by co-flowing air from a contraction with a round cross section and an internal diameter of 190 mm at the exit plane. The round shape has been selected to avoid the formation of corner vortices. For optical access, each bluff-body rises above the co-flow air contractor edge by approximately 10 mm. The entire burner, together with its associated components, was mounted on an electrical traverse to allow measurements to be performed throughout the entire length of the flame, whilst keeping the optical system fixed in place. An exhaust hood was kept at a fixed distance from the flame tip, by traversing it with the burner assembly, to minimize any interaction between the exhaust extraction and the flame. Three cases with a similar bulk Reynolds number of 15,000 have been investigated and labelled as ENB-1, ENB-2, and ENB-3. The fuel stream is a fixed mixture of high-purity ethylene (99%) and ultra-high purity nitrogen (99.99%) at a volume fraction of 4:1, at atmospheric pressure and ambient temperature. The bulk co-flowing air velocity was kept constant at 20 m/s for all cases. The details of the three flames are summarised in Table 1. The flame length (L_f) has been estimated from 10 instantaneous images and measured as the distance between the bluff-body surface and the most visible downstream flamelet. The mean recirculation zone length was determined by the highest axial distance above the burner, where the mean axial and radial velocities are zero. The residence time was obtained using CFD after validation [19]. The calculation method is summarized in the supplementary material (A.S2).

Table 4.1: Summary of the flow conditions. (D_{BB} – bluff-body diameter; D_J – Fuel jet diameter; U_J – Bulk jet exit velocity; Re_J – Jet exit Reynolds; $\dot{m}_f$ – Fuel flow rate; U_C – Bulk co-flowing air velocity; $\overline{L}_f$ – Mean flame length; $\overline{L}_{RZ}$ – Mean recirculation zone length; $\overline{\tau}$ – Mean residence time).

Flame case	C_2H_4:N_2 (%Vol.)	D_{BB} (mm)	D_J (mm)	U_J (m/s)	Re_J (-)	$\dot{m}_f$ (g/s)	U_C (m/s)	$\overline{L}_f$ (mm)(±5%)	$\overline{L}_{RZ}$ (mm)(±1%)	$\overline{\tau}$ (ms)[19]
ENB-1	4:1	38	4.6	32.1	15,000	0.61	20	920	61	8.57
ENB-2	4:1	50	4.6	32.1	15,000	0.61	20	855	86	15.5
ENB-3	4:1	64	4.6	32.1	15,000	0.61	20	780	114	24.4

4.3.2 Planar Polarised Particle Image Velocimetry (2D-P-PIV)

The two-dimensional velocity field was obtained through a planar PIV system, using a 10 Hz dual-head Nd:YAG laser (Quantel BrilliantB/Twins) operated at 532 nm and a maximum energy of 140 mJ/pulse. An inter-pulse period of 14 µs to 60 µs was chosen, depending on the flow conditions between the PIV laser pulses. The laser beam passed through a wave-plate and sheet forming optics and finally collimated to a sheet with dimensions of 70 × 1 mm^2. Both the jet and the co-flow were seeded with 1 µm titanium oxide (TiO_2) particles as flow markers with an in-house built fluidised-bed particle seed generator. The Mie scattering from the TiO_2 particles was detected by a Kodak Megaplus II CCD camera (1920 × 1080 $pixels^2$, 16 bit) equipped with a Sigma lens 105 mm, f-number 2.8 and equipped with a 532 nm bandpass filter (Andover) with an FWHM of 1 nm, for suppressing both laser-induced and natural incandescence. To overcome the soot interference with the Mie scattering from the flow tracers at 532 nm excitation, a novel optical design has been developed using two additional polarising filters to a conventional PIV system. A half-waveplate at 29 degrees to the vertical was placed in front of the incident beam to direct the beam horizontally. A second linear polarizer was attached to the 1 nm bandpass filter to capture the vertically-polarised scattering signals. This optical arrangement can significantly suppress the scattered interference from soot to very low levels. The large scattering from the PIV particles is only reduced by a factor of approximately two. Thus, soot interference on the PIV images was much reduced compared with a conventional PIV system. It is noteworthy that the influence of PIV seeding on the LII signal has been found to be 4.7%. The PIV vectors were obtained by cross-correlation of the 2000 pairs of raw images with the smallest interrogation window of 16×16 $pixels^2$ with a 50% overlap. This leads to a minimum spatial resolution of 0.74×0.74 mm^2.

4.3.3 Planar Laser-induced incandescence (P-LII)

The soot imaging method is the same as in our previous studies [12, 13, 17], so only briefly described here. The planar laser-induced incandescence (LII) technique was employed to measure the soot volume fraction, using a pulsed (10 Hz) Nd:YAG laser (Q-smart 850, Quantel) with the fundamental output (1064 nm). The LII excitation pulse was temporally interlaced between the first and second PIV pulses, with a 5 μs delay between the first PIV pulse and the LII pulse to avoid affecting the LII signals. The induced incandescence was collected with an intensified CCD (ICCD) camera (PI-Max 4 Princeton Instruments, 1024 × 1024 pixels^2). A 430-nm bandpass filter (10 nm FWHM) was used to suppress the C_2 laser-induced emissions, together with minimising the flame radiation interface. The gate-width of the ICCD was set to 50 ns. To reduce the effects of laser fluence variations from the beam steering and attenuation on the LII signals, the laser fluence was kept above 0.50 J/cm^2, in the plateau region of the LII response curve [21]. Sun et al. [22] found a 2 mrad beam steering in turbulent non-premixed jet flames, which accounts for the 50% increase in the laser sheet width, and consequent up to 750 μm out-of-plane direction throughout the flame. To minimize these effects, since they have not been quantified in our flames, the data was only obtained from the beam entrance side of the flame. Quantification of the recorded LII signals was achieved by calibration against the C_2H_4/air premixed flat-flame with $\Phi = 2.34$, using a Mckenna burner [1] to obtain the calibration constant. The 532 nm beam, with a thickness of 1 mm, was overlapped with the 1064 nm LII laser beam, with a thickness of 500 μm, using a dichroic mirror and passed through a combination of two cylindrical lenses and one spherical lens, collimated and directed to the flame. A schematic of the experimental setup, including the burner, optical arrangements for the simultaneous PIV and LII, and the pulse diagram, is depicted in Fig. 4.1. A detailed view of the burner can be found in the supplementary material (Fig. A.S3).

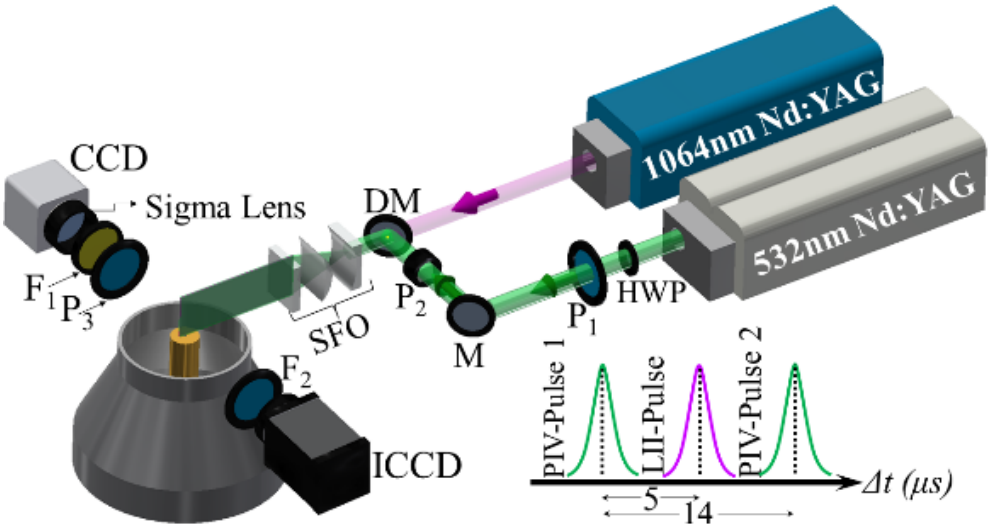

Figure 4.1: Simultaneous LII and PIV setup. (DM – Dichroic mirror; F_1 – 532 nm bandpass filter (FWHM); F_2 – 430 nm interference filter; HWP – $\frac{\lambda}{2}$ wave plate at 29°; M – 532 nm mirror; P_1– 532 nm film polarizer @45°; P_2 – Prism; P_3 – Linear polarizer and SFO – Sheet-forming Optics).

4.4 Results and discussions

4.4.1 Global flame features

The global appearance of the three turbulent non-premixed bluff-body flames is presented on the left-hand-side (LHS) of Fig. 4.2. The flow features on all three burners, including the axial and radial velocity profiles, together with the fluctuating components and mixture strength, exhibit similar features to those reported previously in non-sooting [20, 23] and sooting bluff-body flames [17-19]. Each flame consists of a low-strain, highly-sooting recirculation zone immediately downstream from the exit plane ($x/D_{BB} < 1.6$); a jet-like region downstream of the flame; and a high-strain neck zone, which connects the recirculation zone to the jet region ($1.6 < x/D_{BB} < 2.2$). The total flame length of ENB-3 is ~15% shorter than ENB-1, since a greater fraction of the fuel is burnt in the relatively larger recirculation zone.

Shown on the right-hand-side (RHS) of Fig. 4.2, is a collage of the measured mean soot volume fraction at all sections of the flames, corresponding to the flame photographs on the left. The collage clearly shows the soot concentration in each zone of the flames for all three burners. The larger RZ in ENB-3 leads to an increase in the maximum SVF by ~60%, as well as in the thermal radiation by ~32% [19].

The maximum soot concentration of 240 ppb is found in the recirculation zone of the ENB-3 flame due to the relatively long residence time, whilst this maximum decreases by 40%, to approximately 150 ppb, for flame ENB-1. The neck zone is found to have reduced amounts of soot with a slight increase in the measured SVF as the bluff-body diameter increases. The high strain rate in the neck zone inhibits the formation of soot and is likely to promote soot oxidation due to mixing with oxygen from the co-flow. The jet-like region, downstream of the neck zone, shows a similar trend to that of turbulent non-premixed jet flames [12, 13]. Comparing the soot concentration in the jet regions reveals that the lowest SVF in an EBN-3 flame could be attributed to the 9% reduction in the flame length, the smallest percentage of fuel burnt in this region, leading to a lowering of the SVF in the jet of 12%.

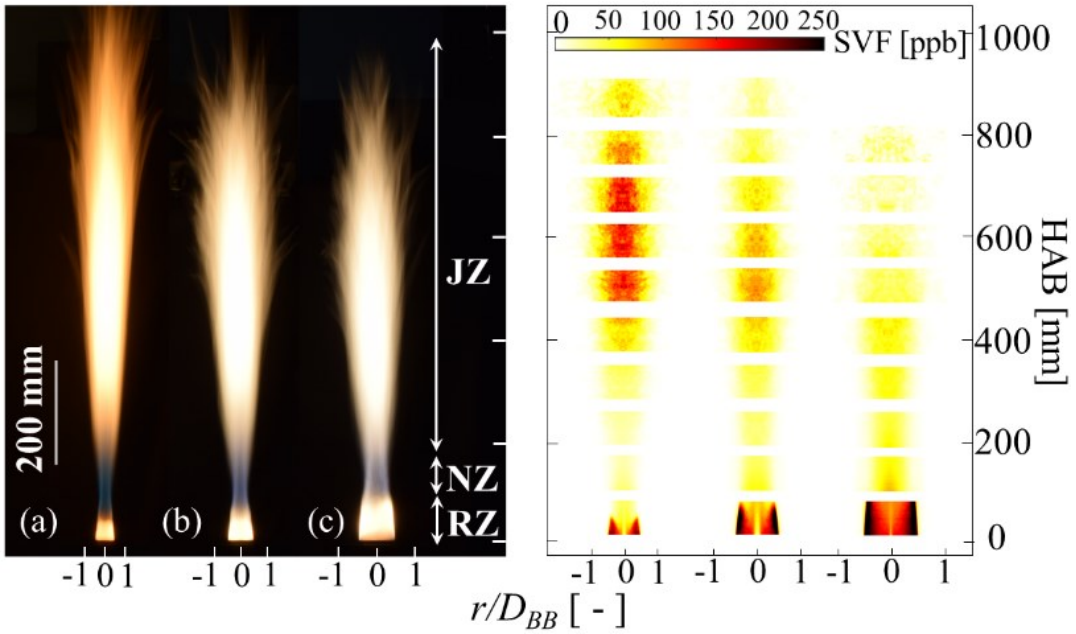

Figure 4.2: Photographs (LHS) of ENB-1 (a), ENB-2 (b), and ENB-3 (c) flames. Collage of the measured mean SVF (RHS), along the full length of the same flames.

Fig. 4.3 shows the axial profile of the radially integrated mean soot volume fraction for each of the flames. The distance above the exit plane is normalized by the bluff-body diameter. For all flames, the total soot inside the RZ increases sharply with the axial distance and peaks at 1.7 ,1.1 and 0.8 bluff-body diameters for ENB-1, ENB-2 and ENB-3, respectively. The soot concentration then drops sharply to a minimum value of around 2.0 D_{BB}. This sharp decrease is deduced to be caused by

enhanced oxidation of the mixture of hot products from the RZ and the fresh oxygen from the co-flow. The accumulated amount of soot inside the RZ almost doubles in flame ENB-2 relative to ENB-1 and doubles again in ENB-3. The amount of soot in the neck zone and the rest of the flames is approximately one-third of the maximum measured in the RZ for each case. In the rest of the flame, the soot production rate is much higher for the smaller bluff-body flames, since more fuel is burned downstream than in the RZ. Interestingly, all flames peak at a downstream position, > 0.7 x/L_f. Mahmoud et al. [12] showed that the soot distribution is markedly different for a similar flame stabilised on a simple jet burner, with an I.D.=4.4 mm, Re=15,000 and $C_2H_4/N_2/H_2$ fuel mixture. The maximum concentration of soot is found at x/L_f =0.6 and the maximum radially integrated soot concentration is 1500 ppm.mm^2, compared with ~900 ppm.mm^2 in our flames. Despite the fact that the Mahmoud flame has a lower ethylene mass flow rate and the presence of hydrogen in the fuel mixture, more soot is found at the peak in their flames than for our bluff-body flames. This seems to be attributed to the burning of fuel in the RZ and the consumption of soot in the neck zone.

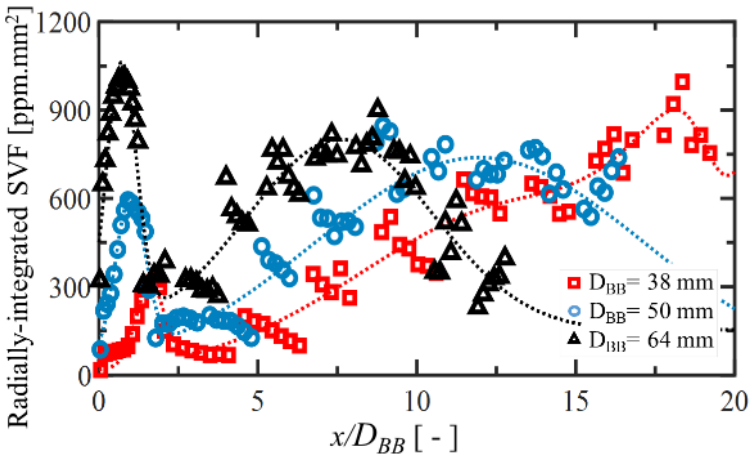

Figure 4.3: Axial profile of radially integrated *SVF*, in ppm.m^2, throughout the flame height. The fitted dotted lines are Gaussian functions.

4.4.2 Mean SVF and flow field in the RZ

The mean flowfield, strain rate and soot volume fraction in the respective recirculation zones of the three flames, are shown in Fig. 4.4. The flow streamlines exhibit two distinct vortical structures within the recirculation zones. An 'inner vortex' *(IV),* which is driven by the fuel jet momentum and an adjacent 'outer vortex' *(OV),* which is driven by the co-flowing stream on the edge of the bluff-body. The size, shape and number of the toroidal structures formed in the RZ are mostly influenced by the momentum flux ratio (jet to co-flow) and the burner geometry. Dally et al. [23] demonstrated that the momentum flux ratio between the jet and the co-flow stream is the dominant parameter that dictates the features, mixture strength and turbulence intensity of the vortices within the RZ. Increasing the momentum flux ratio to above a certain threshold leads to shifting of the inner vortex core downstream, until it becomes part of the expanding fuel jet and is then transported into the neck zone. The threshold of transition between the two regimes was found to be at a ratio of 13 to 15. Since all of the present flames have a constant momentum flux ratio of ~2.47, two distinct vortical structures are found in the RZ of each. Nevertheless, the size of the RZ in each flame differs since this scales with the diameter of the bluff-body. As indicated above, the length of the RZ, which also influences the residence time, is defined by the location of the stagnation point where both the u_x and u_y are equal to zero. The length of the RZ increases by a factor of two for the larger burner, as compared with the smallest bluff-body burner. The measured mean length of the recirculation zone can be seen from Fig. 4.4 and is listed in Table 1. The instantaneous velocity field points to a dynamic interaction between the large vortices shed behind the bluff-body and the momentum-driven jet. This interaction leads to large fluctuations in the size of the recirculation zones and the location of the stagnation points. The effect of these dynamics on soot transport and oxidation is given below. In a recent work [19], we estimated from numerical calculations that increasing the diameter to a 64-mm burner increases the residence time of the pseudo-particles within the RZ by a factor of three. This means that increasing the bluff-body diameter from 38 mm to 64 mm leads to an increase in the mean residence time from 8.57 msec to 24.4 msec. This increase can be deduced to be the primary driver of the measured 60% increase in soot volume inside the recirculation zone. Flow field measurements reveal two strong shear layers at either edge of the RZ, which produce high turbulence intensity. The inner shear layer (ISL) is formed between the fuel jet and the inner vortex, while the outer shear layer (OSL) is formed between the larger outer vortex and the edge of the co-flowing air stream. The interrogation window of the PIV has a spatial resolution of 0.74×0.74

mm^2, which is sufficient to resolve the positions of both shear layers. The locations of the shear layers (ISL, OSL) are shown by a black dashed-lines in the Figure.

The mean 2D shear-strain rate, S_{xy}, has been calculated from the velocity components obtained from the PIV, using the formula $|Sxy| = \frac{1}{2}\left|\left(\frac{\partial u}{\partial y} + \frac{\partial v}{\partial x}\right)\right|$, where u and v are the axial and radial velocity components, respectively. The two highest strain rates are found at the edge of the RZ, specifically at the interaction between the jet and the inner vortex, and the co-flow and the outer vortex. At the shear layers, the strain rate is ~5000 s^{-1}, while inside the RZ the strain rate has a much lower magnitude, typically ~400 s^{-1}, which is well below that needed for extinction. Since there is no swirl in these flows, any out-of-plane motions are expected to be relatively minor. Nevertheless, the present 2D measurements may underestimate somewhat the true 3D shear-strain rate. The lower strain found in the RZ is favourable for soot formation and growth, since the mixture is also rich and at a sufficiently high temperature.

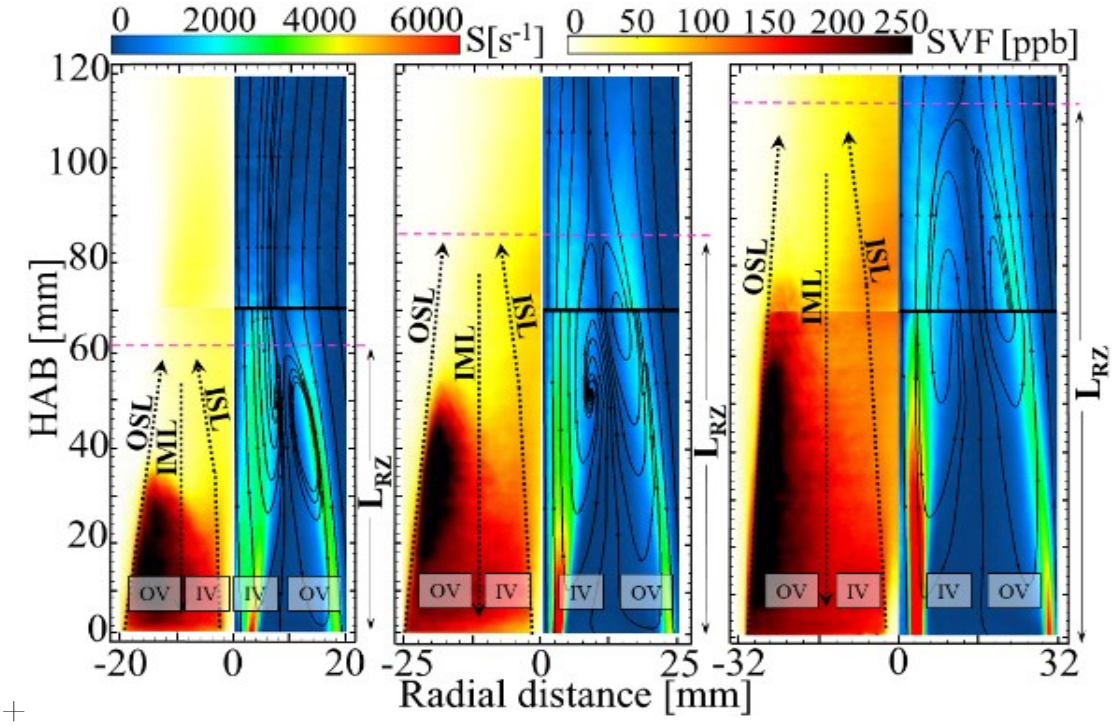

Figure 4.4 Ensemble-averaged S contour overlaid on the streamlines on the RHS of each image and the corresponding mean SVF on the LHS for ENB-1 (left), ENB-2 (middle) and ENB-3 (right) flames. (IV – Inner Vortex; OV – Outer Vortex; ISL – Inner Shear Layer; OSL – Outer Shear Layer; IML – Intermediate Mixing Layer; L_{RZ} – Recirculation zone length).

4.4.3 Instantaneous images of the soot and flowfield

Deeper understanding of soot formation and oxidation beyond the mean and rms values requires the consideration of the instantaneous flow features, together with other parameters, such as temperature and the OH. Representative simultaneous images of instantaneous soot volume fractions and the shear-strain rate along the streamlines are shown in Fig. 4.5. For clarity, coloured-streamlines indicating the shear-strain rate magnitudes are superimposed on the soot volume fraction contours for each flame.

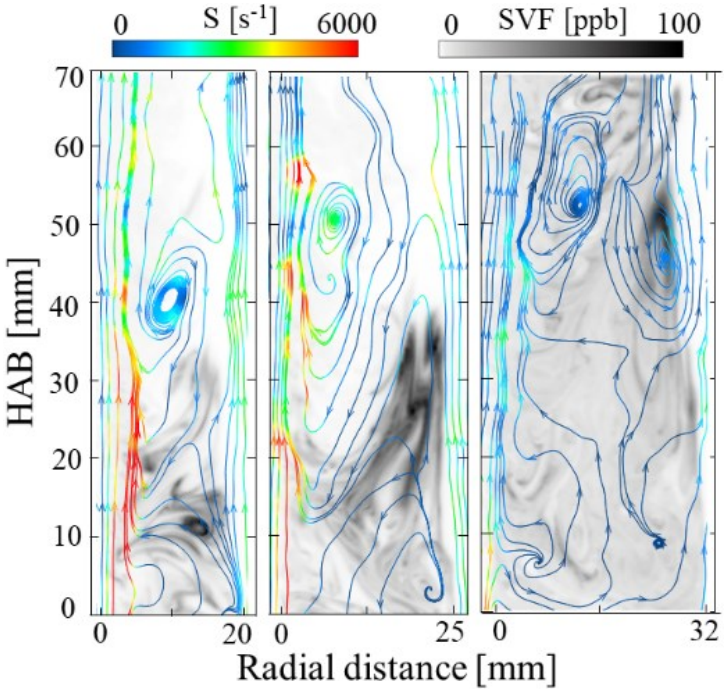

Figure 4.5: Typical instantaneous images of the SVF and the S are superimposed on the flow streamlines for ENB-1 (left), ENB-2 (middle), and ENB-3 (right) flames. The coloured streamlines indicate the strain rate magnitudes.

The instantaneous images of the SVF in the RZ reveal a complex structure that is affected by the flow patterns and the mixing with air from the co-flow. Soot filaments (sheets) can mostly be found in the outer vortex and in the vicinity of the co-flowing air. In some instances, soot filaments are found in a high-strain, high-velocity region within the outer shear layer, where the shear-strain rate exceeds 5000 s^{-1}. These high strain rates suggest that the soot has been transported to these regions from a low-strain high-residence time region, i.e. from within the inner vortex, into the outer shear layer. Consistent with the findings of Mueller et al. [16, 17], soot appears to form in the inner vortex and close to the bluff-body surface. As the diameter of the

bluff-body is increased, more soot is also formed in the vicinity of the jet and closer to the bluff-body surface. This observation is consistent with the longer residence time and reduced strain rate. It is noteworthy that the validated CFD calculations for non-reacting cases show a similar mean mixture fraction distribution for all three flames, ruling out the effect of mixture strength [19].

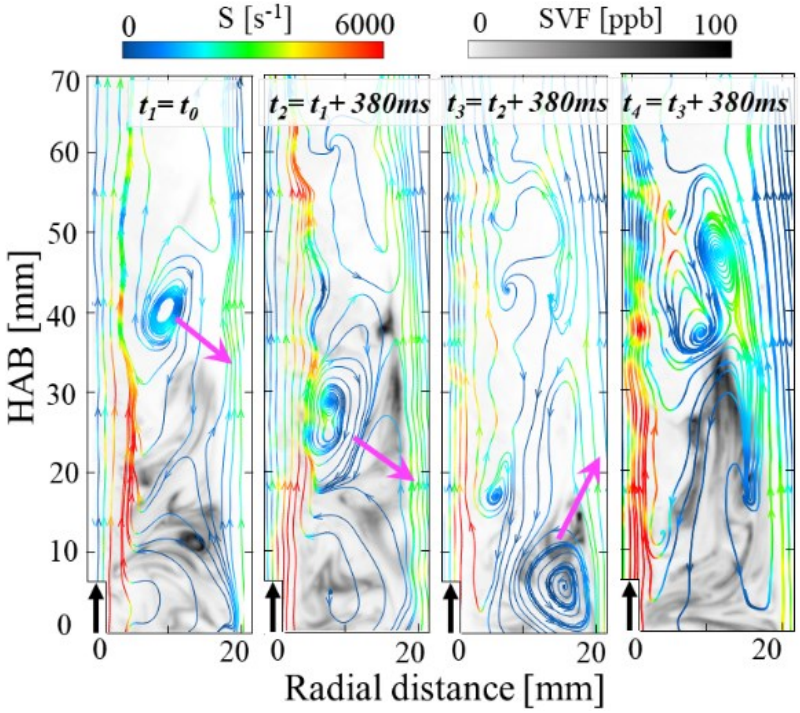

Figure 4.6: Typical time-series of the instantaneous S and SVF for ENB-1 flame, representing the roll-down vortices that affect soot oxidation. The black arrows show the fuel jet entry side. The magenta arrows indicate the vortex location.

Multiple small-scale localised circulation zones are also observed in most images. A typical time series of the rolling vortex is shown in Fig. 4.6. These vortices appear to transport a mixture of air and fuel, together with some products, upstream towards the bluff-body surface in all three cases. Close to the bluff-body surface, the residence time is large, and the turbulence intensity is low, so that more soot is likely to form before it is transported to the outer edge of the OV and towards the outer shear layer. This feature is consistent with the higher mean SVF found in the plots shown earlier in Fig. 4.4. Notable too, is that most of the soot from the outer region is oxidised by the entrained air from the co-flow, so that less than a third reaches the neck zone.

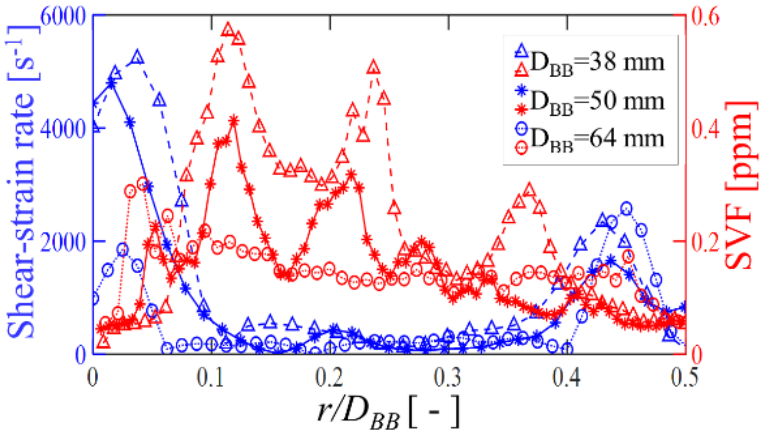

Figure 4.7: Profiles of instantaneous SVF and S at a normalized height of ($x/D_{BB} = 0.4$) above the burner for the three flames.

A typical instantaneous radial profile of the soot volume fraction and the shear strain rate obtained at a normalized height of 0.4 (x/D_{BB} =0.4) above the burner for three flames are compared in Fig. 4.7. The strain rate is shown by blue lines and markers, while the SVF is represented in red. It is clear from this Figure that the instantaneous local strain rate and the SVF vary along the radial direction. It can also be observed that the SVF and local strain rate reveal a trend of being inversely correlated. Two maxima can be found for the strain rate, one in the boundary between the IV and the jet, where the strain is greater than 5000 s^{-1}, for the smallest burner, and the other with a strain rate of 4500 s^{-1} for the larger bluff-body flame. At this location, the soot volume fraction reaches a minimum of about 0.2 ppm. At the position where the strain rate reaches a plateau of $<$ 500 s^{-1}, several peaks for the SVF are observed, with values of about 0.6 ppm for flames stabilised on both the 38-mm and the 50-mm burners. The low-strain region appearing in $0.1 < x/D_{BB} < 0.4$ has a high temperature (around 2000 K which is deduced from previous computations) that is favourable for soot formation. The second maximum of the strain rate is observed in the outer shear layer, where the strain reaches approximately 3000 s^{-1}. These data provide strong evidence that the peak of SVF is associated with the low-strain, high temperature regions of the flame, while the advection processes can explain the presence of soot in the regions of high local strain in the shear layers.

When comparing the three flames in Fig. 4.5, the following observation can be made: (1) increasing the bluff-body diameter leads to a more uniform soot distribution and lower strain-rate inside the RZ; (2) soot appears to form in the inner vortex *(IV)* and is transported to the OV where most of the soot growth seems to happen

(consistent with Mueller et al. [16]); (3) increasing the bluff-body diameter leads to a less distinct localised recirculation zone, which is larger and less intense to provide more time for soot formation and growth; (4) large-diameter burners exhibit less intermittency, perhaps due to the reduced strain rate; (5) most of the soot that ends up in the neck zone appears to originate in the *IV*. It is noteworthy mentioning that the images in Figure 4.5 is only a sample image and the conclusion were drawn from several images and is not limited to a single image. While it is impossible to determine the age of the soot from the current data, the strain rate and flow patterns help to provide new insights that have not been fully understood before. Further planned measurements of temperatures, OH, PAH and soot particle size will be very helpful to complement our current findings and further help in generating statistical data for these flames.

4.5 Conclusion

Measurements of the soot volume fractions and flowfields are reported in this paper from three flames burning a mixture of ethylene and nitrogen (4:1 by vol.) and stabilized on three axisymmetric bluff-body burners. All of the flames had the same Reynolds number and co-flow velocity. The burners had an outer diameter of 38mm, 50mm and 64mm but were otherwise identical. It has been found that, while the overall flame features are the same, the total integrated soot in the flame increases by 35% when using the larger diameter burner, while it increases by a factor of four inside the recirculation zone. Low local strain rates were measured in the recirculation zone for all the flames, leading to higher soot concentrations increasing preferentially with the burner diameter. The total integrated SVF in the recirculation zone is greater by a factor of three in the larger burner, whilst more soot is found in the jet-like region of the smallest burner. A comparison of the mean SVF and the mean strain rate reveals that soot is mostly formed in the inner vortex in the low strain rate region and is transported to the outer vortex where it peaks closer to the outer shear layer for all three cases. Multiple small vortical structures appear to roll upstream and oxidise the soot at the edge of the recirculation zone. Soot transported to the neck zone appears to originate in the inner vortex, rather than being produced in the neck zone, where the strain rate is typically above 1000 s^{-1}, which is unfavourable for soot to form. Further interpretation requires the simultaneous measurements of the OH, PAH or acetylene in the recirculation zone, together with the temperature field.

Acknowledgements

The first author would like to thank the Australian government for scholarship funding through the Research Training Program Scholarship (RTPS). We gratefully acknowledge the support of the Australian Research Council (ARC) for the project funding.

4.6 References

[1] International Sooting Flame (ISF) Workshop. Available: . http://www.adelaide.edu.au/cet/isfworkshop/, (July 23, 2016).

[2] S. Kruse, J. Ye, Z. W. Sun, A. Attili, B. B. Dally, P. R Medwell, and H. Pitsch, "Experimental investigation of soot evolution in a turbulent non-premixed prevaporized toluene flame", Proceedings of the Combustion Institute, vol. 37, pp. 849-857, 2019.

[3] M. J. Evans, J. A. M. Sidey, J. Ye, P. R. Medwell, B. B. Dally, and E. Mastorakos, "Temperature and Reaction Zone Imaging in Turbulent Swirling Dual-Fuel Flames", Proceedings of the Combustion Institute, vol. 37, pp. 2159-2166, 2019.

[4] P. R. Medwell, Q. N. Chan, P. A. M. Kalt, Z. T. Alwahabi, B. B. Dally, and G. J. Nathan, "Development of temperature imaging using two-line atomic fluorescence", Applied Optics, vol. 48, pp. 1237-1248, 2009 .

[5] D. H. Gu, Z. W. Sun, G. J. Nathan, Z. T. Alwahabi, B. B. Dally, "Single-shot, time-resolved planar laser-induced incandescence (TiRe-LII) for soot primary particle sizing in flames", Proceedings of the Combustion Institute, vol. 35, pp. 3673-3680, 2015.

[6] O. Park, R. A. Burns, O. R. H. Buxton, and N. T. Clemens, "Mixture fraction, soot volume fraction, and velocity imaging in the soot-inception region of a turbulent non-premixed jet flame", Proceedings of the Combustion Institute, vol. 36, pp. 899-907, 2017.

[7] T. R. Meyer, S. Roy, V. M. Belovich, E. Corporan, and J. R. Gord, "Simultaneous planar laser-induced incandescence, OH planar laser-induced fluorescence, and droplet Mie scattering in swirl-stabilized spray flames", Applied Optics, vol. 44, pp. 445-454, 2005.

[8] V. Raman, R. O. Fox, "Modeling of Fine-Particle Formation in Turbulent Flames", Annual Review of Fluid Mechanics, vol. 48, pp. 159-190, 2016.

[9] G. J. Nathan, P. A. M. Kalt, Z. T. Alwahabi, B. B. Dally, P. R. Medwell, and Q. N. Chan, "Recent advances in the measurement of strongly radiating, turbulent reacting flows", Progress in Energy and Combustion Science, vol. 38, pp. 41-61, 2012.

[10] N. H. Qamar, G. J. Nathan, Z. T. Alwahabi, and K. D. King, "The effect of global mixing on soot volume fraction: measurements in simple jet, precessing jet, and bluff body flames", Proceedings of the Combustion Institute, vol. 30, pp. 1493-1500, 2005.

[11] M. Köhler, K.-P. Geigle, T. Blacha, P. Gerlinger, and W. Meier, "Experimental characterization and numerical simulation of a sooting lifted turbulent jet diffusion flame", Combustion and Flame, vol. 159, pp. 2620-2635, 2012.

[12] S. M. Mahmoud, G. J. Nathan, Z. T. Alwahabi, Z. W. Sun, P. R. Medwell, and B. B. Dally, "The effect of exit strain rate on soot volume fraction in turbulent non-premixed jet flames", Proceedings of the Combustion Institute, vol. 36, pp. 889-897, 2017.

[13] S. M. Mahmoud, G. J. Nathan, Z. T. Alwahabi, Z. W. Sun, P. R. Medwell, and B. B. Dally, "The effect of exit Reynolds number on soot volume fraction in turbulent non-premixed jet flames", Combustion and Flame, vol. 187, pp. 42-51, 2018.

[14] V. Narayanaswamy and N. T. Clemens, "Simultaneous LII and PIV measurements in the soot formation region of turbulent non-premixed jet flames", Proceedings of the Combustion Institute, vol. 34, pp. 1455-1463, 2013.

[15] K.-P. Geigle, M. Köhler, W. O'Loughlin, and W. Meier, "Investigation of soot formation in pressurized swirl flames by laser measurements of temperature, flame structures and soot concentrations", Proceedings of the Combustion Institute, vol. 35, pp. 3373-3380, 2015.

[16] M.E. Mueller, H. Pitsch, Large eddy simulation of soot evolution in an aircraft combustor, Phys. Fluids 25 (2013) 110812-1.

[17] M. E. Mueller, Q. N. Chan, N. H. Qamar, B. B. Dally, H. Pitsch, and Z. T. Alwahabi, "Experimental and computational study of soot evolution in a turbulent nonpremixed bluff body ethylene flame", Combustion and Flame, vol. 160, pp. 1298-1309, 2013.

[18] S. Deng, M. E. Mueller, Q. N. Chan, N. H. Qamar, B. B. Dally, and Z. T. Alwahabi, "Hydrodynamic and chemical effects of hydrogen addition on soot evolution in turbulent nonpremixed bluff body ethylene flames", Proceedings of the Combustion Institute, vol. 36, pp. 807-814, 2017.

[19] A. Rowhani, Z. W. Sun, P. R. Medwell, Z. T. Alwahabi, G. J. Nathan, and B. B. Dally, "Effects of the bluff-body diameter on the flow field characteristics of non-premixed turbulent highly-sooting flames", Combustion Science and Technology, vol. 194 (2), pp. 378-396, 2022.

[20] B. B. Dally, A. R. Masri, R. S. Barlow, and G.J. Flechtner, "Instantaneous and Mean Compositional Structure of BluffBody Stabilized Nonpremixed flames", Combustion and Flame, vol. 114, pp. 119-148, 1998.

[21] C. Schulz, B. F. Kock, M. Hofmann, H. Michelsen, S. Will, B. Bougie, R. Suntz, and G. Smallwood, "Laser-induced incandescence: recent trends and current questions", Applied Physics B, vol. 83, pp. 336-354, 2006.

[22] Z. W. Sun, Z. Alwahabi, D. H. Gu, S. M. Mahmoud, G. J. Nathan, and B. B Dally, "Planar laser-induced incandescence of turbulent sooting flames: the influence of beam steering and signal trapping", Applied Physics B, vol. 119, pp. 731-743, 2015.

[23] B. B. Dally, D. F. Fletcher, and A. R. Masri, "Flow and mixing fields of turbulent bluff-body jets and flames', Combustion Theory and Modelling, vol. 2, pp. 193-219, 1998.

Chapter 5 Soot-Flowfield Interactions-Statistical Analyses

Statement of Authorship

Title of Paper	Relationships between soot and the local instantaneous strain rate in turbulent non-premixed bluff-body flames
Publication Status	☐ Published ☐ Accepted for Publication ☑ Submitted for Publication ☐ Unpublished and Unsubmitted work written in manuscript style
Publication Details	Amir Rowhani, Zhiwei Sun, Paul. R. Medwell, G. J. Nathan, Bassam. B. Dally, "Relationships between soot and the local instantaneous strain rate in turbulent non-premixed bluff-body flames", Under review.

Principal Author

Name of Principal Author (Candidate)	Amir Rowhani		
Contribution to the Paper	I planned and proposed the experimental plans to the co-authors after a thorough literature review. Together with the co-authors, we decided the experimental cases. I set up experiments to measure soot and flowfield in the three selected flames. I also performed the PIV and LII measurements as well as the LII calibration, with the assistance of the second co-author Dr Zhiwei Sum, for the three flames. I processed the LII and PIV data and analysed the results. After presenting the data for the co-authors, I drafted the manuscript. I Acted as the corresponding author and took primary responsibility for responding the reviewers.		
Overall percentage (%)	65%		
Certification:	This paper reports on original research I conducted during the period of my Higher Degree by Research candidature and is not subject to any obligations or contractual agreements with a third party that would constrain its inclusion in this thesis. I am the primary author of this paper.		
Signature		Date	07-10-2021

Co-Author Contributions

By signing the Statement of Authorship, each author certifies that:

i. the candidate's stated contribution to the publication is accurate (as detailed above);

ii. permission is granted for the candidate in include the publication in the thesis; and

iii. the sum of all co-author contributions is equal to 100% less the candidate's stated contribution.

Name of Co-Author	Dr. Zhiwei Sun		
Contribution to the Paper	This co-author provided assistance with the experimental setup and data collection.		
Signature		Date	08-10-2021

Name of Co-Author	Associate Professor Paul R. Medwell		
Contribution to the Paper	This co-author assisted with revising the manuscript and responding the reviewers' comments.		
Signature		Date	08-OCT-2021

Name of Co-Author	Professor Graham J. Nathan		
Contribution to the Paper	This co-author co-supervised the development of the work. He also helped to evaluate and edit the manuscript. He assisted in rebutting the reviewers and revising the manuscript.		
Signature		Date	14/10/21

Name of Co-Author	Professor Bassam B. Dally		
Contribution to the Paper	This co-author co-supervised the development of the work. He also helped plan and structure the manuscript. He also provided assistance with rebutting reviewers' comments and with revising the manuscript.		
Signature		Date	07-10-2021

Relationships between soot and the local instantaneous strain rate in turbulent non-premixed bluff-body flames

This chapter consists of the submitted journal article:

Amir Rowhani, Zhiwei Sun, Paul. R. Medwell, G. J. Nathan, Bassam. B. Dally, "Differences between local and regional strain rate effects on soot evolution in turbulent non-premixed bluff-body flames", submitted to the Combustion and Flame.

The article is identical to its submitted format with the following exceptions:

1. The typesetting and referencing styles have been altered to maintain a consistent appearance within the thesis.

2. The numbering of tables, figures, and equations has been changed to include the number of the chapter.

5.1 Abstract

In this paper, the simultaneous measurements of the local velocity, using Polarised Particle Image Velocimetry (P-PIV) and soot volume fraction, SVF, using Planar Laser-Induced Incandescence (LII) are reported for turbulent non-premixed ethylene-nitrogen bluff-body flames. The measured data were used to assess the correlation between soot volume fraction, and the shear-strain rate (S), both mean and instantaneous, in different regions of the bluff-body flames. In the recirculation zone, an exponential function was found to reasonably describe the relationship between total SV_{RZ} and S. It was also observed that the strain rate associated with the maximum SVF in the recirculation zone and the jet region are $\lesssim 1000$ s^{-1}, consistent with the soot inception region of simple jet flames. The joint PDFs show that the SVF is not well-correlated with the local instantaneous strain rate in either the recirculation zone or the jet region of these flames. Qualitatively, the correlation of coefficient, R^2, between the local instantaneous SVF and inverse of the strain rate ($1/S$) reveals a low to weak correlation, $0.3 < R^2 < 0.6$, in the recirculation zone and the jet region, which is consistent with the joint PDFs. This suggests that the time-scales for SVF are significantly greater than those driving local fluctuations. In addition, a high-fidelity experimental dataset has been provided for model development and validations.

Keywords: soot, strain rate, simultaneous measurement, bluff-body

Nomenclature

U	Axial velocity – m/s
CCD	charge-coupled device
CW	continuous wave
D_{BB}	bluff-body diameter – m
DC	co-flow contractor inner diameter – m
D_J	jet inner diameter – m
E(m)	soot absorption function
ENB	ethylene nitrogen bluff-body flame
ENH	ethylene nitrogen hydrogen jet flame
f	focal length – m
FWHM	full width at half maximum
HAB	height above the burner – m
I	Intermittency
ICCD	intensified charge-coupled device
ID	internal diameter – m
IML	inner mixing layer
ISF	International Sooting Flame workshop
ISL	inner shear layer
JZ	jet zone
K_e	dimensionless extinction coefficient
$\overline{L}_f$	mean flame length – m
$\overline{L}_{RZ}$	mean recirculation zone length – m
LHS	left-hand side
LII	Laser Induced Incandescence
$\dot{m_f}$	fuel mass flow rate – g/s
NZ	neck zone
OSL	outer shear layer
PDF	probability density function
ppm	part per million
P-PIV	Polarised Particle Image Velocimetry
R^2	R-squared correlation coefficient
$R_{0.5}$	soot field width – m
Re_J	jet Reynolds number
RHS	right-hand side
RMS	root mean square
RZ	recirculation zone
Sxy	2D shear strain rate
S	strain rate – 1/s
SP	Stagnation point
SVF	soot volume fraction – ppb
u	axial velocity – m/s
U_C	co-flow velocity – m/s
U_J	fuel jet velocity – m/s
U_m	mean velocity – m/s
V	radial velocity – m/s
X	axial height – m

Greek Symbols

Φ	equivalence ratio
$\overline{\tau}$	mean residence time – ms

5.2 Introduction

The study of the evolution of carbon nano-particles in turbulent, reducing and oxidising environments remains relevant to the emerging carbon-constrained economy, despite primarily being driven historically by the need to mitigate pollution from the use of fossil fuels [1]. This is due, in-part, to society's long term need for carbon products, spanning tyres and plastics to high-value carbon nano-materials, via materials such as Carbon Black, which is produced from fuel-rich flames [2, 3]. It is also driven, in part, by the anticipated long-term availability of fuels derived from the residues of other processes, such as refuse-derived fuels and biomass, in the emerging more circular economy. Furthermore, soot is desirable in high-temperature flames used to produce materials such as glass, iron pellets and alumina, to enhance thermal radiation, and can be promoted by small fractions of hydrocarbons seeded into hydrogen flames [4]. In addition to its practical relevance, the formation of carbon nano-materials, such as soot, in these environments is also highly non-linear and difficult to predict. Hence, a deeper understanding of the formation and evolution of soot in flames is needed.

Soot evolution in flames is a complex process that is governed by interdependent parameters, including temperature [5, 6], mixture fraction [7], strain rate [8] and fuel type [9, 10]. The localised dependency and the non-linearity of these controlling parameters require advanced, simultaneous and non-intrusive measurement techniques to quantify these interactions. Mixing, quantified by the local flame strain rate, is a crucial effective parameter in soot formation since sufficiently-fast mixing can suppress soot growth by lowering the soot residence time [11, 12]. Hence, deep understanding of the mixing effects by quantifying the global and local strain rate on soot evolution in different flames.

A large body of the literature has engaged to the global correlations between soot volume fraction and strain rate in laminar and turbulent regimes. It is generally well accepted that the increased strain rate reduces the local soot concentration in both regimes [13-15]. That is, the soot volume fraction scales inversely with either the global residence time ($1/\bar{\tau}$), or the characteristic exit strain rate, U_J/D_J, where U_J and D_J are jet velocity and jet diameter [21, 24]. For simple jet flames the mean soot volume fraction decreases with increasing the characteristic strain rate [16]. An inverse correlation for one or more of these strain measures has been found to characterise three different types of turbulent flames, spanning simple lifted jet flames [17-19] attached jet flames [20-22], precessing jets, and bluff-body flames [23, 24].

However, the local instantaneous measurement of flowfield features is quite challenging in sooting flames due to substantial interference from elastic scattering and spontaneous flame radiation [25-27]. Due to the complexity in local measurements, only a limited number of studies report local correlations of soot and flow field parameters. In a narrow soot inception region in simple jet flames, a preferred velocity of 3 m/s and the strain rate of 700 s^{-1} was found as most favourable for soot formation [7, 28]. In a series of turbulent swirling flames [29-32], simultaneous soot-flow measurement reveals that soot is formed in the inner recirculation zone and partly transported to the high-velocity in-flow region. However, these measurements have not systematically investigated the local mixing effects by measuring the local strain rates on *SVF* in their flames.

While previous studies have provided important insights into the relationships between global soot and strain rate, a direct comparison between local strain rate and *SVF* in different zones of the flames (recirculation zone, neck, and jet region) has not been reported previously. The lack of data in the literature could stem from the complexity of the simultaneous measurement in a highly-sooting environment. Notwithstanding that, we have recently developed a novel technique that uses polarisers to reduce the interference from soot on the signal from a flow tracer, thereby enabling reliable measurements of local flowfield [33]. In earlier work [4], we quantified the effect of bluff-body diameter on the soot and flowfield within the recirculation zone in a series of bluff-body flames. The present paper, however, has extended the previous work, aiming to quantify the relationships between local strain rate and *SVF* in the recirculation zone and the jet region of the bluff-body flames. A high-fidelity data set including the time-averaged and statistical data is also provided for model validation [34].

5.3 Experimental methods

5.3.1 Burners and flames

Three non-premixed bluff-body burners were used for these measurements. All burners are identical to our recent work, so a brief is presented here [4, 33]. All burners specifications are identical except for the outer bluff-body diameter, which was varied between the values of 38, 50, and 64 mm. The bluff-body burners, made from brass, were surrounded by a co-flowing air stream with a round cross-section air flow contraction (D_c = 190 mm). To allow optical access, the burner was mounted 10 mm above the edge of the air contractor. Three turbulent flames were used in

this study, each with a bulk mean Reynolds number of 15,000 ($\dot{m_f}$ = 0.61 g/s) burning an identical mixture of high-purity ethylene (99%) and ultra-high purity nitrogen (99.99%), C_2H_4/N_2 (80:20 by volume) and emerging from a central fuel nozzle of 4.6 mm. A uniform co-flow of air with a constant velocity of 20 m/s at ambient temperature surrounded the burner. The flames stabilised on the 38 mm, 50 mm, and 64 mm bluff-bodies were labelled as *ENB-1*, *ENB-2*, and *ENB-3* flames, respectively, to denote and Ethylene-Nitrogen-Bluff-body series [4, 33]. Full details of the flow conditions are presented in Table 1. The "mean residence time" refers to the averaged time for a flow-tracer to pass through the recirculation zone. Here we have estimated it by calculating the trajectory of the pseudo-particles in a Lagrangian frame as previously reported [33].

Table 5.1: Experimental flow conditions for the flames reported in this study [4].

Flame	Bluff-body diameter (D_{BB})	Central jet diameter (D_J)	Mean jet exit velocity (U_J) (±2%)	Exit Reynold number (Re_J) (±2%)	Fuel flow rate ($\dot{m_f}$)	Bulk Co-flow air velocity (U_C)	Mean flame length ($\overline{L}_f$) (±5%)	Mean Recirculation zone length ($\overline{L}_{RZ}$) (±1%)	Mean residence time ($\overline{\tau}$)*
	(mm)	(mm)	(m/s)	(-)	(g/s)	(m/s)	(mm)	(mm)	(ms)
ENB-1	38	4.6	32.1	15,000	0.61	20	920	61	8.57
ENB-2	50	4.6	32.1	15,000	0.61	20	855	86	15.5
ENB-3	64	4.6	32.1	15,000	0.61	20	780	114	24.4

**The mean residence time was obtained from CFD [30].*

5.3.2 Measurement techniques and data processing

The turbulent bluff-body flames were simultaneously probed with two laser pulses to conduct the planar laser-induced incandescence (LII) and polarised two-dimensional Particle Image Velocimetry (PIV) measurements. The LII system employed to measure soot volume fraction comprised an Nd:YAG laser (Q-smart 850, Quantel) with the fundamental output (1064 nm) and a frequency of 10 Hz. The LII laser fluence was kept above 0.50 J/cm^2, in the plateau region of the LII response curve to minimise the effects of laser fluence variations (e.g. from any beam steering and attenuation) on the LII signals [35]. The induced incandescence was collected with an ICCD (intensified CCD) camera (PI-Max 4 Princeton Instruments, 1024 × 1024 pixels^2) equipped with a 430-nm bandpass filter (10 nm FWHM) to suppress the C_2 laser-induced emissions, together with interference from the flame radiation. A 50-ns gate width was set for all the LII measurements. Quantification of the recorded LII signals was achieved by calibration against one of the

International Sooting Flame (ISF) McKenna target flames ($\Phi = 2.34$) [34]. Briefly, a line-of-sight laser extinction setup was used to calibrate the recorded LII signals to convert to soot volume fraction, *SVF*. Soot extinction measurements in the McKenna flame was performed using a 1064-nm continuous-wave (CW) diode-pumped-solid-state laser (DPSS). To calculate the soot volume fraction, values of 5.66 and 0.3±0.06 were selected for the dimensionless extinction coefficient, K_e, and soot absorption function, *E(m)*, respectively, noting that the *E(m)* was assumed to be constant throughout the visible to near-IR region of the spectrum [35]. Further details of the calibration can be found elsewhere [21, 22]. The minimum detection limit in the collected data is 1 ppb. The shot-to-shot variation in the LII signal was estimated from the LII signal obtained from the laminar McKenna flame. The shot-to-shot variation of the 1000 consecutive LII images has a standard deviation of 11.3%. In addition, the laser fluence was measured in the plateau region and the LII data was only obtained from the laser-in side and central region of the images to ensure that the deviation in the LII signal was kept within 12%. Furthermore, to reduce beam steering effects, data was only obtained in the beam entrance side of the flame. Sun et al. [36] assessed the beam steering effects in a turbulent jet flame of similar size to be 2 mrad which accounts for 50% increase in the laser sheet width and 750 µm out-of-plane direction throughout the flame. Signal trapping has previously been shown to be negligible in ethylene flames, even with higher soot loading than the current turbulent flames [37].

Simultaneously with the LII system, a 10-Hz pulsed dual-head Nd:YAG laser (Quantel BrilliantB/Twins) with a second harmonic generator performed P-PIV measurements. Depending on the flow velocities, the PIV pulses were separated by times of between 14 µs and 60 µs, depending on the flow velocities. The LII excitation pulse was temporally interlaced between the first and second PIV pulses and was delayed by 5 µs after the first PIV pulse to avoid affecting the LII signals. Titanium oxide (TiO_2) particles with a nominal 1 µm were used in both the jet and the co-flow sides as flow markers. The Mie scattering from these particles was collected using a Kodak Megaplus II CCD camera (1920 × 1080 pixels^2, 16 bit) equipped with a Sigma lens (105 mm, $f = 2.8$). A novel optical modification to a conventional PIV system was developed by adding two additional polarising filters to substantially suppress the scattered interference from soot particles [4]. A 532 nm film polariser oriented at 45° to the laser beam axis was placed in front of the vertical YAG output to clean up the incident beam polarisation. It was found that the polariser plate has the minimum reflection when its normal has a 45° to the beam propagation. A second high-transmission linear polariser was placed in front of the CCD camera to cut the

PIV signal. Both laser beams with a thickness of 500 µm (1064 nm beam) and 1 mm (532 nm beam) were directed to the flame, passing through the sheet forming optics. One thousand LII and 2000 pairs of PIV images were simultaneously recorded. The PIV raw images were processed by removing the background and then employing the commercial PIVLab 2.20 software [38, 39]. The interrogation window was sequentially reduced from 64×64, to 32×32, and ultimately to 16×16 pixels^2 with 50% overlap, to provide a minimum spatial resolution of 1.48 × 1.48 mm^2. The total uncertainty was determined from the ratio of the nominal peak value of the correlation, whose size is 0.1 pixel, to the maximum displacement of the particles which is not more than one-third of the smallest interrogation window size, 16×16 pixels^2. On this basis, the accuracy of each measured velocity component is estimated to be ±1.09 m/s. A schematic diagram of the experimental apparatus is shown in Fig. 5.1.

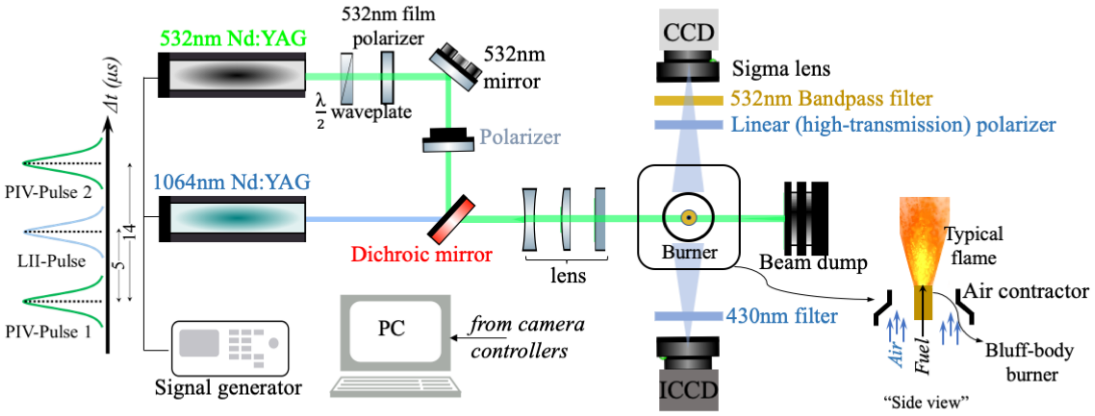

Figure 5.1: A schematic experimental layout showing the bluff-body burner and co-flow air contraction as well as the simultaneous LII and PIV systems adapted from earlier work [4].

5.4 Results and discussion

5.4.1 Characteristic of bluff-body flames

Figure 5.2 presents three images of flame ENB-2 as a key reference, a photograph of the natural radiation (Figure 2a), the mean and Root-Mean Square (*RMS*) of the soot volume fraction (Figure 2b), and the mean velocity (left) and strain-rate (right) (Figure 2c). The 2D shear-strain rate, S_{xy}, has been calculated from the velocity components obtained from the PIV, using the following formula:

$$|S_{rx}| = \frac{1}{2}\left|\left(\frac{\partial u_r}{\partial x} + \frac{\partial u_x}{\partial r}\right)\right| \quad (1)$$

where u and v are the axial and radial velocity components, respectively [4]. Figure 5.2 exhibits all the key features of a classical bluff-body flame which are a low-strain recirculation zone close to the bluff-body surface with a high soot concentration ($x/D_{BB} \lesssim 1.6$), a jet-like region downstream ($x/D_{BB} \gtrsim 2.2$), and a highly-strained neck zone, which connects the recirculation zone to the jet-like region ($1.6 \lesssim x/D_{BB} \lesssim 2.2$) [4, 40-45]. The bluff-body flames are symmetrical; hence, the dataset obtained from this work are suitable for model validation purposes. Consistent with previous findings [28], the recirculation zone's high temperature and low strain region favour soot inception and growth. The other two flames exhibit the same general flow features to the ENB-2 flame, but the details differ because of their differently-sized recirculation zones. The progressive increase in bluff body diameter from flames ENB-1 to ENB-3 leads to increased residence times of 3 msec for ENB-1 flame, 15 msec for ENB-2 flame, and 24 msec for ENB-3 flame [4]. This, in turn, leads to a progressive increase in soot volume fraction.

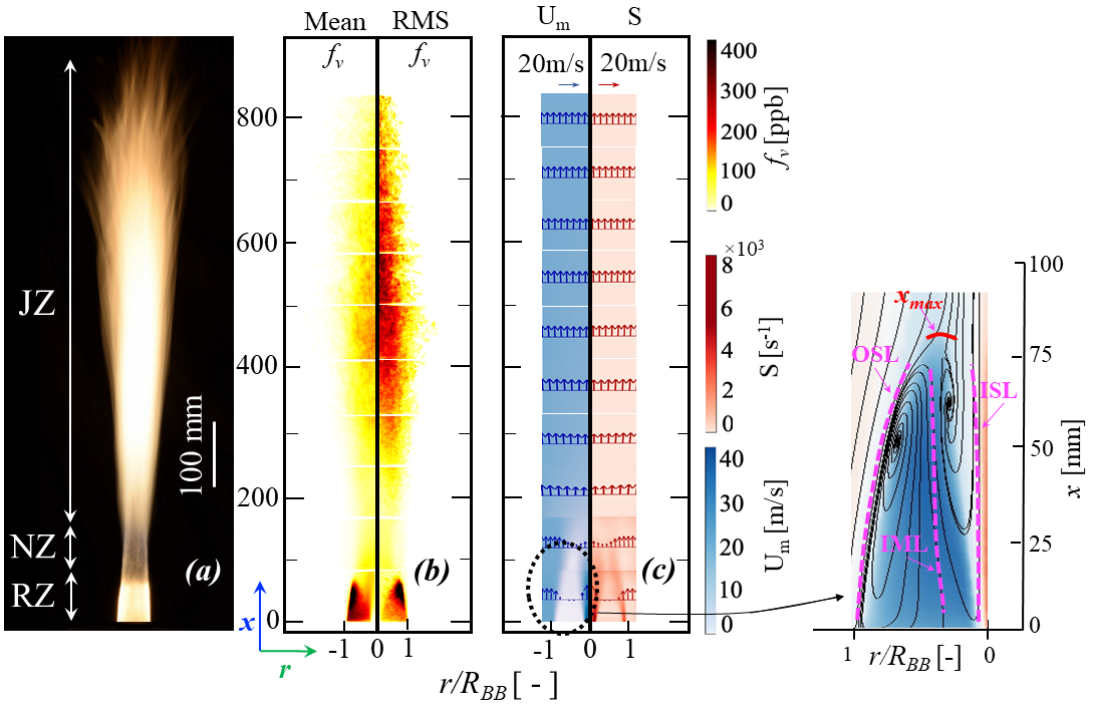

Figure 5.2: (a) A collage of images from the turbulent bluff-body flame stabilised on the 50mm diameter burner (*ENB-2*), showing a photograph of the natural radiation from the flame, together with the three distinct zones: the Recirculation Zone (*RZ*), the Neck Zone (*NZ*) and the Jet Zone (*JZ*). (b) Pseudo colour images of mean soot volume fraction (LHS) and the corresponding *RMS* (RHS); (c) Time-averaged velocity vectors superimposed on the mean velocity pseudo-colour values (left) and time-averaged shear-strain rate (right). A close-up of the recirculation zone (*RZ*) indicating the shear layers is presented on the right-hand side of the figure. The (x_{max}) red line shows the end of the recirculation zone.

5.4.2 Effect of Bluff-Body diameter on the axial distribution of SVF

The axial profiles of *SVF* along the burner centreline are presented for the three flames in Figure 5.3 and compared with ENH-3 flames. The axial height above the jet exit plane is normalised by the mean length of the visible flame ($\overline{L}_f$) to enable the direct comparison with the simple jet flames. [21, 22]. The symbols in the figure represent the experimental data, whilst the dotted line presents the Gaussian fit.

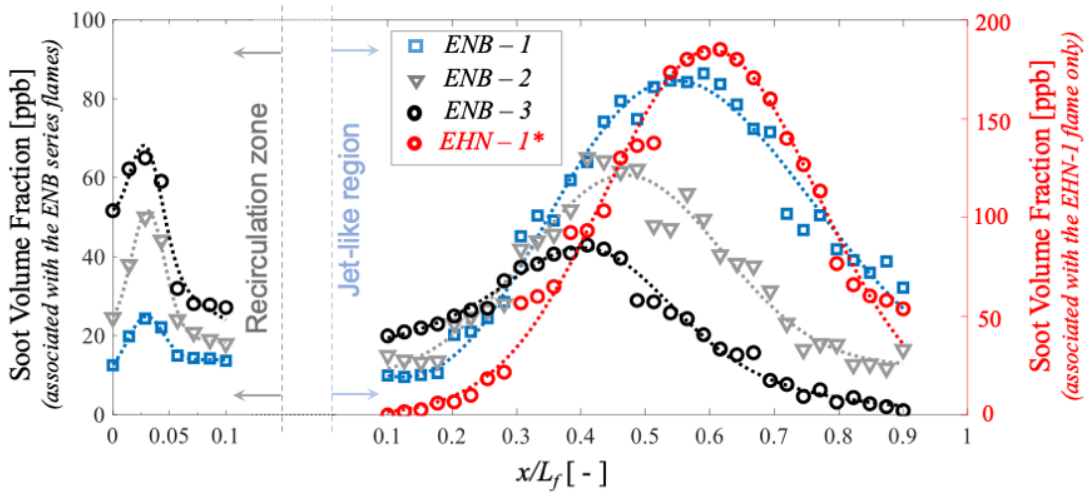

Figure 5.3: Axial profiles of centreline mean soot volume fraction SVF as a function of flame length for *ENB-1* (D_{BB} = 38 mm), *ENB-2* (D_{BB} = 50 mm), and *ENB-3* (D_{BB} = 64 mm) covering the recirculation zone (*LHS*) and the jet-like region (*RHS*). The dotted lines indicate Gaussian fits to the experimental data. *The EHN-1 simple jet flame [21, 22] is shown with red in order to compare with *ENB* flame series. Note that only the *EHN-1* flame is scaled on the *RHS* red axis.

The SVF distribution along the centreline was found to exhibit two distinct peaks, one in the recirculation zone and the other in the jet-like region. The peak in the RZ is found at a similar axial location, $x/L_f \approx 0.04$, for the three flames. The increase in bluff-body diameter from 38 mm to 64 mm increases the magnitude of the peak mean SVF at the centreline by a factor of three. This is attributed to the increased residence time of the larger recirculation zone. In the jet-like region, the *ENB-1* and *ENB-2* flames exhibit similar trends to the simple jet flames of the same Reynolds number (15,000) [21, 22] with the SVF peaking at $0.48 < x/L_f < 0.6$. However, the relative magnitude of the peaks depends strongly on D_{BB}. That is, an increase in D_{BB} causes both the magnitude of the first peak to increase and the second peak to decrease until, for *ENB-3*, the first peak is greater than the second. More specifically, the peak of SVF in the jet-like region of *ENB-2* and *ENB-3* flames drops by almost 23% and 47% and shifts to the upstream location at around $x/L_f \approx 0.40$. These trends are consistent with the 15% and 9% reduction in the flame length for *ENB-2* and *ENB-3* flames relative to *ENB-1*, respectively [33]. These profiles are also consistent with the radially-integrated SVF axial profiles [1] in their general features and reveal a consistent trend that larger bluff-body diameter burners produce more soot in the recirculation zone and result in shorter flames.

The reduction of SVF through the neck zone, $0.8 \lesssim x/L_f \lesssim 1.5$ implies high rates of soot oxidation through intense mixing with co-flowing air. A closer look at the soot profile reveals that the level of SVF in the neck zone also increases with D_{BB}. That is, the amount of soot in the neck zone scales with the amount of soot produced in the bluff-body zone. Since the fuel and air momentum fluxes are the same for all flames, this suggests that the overall mixing rates in the three flames are also similar. Hence, overall, these trends indicate that an increase in D_{BB} results in a more significant overall fraction of partial fuel conversion in the RZ, a similar degree of partial oxidation in the neck zone and a reduced level of both reaction and soot production in the jet zone. That is, the amount of soot in the jet flame can be deduced to be controlled by the extent to which the fuel composition in the jet zone contains soot precursors or other fuels with a strong sooting propensity, some of which are produced in the recirculation zone through the pyrolysis process, but are oxidised partially through the neck zone.

5.4.3 Radial distribution of SVF in Flames

5.4.3.1 SVF distribution in the recirculation zone (RZ)

Figures 5.4 compares the time-averaged and the RMS radial profiles of soot volume fraction in the recirculation zone for all three flames. The profiles are plotted at two different axial locations above the jet exit plane within the recirculation zone. More axial heights are provided in the supplementary material (Fig. B.S1 and Fig. B.S2). The red, blue, and black symbols represent the experimental data for *ENB-1, ENB-2,* and *ENB-3* flames, respectively. The corresponding lines were obtained from the best Gaussian fit (with three terms) to the experimental data. Due to interference from elastic scattering from the bluff-body surface and the LII signal variation at the very lowest part of the laser sheet, results are only reported at normalised locations of $0.4 < x/D_{BB} < 1.4$. The corresponding bluff-body diameter normalises both axial and radial distances.

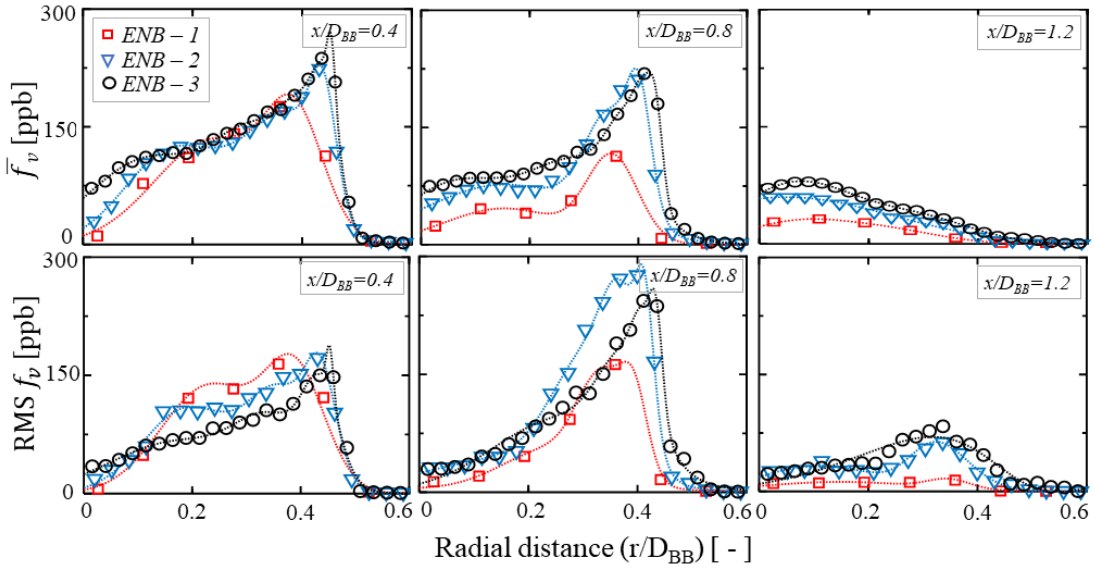

Figure 5.4: Radial profiles of the time-averaged (top) and *RMS* (bottom) soot volume fraction within the recirculation zone at two different heights above the burner ($x/D_{BB} = 0.4, 0.8$). The symbols are experimental data, while the lines indicate the best fits. Consistent with the entire paper, the blue, red, and black colours correspond to *ENB-1*, *ENB-2*, and *ENB-3* flames, respectively.

The normalised mean radial profiles of *SVF* exhibit similar features at all axial locations. A dominant outer peak is found at $x/D_{BB} < 1$ for all three cases near to the stream of coflowing air (inside the outer vortex at $r/D_{BB} \approx 0.35$–0.42) from which it declines smoothly toward the centreline. However, the magnitude of this outer peak soot depends on both the diameter of the *RZ* and the strength of the inner vortex. At axial locations above 1.0 ($x/D_{BB} > 1.0$), no explicit peak is observed due to the high rate of soot oxidation. It is also notable that the gradient is steep in the outer shear layer, $r/D_{BB} > 0.42$, for all profiles. This can be attributed to the high rates of oxidation by air, and possibly too, the OH radical [33].

A closer examination of these flames shows that while some differences can be observed, all flames share similar trends. Increasing D_{BB} from the smallest case causes a noticeable increase in the highest peaks of *SVF* by almost 50% to around ≈ 280 ppb for the *ENB-2,* but no further change for *ENB-3*. The normalised radial location at which the peak occurs is relatively closer to the edge of each bluff-body burner, so that a slight radial shift in the normalised position is observed compared to the *ENB-1* flame. The corresponding radial profiles of *RMS SVF* shown in Figure 4. The *RMS SVF* profiles exhibit broadly similar trends to the mean counterparts,

with the peaks occurring at similar locations. However, the highest values of *RMS* are found for the *ENB-1* flame, which is attributed to the higher rates of shear relative to the other two flames.

5.4.3.2 SVF distribution in the jet-like region

The radial profiles of mean and *RMS SVF* in the neck zone ($x/L_f = 0.1$) and in the jet region ($0.1 < x/L_f < 0.75$) for the three flames are compared in Fig. 5.5. Three axial locations are presented here, although more data within the jet zone is provided in the supplementary material (Fig. B.S3). Symbols represent the experimental data, and the dotted lines are the best Gaussian fits. Each row represents data at the same normalised axial location above the burner, which is normalised by each flame's mean visible flame length (L_f). The radial distance is normalised by the jet nozzle diameter (D_J).

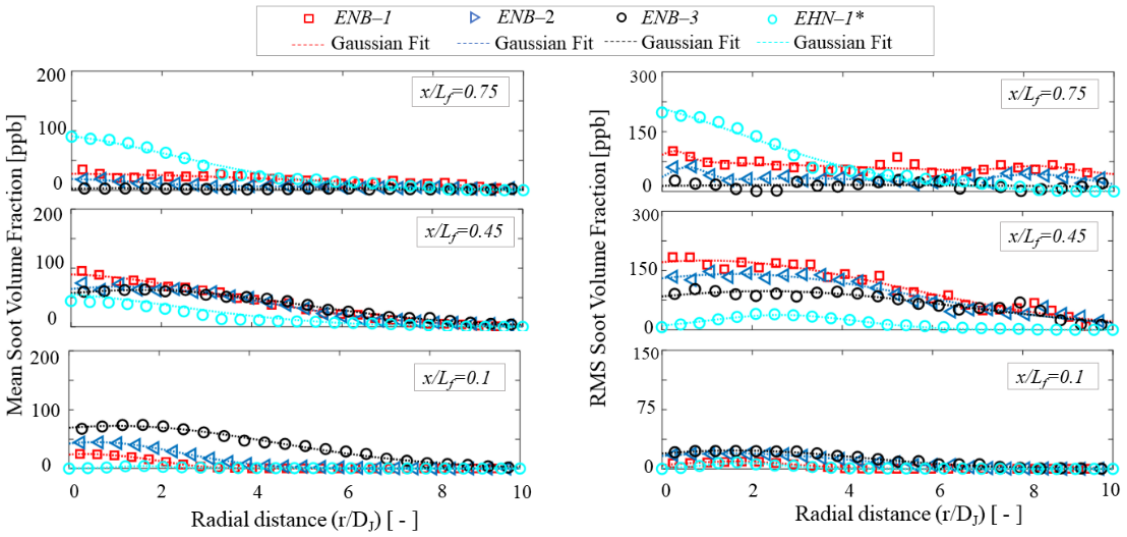

Figure 5.5: Radial profile of the time-averaged (left) and the *RMS* (right) of soot volume fraction at different heights in the downstream of the flame, spanning the neck and jet zones. The symbols represent experimental data whilst the dotted lines indicate the best Gaussian fits. *The *EHN-1* simple jet flame [21, 22] is shown in light blue from a previous flame series.

Figure 5 shows that a similar distribution occurs for all three flames at a given normalised axial location above the burner. Each has a maximum value of *SVF* on the centreline at $x/L_f > 0.45$ followed by a smooth decrease toward the reaction zone where most of the soot is oxidised. This trend in the jet region of the bluff-body flames follows the same trend as simple jet flames, although the peaks in simple jet flames are considerably higher by a factor of two to three [21]. While the maximum soot in the recirculation zone was found to be around 300 ppb, it drops to ~100 ppb in the jet zone, which is almost one-third that of the *RZ*. At $x/L_f < 0.45$, the maximum soot is found for the *ENB-3* (~80 ppb). However, the trend is reversed at higher locations $x/L_f > 0.45$. In the upper half of the flame, the larger burner (*ENB-3* flame) has the lowest soot concentration, consistent with a 9% reduction in the total flame volume and 15% reduction in total radiation from this flame [33].

The *RMS* data in the jet-like region, shown on the *RHS* of Figure 5, follow some similar trends to the mean *SVF* and the *RMS* profiles of simple jet flames, although the profiles tend to be flatter or to peak further from the axis. Similar to simple jet flames, the ratio of the peaks of mean to the *RMS*, are close to unity in the upstream region of the flame ($x/L_f < 0.25$), where the lower soot fluctuations were reported [21, 22]. Higher fluctuations in the jet region are observed close to the flame tip ($0.45 < x/L_f < 0.60$). It is noticeable that in the lower jet-like region ($0.1 < x/L_f < 0.45$), soot fluctuations for all three flames are similar. However, towards the flame tip ($x/L_f > 0.45$), the *RMS* for *ENB-1* is almost twice that for the *ENB-2* and *ENB-3* flames, with the maximum (~300 ppb) found at $x/L_f = 0.60$.

5.4.4 Soot intermittency

The intermittency of soot—defined as the probability of finding no soot at any given spatial location— is presented in Figs. 5.6 and 5.7 for the recirculation zone and the jet region, respectively. The intermittency is zero for almost the entire width of *RZ*, particularly in the lower regions, implying that soot is constantly present throughout this zone for all three flames. The width of the region of zero intermittency scales with the size of the *RZ* so that it decreases with axial height. The normalised size of this zero-intermittency region is the smallest for *ENB-1* flame. This is consistent with the *RMS* plots here. That is, lower values of intermittency in the recirculation zone correlate with lower values of *RMS*. At the edge of the recirculation zone, $x/D_{BB} > 1.2$, the *RMS* drops to below 50 ppb (Fig. 5.4) and even less at $x/D_{BB} = 1.4$. This

is consistent with the earlier observation that the soot filaments align within the recirculation zone [4]. Soot structures in the *ENB-3* flame are uniformly distributed and are present in multiple interlaced sheets and the whole area of the recirculation zone due to the long residence time in this flame. In the *ENB-1* flame with the shortest residence time amongst the three flames, the probability of having no soot at radial locations of $0.2 < r/D_{BB} < 0.4$ is decreased to almost half of intermittency values at the end of the recirculation zone. The intermittency in the *ENB-2* flame is similar to *ENB-3* close to the burner and becomes closer to *ENB-1* at higher axial positions. These trends are consistent with trends in *SVF* fluctuations observed in Figure 4.

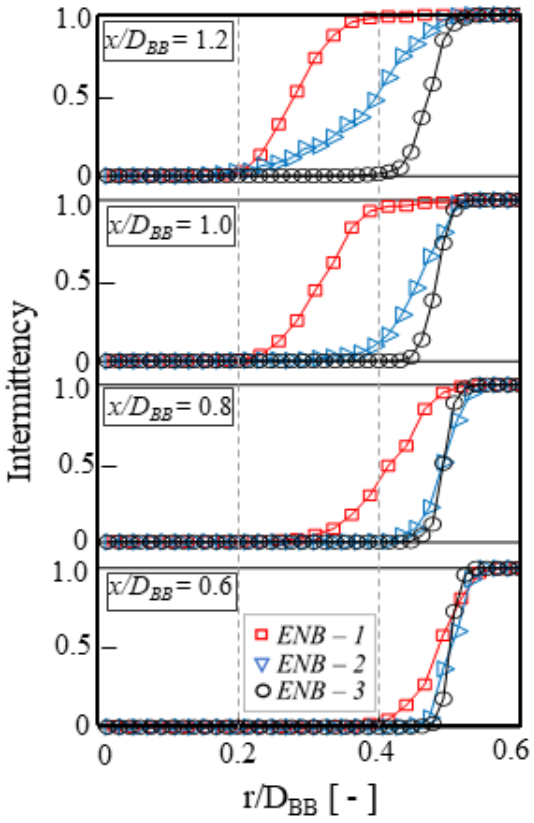

Figure 5.6: Radial profile of soot intermittency at different heights in the recirculation zone. The symbols represent experimental data whilst the solid lines indicate the best fits with Gaussian functions.

Soot intermittency in the jet region of the bluff-body flames is presented in Fig. 5.7. The intermittency increases with radial distance from a minimum on the axis to unity at the edge of the flame for each axial height.

Along the centreline ($r/D_J = 0$), the soot intermittency increases with distance from the burner until at the axial location of $x/L_f = 0.75$, soot is rarely found, and the probability of having no soot is close to unity for all the three flames. At the upstream region of the jet zone, $0.1 < x/L_f < 0.45$, the probability of having no soot is greater for *ENB-1* flame. However, the trend reverses at $x/L_f = 0.45$, beyond which the intermittency is found to be lower for *ENB-3* flame. This transition is consistent with the trends in the maximum of the mean and the *RMS* of the *SVF* profiles. This provides further evidence that the soot which survives the neck zone plays little or no role in the formation of soot in the jet zone. Instead, the surviving soot is progressively burned out to become of secondary significance for $x/L_f < 0.45$. Instead, the new soot formed within the jet flame dominates the intermittency in this region of the flame.

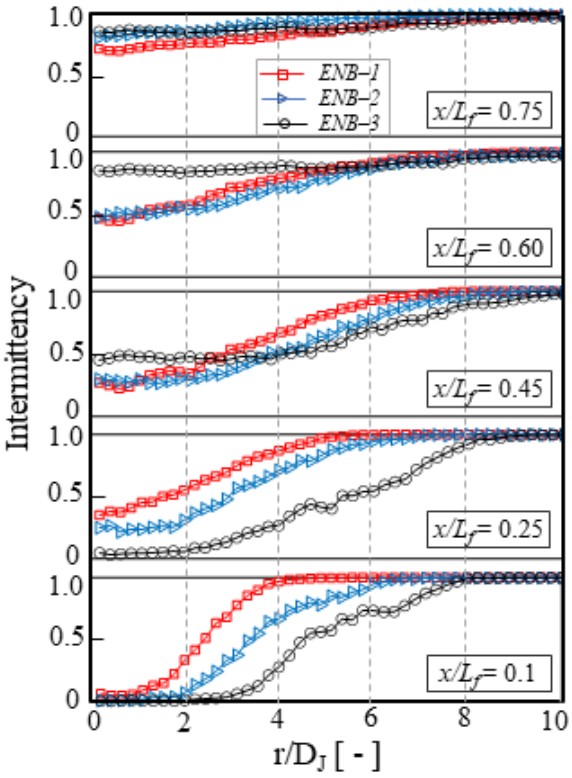

Figure 5.7: Radial profile of soot intermittency at different heights in the jet zone. The symbols represent experimental data whilst the solid lines indicate the best fits with Gaussian functions.

5.4.5 Soot and strain-rate statistics

Fig. 5.8 presents an image of the positions in a typical bluff-body flame (ENB-1) where Probability Density Functions (PDFs) of *SVF* and *S* were calculated. The PDFs were calculated from 5 × 5 pixels^2 (0.17 mm^2) arrays from 1000 instantaneous image pairs. The data from within the *RZ* were obtained at six different axial heights above the burner, ranging from $0.4 < x/D_{BB} < 1.4$. Three radial positions were selected for each axial position, namely in the Inner Shear Layer (*ISL*), in the Intermediate Mixing Layer (*IML*), and in the Outer Shear Layer (*OSL*). These locations were selected based on our previous study [4], which highlighted the importance of the interactions between inner and outer vortices in generating and transporting soot as well as the entrainment of fresh air into the recirculation zone. In the jet-like zone, five axial locations above the burner ($2.2 < x/D_{BB} < 10.0$) and three radial positions on the 0%, 50%, and 90% of the soot field widths ($R_{0.5}$) were selected at which to calculate the statistical correlations. For brevity, one axial height in the *RZ* and one in the jet region has been presented here. More data is provided in the supplementary material (Fig. B.S4) to cover different axial heights above the burner.

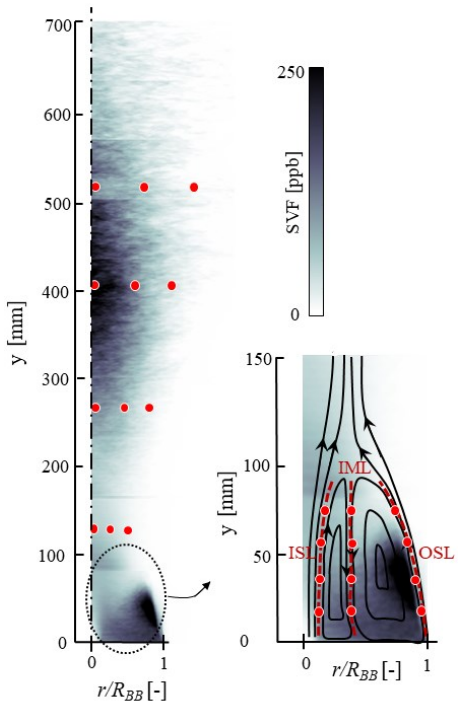

Figure 5.8: Image of the time-averaged soot volume fraction, presented as a grey-scale, overlaid with the selected locations (red dots) at which the statistics for strain rate have been calculated for the *ENB-1* flame. A close-up of the recirculation zone is presented on the right-hand side of the figure.

Figure 5.9 presents the PDFs of both the *SVF* and of the strain rate at $x/D_{BB} = 0.6$. A general trend can be seen in which the flame with the highest probability of low strain (*IML*) also has the highest probability of high *SVF*, while that the highest probability of high strain (*ISL*) also has the highest probability of low *SVF*. The values for the *OSL* are intermediate, both for strain and for *SVF*. These trends are consistent with those from earlier studies in simple jet flames [21,24]. More specifically, for the ENB-1, regardless of the radial location, soot is found the range 1 ppb $<$ *SVF* $<$ 50 ppb. No events greater than 50 ppb can be found, while the maximum value is almost double this for the ENB-2 and ENB-3 flames. In the *IML*, where the strain rate is lower than the other shear layers (*ISL* and *OSL*), range of soot concentration is the widest.

Increasing the bluff-body diameter caused the soot distribution to become wider in the *OSL* and the *IML*. The maximum probable soot in ENB-3 is increased by a factor of three, ~160 ppb, comparing to ENB-1. This is attributed to the increased residence time. It is worth mentioning that the maximum soot found in these flames is almost one order of magnitude less than the *SVF* measured in laminar diffusion flames, 3400 ppb, fuelled with the same ratio of ethylene/nitrogen blend [46].

Similarly, the PDFs of strain rate show that the strain is below 1000 s^{-1} in the *IML* of all flames, whilst in the shear layers, the strain rate extends up to 6000 s^{-1} and 4500 s^{-1} for the *ISL* and *OSL*, respectively. It is also observed that increasing the bluff-body diameter results in a decrease in the strain rate so that the maximum probable strain rate is reduced by almost 25-30% in the shear layers. However, no significant change is observed in the strain rate distribution in the *IML*. Consistent with the findings of Mueller et al. [41], the width of the PDFs is increased in the *OSL,* which is associated with the low-strain and high-residence time favours acetylene-based surface growth mechanism. The narrower profiles in the *ISL* account for the soot inception region in this location. Also, on the *OSL*, the high strain rate hinders soot inception and most likely that soot is transported to this zone, as discussed in Rowhani *et al.* [4].

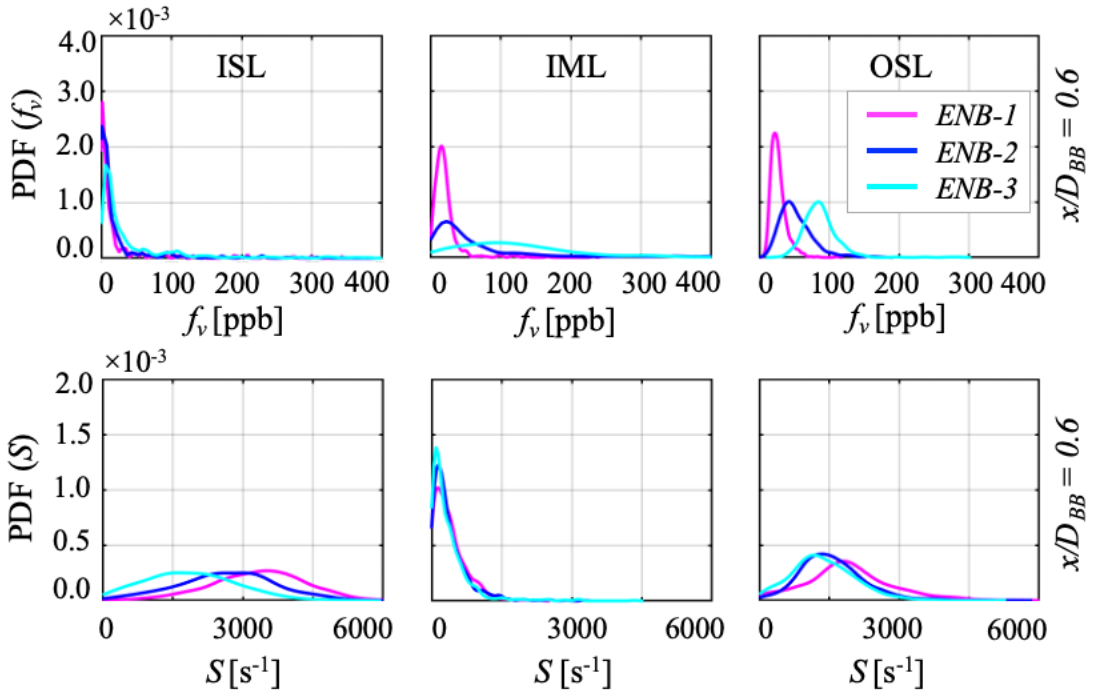

Figure 5.9: Axial distribution of probability density functions (PDFs) of soot volume fraction within the recirculation zone at a series of radial locations. The solid magenta, blue and cyan lines represent the pdfs for *ENB-1*, *ENB-2* and *ENB-3* flames corresponding to D_{BB}=38 mm, 50 mm, and 64 mm, respectively.

Figure 5.10 compares the PDFs of soot volume fraction at x/D_{BB} = 4.4 in the jet-like region of all flames. Since a similar trend was observed at certain axial locations in the jet region, only one height is presented in this section. A comparison of the different axial heights is shown in the supplementary material (Fig. B.S5). Close to the flame edge ($r/R_{0.5}$= 0.9), the PDF profiles behave quite similarly in the number of occurrences and the maximum probable soot for all three flames. The most probable *SVF* is found below 20 ppb, and no events greater than 35 ppb can be found. The profile shape at this location resembles a log-normal distribution, which seems to be independent of the bluff-body diameter. Interestingly, the width of the PDFs is found to be the widest at the flame centreline. In the *ENB-3* flame, the PDF width is highest, which suggests more soot is transported from the recirculation zone. Also, the most probable *SVF* greater than 60 ppb is rarely observed, and the maximum measured *SVF* is less than 100 ppb. It is worth mentioning that there is a significant drop in the most probable soot in the jet zone (70 ppb) compared with the recirculation zone (300 ppb). This trend in the jet region of the bluff-body flames is consistent with the simple jet flames of $C_2H_4/N_2/H_2$, with the similar Reynolds

number of 15,000, which reported that at the axial locations of $x/L_f < 0.6$ most probable value of the local instantaneous soot volume fraction increases with increasing the global strain rate [21].

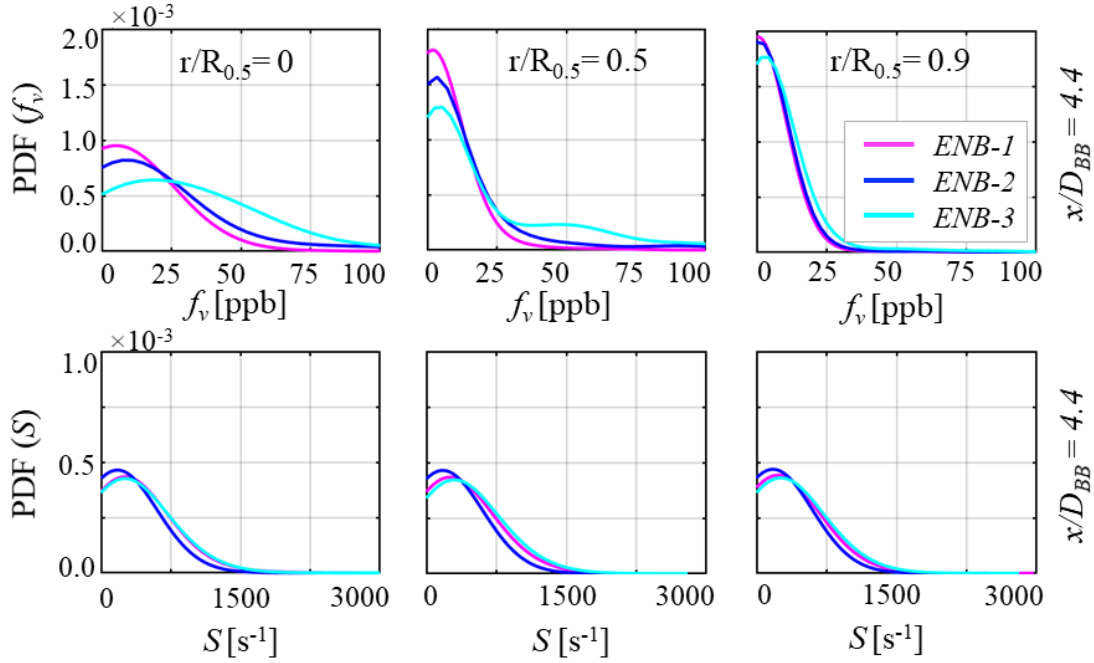

Figure 5.10: Probability density functions (PDFs) of soot volume fraction distributions in the jet zone at radial locations at 0%, 50%, and 90% of the half-width of the flame ($R_{0.5}$). The solid magenta, blue and cyan lines represent the pdfs for *ENB-1*, *ENB-2* and *ENB-3* flames corresponding to D_{BB}=38 mm, 50 mm, and 64 mm, respectively.

5.4.6 Correlations between total soot (SV_{RZ}) and mean flowfield features in the recirculation zone

The correlations between total soot in the recirculation zone (SV_{RZ}), and both the mean strain rate ($\overline{S}$) and mean residence time ($\overline{\tau}$) within the recirculation zone have been presented in Fig.5.11. The total soot volume can be expressed as

$$SV_{RZ} = 2\pi r \int_0^{x_{max}} \int_0^{r_{max}} SVF\,(r,x)\,dr.dx \qquad (2)$$

where $SVF\,(r,x)$ is the local soot volume fraction at a certain height above the burner, x, and a radial distance from the axis, r. For the recirculation zone, the x_{max} equals the length of the recirculation zone for each flame defined by the distance from the jet exit plane up the stagnation point where the mean axial velocity of the

flame is zero. The strain rate, S, is calculated based on the formula presented in section 3.1 of the current paper. The mean strain rate is calculated based on the averaged values of strain in the recirculation zone obtained from equitation (2). The mean residence time ($\bar{\tau}$), defined as the time required for pseudo-particles to pass through the RZ, has been estimated computationally and presented in earlier work [33, 47]. The dependence between total SV_{RZ} on both the mean residence time and mean strain rate can be characterised for the present measurements with an exponential function following previous work [21]; $SV_{RZ} = a_1 \times \exp(b_1 \times \bar{\tau})$, where coefficients a_1 and b_1 are 8.23×10^{-3} and 5.54×10^{-2}, respectively. Nevertheless, more data are needed to determine the most appropriate function. Another exponential function characterises the total SV_{RZ} from the mean strain rate in the recirculation zone of these flames, namely $SV_{RZ} = a_2 \times \exp(b_2 \times \bar{S})$, where coefficients a_2 and b_2 are 5.22×10^{-1} and -3.1×10^{-3}, respectively. This trend between the mean strain rate and SV_{RZ} in the present flames is similar to that measured previously for simple jet flames, where the global strain rate was defined as U_J/D_J [21].

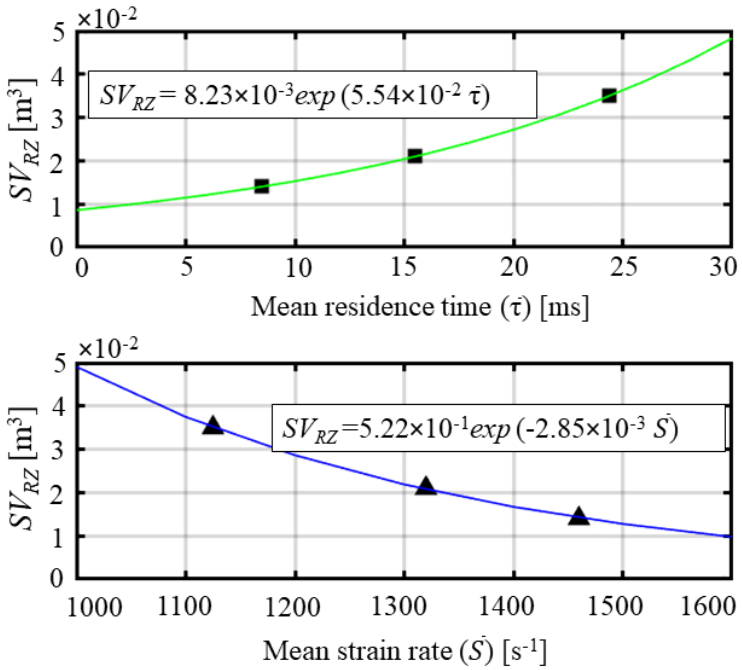

Figure 5.11: The total soot in the recirculation zone, SV_{RZ}, plotted as a function of mean residence time (top) and mean strain rate (bottom) in this zone. Symbols represent integrated values obtained from the experiments. Solid lines show the best exponential fits.

5.4.7 Joint statistics of soot (SVF) and strain rate (S)

The axial and radial sampling positions are consistent with the locations explained in Fig. 5.8 in section 3.5. The statistics were compiled from the average pixel values in an area of 5×5 pixels^2 at each location from 1000 instantaneous images.

Figure 5.12 presents the joint PDF of *SVF* and strain rate (*S*) for the *ENB-1* flame at two axial and three locations within the recirculation zone. A comparison of five axial heights is presented in the supplementary material (Fig. B.S6). The most probable combination of strain rate and soot at $x/D_{BB} = 0.6$ is found to have a similar value of SVF (~30 ppb) even though the corresponding values of most probably strain are quite different at be 3700 s^{-1} and 2000 s^{-1} in the *ISL* and *OSL*, respectively, and with a much lower value of 500 s^{-1} in the *IML*. This suggests that the effect of transport dominate over those of the local conditions in controlling this parameter. Similarly, the local values of strain do not appear to dominate the magnitude of the peak values of *SVF*, although they do have an influence as already noted above. That is, the peak values of *SVF* are similar for the *IML* and the *OSL*, despite significant differences in strain, while those in the *ISL* are lower. This is likely to be due to the soot in the *ISL* being at an earlier stage of evolution, which gives further evidence of the strong influence of transport over that of the local strain.

The influence of axial distance has little influence on the most probable combination of SVF and strain in the *RZ*, except for a slight shift toward lower strain in the *ISL*. However, it has a significant influence on the magnitude of *SVF*. Also, the distribution of the *SVF* in the *OSL* and *IML* are about the same, even though the strain rates in these two zones are very different (~2000 s^{-1} for the *OSL* and near zero for the *ISL*). It is also observed that the PDFs of *SVF* in the *ISL* do not change much with axial distance even though the strain increases by a factor of two from 2000 s^{-1} to 4000 s^{-1}. Together these give further evidence that the effects of transport history of the soot through the *RZ* are very important drivers of the local values of *SVF*.

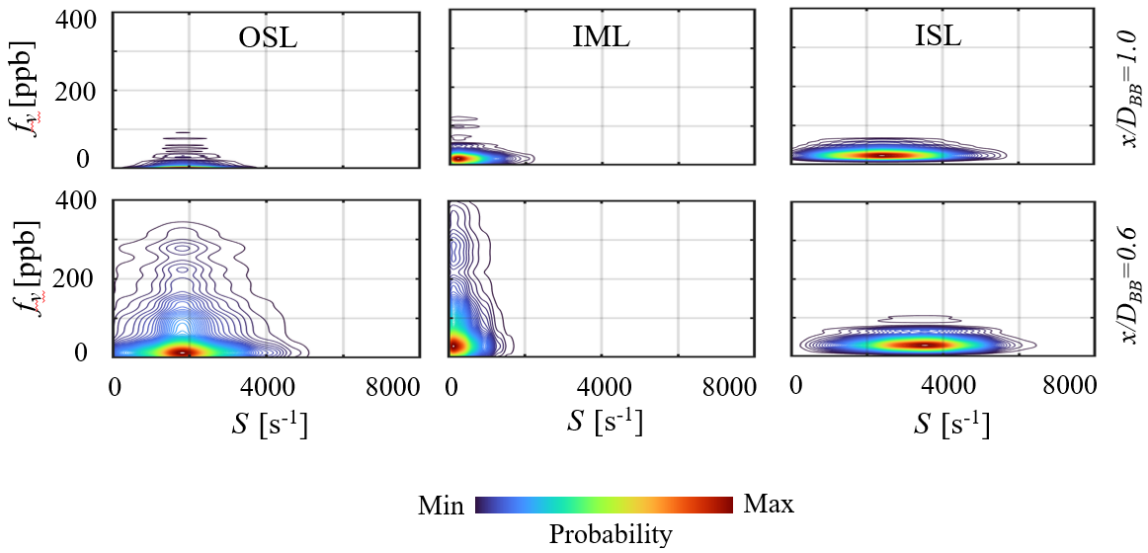

Figure 5.12: Joint probability distribution of *SVF* and S along for two axial and three radial locations (*ISL*, *IML*, and *OSL*) in the recirculation zone for *ENB-1* flame (D_{BB}=38mm).

Figure 5.13 presents the joint statistics between soot and strain rate in the jet region of the *ENB-1* flame at the axial height of x/D_{BB} = 4.4. More axial heights (2.2 < x/D_{BB} < 8.1) have been analysed, and the data is presented in the supplementary material (Fig. B.S7). It can be seen that most probable values of *SVF* in the jet region are some 70% lower (~40 ppb) than those in the *RZ*, despite relatively low values of local strain (~50 s^{-1}). This can be attributed to the role of the partial oxidation of the fuel prior to entering the jet zone, showing the additional influences of parameters other than strain that are not measured here.

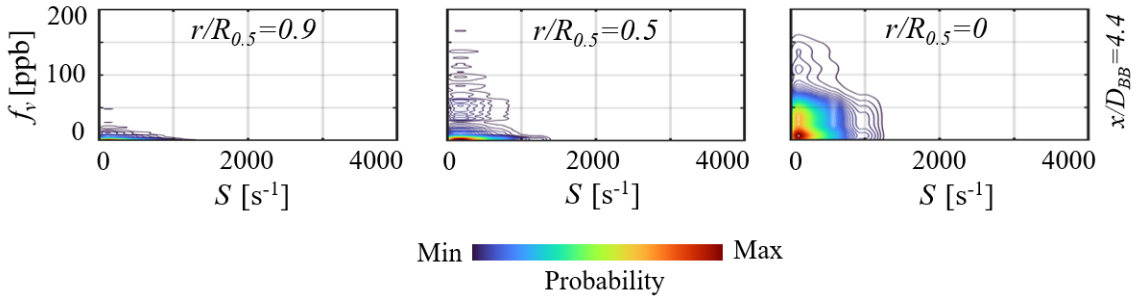

Figure 5.13: Joint probability distribution of *SVF* and strain rate for three radial locations (r/$R_{0.5}$ = 0, 0.5, and 0.9), where $R_{0.5}$ is half-width of the flame in the jet zone for *ENB-1* flame (D_{BB}=38mm).

5.4.8 Effects of the bluff-body diameter on joint PDFs between SVF and S

Figures 5.14 presence the effect of bluff-body diameter on the joint statistics between *SVF* and the strain rate at the axial height of $x/D_{BB} = 0.6$ for three radial locations within the *RZ* (shear layers and the *RZ* core).

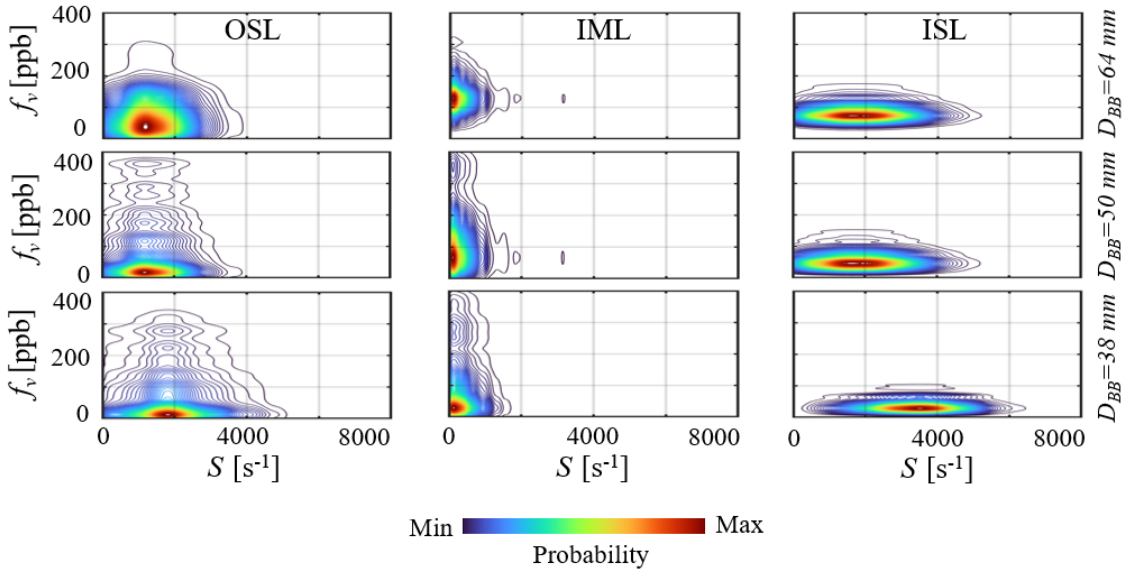

Figure 5.14: Joint probability distributions of *SVF* and strain rate for three values of bluff-body diameter and radial locations at $x/D_{BB} = 0.6$, which is within the recirculation zone. The bottom row corresponds to *ENB-1*, the middle to *ENB-2*, and the top row to the *ENB-3* flame.

It can be seen that the general shapes of the distributions do not change much with D_{BB} for a given region of the *RZ*, although increasing D_{BB} trends both to decrease the most probable value of strain and increase the most probable value of *SVF*. This trend is, perhaps, most obvious in the *ISL,* and confirms the importance of local strain rate in influencing *SVF*. The effect of bluff-body diameter on the *SVF* and strain rate correlations at $x/D_{BB} = 1.2$ have been investigated, and similar trends to $x/D_{BB} = 0.6$ are observed. Barring a slight increase in the *SVF* range on the *OSL* of the *ENB-3* flame, the other axial and radial positions at $x/D_{BB} = 1.2$ share similar trends to $x/D_{BB} = 0.6$. The joint PDFs between *SVF* and strain rate at the axial height of $x/D_{BB} = 1.2$ is presented in the supplementary material (Fig.B.S8).

Qualitatively, the joint PDFs show that the instantaneous *SVF* and the strain rate (S) in the recirculation zone and in the jet region are not well correlated. For

example, the ridge of most probable values in the *OSL* and *IML* is approximately vertical, implying it is independent of the local strain, while that in the *ISL* lies along a line of constant *SVF*, which also implies no dependence on *S*. Table 5.2 presents the correlation coefficient, R^2, for each data set in Figures 13 and 14 against the function $SVF = 1/S$. This function is chosen because *SVF* is well known to depend inversely on local strain rate in a laminar flame [14, 15] and on global strain rate in a turbulent flame [21, 24]. It can be seen that the value of the (R^2) varies between 0.33 and 0.68 in the *RZ*, corresponding to the *ISL* and *IML*, respectively, while in the jet region it is found to be between 0.29 to 0.37 at $r/R_{0.5} = 0$, 0.5 and 0.9. The strength of the correlations is considered as low when the R^2 is below 0.5, while a correlation can be considered to be high when the R^2 is between 0.9 and 1.0 [48]. Hence, these data show that the local instantaneous *SVF* is poorly correlated to the inverse of the local strain rate in the jet zone and weakly correlated in the *RZ*. This is consistent with our qualitative assessment of the joint PDFs. Furthermore, these measurements are consistent with the numerical work of Couci et al. [8, 49], who found that the flame response to strain rate oscillation is influenced by past history, so that the formation of soot and PAH species depends on the initial strain. Overall, these trends imply that the time-scales for soot formation in these flames are typically longer than those associated with the local strain rate, so that the variations induced by different histories at different times or places effects dominate over the influence of the values of the local strain rate.

Table 5.2: The values of R^2 of the function $SVF = 1/S$ obtained at different axial and radial locations. The axial locations of $x/D_{BB} = 0.6$ and 1.0 are related to the recirculation zone, while the $x/D_{BB} = 4.4$ and 8.1 are corresponded to the jet region.

	$x/D_{BB}= 0.6$	$x/D_{BB} = 1.0$	$x/D_{BB} = 4.4$	$x/D_{BB} = 8.1$
ISL	0.33	0.34	–	–
IML	0.68	0.67	–	–
OSL	0.52	0.64	–	–
$r/R_{0.5}= 0.0$	–	–	0.30	0.31
$r/R_{0.5}= 0.5$	–	–	0.37	0.31
$r/R_{0.5}= 0.9$	–	–	0.34	0.29

5.5 Conclusion

Measurements in a series of turbulent non- premixed bluff-body flames of ethylene/nitrogen (80:20 by vol.) have revealed that, while local values of strain rate do have an influence on local soot volume fraction, the effects of transport and history are greater than those of the local strain rate in both the *RZ* and the jet regions of the present flames. This is consistent with the time-scales for soot evolution in these regions being significantly longer than those associated with the local strain rate. In addition:

- The joint PDFs between the local instantaneous *SVF* and *S* reveal little qualitative correlation between these two parameters, while the correlation of the data to the function $SVF = 1/S$ is found to be poor in the jet zone ($R^2 \sim 0.3$) and weak in the recirculation zone ($0.3 < R^2 < 0.6$).

- Probability density functions of the *SVF* and strain rate reveals a generic trend in which the most probable soot is found in the low-strain core of the recirculation zone at all measured radial locations in the flame. This provides further evidence that the high concentration of soot in the *OSL*, where the strain rate is high, is attributed to the transport of soot through this zone.

- An exponential function was found to reasonably characterise the relationship between total soot in the recirculation zone, SV_{RZ}, and both the mean strain rate and the mean residence time. This trend is similar to that from earlier measurements in simple jet flames [21].

In the jet region, the value of strain rate corresponding to the most probable soot is not substantially dependent on either the axial and radial locations. The strain rate value associated with the maximum soot is found to be around 500 s^{-1} which is consistent with earlier findings in simple jet flames [28].

Acknowledgements

The first author would like to thank the Australian government for scholarship funding through the Research Training Program Scholarship (RTPS). We gratefully acknowledge the support of the Australian Research Council (ARC) for the project funding.

5.6 References

[1] I. M. Kennedy, "The health effects of combustion-generated aerosols", Proceedings of the Combustion Institute, vol. 31, pp. 2757-2770, 2007.

[2] J. E. Penner, "Soot, sulfate, dust and the climate - three ways through the fog", Nature, vol. 570, pp. 158-159, 2019.

[3] G. M. Rodney, L. Rouse, M. J. Boudreaux, D. B. Paulsen, and A. L. Pann, "Soot nanoparticles promote biotransformation, oxidative stress, and inflammation in murine lungs", American Journal of Respiratory Cell and Molecular Biology, vol. 39, pp. 198-207, 2008.

[4] A. Rowhani, Z. W. Sun, P. R. Medwell, G. J. Nathan, and B. B. Dally, "Soot-flowfield interactions in turbulent non-premixed bluff-body flames of ethylene/nitrogen", Proceedings of the Combustion Institute, vol. 38, pp. 1125-1132, 2021.

[5] A. Ciajolo, A. D'Anna, R. Barbella, A. Tregrossi, and A. Violli, "The effect of temperature on soot inception in premixed ethylene flames", Proceedings of the Combustion Institute, vol. 26, pp. 2327-2333, 1996.

[6] A. Omrane, P. Petersson, M. Aldén, and M. A. Linne, "Simultaneous 2D flow velocity and gas temperature measurements using thermographic phosphors", Applied Physics B, vol. 92, pp. 99-102, 2008.

[7] O. Park, R. A. Burns, O. R. H. Buxton, and N. T Clemens, "Mixture fraction, soot volume fraction, and velocity imaging in the soot-inception region of a turbulent non-premixed jet flame", Proceedings of the Combustion Institute, vol. 36, pp. 899-907, 2017.

[8] A. Cuoci, A. Frassoldati, T. Faravelli, and E. Ranzi, "Formation of soot and nitrogen oxides in unsteady counterflow diffusion flames", Combustion and Flame vol. 156, pp. 2010-2022, 2009.

[9] D. B. Olson and J. C. Pickens, "The effects of molecular structure on soot formation, I. Soot thresholds in premixed flames", Combustion and Flame, vol. 57, pp. 199-208, 1984.

[10] V. Chernov, M. J. Thomson, S. B. Dworkin, N. A. Slavinskia, and U. Riedel, "Soot formation with C1 and C2 fuels using an improved chemical mechanism for PAH growth", Combustion and Flame, vol. 161, pp. 592-601, 2014.

[11] K. -C. Lin and G. M. Faeth, "Effects of hydrodynamics on soot formation in laminar opposed-jet diffusion flames", Journal of Propulsion and Power, vol. 12, pp. 691-698, 1996.

[12] J. H. Kent and D. Honnery, "Soot and mixture fraction in turbulent diffusion flames", Combustion Science and Technology, vol. 54, pp. 383-398, 1987.

[13] H. Wang, D. X. Du, C. J. Sung, and C. K. Law, "Experiments and numerical simulation on soot formation in opposed-jet ethylene diffusion flames", Proceedings of the Combustion Institute, vol. 26, pp. 2359-2368, 1996.

[14] M. E. Decroix and W. L. Roberts, "Transient flow field effects on soot volume fraction in diffusion flames", Combustion Science and Technology, vol. 160, pp. 165-189, 2000.

[15] A. Beltrame, P. Porshnev, W. Merchan-merchan, A. Saveliev, A. Fridman, and L. A. Kennedy, "Soot and NO formation in methane–oxygen enriched diffusion flames", Combustion and Flame, vol. 124, pp. 295-310, 2001.

[16] J. H. Kent and S. J. Bastin, "Parametric effects on sooting in turbulent acetylene diffusion flames", Combustion and Flame, vol. 56, pp. 29-42, 1984.

[17] M. Köhler, I. Boxx, K. P. Geigle, and W. Meier, "Simultaneous planar measurements of soot structure and velocity fields in a turbulent lifted jet flame at 3 kHz", Applied Physics B, vol. 103, pp. 271-279, 2011.

[18] M. Köhler, K.-P. Geigle, T. Blacha, P. Gerlinger, and W. Meier, "Experimental characterisation and numerical simulation of a sooting lifted turbulent jet diffusion flame", Combustion and Flame, vol. 159, pp. 2620-2635, 2012.

[19] M. Köhler, K. P. Geigle, W. Meier, B. M. Crosland, K. A. Thomson, and G. J. Smallwood, "Sooting turbulent jet flame: characterisation and quantitative soot measurements", Applied Physics B, vol. 104, pp. 409-425, 2011.

[20] S. M. Mahmoud, G. J. Nathan, P. R. Medwell, B. B. Dally, and Z. T. Alwahabi, "Simultaneous planar measurements of temperature and soot volume fraction in a turbulent non-premixed jet flame", Proceedings of the Combustion Institute, vol. 35, pp. 1931-1938, 2015.

[21] S. M. Mahmoud, G. J. Nathan, Z. T. Alwahabi, Z. W. Sun, P. R. Medwell, and B. B. Dally, "The effect of exit strain rate on soot volume fraction in turbulent non-premixed jet flames", Proceedings of the Combustion Institute, vol. 36, pp. 889-897, 2017.

[22] S. M. Mahmoud, G. J. Nathan, Z. T. Alwahabi, Z. W. Sun, P. R. Medwell, and B. B. Dally, "The effect of exit Reynolds number on soot volume fraction in turbulent non-premixed jet flames", Combustion and Flame, vol. 187, pp. 42-51, 2018.

[23] N. H. Qamar, Z. T. Alwahabi, Q. N. Chan, G. J. Nathan, D. Roekaerts, and K. D. King, "Soot volume fraction in a piloted turbulent jet non-premixed flame of natural gas", Combustion and Flame, vol. 156, pp. 1339-1347, 2009.

[24] N. H. Qamar, G. J. Nathan, Z. T. Alwahabi, and K. D. King, "The effect of global mixing on soot volume fraction: measurements in simple jet, precessing jet, and bluff body flames", Proceedings of the Combustion Institute, vol. 3, pp. 1493-1500, 2005.

[25] G. J. Nathan, P. A. M. Kalt, Z. T. Alwahabi, B. B. Dally, P. R. Medwell, and Q. N. Chan, "Recent advances in the measurement of strongly radiating, turbulent reacting flows", Progress in Energy and Combustion Science, vol. 38, pp. 41-61, 2012.

[26] P. R. Medwell, Q. N. Chan, P. A. M. Kalt, Z. T. Alwahabi, B. B. Dally, and G. J. Nathan, "Development of temperature imaging using two-line atomic fluorescence", Appllied Optics, vol. 48, pp. 1237-1248, 2009.

[27] Z. W. Sun, D. Gu, G. J. Nathan, Z. T. Alwahabi, and B. B. Dally, "Single-shot, time-resolved planar laser-induced incandescence (TiRe-LII) for soot primary particle sizing in flames", Proceedings of the Combustion Institute, vol. 35, pp. 3673-3680, 2015.

[28] V. Narayanaswamy and N.T. Clemens, "Simultaneous LII and PIV measurements in the soot formation region of turbulent non-premixed jet flames", Proceedings of the Combustion Institute, vol. 34, pp. 1455-1463, 2013.

[29] K. -P. Geigle, M. Köhler, W. O'Loughlin, and W. Meier, "Investigation of soot formation in pressurised swirl flames by laser measurements of temperature, flame structures and soot concentrations", Proceedings of the Combustion Institute, vol. 35, pp. 3373-3380, 2015.

[30] K. -P. Geigle , R. Hadef, and W. Meier, "Soot formation and flame characterisation of an aero-engine model combustor burning ethylene at elevated pressure", Journal of Engineering and Gas Turbines Power, vol. 136, pp. 021505, 2014.

[31] C. Eberle, P. Gerlinger, K.-P. Geigle, and M. Aigner, "Numerical investigation of transient soot evolution processes in an aero-engine model combustor", Combustion Science and Technology, vol. 187, pp. 1841-1866, 2015.

[32] M. Grader, Z. Yin, K. -P. Geigle, and P. Gerlinger, "Influence of flow field dynamics on soot evolution in an aero-engine model combustor", Proceedings of the Combustion Institute, vol. 38, pp. 6421-6429, 2020.

[33] A. Rowhani, Z. W. Sun, P. R. Medwell, Z. T. Alwahabi, G. J. Nathan, and B. B. Dally, "Effects of the bluff-body diameter on the flow field characteristics of

non-premixed turbulent highly-sooting flames", Combustion Science and Technology, vol. 194 (2), pp. 378-396, 2022.

[34] International Sooting Flame (ISF) Workshop. (accessed on 15-08-2021), http://www.adelaide.edu.au/cet/isfworkshop.

[35] C. Schulz, B. F. Kock, M. Hofmann, H. Michelsen, S. Will, B. Bougie, R. Suntz, and G. Smallwood, "Laser-induced incandescence: recent trends and current questions", Applied Physics B, vol. 83, pp. 336-354, 2006.

[36] Z. W. Sun, Z. T. Alwahabi, D. H. Gu, S. M. Mahmoud, G. J. Nathan, and B. B. Dally, "Planar laser-induced incandescence of turbulent sooting flames: the influence of beam steering and signal trapping", Applied Physics B, vol. 119, pp. 731-743, 2015.

[37] S. Kruse, P. R. Medwell, J. Beeckmann, and H. Pitsch, "The significance of beam steering on laser-induced incandescence measurements in laminar counterflow flames", Applied Physics B, vol. 124, pp. 212, 2018.

[38] W. Thielicke and E. J. Stamhuis, "PIVlab - Towards user-friendly, affordable and accurate digital particle image velocimetry", Journal of Open Research Software, vol. 2, 2014.

[39] W. Thielicke, "The flapping fligh of birds - analysis and application", Rijksuniversity Groningen, pp.1-10, 2014.

[40] S. Deng, M. E. Mueller, Q. N. Chan, N. H. Qamar, B. B. Dally, Z. T. Alwahabi, and G. J. Nathan, "Hydrodynamic and chemical effects of hydrogen addition on soot evolution in turbulent nonpremixed bluff body ethylene flames", Proceedings of the Combustion Institute, vol. 36 , pp. 807-814, 2017.

[41] M. E. Mueller and H. Pitsch, "Large eddy simulation of soot evolution in an aircraft combustor", Physics of Fluids, vol. 25, ,pp. 110812, 2013.

[42] B. B. Dally, A. R. Masri, R. S. Barlow, and G. J. Fiechtner, "Instantaneous and mean compositional structure of bluff-body stabilised nonpremixed flames", Combustion and Flame, vol. 114, pp. 119-148, 1998.

[43] B. B. Dally, D. F. Fletcher, and A. R. Masri, "Flow and mixing fields of turbulent bluff-body jets and flames", Combusion Theory and Modelling, vol. 2, pp. 193-219, 1998.

[44] A. R. Masri, B. B. Dally, R. S. Barlow, and J. G. Fiechtner, " Instantaneous and Mean Compositional Structure of Bluff-Body Stabilized Nonpremixed flames", Combustion and Flame, vol. 114, pp. 119-148, 1998.

[45] A. R. Masri, B. B. Dally, " Modelling of Bluff-body recirculating flows", In: Proceeding of the 12st Australasian Fluid Mechanics Conference, Sydney, Australia, 1995.

[46] M. D. Smooke, M. B. Long, B. C. Connelly, M. B. Colket, and R. J. Hall, "Soot formation in laminar diffusion flames", Combustion and Flame, vol. 143, pp. 613-628, 2005.

[47] A. Rowhani, A. Chennici, M. J. Evans, P. R. Medwell, G. J. Nathan, and B. B. Dally, "Variation of residence time in non-premixed turbulent bluff-body ethylene flames as a function of burner diameter", 21st Australasian Fluid Mechanics Conference (2018), paper 318.

[48] A. G. Asuero, A. Sayago, and A. G. González, "The Correlation Coefficient: An Overview", Critical Reviews in Analytical Chemistry, vol. 36, pp. 41-59, 2006.

[49] A. Cuoci, A. Frassoldati, T. Faravelli, and E. Ranzi, "Soot formation in unsteady counterflow diffusion flames", Proceedings of the Combustion Institute, vol. 32, pp. 1335-1342, 2009.

Chapter 6 Soot-Flow Interaction in Methane Flames

Statement of Authorship

Title of Paper	Soot structure and flow characteristics in turbulent non-premixed methane flames stabilised on a bluff-body
Publication Status	☐ Published ☐ Accepted for Publication ☑ Submitted for Publication ☐ Unpublished and Unsubmitted work written in manuscript style
Publication Details	Amir Rowhani, Zhiwei Sun, Paul. R. Medwell, G. J. Nathan, Bassam. B. Dally, "Flow dynamics and soot evolution in turbulent methane flames stabilised on a bluff-body", under review.

Principal Author

Name of Principal Author (Candidate)	Amir Rowhani		
Contribution to the Paper	Developed ideas, conducted experiments, performed data analysis and interpreted results, wrote manuscript, and acted as corresponding author.		
Overall percentage (%)	65%		
Certification:	I planned and proposed the experimental plans to the co-authors after a thorough literature review. Together with the co-authors, we decided the experimental cases. I set up experiments to measure soot and flowfield in the three selected methane flames. I also performed the PIV and LII measurements as well as the LII calibration, with the assistance of the second co-author Dr Zhiwei Sum, for the three flames. I processed the LII and PIV data and analysed the results. I also analysed the CFD results. After presenting the data for the co-authors, I drafted the manuscript. I Acted as the corresponding author and took primary responsibility for responding the reviewers.		
Signature		Date	70-10-2021

Co-Author Contributions

By signing the Statement of Authorship, each author certifies that:

i. the candidate's stated contribution to the publication is accurate (as detailed above);

ii. permission is granted for the candidate in include the publication in the thesis; and

iii. the sum of all co-author contributions is equal to 100% less the candidate's stated contribution.

Name of Co-Author	Dr. Zhiwei Sun		
Contribution to the Paper	This co-author provided assistance with the experimental setup and data collection.		
Signature		Date	08-10-2021

Name of Co-Author	Dr. Alfonso Chinnici		
Contribution to the Paper	This co-author provided assistance for the CFD section.		
Signature		Date	08-10-2021

Name of Co-Author	Associate Professor Paul R. Medwell		
Contribution to the Paper	This co-author helped with the experimental setup and with editing and revising the manuscript.		
Signature		Date	08-OCT-2021

Name of Co-Author	Graham J. Nathan		
Contribution to the Paper	This co-author co-supervised the development of the work. He also helped to evaluate and edit the manuscript.		
Signature		Date	14/10/2021

Name of Co-Author	Bassam B. Dally		
Contribution to the Paper	This co-author co-supervised the development of the work. He also helped plan and structure the manuscript. He also provided assistance with rebutting reviewers' comments and with revising the manuscript.		
Signature		Date	07-10-2021

Soot structure and flow characteristics in turbulent non-premixed methane flames stabilised on a bluff-body

This chapter consists of the submitted journal article:

Amir Rowhani, Zhiwei Sun, Paul. R. Medwell, G. J. Nathan, Bassam. B. Dally, "Flow dynamics and soot evolution in turbulent methane flames stabilised on a bluff-body". submitted to the Combustion and Flame

The article is identical to its submitted format with the following exceptions:

1. The typesetting and referencing styles have been altered to maintain a consistent appearance within the thesis.

2. The numbering of tables, figures, and equations has been changed to include the number of the chapter.

6.1 Abstract

The current study presents detailed measurements of the soot and flowfield characteristics of three turbulent non-premixed pure methane bluff-body flames. Planar laser-induced incandescence (P-LII) and 2D-polarised particle image velocimetry (P-PIV) were simultaneously employed to measure soot volume fraction (SVF) and the flowfield features. The measured mean and instantaneous scalar data for all three flames are presented and analysed along with the computed mean mixture fraction, temperature and species concentration (OH and C_2H_2), utilizing previously validated CFD model. Results show that the SVF in the recirculation zone (RZ) have strong dependency on the momentum flux ratio of fuel jet and coflowing air. Increasing the momentum flux ratio shifts the location of the mean stoichiometric mixture fraction to the rich inner vortex, leading to a significant increase in SVF in the RZ. The results reveal that the impact of the momentum flux ratio is evident on soot formation, transport and oxidation within the RZ, and that also impacts on soot in the rest of the flame. Comparison with ethylene/nitrogen bluff-body flame, with the same operating conditions reveal that the equivalent methane flame produces significantly less soot in both the recirculation zone and the jet region. Also, instantaneous images of the SVF in the recirculation zone, in both flames, highlight significant differences in soot sheet structures for each flame, consistent with known soot formation pathways for ethylene and methane. In addition, the study has generated a database of soot and flowfield results, which can be helpful for future model development.

Keywords: soot, methane, bluff-body, turbulence, simultaneous measurement, PIV,

LII

Nomenclature

A_C	Air contractor
BD	beam dump
CL	cylindrical lens
CW	continuous wave
D_{BB}	bluff-body diameter – m
DC	co-flow contractor inner diameter – m
D_J	jet inner diameter – m
DPSS	diode-pumped-solid-state laser
DM	dichroic mirror
ENB	ethylene nitrogen bluff-body flame
f	focal length – m
f_v	soot volume fraction – ppb
FWHM	full width at half maximum
G	momentum flux ratio
HAB	height above the burner – m
ICCD	intensified charge-coupled device
IML	inner mixing layer
ISF	International Sooting Flame workshop
ISL	inner shear layer
JZ	jet zone
$\overline{L}_f$	mean flame length – m
$\overline{L}_{RZ}$	mean recirculation zone length – m
LHS	left-hand side
MB	methane bluff-body flame
$\dot{m_f}$	fuel mass flow rate – g/s
NZ	neck zone
OSL	outer shear layer
PAH	polyaromatic hydrocarbon
PDF	probability density function
ppm	part per million
P-LII	Polarised Laser Induced Incandescence
P-PIV	Polarised Particle Image elocimetry
QLHV	low-heating value of the fuel
r	radial distance – m
Re_J	jet Reynolds number
RHS	right-hand side
RZ	recirculation zone
S	strain rate – 1/s
SL	spherical lens
SVF	soot volume fraction – ppb
u	axial velocity – m/s
UC	co-flow velocity – m/s
U_J	fuel jet velocity – m/s
U_m	mean velocity – m/s
v	radial velocity – m/s
x	axial height – m

Greek Symbols

Φ	equivalence ratio
$\overline{\tau}$	mean residence time - ms

6.2 Introduction

Research into the control of soot formation and the mitigation of its emission from flames has been ongoing for decades due to ever-increasing environmental and health concerns. The primary fuel used in most of these studies is ethylene due to its high soot propensity as the simplest alkene and the relatively simple chemistry, which is desirable for modelling purposes. Consequently, a detailed understanding of ethylene kinetics and soot formation and oxidation mechanisms were developed over the years [1-3]. On the other hand, as the main constituent of natural gas, methane fuel is widely used in domestic and industrial applications, such as gas turbines, furnaces, and kilns. The use of natural gas as a transitional fuel to replace other fossil-based fuels, such as coal, has increased over the last two decades due to its lower carbon intensity. It is projected that by 2035, natural gas will contribute ~26% of the global energy requirement worldwide [4]. Hence, further research into the combustion of methane and its emission characteristics (soot in particular) under practical operating conditions is warranted.

It is well known that the molecular structure of fuels plays a significant role in the onset of soot formation [5, 6]. In non-premixed mode, the sooting tendency for alkenes is higher than alkanes. The differences between soot formation in C1 and C2 fuels stem from the makeup of the radical pool, acetylene concentrations, PAH formation pathways, and the residence time [7-10]. In the laminar regime, methane is only slightly sooting at atmospheric pressure, making it difficult to measure on the lab scale. However, increasing the pressure (up to 60 bar) accelerates the PAH condensation rate followed by acetylene addition, which enhances soot by a factor of five to six [11-13]. In methane flames, inception is the dominant mechanism with no measurable soot growth after inception [14]. In ethylene flame, the inception phase is relatively short, and the surface growth and agglomeration dominate the soot formation mechanism [15]. Additionally, the stronger soot propensity of ethylene is attributed to the faster reaction as compared to methane. For instance, while the soot graphitisation starts at 2.5 ns for C_2H_4, for CH_4 such time is within the surface growth and coalescence period. In addition, the C_2H_2 concentration, which is a key species in the soot surface growth mechanism, is found to be higher in C_2H_4 when compared to CH_4 [16]. Such differences result in additional difficulties in predicting soot in methane-based flames where the inception mechanism is poorly understood. In this context, flames with well-defined initial and boundary conditions and sufficiently long residence time, favouring soot inception, are needed to better

understand the formation of alkanes-based flames. Bluff body flames offer such conditions and hence are the target in this study.

Several groups have investigated the soot-flowfield interaction to quantify the mixing and strain rate effects using different fuels in turbulent flames. Global correlations have been established for a range of turbulent flames, including simple jets [17-24], bluff-body [25, 26], and swirling burners relevant to gas turbines [27]. These global parameters are characterised mainly by the global fuel exit strain rate, U/D_J, and the global mixing rate, defined as the inverse of the residence time, $1/\tau_G$. Mahmoud et al. [19-21] reported a linear correlation between the exit strain rate and the global mixing rate in momentum-dominated jet flames fuelled with ethylene, nitrogen and hydrogen fuel mixture. Qamar et al. [17, 18] investigated natural gas combustion in the turbulent regime and provided detailed correlations between the global mixing rate and soot formation for different burner geometries. Other flames, including swirl-stabilised flames, were also investigated using ethylene [27, 28] and Jet A-1 [29] fuels to provide further insight into the soot-flowfield interactions in flames with the recirculating flow. Our study on bluff-body turbulent flames fuelled by ethylene-nitrogen mixture has shown that there are no clear correlations between the local instantaneous SVF and strain rate within the recirculation zone and the bluff-body flames' jet region, which suggests that the time-scales for SVF are significantly greater than those driving local fluctuations [30]. While these studies provide an insightful understanding of the soot-flowfield interactions for flames fuelled with ethylene, there is only limited to similar studies for methane flames.
In this work, a series of non-premixed methane flames stabilised on a bluff-body are used to experimentally investigate the soot formation and oxidation under different operating conditions. These flames feature a recirculation zone at the base of the flame, which helps stabilise the flames at a higher strain rate. Moreover, such flames provide a measure of control on average mixture strength and residence time, in RZ, while maintaining a jet-like zone in the downstream part of the flame. Using this burner, the study aims to better understand the impact of the mean mixture fraction and residence time in the recirculation zone by systematically changing the jet and coflow velocities and the momentum flux ratio, for constant fuel nozzle diameter. The simultaneous measurements also provide statistical correlations between soot and the flow characteristics to better understand the local strain rate's dependency and impact on soot formation and transport. The high-fidelity data will also be beneficial as a benchmark for model validation.

6.3 Experimental setup

6.3.1 Bluff-body burner

An axisymmetric bluff-body burner that has been employed in earlier work [30, 31], with a fixed outer diameter of 64 mm, was used in this experimental campaign. With a central jet diameter of 4.6 mm, the capped brass tube is surrounded by a co-flowing air stream introduced through a round cross-section air contractor with an inner diameter of 190 mm. The round contractor helps avoid the formation of corner vortices that occur in square cross-section contractions. To allow optical access, the bluff-body was mounted 10 mm above the exit plane of the air contractor. The burner tunnel assembly was translated vertically, using an electrically powered traverse to measure the entire flame length. A large extraction hood (800 mm diameter) was also traversed with the burner tunnel assembly, such that a fixed distance of 300 mm from the flame tip to the hood inlet was kept, and where the hot combustion products were extracted. This arrangement reduces any effect from the exhaust hood on the flame as the burner and contraction assembly is traversed vertically.

6.3.2 Flow conditions

Table 1 shows a summary of the flow parameters investigated in this study. Methane with a purity of 99.99% was used as fuel. The co-flowing air and the fuel were at ambient temperature and atmospheric pressure. The resulting flames are labelled as MB series flames, where M and B stand for methane and bluff-body. The fuel flow rate was set to 0.32 g/s for the MB-1 flame, giving a bulk mean exit Reynolds number, based on the jet inner diameter, of 8,000, while the coflow air velocity was set to 14.1 m/s. The Reynolds number for flames MB-2 and MB-3 was increased to 15,000 (methane flow rate of 0.61 g/s) while the coflow was set to 14.1 and 20 m/s, respectively. The increase in the coflow air velocity aims to investigate the effect of mixture strength in the recirculation zone corresponding to the reduction in momentum flux ratio of jet to coflow [32, 33], defined as, $G = (\rho U^2)_{Fuel}/(\rho U^2)_{Air}$.

Table 6.1: Summary of the flow conditions of the bluff-body flames. (D_{BB} – bluff-body diameter; D_J – Fuel jet diameter; G –momentum flux ratio; $\overline{L}_f$ – Mean visible flame length; $\dot{m}_f$ – Fuel flow rate; QLHV– Heat input by fuel; Re_J – Jet exit Reynold; U_C – Bulk co-flowing air velocity; U_J – Bulk jet exit velocity).

Flame case	CH_4 (%Vol.)	D_{BB} (mm)	D_J (mm)	U_J (m/s)	Re_J (-)	$\dot{m}_f$ (g/s)	Q_{LHV} (kW)	U_C (m/s)	$\overline{L}$ (mm) (±5%)	L_{RZ} (mm)	G (-)
MB-1	99.99	64	4.6	31.8	8,000	0.34	17	14.1	736	92.4	2.63
MB-2	99.99	64	4.6	59.6	15,000	0.61	30.5	14.1	928	111.4	9.21
MB-3	99.99	64	4.6	59.6	15,000	0.61	30.5	20	806	106.1	4.57

6.3.3 LII and PIV setup

The diagnostic system is identical to earlier research and the details can be found in the publications by the same authors [31]. A schematic of the experimental apparatus is also shown in Figure 6.1. In brief, the apparatus comprises planar laser-induced incandescence, P-LII, aligned with a 2D-polarised particle image velocimetry system. A pulsed Nd:YAG laser (Q-smart 850, Quantel) with the fundamental output (1064 nm) operating at 10 Hz is used for the P-LII measurements. The incandescence from soot particles was collected through an intensified (ICCD) camera through a 430 nm (10 nm bandwidth) filter to suppress interference from the C_2 laser-induced emissions and flame radiation [31]. The gate width of the LII camera was set to 50 ns with prompt timing relative to the LII excitation. The LII beam was formed into a sheet by passing it through the sheet-forming lenses, with the dimensions of 0.5 mm × 70 mm. The LII laser fluence was kept above 0.5 J/cm^2, in the plateau region of the LII response curve to minimise the laser energy variation effects from the beam steering and attenuation on the resulting LII signals [32]. The P-LII signal was converted to soot volume fraction (SVF) by calibration against one of the flat premixed McKenna burner target flames ($\Phi = 2.34$) from the International Sooting Flame Workshop (ISF) [33]. A 1064-nm continuous-wave (CW) diode-pumped-solid-state laser (DPSS) was utilised to perform the laser extinction calibration measurements in the McKenna target flames. The minimum detection limit in the collected data was determined to be 1 ppb. The details of the calibration were reported previously [19, 20]. The P-LII data was only extracted from the core of the images due to the signal variation in the upper and lower sides of the laser sheet. A standard deviation of 13% was observed in P-LII data extracted from the laminar McKenna burner flame. Also, the data was only processed in the beam entrance side of the flame to avoid beam steering effects. Sun et al. [34] reported a 2 mrad and consequently 50% increase in the laser sheet width and 750 µm out-of-plane direction

throughout the flame. Signal trapping has been previously quantified in a series of ethylene flames and is considered negligible. Since the soot concentration in the methane flames is significantly lower than the ethylene counterparts, the signal trapping is assumed to be minor [35].

The PIV measurements were performed using a 10 Hz pulsed dual-head Nd:YAG laser (Quantel BrilliantB/Twins) frequency-doubled (532 nm). The PIV pulses were offset by 10 µs to 60 µs, depending on the exit jet and co-flow velocities. The Mie scattering from the 1-micron titanium oxide (TiO_2) seeding particles were collected using a CCD Kodak Megaplus II camera (1920 × 1080 pixels^2, 16 bit), equipped with a Sigma lens (105 mm, f = 2.8). Two additional polarisers to a conventional PIV system were utilised to significantly suppress the scattered interference from soot particles [31, 36]. A 532 nm bandpass filter (Andover) with an FWHM of 1 nm was fitted to the camera lens to suppress laser-induced natural incandescence. One thousand PIV image pairs were recorded and processed using commercial software, PIVLab 2.20 [37]. Background noise was removed from raw images in the post-processing step. The interrogation window was sequentially reduced from 64×64 to 32×32, and ultimately to 16×16 pixels^2 with 50% overlap, to provide a minimum spatial resolution of 1.48 × 1.48 mm^2. The total error of the PIV measurements was estimated to be ±1.16 m/s [31].

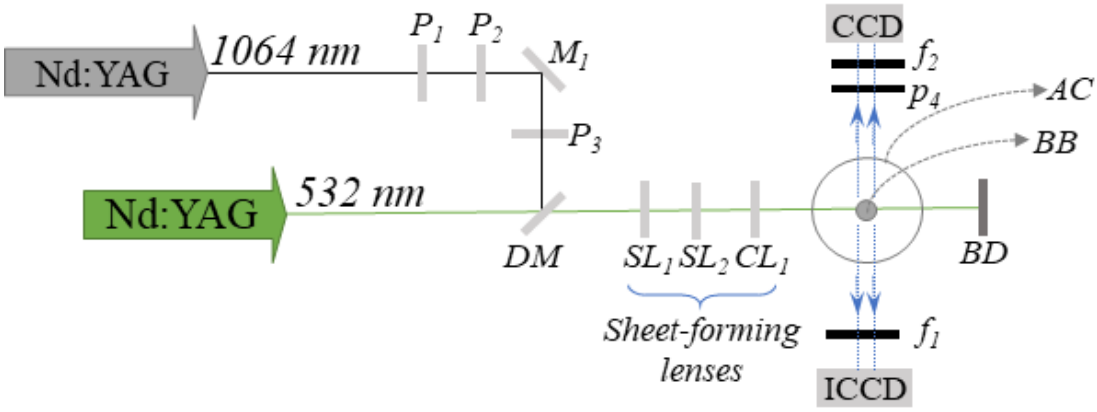

Figure 6.1: Experimental layout adopted from earlier work [30]. (AC – Air contractor; BB – Bluff-body burner; BD – Beam dump; CCD – Charged-coupled device; CL_1 – Cylindrical lens; DM – Dichroic mirror; f_1 – 430 nm filter; f_2 – 532 nm bandpass filter; ICCD – Intensified charged-coupled device; M_1 – 532 nm mirror; P_1 – λ/2 wave plate; P_2 – 532 nm film polariser; P_3 – Linear polariser; P_4 – linear polariser and SL_1/ SL_2 – Spherical lenses).

6.3.4 Numerical model

The CFD method was used in this work to assist in better interpreting the observed trends using the same model from our earlier work [31]. The MB-1, MB-2, and MB-3 flames were modelled using ANSYS Fluent 21 R1 [38]. A 2-D axisymmetric model of the bluff-body burner was developed, with a fuel jet in the centre surrounded by a concentric coflow air. Following a mesh-independence study, a structured mesh with 550,000 cells was generated [27]. The governing equations for mass, momentum and energy were solved using steady, incompressible Reynolds-averaged Navier−Stokes (RANS) equations. The standard k-ε model with modified coefficients [39, 40] was selected for turbulence closures. The steady flamelet model, coupled with the DRM-22 reduced kinetic mechanism (22 species and 104 reactions), was used for the combustion model. The COUPLED algorithm was employed to solve the flowfield, with second-order spatial discretisation for all variables. The CFD was validated against the current velocity measurements with a very good agreement (less than 4% differences). To validate the model, a comparison of the predicted and measured mixture fraction, temperature, and velocity components have been performed in a similar version of non-sooting bluff-body flames. Additionally, a comparison of the current work's measured axial and radial velocity components with the calculated values have been performed. The validation data is presented in the supplementary material (Fig. D.S1 and Fig. D.S2).

6.4 Results and discussion

6.4.1 Global flame structure

The global appearance of the three methane flames stabilised on the bluff-body burner, shown in Figure 6.2, is similar to earlier studied non-premixed bluff-body flames [25, 31, 39-41]. Regardless of the fuel type, these flames typically feature a recirculation zone at the upstream and close to the bluff-body surface, a jet-propagation region in the downstream, and a soot-free neck zone, which connects these two regions. The blue length of the region above the recirculation zone increases with both the increase in the jet (MB-2) and co-flow (MB-3) velocities, where MB-3 shows the largest soot-free zone. The neck zone region is characterised by a high strain rate, enhanced mixing with the coflowing air and the hot products from the recirculation zone, and a central fuel stream [41]. The mean flame visible

length ($\overline{L}_f$), which is estimated from 10 binarised instantaneous flame images, is found to be 736 mm, 928 mm, and 806 mm for MB-1, MB-2, and MB-3 flames, respectively. As expected, the maximum flame length corresponds to the MB-2 flame with the highest fuel jet velocity (59.6 m/s) and the lowest co-flow air velocity (14.1 m/s). Increasing the co-flow velocity to 20 m/s, in MB-3 flame, helps induce more fuel into the recirculation zone, reducing the amount of fuel reaching the rest of the flame, and leading to a reduction in the overall length by 13%, as compared with MB-2. This is found to be directly linked with the momentum flux ratio, as shown in Fig. 6.3.

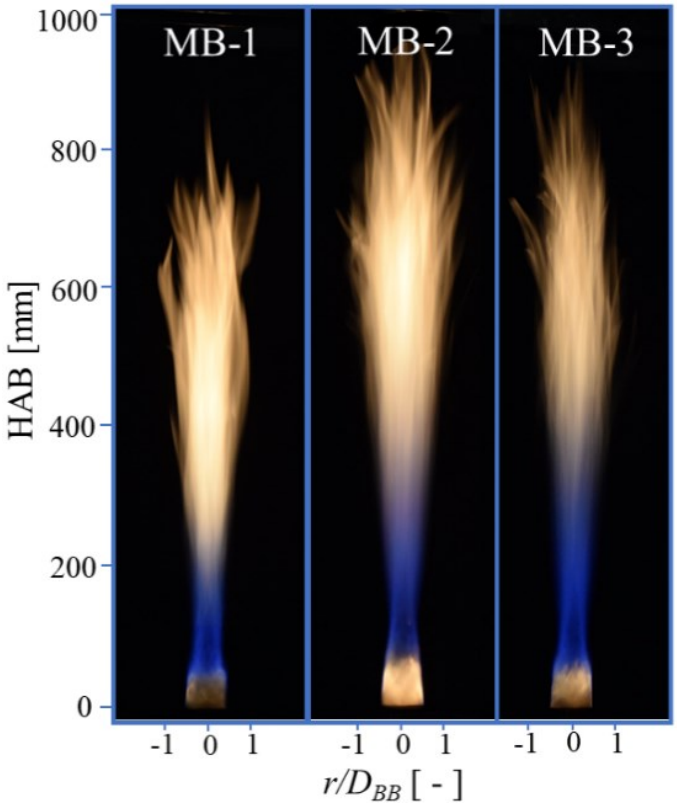

Figure 6.2: Photographs of the pure methane flames stabilised on the bluff-body burner; MB-1 (left), MB-2 (middle), and MB-3 (right).

The momentum flux ratio (G), defined as $G = (\rho U^2)_{Fuel}/(\rho U^2)_{Air}$ is calculated for the three flames and presented in Table 6.1. This ratio is found to be 2.63, 9.21, and 4.57 for the MB-1, MB-2, and MB-3 flames, respectively. Dally et al. [41] showed that for a series of flames operating with various fuels, including H_2, CNG, LPG, and C_2H_4, the transitional momentum flux ratio between the single and double vortex structure in the bluff-body flames happens at G between 13 – 15. Consistent with this, the momentum flux ratio calculated for these flames is below the transition threshold to a single vortex flame. Hence, all three flames include two vortices, an inner and an outer vortex within the recirculation zone. The correlations between the momentum flux ratio (G) and both the mean flame length ($\overline{L}_f$) and total soot in the recirculation zone (SV_{RZ}) are presented in Fig. 6.3. The total soot volume can be expressed as

$$SV_{RZ} = 2\pi r \int_0^{x_{max}} \int_0^{r_{max}} SVF\ (r,x)\, dr.dx \qquad (1)$$

where $SVF\ (r,x)$ is the local soot volume fraction at a certain height above the burner, x, and a radial distance from the axis, r. For the recirculation zone, the parameter x_{max} is set to the length of the recirculation zone (L_{RZ}), as defined in Section 3.2. The dependence on the momentum flux ratio of both mean flame length and the total soot in the recirculation zone can be reasonably characterised for the present flames with exponential fits. It is notable too that more data points are needed to establish a generic correlation for these flames, and the current fit appears plausible for the range of conditions considered in this work.

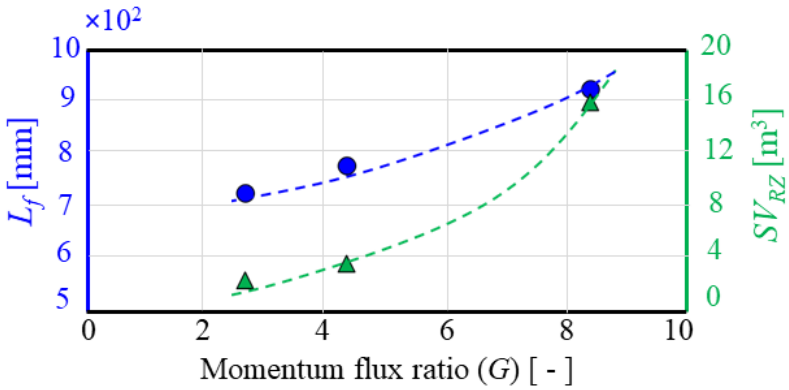

Figure 6.3: The momentum flux ratio, G, plotted as a function of mean total flame length ($\overline{L}_f$) in blue and total soot in the recirculation zone (SV_{RZ}) in green. The symbols present the measured data and the dashed-lines show the best exponential fits

6.5 Time-averaged flowfield features

The mean flowfield features for the three flames were calculated from 1000 instantaneous image pairs obtained from the PIV measurements. Figure 6.4 presents the typical mean vector field overlaid on the mean velocity and mean shear strain rate for MB-1 flame, as a reference flame, at axial locations up to x/D_{BB}=2.0. The 2D shear-strain rate, S_{xy}, has been calculated from the velocity components obtained from the PIV, using the following formula:

$$|S_{rx}| = \frac{1}{2}\left|\left(\frac{\partial u_r}{\partial x} + \frac{\partial u_x}{\partial r}\right)\right| \tag{2}$$

where u and v are the axial and radial velocity components, respectively. Since all three flames exhibit similar characteristics within the recirculation zone, namely two vortices between the inner and outer shear layers, only the MB-1 flame is represented in Fig. 6.4.

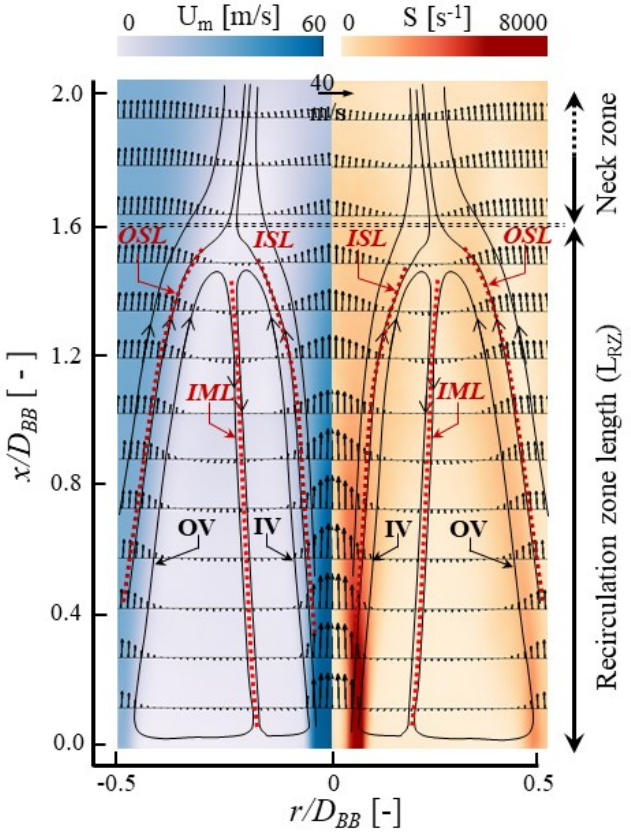

Figure 6.4: Ensemble-averaged mean velocity contour (left) and mean strain rate contour (right) overlaid on the vector field for a typical methane bluff-body flame (MB-1). The dashed-lines show the inner shear layer (*ISL*), intermediate mixing layer (*IML*) and outer shear layer (*OSL*).

The length of the recirculation zone (L_{RZ}) is defined by the distance from the jet exit plane to the stagnation point, where the mean axial velocity of the flame is zero. The L_{RZ} for each flame is presented in Table 1. The recirculation zone length for the MB-1 flame is measured to be 87.7 mm. Increasing the fuel jet velocity, and consequently, the jet Reynolds number to 15,000, while the co-flow velocity is kept constant, results in an increase in the recirculation zone length by ~21% to 105.1 mm, in MB-2 flame. This is the largest recirculation zone amongst the three flames. In MB-3 flame, where the co-flow air velocity increases to 20 m/s, the recirculation zone length is ~91.5 mm, due to a stronger outer shear layer (OSL) leading to an outer vortex restricting the extension of the recirculating upwards. For all three flames, the ratio of the recirculation zone length to the bluff-body diameter (L_{RZ}/D_{BB} < 1.65) is 1.37, 1.63, and 1.49 for MB-1 MB-2 MB-3 flames, respectively. This is consistent with earlier investigations in non-premixed bluff-body flames [30], which further shows that mixing and flow dynamics have more significant effects than the heat release on the recirculation zone length.

The mean profiles of axial velocity, u, and radial velocity, v, together with the strain rate (S) and turbulence intensity are presented in Fig. 6.5 at $x/D_{BB} = 0.4$ for the MB-1 flame as a reference. Due to the similarities between the mean flowfield profiles of the three flames, one axial location is presented here. However, more locations including in the RZ and the jet region are presented in the supplementary material (Fig C.S3 and C.S4). The axial and radial mean velocity profiles show the two counter-rotating vortices in the recirculation zone, with a negative axial velocity between $r/D_{BB} = 0.13$ and $r/D_{BB} = 0.42$ and radial velocity changing sign at the point of interaction of the two vortices. Also noticeable in Figure 6.5, is the large nearly homogeneous region with constant strain rate and minimal turbulent mixing. This feature in turbulent bluff-body flames provides relatively long residence time for soot to form at an almost uniform mean mixture fraction and temperature, as we will see later from the computational study.

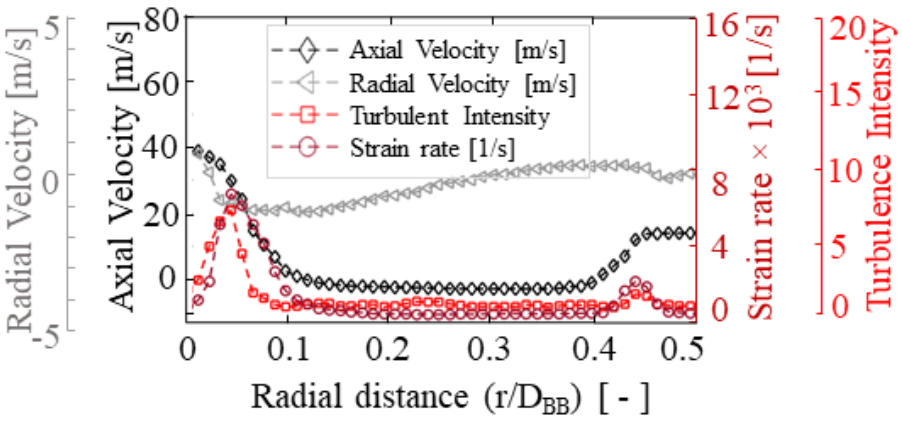

Figure 6.5: Measured radial profile of time-averaged axial (u) and radial (v) velocity components, strain rate (S) and turbulent intensity (I) at the axial location of x/D_{BB}= 0.4 in the recirculation zone of the MB-1 flame

6.6 Time-averaged soot volume fraction

6.6.1 Radially-integrated *SVF*

Figure 6.6 presents a collage of the measured time-averaged soot volume fraction (left) for all three flames together with the axial profiles of radially integrated soot volume fraction, in ppm.mm^2 (right). Soot concentrations in the three flames exhibit significant differences in quantity and trends. In MB-1 and MB-3 flames, minimal soot is observed in the recirculation zone, while a distinct peak appears in the jet-like zone. However, in MB-2 flame, two peaks are found; one in the recirculation zone and the other one in the jet-like region. The maximum radially integrated soot in the recirculation zone is 130 ppm.mm^2 for MB-2 flame while it drops to almost 18 to 20 ppm.mm^2 for MB-1 and MB-3 flames. In the jet region, however, the maximum total soot in MB-1 flame is around 175 ppm.mm^2 while in the MB-2 and MB-3 flames, it drops to less than a third of the MB-1, (~50 ppm.mm^2 and 34 ppm.mm^2). Noteworthy is that MB-1 has the lowest jet Reynolds number and air coflow velocity and more fuel burns in the jet-like zone.

Contrasting the methane bluff-body flames (MB flames) with ethylene/nitrogen bluff-body flames (ENB flames) [30] as well as the simple jet flames [19, 20] reveal that the maximum radially integrated soot volume fraction in the jet region is found at similar axial location (normalised by the flame length) above the burner of between $0.6 < x/L_f < 0.7$. Also noticeable is that while the methane (MB-3) and ethylene/nitrogen flames (ENB-3) are stabilised on the same burner and operating

conditions, the maximum radially-integrated soot in the recirculation zone for the MB-3 (~20 ppm.mm^2) flame is reduced by more than one order of magnitude, as compared to ENB-3 (~300 ppm.mm^2). It is deduced that this difference is related to the difference in the oxidation level and the mean mixture fraction distribution in two flames. This difference is further discussed in Section 3.4.

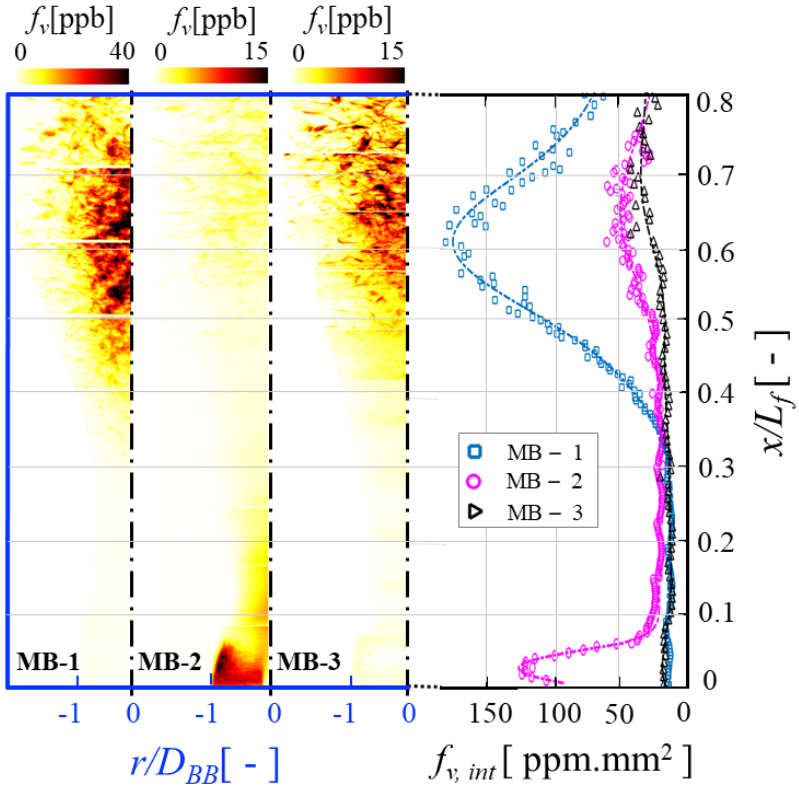

Figure 6.6: A collage of the measured time-averaged soot volume fraction (left) for the three flames, together with the axial profiles of radially integrated soot volume fraction, in ppm.mm^2, along the flames' length (right). Please note the different colour scales for MB-1 and the one for both MB-2 and MB-3.

6.6.2 Axial distribution of *SVF*

The axial profile of soot volume fraction (*SVF*) at the flame centreline of each flame is presented in Figure 6.7. The symbols represent the experimental data, and the dashed lines provide reasonable Gaussian fits. The axial height is normalised by the overall flame length (x/L_f), which enables us to compare the results with the ethylene/nitrogen flame (ENB-3) and the simple jet flames [20].

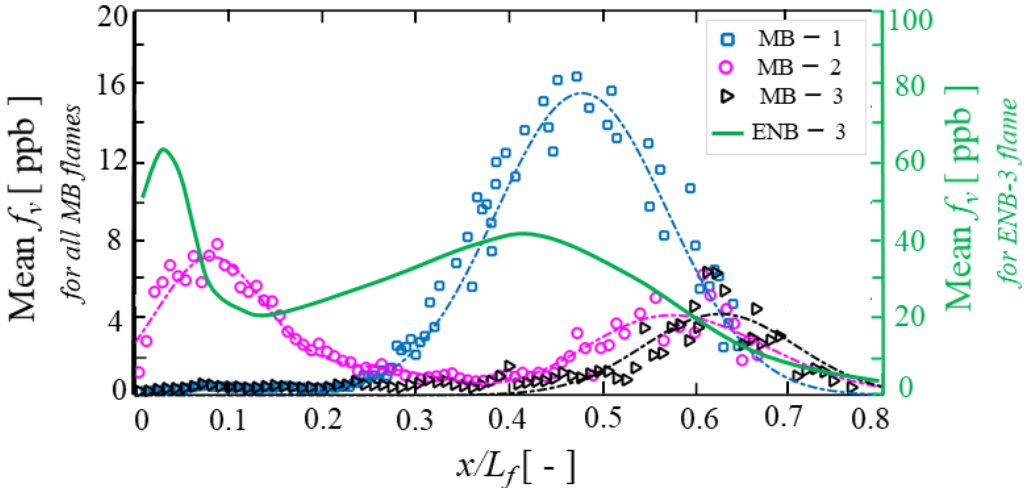

Figure 6.7: Axial profiles of centreline distribution of mean soot volume fraction as a function of normalised flame length. The dashed lines indicate Gaussian fits to the experimental data. The *ENB-3* ethylene/nitrogen bluff-body flame is shown with solid green line from a previous flame series [30].

The *SVF* distribution along the centreline has two distinct peaks in the MB-2 flame: one in the recirculation zone, at $x/L_f = 0.093$, and the other in the jet-like region, found at $x/L_f = 0.59$. This trend is similar to ENB flames. On the other hand, MB-1 and MB-3 flame exhibit only one peak in the jet region. The *SVF* in the jet region peaks to around 17 ppb in the MB-1 flame, which is greater than those in MB-2 and MB-3 flames by a factor of almost three. It is also observed that the peak of *SVF* in MB-2 and MB-3 flames is shifted axially as the Reynolds number is increased in these two flames. The axial location of the maximum *SVF* in the jet region is found to be at $x/L_f = 0.48$, while this location is shifted to x/L_f =0.59 and 0.63 for MB-2 and MB-3 flames, respectively.

When comparing MB-3 flame with ENB-3 flame [27], noticeable differences are observed. For ENB-3 flame, the axial location of the peak of the SVF profiles on the flame centreline is closer to the upstream region of the flame (at x/L_f =0.38), valued at 45 ppb. On the other side, in methane flame (MB-3), the peak is shifted downstream and found at around x/L_f =0.63, and the value dropped by a factor of more than eight to around 5 ppb. Interestingly, the peak soot in the methane flame is coincident at a similar position, x/L_f =0.60, in the simple jet flames with the same Reynolds number (15,000) [19, 20]. This indicates that the axial location of the maximum measured *SVF* on the flames centre line is primarily controlled by the flowfield in these turbulent flames while the fuel chemistry has a secondary effect.

6.6.3 Radial distribution of *SVF*

Figure 6.8 compares the mean radial profiles of *SVF* in the recirculation zone for the three flames. The profiles are plotted at four different axial locations above the jet exit plane within the recirculation zone (x/D_{BB} = (0.6, 0.8, 1.2, 1.4). The symbols represent the experimental data. The solid lines were obtained from the best Gaussian fit (with three terms) to the measured data. The bluff-body diameter is used to normalise both axial and radial distances. Consistent with ethylene/nitrogen flames (ENB-1, ENB-2, and ENB-3 flames) [30], a dominant outer peak is found at $x/D_{BB} < 1$ for all three methane flames near to the coflowing air (inside the outer vortex at $r/D_{BB} \approx 0.35$–0.42) from which it decreases smoothly toward the centreline. An explicit peak is observed at lower axial heights, where the mixture fraction is rich compared with the end of the *RZ*. At higher locations, $x/D_{BB} > 1.0$, no distinct peak can be identified, and that is attributed to the high rate of oxidation due to the intense coflow air entrainment and higher temperatures from products leaving the recirculation zone. Such similarities highlight the role of soot transport within the recirculation zone irrespective of the difference in soot inception and chemical effects between the two fuels. The three flames share similar trends in the mean *SVF* profiles, albeit with different peaks.

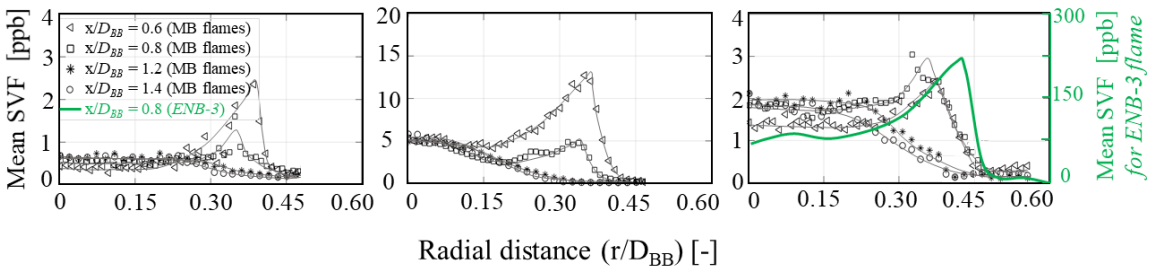

Figure 6.8: Radial profiles of mean soot volume fraction of the a) MB-1, b) MB-2, and c) MB-3 flames within the recirculation zone at different heights above the burner (HAB). The *ENB-3* ethylene/nitrogen bluff-body flame is shown with solid green line from a previous flame series [30].

The radial profiles of mean *SVF* in the jet region ($0.25 < x/L_f < 0.65$) for the three flames are compared in Fig. 6.9. The heights are normalised by the overall flame length (L_f). The three flames exhibit similar trends showing a maximum for *SVF* on the flame centreline (r = 0 mm), followed by a smooth decrease towards the flame edge, where most of the soot is oxidised. In MB-1 flame, the maximum soot volume

fraction SVF_{max} in the jet region is around 22 ppb which is one order of magnitude greater than the maximum SVF in the recirculation zone. Similarly, in the MB-3 flame, where the jet and co-flow velocities are maximum among the three flames, the SVF_{max} in the jet region is around 16 ppb which is greater than the SVF_{max} in the RZ by a factor of two to three. Conversely, the MB-2 flame behaves differently. The SVF_{max} in the recirculation zone is found to be around 13 ppb, while a 30% drop in the max SVF is observed for this flame in the jet region (7 ppb). Based on this observation in the SVF values as well as the flame photos, it is deduced that more PAH is transported from the recirculation zone to the jet-like region through the neck zone, which initiates the soot inception in the jet region. Also, it is deduced that soot inception in the MB-2 flame starts earlier comparing to the other flames, and therefore, there is sufficient time for soot to be formed in the recirculation zone. These observations require further experimental evidence to examine the PAH in the neck zone of the three flames and correlate them with the trends found in these flames.

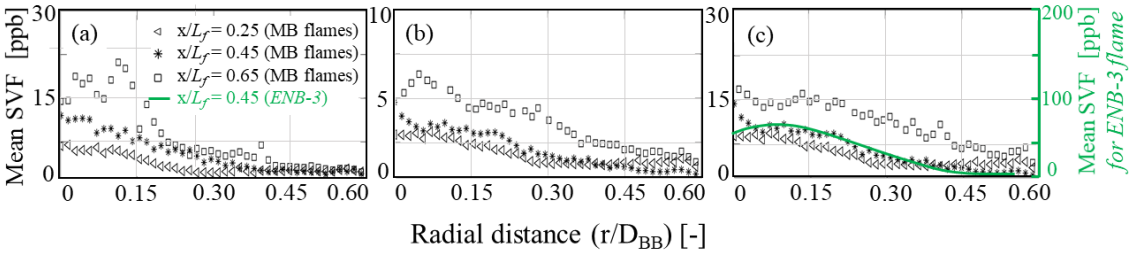

Figure 6.9: Radial profiles of mean soot volume fraction a) MB-1, b) MB-2, and c) MB-3 flames in the jet zone at different normalised heights above the burner. Note that the y-axis values differ in each profile. The *ENB-3* ethylene/nitrogen bluff-body flame is shown with solid green line from a previous flame series [30].

6.6.4 Soot intermittency

Fig. 6.10 presents the profiles of soot intermittency, defined as the probability of finding no soot at any given spatial location, along with flames centreline [17, 20]. The intermittency profiles exhibit two distinct minima for each flame; one in the recirculation zone and a second one in the jet-like region. As expected, at the jet exit, $x/L_f = 0$, the intermittency equals 1.0, and then the profile follows a sharp decrease to around 0.32 for MB-1 and MB-3 flames within the recirculation zone.

For MB-2 flames, the intermittency reaches less than 0.1, consistent with a higher concentration of soot found in the recirculation zone of this flame. The sharp decrease observed in the intermittency profile and the SVF measured on the flame centreline highlights the effect of transport of soot from the vortices into the central jet and further downstream to the rest of the flame. At $x/L_f \approx 0.12$, it is surprising that the intermittency for all three flames is almost identical at (~0.42). This location is identified as the transition from the recirculation zone to the jet-like region.

In the jet region, the minimum of the intermittency profile, which corresponds to the maximum axial soot volume fraction on the centreline, is found to be at $x/L_f =$ 0.48 for MB-1 flame and at x/L_f = 0.59-0.63 for MB-2 and MB-3 flames. The locations of maximum soot, which are related to the minimum intermittency in the MB-1 and MB-2 flames, are similar to simple jet flames ($0.4 < x/L_f < 0.55$) [20]. In MB-3, although similar to the other two flames, the minimum intermittency is shifted downstream and found at $x/L_f \approx 0.62$. Noteworthy, is that the difference shown earlier in the appearance and behaviour of soot in MB-2 flame, compared with MB-1 and MB-3 flames, can be explained by the intermittency in the neck zone. It is clear that more soot (and its precursors) is transported through the neck zone in MB-2 flame than the other two flames, leading to a higher amount of soot in the jet-like region.

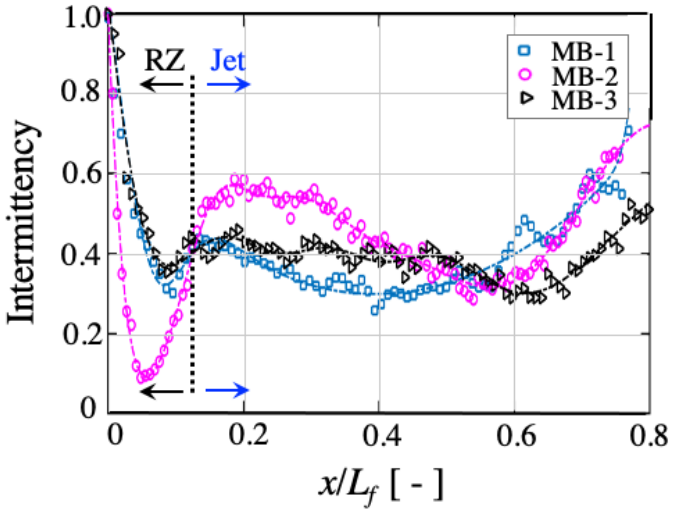

Figure 6.10: Axial Profile of soot intermittency along the burner axis. The black arrow specifies the recirculation zone (RZ), and the blue arrows show the jet-like region.

6.6.5 Calculated mixture fraction and temperature

In order to better interpret the differences in soot concentration measured in the three flames, the mixture fraction together with the temperature profile is estimated numerically and presented in Fig. 6.11. The flame temperature and mixture fraction are reported at axial heights of $x/D_{BB} = (0.6, 0.9, 1.2)$, as presented in Fig. 6.11. It is noted that soot and its impact on thermal radiation from the flame is not computed in this study. The objective is to better understand the differences in flame structure and temperature, rather than to 'predict' soot. The mixture fraction profiles exhibit similar features for the MB-1 and MB-3 flames. That is, a rich mixture is found at almost all locations $r/D_{BB} < 0.42$ and axial height of $x/D_{BB} = 0.6$. However, for MB-2 flame, the mixture fraction profile crosses the stoichiometric value at $r/D_{BB} = 0.24$ at all heights, suggesting a leaner outer vortex, and a shift of the mean stoichiometric mixture to a distinct location closer to the centreline. The calculated peak mean temperature for the MB-2 flames at the axial height of $x/D_{BB} = 0.6$ is found at $r/D_{BB} \sim 0.19$, within the ISL, at around 1600 K, which is almost 14% lower than those found in the MB-1 and MB-3 flames. The radial location at which the mean temperature peaks are found in MB-1 and MB-3 flames is $r/D_{BB} \sim 0.38$, within the *OSL*, and the computed values are found to be 1880 K and 1870 K, respectively. A similar trend was observed for the calculated OH profile. That is, the OH peak is found at $r/D_{BB} \sim 0.2$ for MB-2 flame, while the peak is shifted toward the *OSL* at $r/D_{BB} \sim 0.39$ for the MB-1 and MB-3 flames. The lower concentration of OH in MB-2 flames is consistent with a lower temperature peak in this flame. Furthermore, a sharp decline is seen in the OH profiles for MB-1 and MB-3, which shows the high rate of oxidation. Notable too is that the calculated OH concentration in MB-1 and MB-3 flames is almost 40% greater than that of MB-2. Although we do not expect that a simplified DRM-22 mechanism may be enough to accurately predict the intermediate species, such as acetylene, it provides trends in the anticipated C_2H_2 concentration in all three cases. In MB-2 flame, the peak of calculated acetylene is almost 40% lower than those of MB-1 and MB-3 flames which again is expected to lead to lower soot, instead of the observed higher soot in MB-2. Based on these observations, it is clear that in MB-2 soot is formed and circulated within the inner vortex and then transported further downstream through the neck zone to the jet-like zone. While in MB-1 and MB-3 the soot is formed in the outer vortex where it has a higher chance to be oxidised and not reach the central jet and the neck zone. The trend found in section 3.3.3, where higher soot in the recirculation zone is recorded in MB-2, while is inconsistent with the lower temperature, and lower

C_2H_2 found there, is consistent with the lower oxidation rate expected in the rich inner vortex. Worth noting is that the photographs of the flames, presented in Figure 6.2, while showing faint soot in the recirculation zone of MB-1 and MB-3 flames, are long term exposure images and the blue colour from regions of the flame does not necessarily imply the absence of soot.

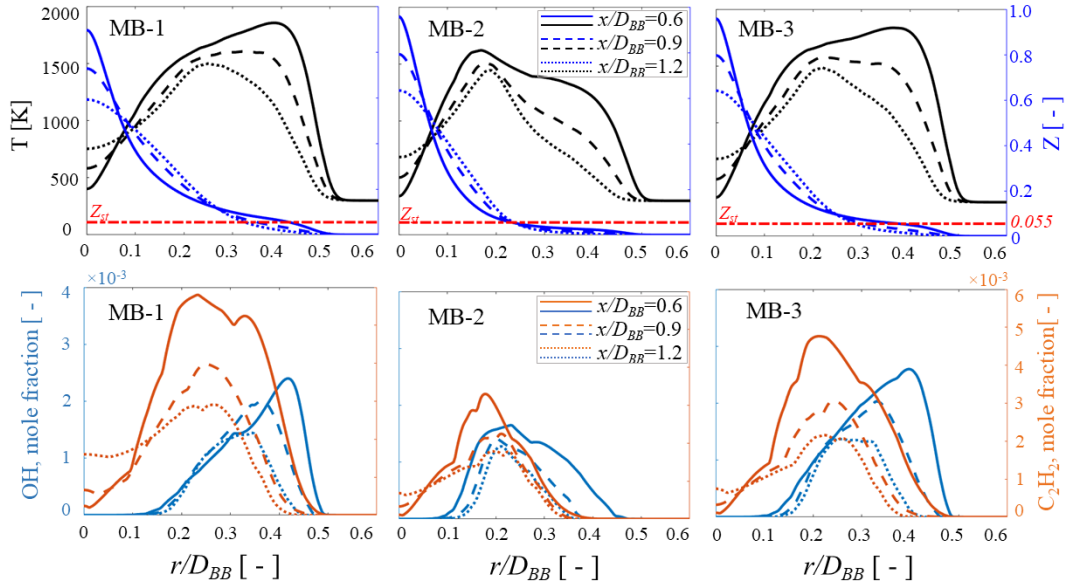

Figure 6.11: Calculated mean radial profile of temperature and mixture fraction (top row) together with the OH and acetylene mole fraction (bottom row) for the three flames and at three axial locations.

6.6.6 Relations between instantaneous soot and strain rate

Fig. 6.12 presents a typical instantaneous P-LII soot sheet from a methane flame (MB-3) on the *RHS* and another from the ethylene/nitrogen flame (ENB-3) on the *LHS*. As noted earlier, these two flames run under identical operating conditions. Although the flowfield behaves similarly for both fuels, the distribution of soot is different. In the ENB-3 flame, soot filaments are chaotic and found almost in the entire recirculation zone length, whilst in the MB-1 flame, the soot filaments are more concentrated in the outer shear layer close to the outer flame edge and rarely in the inner vortex. The maximum instantaneous soot in methane is almost one order of magnitude lower than the ethylene/nitrogen (ENB-3) flame. Given that the mixing is similar for the two flames, it is evident that differences in fuel composition and subsequent reaction chemistry is dominant and appears to impact the formation and growth of soot particulates.

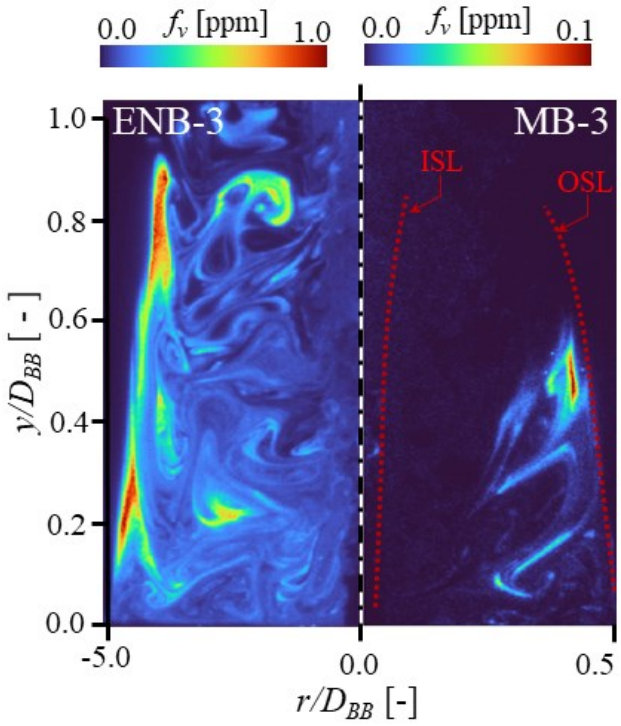

Figure 6.12: Comparison of a typical instantaneous soot filament of the (LHS) ENB-3 [30] and (RHS) MB-3 flame. Note that the colour bars scale differently for two flames. Dotted lines indicated the inner (*ISL*) and outer (*OSL*) shear layers.

Figure 6.13 presents a typical instantaneous radial profile of *SVF* and strain rate at one axial height above the burner ($x/D_{BB} = 0.6$) for the three flames. The *SVF* and strain rate are shown in orange and blue colours, respectively.

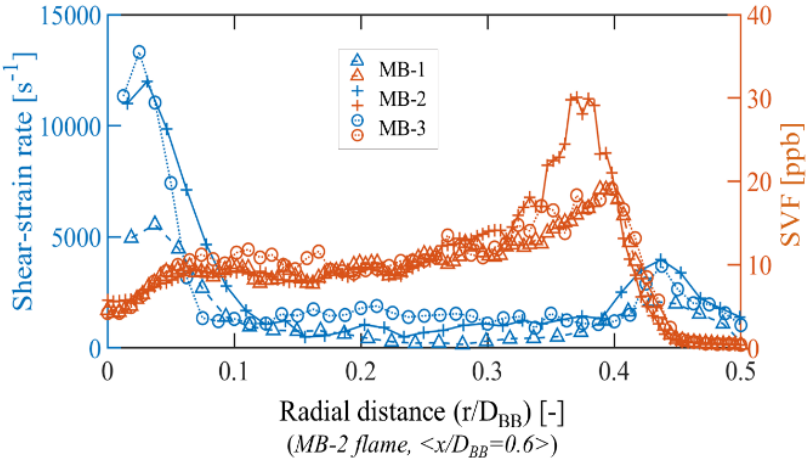

Figure 6.13: Profiles of instantaneous *SVF* and *S* at the axial height of $x/D_{BB} = 0.6$ above the burner for the MB-2 flame.

It is clear from this figure that the local instantaneous *SVF* and *S* peak at the inner and outer locations while shows a plateau distribution in the middle of the profiles. A noticeable amount of soot is found in the low strain region (S <5000 s^{-1}) with a soot concentration of 10 ppb. In contrast, in MB-3 flame, a peak of ≈ 30 ppb is observed at r/D_{BB} = 0.38 at the same strain rate compared to the other two flames. The lack of direct correlation between the instantaneous soot volume fraction and instantaneous strain provides further evidence of the impact of transport in the recirculation zone.

6.6.7 Soot statistics

The probability density functions (PDFs) of *SVF* have been calculated in the recirculation zone of the three flames. The axial and radial positions at which the PDFs have been calculated are shown in Fig. 6.14. The PDFs were calculated from arrays of 5 × 5 pixels^2 (0.17 mm^2) from 1500 instantaneous image pairs. The data used are from two axial heights above the burner within the recirculation zone (x/D_{BB}=0.6, 1.0) and at three radial positions, two of which are on the high-strain inner and outer shear layers (*ISL* and *OSL*), and the third one is in the core of the recirculation zone between the *ISL* and the *OSL*.

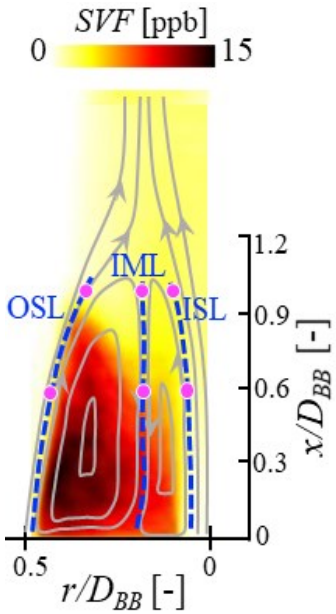

Figure 6.14: Image of the time-averaged soot volume fraction, presented as a coloured-scale, overlaid with the selected locations (magenta dots) at which the statistics for *SVF* have been calculated for the *MB-2* flame adopted from earlier work [29].

Figure 6.15 presents the PDFs of the SVF at $x/D_{BB} = 0.6$ and $x/D_{BB} = 1.0$. The shapes of the PDFs indicate different soot concentrations for the three flames. The width of the pdfs for the MB-2 flames is significantly broader than the other two flames, which is deduced to be the oxidation effects, while only a peak following a sharp decrease is seen in MB-1 and MB-3 flames. While the probability of finding soot in the MB-1 is the least, increasing the Reynolds to 15,000 (MB-2) increases the maximum probable soot to 7 ppb. For the MB-2 flame, no events higher than 25 ppb are found.

In contrast, in MB-1 and MB-3 flames, the maximum probable soot is reduced by a factor of more than two, to less than 10 ppb. This is consistent with the total soot calculated for the recirculation zone of each flame in Fig.6.15. It is also deduced that the effect of soot oxidation is significant at lower momentum flux ratio. Noting that the MB-2 flame has the higher momentum flux ratio amongst the three flames, it can be deduced that the lower momentum flux ratio correlates with higher soot oxidation and less probability of having soot in a specific region. Comparing the soot PDFs in methane with the ethylene flame (not shown) operating on the same burner and initial conditions (ENB-3) [30] indicate that the soot distribution in the ISL for ethylene flame is similar to the methane (MB-3); except that the core of the recirculation zone has a wide range of soot extending up to 200 ppb. However, in methane flames, maximum instantaneous soot is found to be less than 10 ppb.

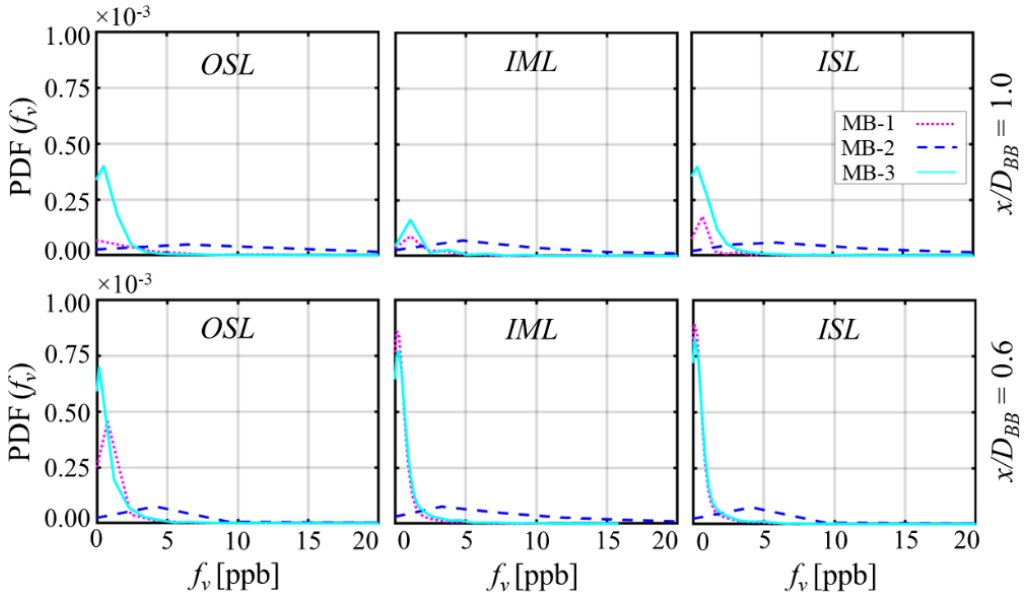

Figure 6.15: Axial distribution of probability density functions (PDFs) of soot volume fraction within the recirculation zone at a series of radial locations and at two axial locations above the burner $x/D_{BB} = 0.6$ (bottom row) and $x/D_{BB} = 1.0$ (top row).

6.7 Conclusion

A joint experimental and computational work was performed to investigate the soot formation and oxidation in a series of turbulent non-premixed bluff-body flames burning pure methane. Simultaneous planar laser-induced incandescence (P-LII) and 2D polarised particle image velocimetry (P-PIV) techniques have been employed to measure soot and flowfield features, respectively. Three flames stabilised on the 4.1 mm fuel jet and 64 mm bluff body diameters burner using a combination of the jet Reynolds number, 8,000 and 15,000, and co-flowing air velocity, 14 m/s and 20 m/s are presented in this paper.

Although all flames exhibit similar features, namely two vortices within the recirculation zone, a significant increase is observed in the mean SVF and the soot intermittency profiles for the MB-2 flame. The difference mainly arises from the mixture fraction distribution resulting in a mean stoichiometric mixture in the inner vortex, closer to the jet, in MB-2, while for the MB-1 and MB-3 flames a broader distribution of the mixture fraction is found in the outer vortex. This difference results in less soot concentration in the MB-1 and MB-3 flames as compared with MB-2. Also, the leaner mixture fraction in the inner recirculation zone for the MB-1 and MB-3 flames results in less soot being formed and a higher probability of it being oxidised in the neck zone.

The total integrated soot exhibited two maxima in the recirculation zone of the MB-2 flame versus one peak in the other two flames. This difference could be attributed to the mean mixture fraction in the recirculation zone of MB-2 flame, which is relatively higher than those in MB-1 and MB-3 flames considering the similar mean residence time within this region. All soot events were found to be in the range of 1 ppb $< SVF <$ 6 ppb in the MB-1 and MB-3 flame, while a uniform SVF distribution is observed for the MB-2 flame with the maximum number of events found in the range 1 ppb $< SVF <$ 25 ppb. It is observed that although the maximum local instantaneous soot is around 25 ppb, the time-averaged soot is less than 10 ppb which could be related to the high soot intermittency and turbulence fluctuations. The high intermittency is evident in the local instantaneous soot sheets. The soot and flowfield data presented in this work is expected to be useful for further model validations and development.

Acknowledgement

The first author would like to thank the Australian government for scholarship funding through the Research Training Program Scholarship (RTPS). We gratefully acknowledge the support of the Australian Research Council (ARC) for the project funding.

6.8 References

[1] M. J. Castaldi, N. M. Marinov, C. F. Melius, J. Huang, S. M. Senkan, W. J. Pitz, and C. K. Westbrook, "Experimental and modeling investigation of aromatic and polycyclic aromatic hydrocarbon formation in a premixed ethylene flame", Proceedings of the Combustion Institute, vol. 26, pp. 693-702, 1996.

[2] M. D. Smooke, R. J. Hall, M. B. Colket, J. Fielding, M. B. Long, C. S. McEnally , and L. D. Pfefferle, "Investigation of the transition from lightly sooting towards heavily sooting co-flow ethylene diffusion flames", Combustion Theory and Modeling, vol. 8, pp. 593-606, 2004.

[3] H. A. Michelson, M. B. Colket, P. -E. Bengtsson, A. D'Anna, P. Desgroux, B. S. Haynes, J. H. Miller, G. J. Nathan, H. Pitsch, and H. Wang, "A Review of Terminology Used to Describe Soot Formation and Evolution under Combustion and Pyrolytic Conditions", ACS Nano , vol. 14, pp. 12470-12490, 2020.

[4] J. Kopyscinski, T. J. Schildhauer, and S. M. A. Boillaz, "Production of synthetic natural gas (SNG) from coal and dry biomass – A technology review from 1950 to 2009", Fuel, vol. 89, pp. 1763-1783, 2010.

[5] H. F. Calcote and D.M. Manos, "Effect of Molecular Structure on Incipient Soot Formation", Combustion and Flame, vol. 49 pp. 289-304, 1983.

[6] K. P. Schug, Y. Manheimer-Timnat, P. Yaccarino , and I. Glassman, "Sooting Behavior of Gaseous Hydrocarbon Diffusion Flames and the Influence of Additives", Combustion Science and Technology, vol. 22, pp. 235-250, 1980.

[7] A. Cuoci, A. Frassoldati, T. Faravelli, and E. Ranzi, "Formation of soot and nitrogen oxides in unsteady counterflow diffusion flames", Combustion and Flame, vol. 156, pp. 2010-2022, 2009.

[8] A. Cuoci, A. Frassoldati, T. Faravelli, and E. Ranzi, "Soot formation in unsteady counterflow diffusion flames", Proceedings of the Combustion Institute, vol. 32, pp. 1335-1342, 2009.

[9] V. Chernov, M. J. Thomson, S. B. Dworkin, N. A. Slavinskaya, and U. Riedel, "Soot formation with C1 and C2 fuels using an improved chemical mechanism for PAH growth", Combustion and Flame, vol. 161, pp. 592-601, 2014.

[10] S. Liu, T. L. Chan, Z. He, Y. Lu, X. Jiang, and F. Wei, "Soot formation and evolution characteristics in premixed methane/ethylene-oxygen-argon burner-stabilised stagnation flames", Fuel, vol. 242, pp. 871-882, 2019.

[11] Ö.L. Gülder, G. Intasopa, H. I. Joo, P. M. Mandatori, D.S . Bento, and M. E. Vaillancourt, "Unified behaviour of maximum soot yields of methane, ethane and

propane laminar diffusion flames at high pressures", Combustion and Flame, vol. 158, pp. 2037-2044, 2011.

[12] C. R. Christopher and T.C. Williams, "The effect of oxygen enrichment on soot formation and thermal radiation in turbulent, non-premixed methane flames", Proceedings of the Combustion Institute, vol. 36, pp. 4051-4059, 2017.

[13] C. R. Shaddix, J. Zhang, and T. C. Williams, "Soot Concentration, Temperature, and Radiant Emission Measurements in a Turbulent Ethylene Jet Flame", presented at the 11th USS National Combustion Meeting, Pasadana, California, 2019.

[14] P. Desgroux, A. Faccinetto, X. Mercier, T. Mouton, D. A. Karkar, and A. E. Bakali, "Comparative study of the soot formation process in a "nucleation" and a "sooting" low pressure premixed methane flame", Combustion and Flame, vol. 184, pp. 153-166, 2017.

[15] Y. Wang and S. H. Chung, "Soot formation in laminar counterflow flames", Progress in Energy and Combustion Science, vol. 74, pp. 152-238, 2019.

[16] Y. Wang, M. Gu, J. Wu, L. Cao, Y. Lin, and X. Huang, "Formation of soot particles in methane and ethylene combustion: A reactive molecular dynamics study", International Journal of Hydrogen Energy (2021), https://doi.org/10.1016/j.ijhydene.2021.08.125.

[17] N. H. Qamar, G. J. Nathan, Z. T. Alwahabi, and K. D. King, "The effect of global mixing on soot volume fraction: measurements in simple jet, precessing jet, and bluff body flames", Proceedings of the Combustion Institute, vol. 30, pp. 1493-1500, 2005.

[18] N. H. Qamar, Z. T. Alwahabi, Q. N. Chan, G. J. Nathan, D. Roekaerts, and K. D. King, "Soot volume fraction in a piloted turbulent jet non-premixed flame of natural gas", Combustion and Flame, vol. 156, pp. 1339-1347, 2009.

[19] S. M. Mahmoud, G. J. Nathan, Z. T. Alwahabi, Z. W. Sun, P. R. Medwell, and B. B. Dally, "The effect of exit Reynolds number on soot volume fraction in turbulent non-premixed jet flames", Combustion and Flame, vol. 187, pp. 42-51, 2018.

[20] S. M. Mahmoud, G. J. Nathan, Z. T. Alwahabi, Z. W. Sun, P. R. Medwell, and B. B. Dally, "The effect of exit strain rate on soot volume fraction in turbulent non-premixed jet flames", Proceedings of the Combustion Institute, vol. 36, pp. 889-897, 2017.

[21] S. M. Mahmoud, G. J. Nathan, P. R. Medwell, B. B. Dally, and Z. T. Alwahabi, "Simultaneous planar measurements of temperature and soot volume fraction in a turbulent non-premixed jet flame", Proceedings of the Combustion Institute, vol. 35, pp. 1931-1938, 2015.

[22] M. Köhler, K. -P. Geigle, T. Blacha, P. Gerlinger, and W. Meier, "Experimental characterisation and numerical simulation of a sooting lifted turbulent jet diffusion flame", Combustion and Flame, vol. 159, pp. 2620-2635, 2012.

[23] M. Köhler, I. Boxx, K. -P. Geigle, and W. Meier, "Simultaneous planar measurements of soot structure and velocity fields in a turbulent lifted jet flame at 3 kHz", Applied Physics B, vol. 103, pp. 271-279, 2011.

[24] M. Köhler, K. P. Geigle, W. Meier, B. M. Crosland, K. A. Thomson, and G. J. Smallwood, "Sooting turbulent jet flame: characterisation and quantitative soot measurements", Applied Physics B, vol. 104, pp. 409-425, 2011.

[25] M. E. Mueller, Q. N. Chan, N. H. Qamar, B. B. Dally, H. Pitsch, and Z. T. Alwahabi, "Experimental and computational study of soot evolution in a turbulent nonpremixed bluff body ethylene flame", Combustion and Flame, vol. 160, pp. 1298-1309, 2013.

[26] S. Deng, M. E. Mueller, Q. N. Chan, N. H. Qamar, B. B. Dally, and Z. T. Alwahabi, "Hydrodynamic and chemical effects of hydrogen addition on soot evolution in turbulent nonpremixed bluff body ethylene flames", Proceedings of the Combustion Institute, vol. 36, pp. 807-814, 2013.

[27] K. -P. Geigle, M. Köhler, W. O'Loughlin, and W. Meier, "Investigation of soot formation in pressurised swirl flames by laser measurements of temperature, flame structures and soot concentrations", Proceedings of the Combustion Institute, vol. 35, pp. 3373-3380, 2015.

[28] S. Chatterjee and Ö.L. Gülder, Soot concentration and primary particle size in swirl-stabilised non-premixed turbulent flames of ethylene and air, Experimental Thermal and Fluid Science, vol. 95, pp. 73-80, 2009.

[29] L. -Y. Wang, C. K. Bauer, and Ö. L. Gülder, "Soot and flow field in turbulent swirl-stabilised spray flames of Jet A-1 in a model combustor', Proceedings of the Combustion Institute, vol. 37, pp. 5437-5444, 2019.

[30] A. Rowhani, Z. W. Sun, P. R. Medwell, G. J. Nathan, and B. B. Dally, "Soot-flowfield interactions in turbulent non-premixed bluff-body flames of ethylene/nitrogen", Proceedings of the Combustion Institute, vol. 38, pp. 1125-1132, 2021.

[31] A. Rowhani, Z. W. Sun, P. R. Medwell, Z. T. Alwahabi, G. J. Nathan, and B. B. Dally, "Effects of the bluff-body diameter on the flow field characteristics of non-premixed turbulent highly-sooting flames", Combustion Science and Technology, vol. 194, no.2, pp. 378-396, 2022.

[32] C. Schulz, B. F. Kock, M. Hofmann, H. Michelsen, S. Will, B. Bougie, R. Suntz, and G. Smallwood, "Laser-induced incandescence: recent trends and current questions", Applied Physics B, vol. 83, pp. 336-354, 2006.

[33] International Sooting Flame (ISF) Workshop (2021). http://www.adelaide.edu.au/cet/isfworkshop/ (accessed 23 July 2016).

[34] Z. W. Sun, Z. T. Alwahabi, D.H. Gu, S. M. Mahmoud, G. J. Nathan, and B. B. Dally, "Planar laser-induced incandescence of turbulent sooting flames: the influence of beam steering and signal trapping", Applied Physics B, vol. 119, pp. 731-743, 2015.

[35] S. Kruse, P. R. Medwell, J. Beeckmann, and H. Pitsch, "The significance of beam steering on laser-induced incandescence measurements in laminar counterflow flames", Applied Physics B, vol. 124, pp. 212, 2018.

[36] A. Rowhani, A. Chennici, M. J. Evans, P. R. Medwell, G. J. Nathan, and B. B. Dally, "Variation of residence time in non-premixed turbulent bluff-body ethylene flames as a function of burner diameter", 21st Australasian Fluid Mechanics Conference, Adelaide, Australia, 2018.

[37] W. Thielicke and E. J. Stamhuis, "PIVlab - Towards User-friendly, Affordable and accurate digital particle image velocimetry", Journal of Open Research Software, vol. 2 (2014).

[38] ANSYS® Fluent, Release 21.1.

[39] B. B. Dally and A. R. Masri, "Modelling of Bluff-body recirculating flows", 12st Australasian Fluid Mechanics Conference, Sydney, Australia, 1995.

[40] B. B. Dally, D. F. Fletcher, and A. R. Masri, "Flow and mixing fields of turbulent bluff-body jets and flames", Combustion Theory and Modelling, vol. 2, pp. 193-219, 1998.

[41] B. B. Dally, A. R. Masri, R. S. Barlow, and G. J. Fiechtner, "Instantaneous and Mean Compositional Structure of Bluff-Body Stabilized Nonpremixed flames", Combustion and Flame, vol. 114, pp. 119-148, 1998.

Chapter 7 Summary, Conclusions and Future Work

7.1 Summary and conclusions

The findings of the current research have improved our understanding of the effects of local and regional strain rate, and residence time on soot formation and oxidation in a series of non-premixed bluff-body flames in the turbulent regime. These findings were deduced through the investigation of flames stabilized on three bluff-body burners with a central fuel jet of 4.6 mm and an out bluff body diameter of 38, 50 and 64 mm. Each burner was mounted centrally in a contraction; 190 mm dimeter, where the conditioned coflow air was introduced at a velocity of 20 m/s. Two fuel mixtures; ethylene/nitrogen (80:20 by vol.) and pure methane, were used to investigate the soot evolution sensitivity to the fuel chemistry when burning under similar operating conditions, stabilized on the same bluff-body burners.

The first part of the research, which comprised a joint experimental and computational work, investigated the effect of the bluff-body diameter on the flowfield and residence time, in a series of non-premixed bluff-body flamed fuelled with ethylene/nitrogen, whilst every other aspect of the experiments was unchanged. Computationally, using steady RANS model, it was shown that increasing the bluff-body diameter from 38mm to 64mm substantially increased the mean residence time (by a factor of two to three) of the pseudo particles within the recirculation zone of the bluff-body flames. However, it was also shown that the diameter did not affect any other soot controlling parameter, including temperature and mixture fraction who exhibited similar profiles especially in the recirculation zone. These two features, change in residence time while all other parameter remain the same, help in isolating the effect of residence time. Noteworthy, is that the fuel and coflow velocities remained constant. In order to better understand the impact of flowfield features on the soot volume fraction in these flames, a novel optical arrangement was developed and employed in a conventional PIV system to enable a high fidelity PIV measurements in a highly sooting environment, particularly in the recirculation zone of the bluff-body flames. This modification included a half wave-plate in front of the incident beam to polarize the beam horizontally and a second linear polarizer attached to the 1 nm bandpass filter to capture vertically-polarized scattering signals. This optical arrangement substantially suppresses the scattering signals from soot to very low levels and only reduces scattering from relatively large PIV signals by a factor of approximately two. Having established a feasible PIV technique in flames with high soot loads, new measurements were conducted and analysed in these turbulent non-premixed bluff-body flames. Simultaneous measurements of soot

and flowfield features were also performed and correlation with strain rate was deduced and analysed.

The time-averaged soot volume fraction within the recirculation zone was found to increase from 160 ppb in ENB-1(D_{BB}=38mm) flame to 250 ppb in ENB-3 flame (D_{BB}=64 mm), which is attributed to the effect of increased residence time in the recirculation zone with increase of bluff body diameter. All measured flames exhibited low local strain rates in the recirculation zone, leading to higher soot concentrations that increased preferentially with burner diameter. A comparison of the mean SVF and strain rate for the three flames provided further evidence that soot is mostly formed in the inner vortex, in the low strain rate region, and is transported to the outer vortex where it peaks closer to the outer shear layer for all three cases. It was observed that in the recirculation zone, several small vortices roll upstream from the air side and help oxidise the soot within the outer vortex of the recirculation zone. Soot carried to the neck zone appears to originate in the inner vortex rather than in the neck zone, where the measured strain rate is found to be above 1000 s^{-1}, which is unfavourable for soot to form.

Further analysing the instantaneous correlations between the SVF and the strain rate throughout the flame revealed that the formation and growth of soot is primarily controlled by the residence time in these flames rather than the local strain rates. Given that the entire recirculation zone is a low-strain region (except for the shear layers where the strain rate exceeds 10,000 s^{-1}), it is deduced that the regional strain governed by the residence time is the soot controlling parameter than the local strain.

The joint statistics between the SVF and the strain rate were found to be not well-correlated. That is, the local instantaneous soot is poorly correlated to the inverse of the local strain rate in the jet propagation region and weakly correlated in the recirculation zone. A quantitative assessment of the correlation coefficient, R^2, is found to range from 0.33 to 0.68 in the RZ, and 0.29 to 0.37 at $r/R_{0.5}$ = 0, 0.5 and 0.9 in the jet region, which is consistent with our observation in the joint PDFs. This provided further evidence that soot is mostly affected by transport and history of strain rate, rather than the local strain. The statistical analyses also showed that the strain rate associated with the maximum SVF, which varies along the axial and radial directions, was found to be around 500 s^{-1} at the intermediate mixing layer (IML). Soot is not formed in the high-strain regions (inner and outer shear layers), so less soot is found in these radial locations. Further downstream, in the neck zone and the jet-propagation region, the range of strain rate that can be found is

significantly lower than the recirculation zone; 1000 s^{-1} is typical of the neck zone and 500 s^{-1} is common in the jet region. This finding has direct implication on the design of these flows and the realisation that soot can survive very high strain rate and some of it will be transported further downstream, even in highly diluted mixtures.

Flames with pure methane as the fuel were used to investigate soot formation, oxidation and transport under increased residence time condition in the turbulent regime, and to contrast the findings with the previously measured ethylene based flames. Three flames (MB-1, MB-2 and MB-3) with different operating conditions have been investigated. Flames MB-1 and MB-2 have a coflow velocity of 14.1 m/s and Reynolds numbers of 8000 and 15000, respectively. Flame MB-3 has a Reynolds number of 15000 and a coflow velocity of 20 m/s. The measured methane flames exhibited similar characteristics to the previously-studied ethylene/nitrogen bluff-body flames, however with one order of magnitude lower soot loading. Among the methane flames, substantial differences in the mean SVF and the soot intermittency profiles for the MB-2 flame was observed. The difference was mainly associated with the higher mean mixture fraction (calculated) in the recirculation zone comparing in MB-2 as compared to the MB-1 and MB-3 flames. The leaner mixture fraction in the MB-1 and MB-3 flames resulted in less soot concentration and higher oxidation rate. Furthermore, the total integrated soot showed two peaks in the profiles for the MB-2 flame; one in the RZ and the second one in the jet region. In contrast, only one maximum was found in the other two flames. Similar to the ethylene/nitrogen flames it was found that soot in methane fuelled flames in the high strain region (shear layers) and within the recirculation zone, is transported from the low-strain core region of the RZ. This reveals that although fuel chemistry has a primary effect on soot formation, the dynamics of the flow and transport in particular play a pivotal controlling role that affects soot inception, growth and oxidation in strongly circulation flow.

The experimental data for all flames are available on the International Sooting Flames Workshop website for use in model development and validation.

7.2 Recommendations for future work

Soot formation is a complex process and further interpretation of the soot controlling parameters requires the simultaneous measurements of the combination of parameters including SVF, flowfield features, temperature field, OH radicals, PAH, acetylene, and mixture fraction under conditions relevant to practical combustion conditions.

In this thesis, simultaneous measurements of SVF and velocity components, were conducted in order to shed more light on the formation, growth, oxidation and transport of soot particles in turbulent flames with recirculating regions, bluff-body flames. The following recommendations are made to further expand our knowledge in the context of soot formation in such flames:

- Understanding the effect of residence time on soot particles' size distribution will be of interest to the community and our understanding of soot growth and the mechanism that controls it. Therefore, soot particle size measurement is one the key future activity that can help understand the history of soot growth under increased residence time;
- It was shown that the formation and growth mechanism of soot particles in bluff-body flames are acetylene-based whereas in simple jet flames the PAH-growth is dominant. Hence, quantification of PAH and acetylene is quite beneficial to better understand the growth mechanism in bluff-body flames;
- The temperature is a key controlling parameter which is inter-correlated with soot formation and growth in flames. The simultaneous measurements of soot and temperature for these flames, where the residence time is systematically increased can develop our understanding of the correlations between soot and temperature fields under these operating conditions;
- Mixing and the mixture strength, especially in the recirculation zone, are other key parameters to understand soot formation in these flows. Knowledge of the instantaneous mixture fraction distribution and its correlation with soot can help interpret the soot evolution in bluff-body flames;
- Many practical combustion systems operate at elevated pressure higher than the atmosphere. Since in this research we only dealt with the atmospheric pressure, and due to the non-linear correlations between soot and pressure, soot measurement at high pressure is a stepping stage toward practical applications;

- Although we have examined two different fuel mixtures in this thesis in order to assess the soot sensitivity to fuel composition in the turbulent regime, more complex and practical fuels which are used in the technically-relevant conditions including n-heptane and DME (Dimethyl ether) are beneficial to be assessed under different operating conditions.

Appendix A: Supplementary material to Chapter 4

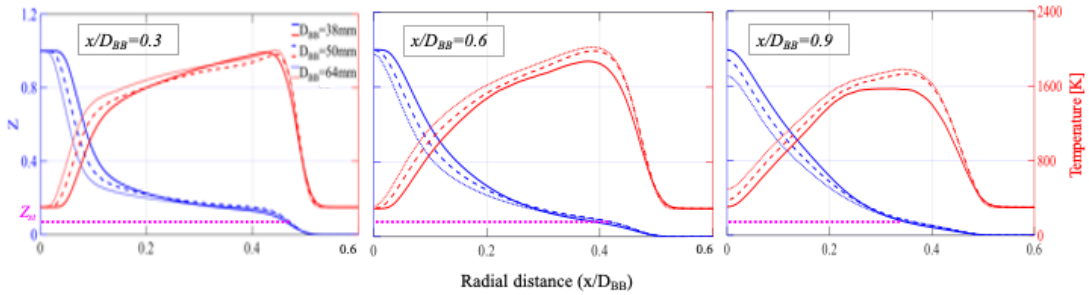

Figure A.S1: Calculated temperature together with the mixture fraction distribution at certain heights above the burner: x/D_{BB} = 0.3 (left), x/D_{BB} = 0.6 (middle), and x/D_{BB} = 0.9 (right) [19]. The magenta dashed line indicates the stoichiometric mixture fraction which is 0.078 for the used fuel mixture.

A.S2. The residence time calculation

A lagrangian particle tracking method was used to calculate the trajectory of the 1-nm pseudo-particles injected to the domain from the fuel jet inlet. The exit plane was selected at the end of the recirculation zone (RZ) where the axial velocity components are positive. The path was calculated by solving the following equation:

$$\frac{du}{dt} = F_D + \frac{(\rho_P - \rho_F)}{\rho_P} \times g$$

where u is the particle velocity, F_D is the drag force which is a function of velocity, p and f denoted for the particles and the fluid, respectively [19].

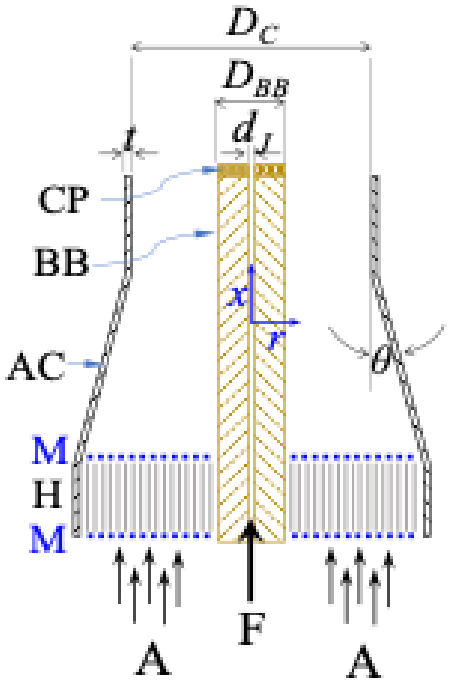

Figure A.S3: Detailed view of the bluff-body burner surrounded by the air contractor. (A – Co-flowing air from the wind tunnel; AC – Air contractor; BB – Bluff-body burner; CP – Heat resistant ceramic plate; D_{BB} – Bluff-body diameter (38, 50 and 64 mm); D_C – Inner diameter of the air contractor (190 mm); d_J – Fuel jet diameter (4.6 m); F– Fuel inlet; H – Honeycomb; M – Mesh screen; t – Thickness of the air contractor (5mm) and ϑ – Divergence angle of the contractor (14.7°)).

Appendix B: Supplementary material to Chapter 5

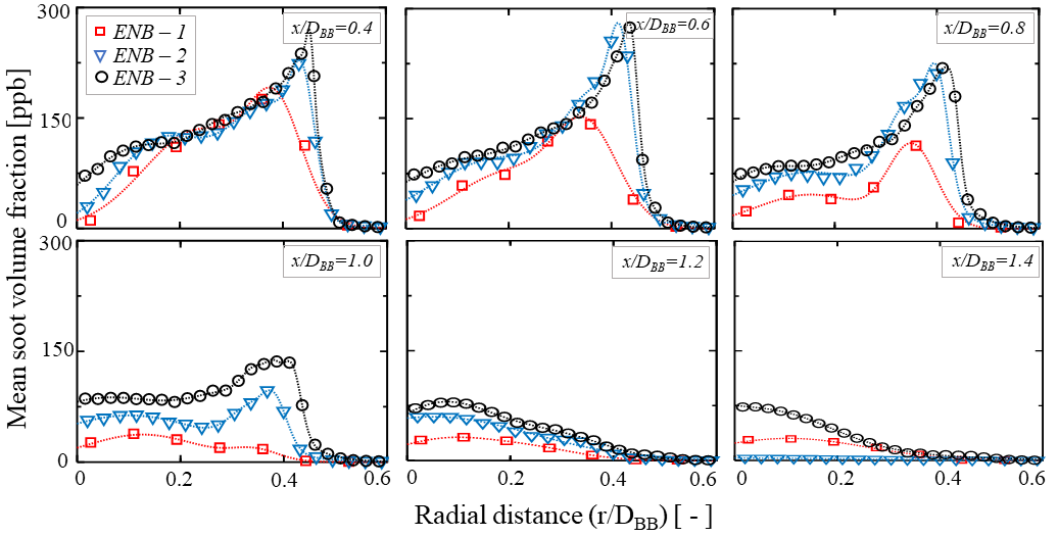

Figure B.S1: Radial profiles of the time-averaged soot volume fraction within the recirculation zone at different heights above the burner (x/D_{BB}). The symbols are experimental data while the lines indicate the best fits. Consistent with the entire paper, the blue, red, and black colours correspond to *ENB-1*, *ENB-2*, and *ENB-3* flames, respectively.

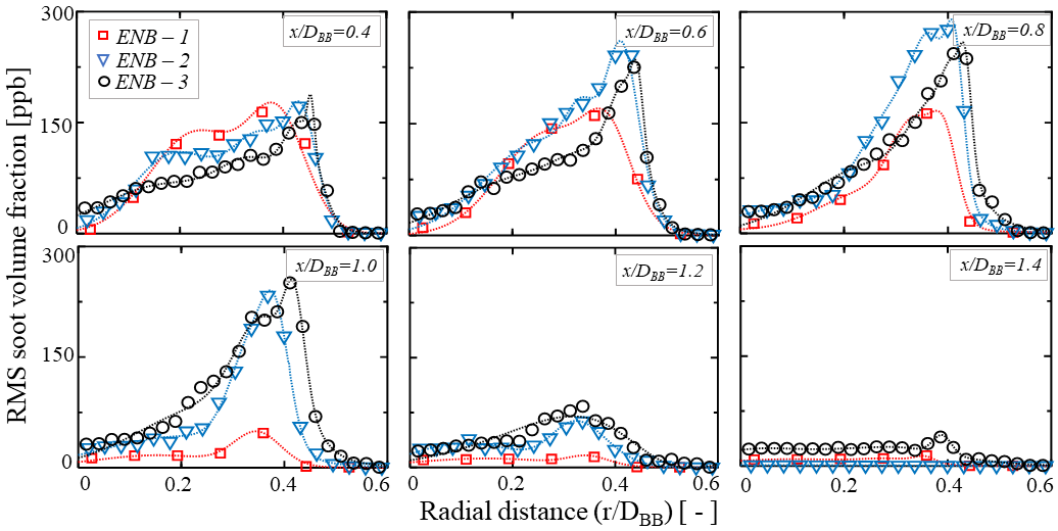

Figure B.S2: Radial profiles of the *RMS* soot volume fraction within the recirculation zone at different heights above the burner (x/D_{BB}). The symbols are experimental data while the lines indicate the best fits. Consistent with the entire paper, the blue, red, and black colours correspond to *ENB-1*, *ENB-2*, and *ENB-3* flames, respectively.

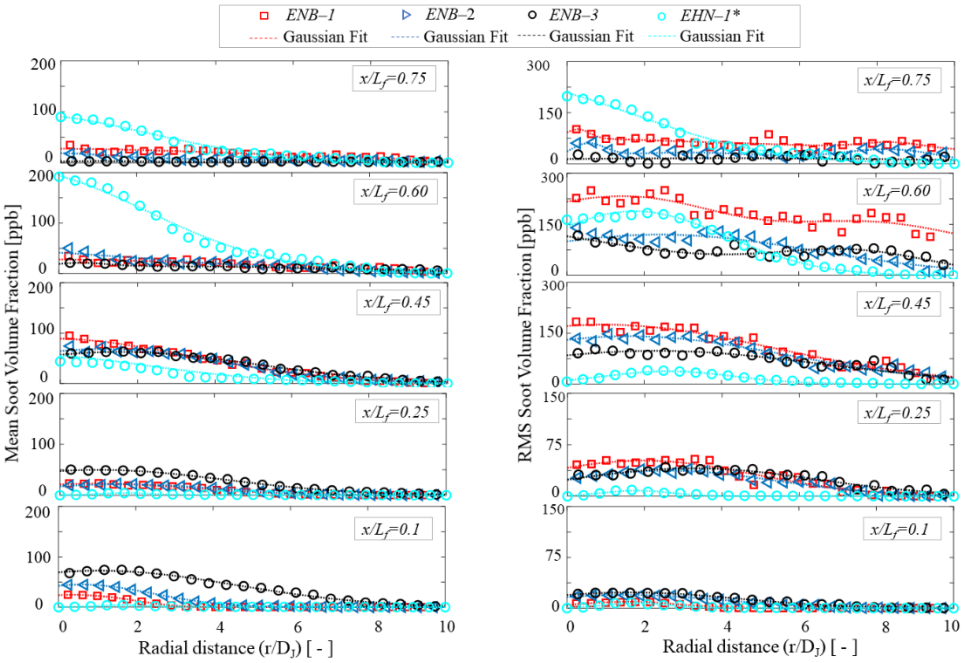

Figure B.S3: Radial profile of the time-averaged (left) and the *RMS* (right) of soot volume fraction at different heights in the downstream covering the neck and jet zones. The symbols represent experimental data whilst the dotted lines indicate the best Gaussian fits. *The *EHN-1* simple jet flame [21, 22] is shown with light blue in order to compare with *ENB* flame series.

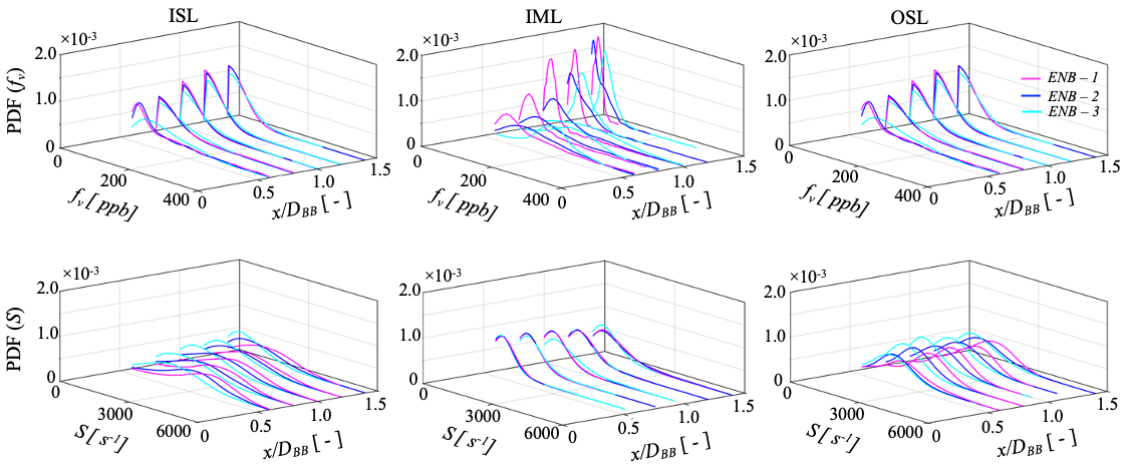

Figure B.S4: Axial distribution of probability density functions (PDFs) of soot volume fraction (top), and shear-strain rate (bottom) within the recirculation zone at radial locations at 0%, 50%, and 90% of the half-width of the flame (W). The solid blue, red, and black lines represent the pdfs for *ENB-1*, *ENB-2* and *ENB-3* flames corresponding to D_{BB} = 38mm, 50 mm, and 64 mm, respectively.

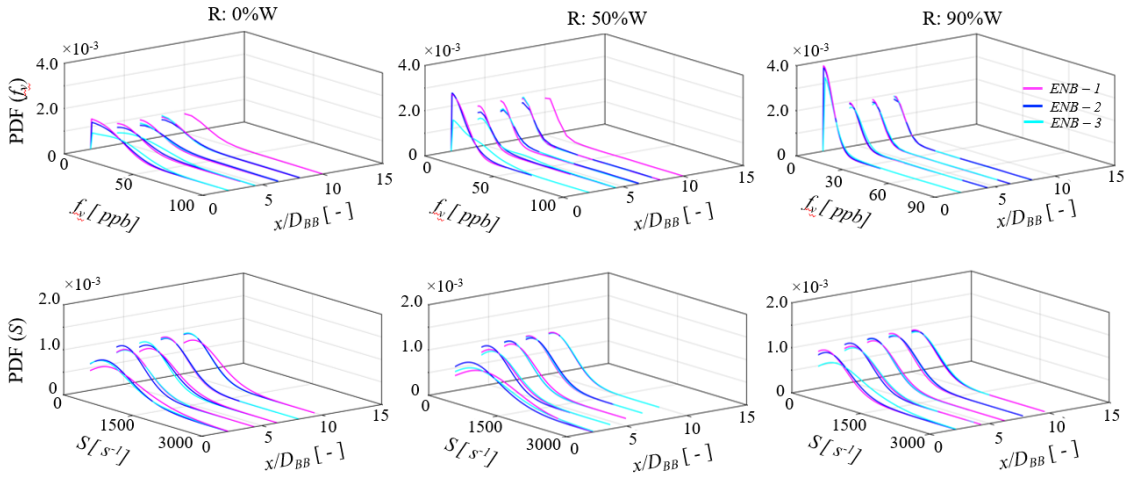

Figure B.S5: Probability density functions (PDFs) of soot volume fraction (top), and shear-strain rate (bottom) distributions in the jet zone at radial locations at 0%, 50%, and 90% of the half-width of the flame (W). The solid blue, red, and black lines represent the pdfs for *ENB-1*, *ENB-2* and *ENB-3* flames corresponding to D_{BB}=38 mm, 50 mm, and 64 mm, respectively.

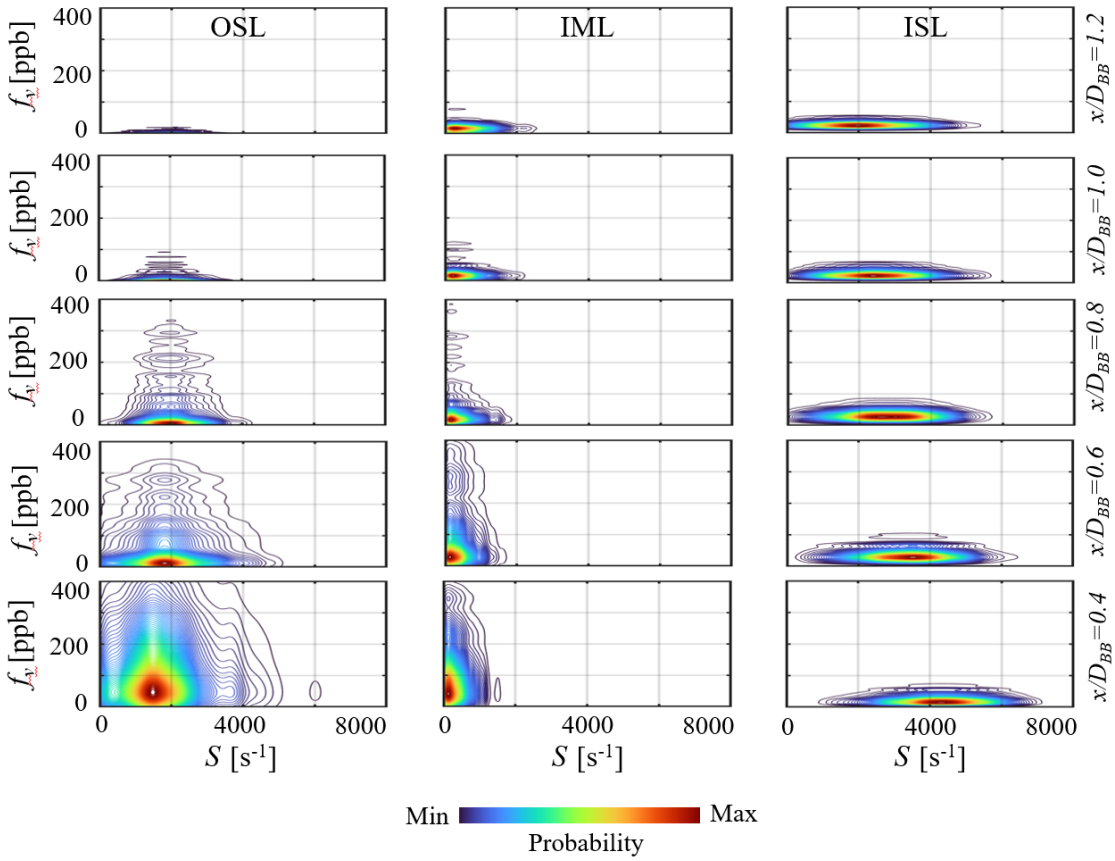

Figure B.S6: Joint histograms of event probability between *SVF* and strain rate (S) along with the different axial and radial locations in the recirculation zone for *ENB-1* flame (D_{BB}=38mm).

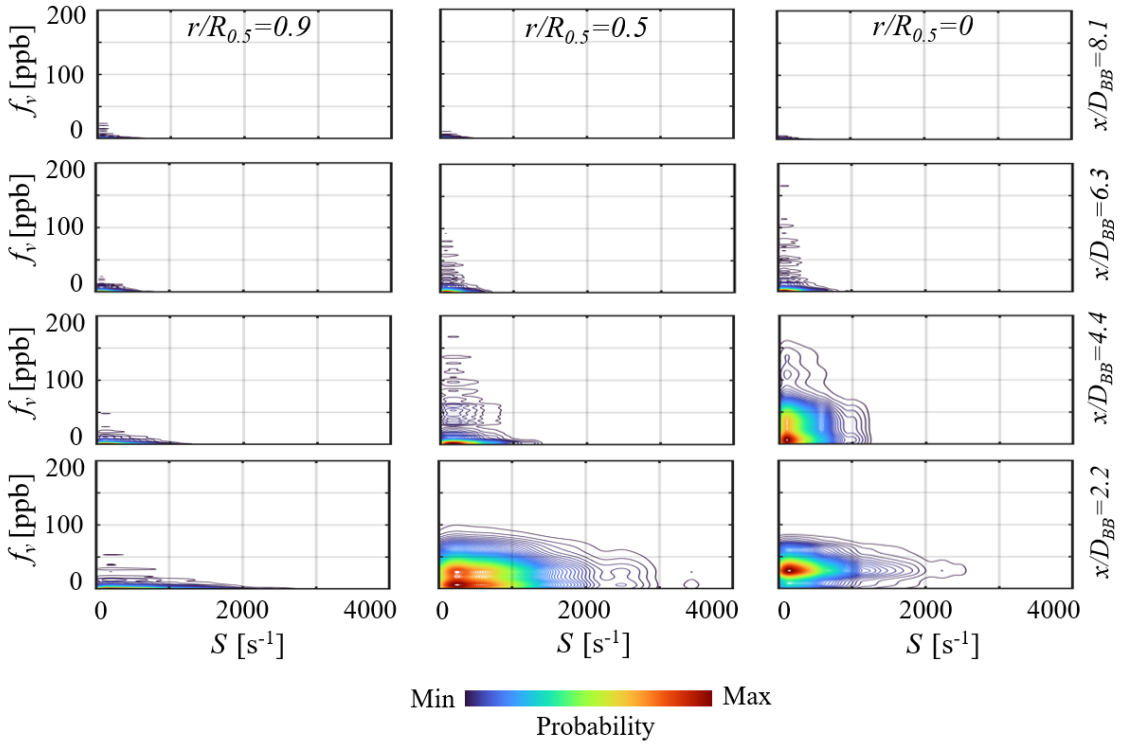

Figure B.S7: Joint histograms of event probability between *SVF* and strain rate along with the different axial and radial locations (0%, 50%, and 90% of the half-width of the flame, *W*) in the neck and jet zones for *ENB-1* flame (D_{BB}=38mm).

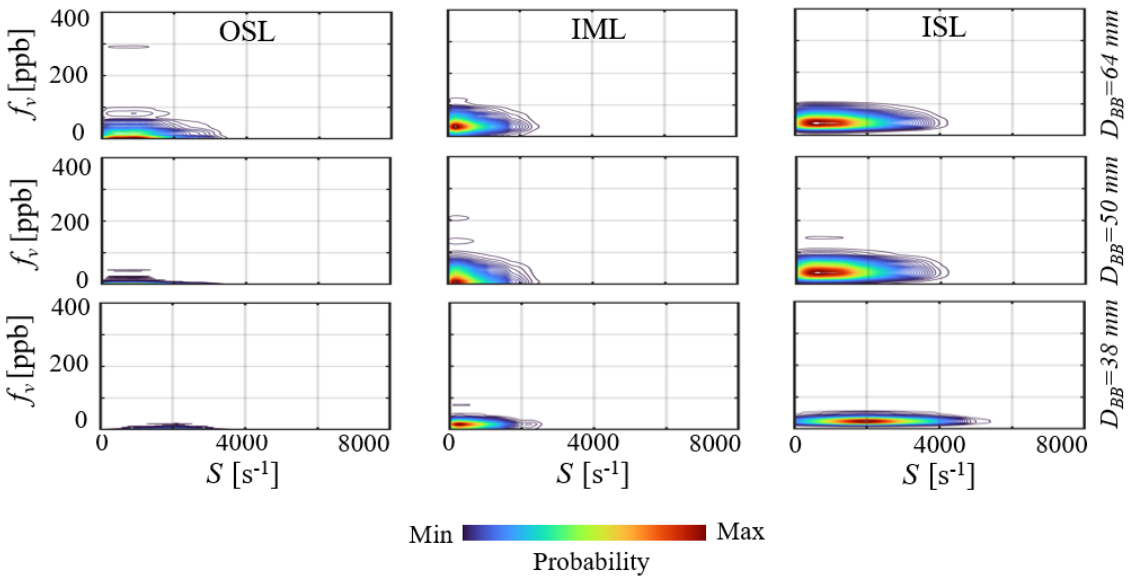

Figure B.S8: Joint histograms of event probability between *SVF* and strain rate depending on the bluff-body diameter along with the different radial locations at $x/D_{BB} = 1.2$ in the recirculation zones for three flames. Bottom row, *ENB*-1, middle, *ENB-2*, and the top row is the *ENB-3* flames.

Appendix C: Supplementary material to Chapter 6

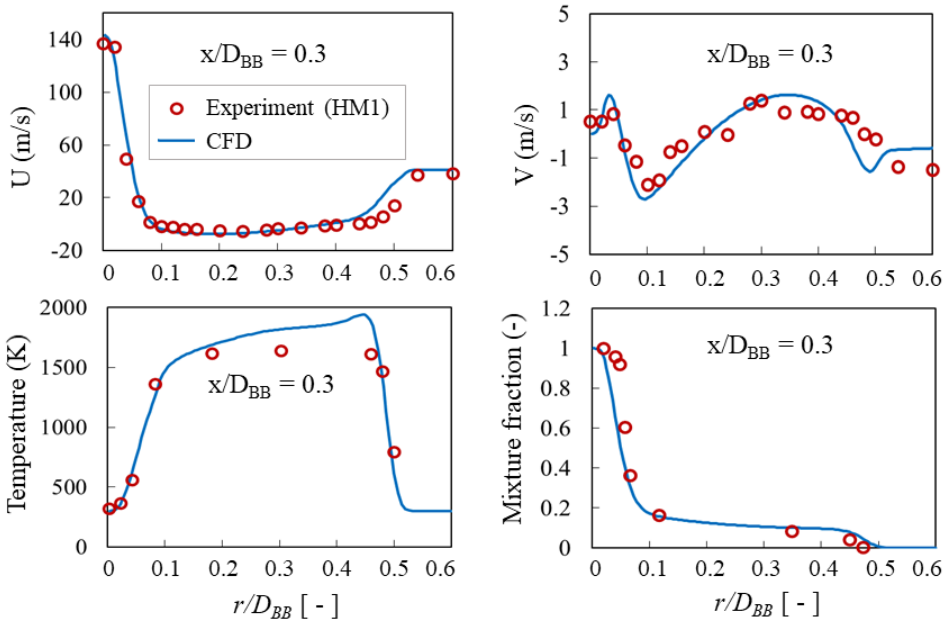

Fig. C.S1. Comparison of the axial (U) and radial velocity (V), mixture fraction and the temperature profiles of CFD results with the experimental data for a non-sooting bluff-body HM1 flame [41].

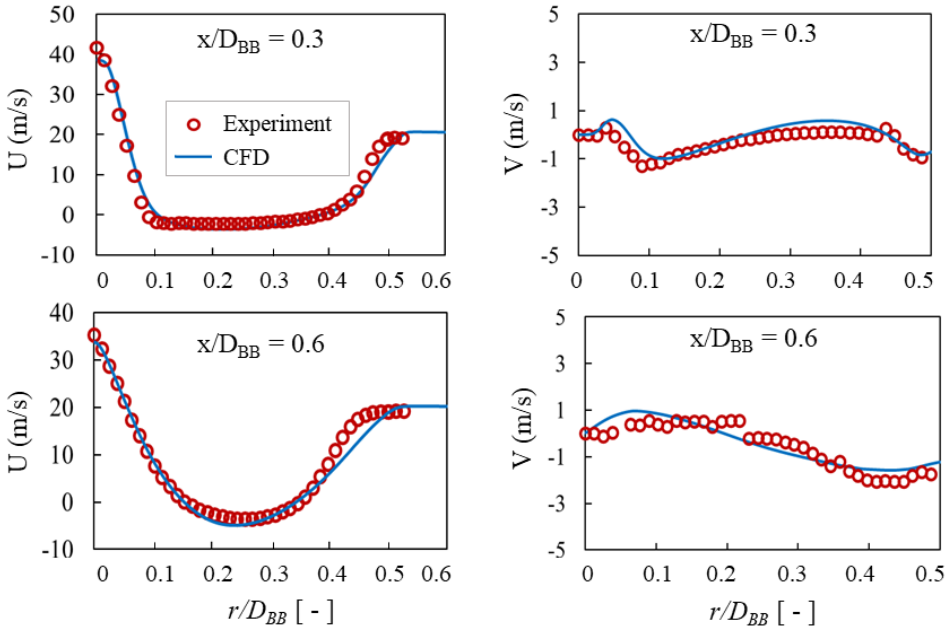

Fig. C.S2. Comparison of the axial (U) and radial velocity (V) profiles of CFD results with the experimental data for the sooting bluff-body MB-1 flame (measured in the current study).

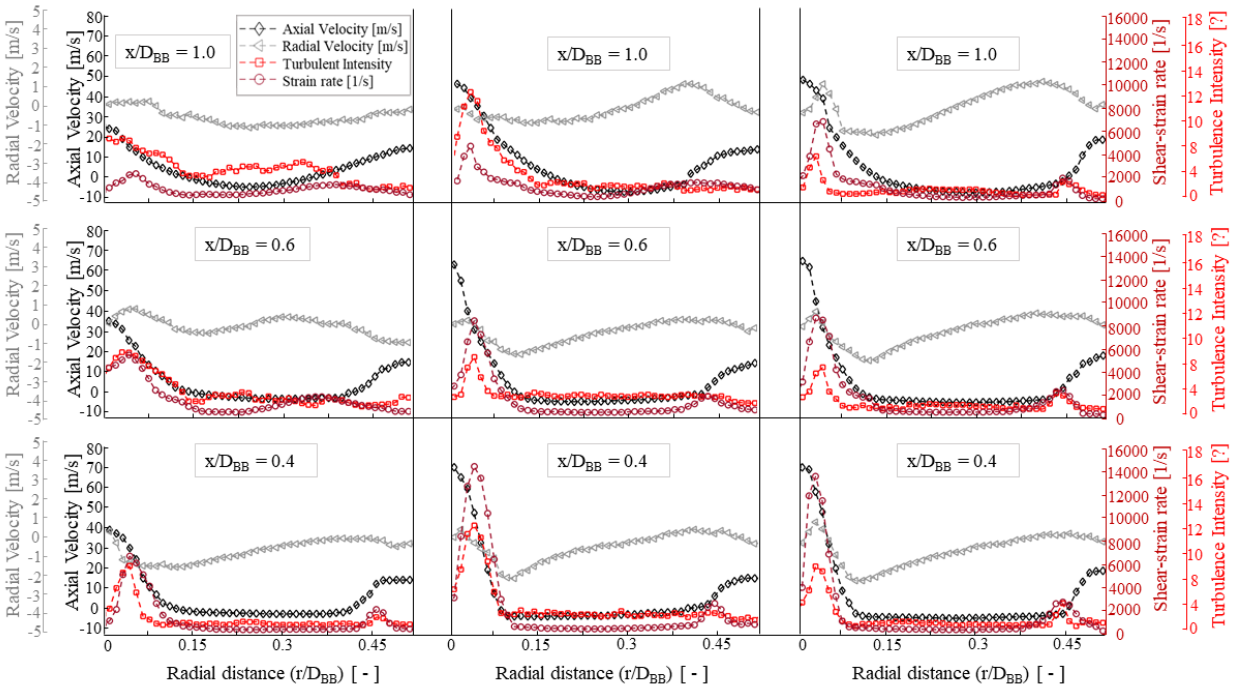

Fig. C.S3: Radial profile of axial velocity, radial velocity, turbulent intensity and the strain rate for the axial height of x/D_{BB}= 0.4 (bottom row), x/D_{BB}= 0.6 (middle row), and x/D_{BB}= 1.0 (top row) in the recirculation zone of the MB-1 (left), MB-2 (middle), and MB-3 (right) flames.

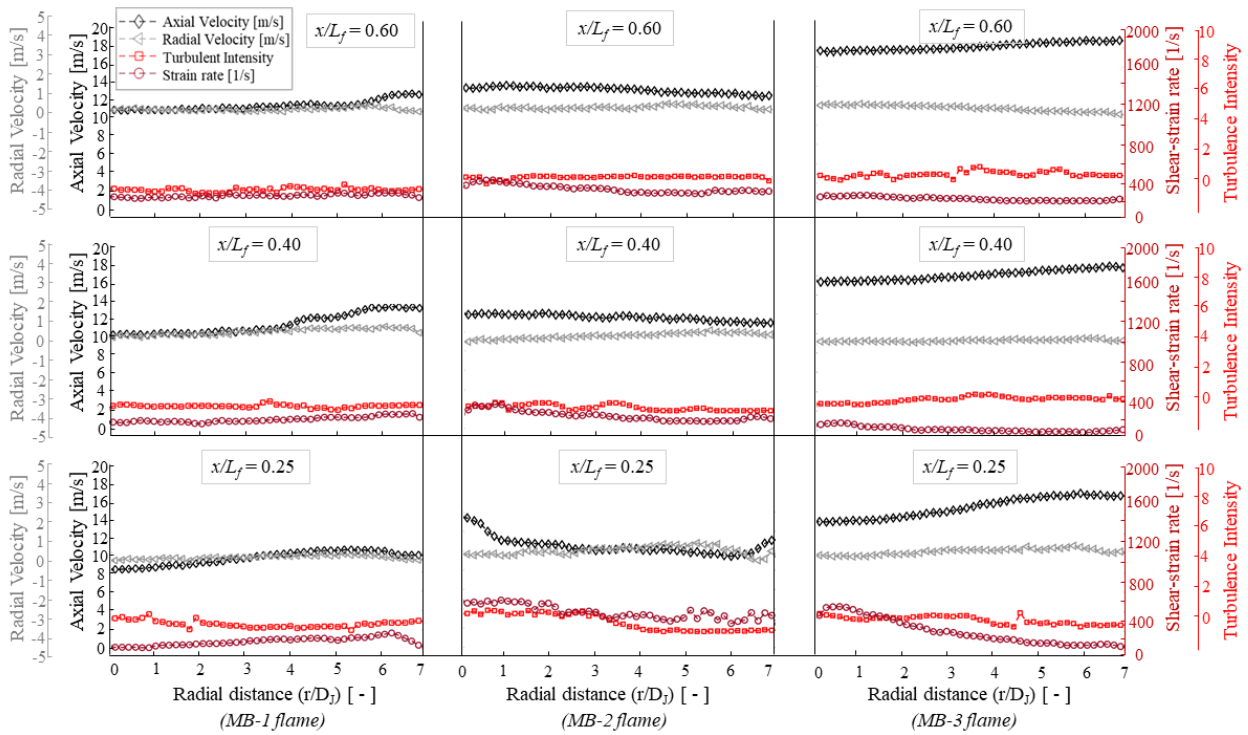

Fig. C.S4: Radial profile of axial velocity, radial velocity, turbulent intensity and the strain rate for the axial height of $x/L_f = 0.25$ (bottom row), $x/L_f = 0.4$ (middle row), and $x/L_f = 0.6$ (top row) in the jet zone of the MB-1 (left), MB-2 (middle), and MB-3 (right) flames.

Appendix D: Papers included in this thesis by publication

Journal papers

- Amir Rowhani, Zhiwei Sun, Paul. R. Medwell, Zeyad. T. Alwahabi, Graham. J. Nathan, Bassam. B. Dally, "Effects of the Bluff-Body Diameter on the Flow-Field Characteristics of Non-Premixed Turbulent Highly-Sooting Flames", Combustion Science and Technology, vol. 194 (2), 378-396, 2022.

- Amir Rowhani, Zhiwei Sun, Paul. R. Medwell, G. J. Nathan, Bassam. B. Dally, "Soot-flowfield interactions in turbulent non-premixed bluff-body flames of ethylene/nitrogen", Proceeding of the Combustion Institute, Vol. 38 (1), 2021, 1125-1132.

- Amir Rowhani, Zhiwei Sun, Paul. R. Medwell, G. J. Nathan, Bassam. B. Dally, "Differences between local and regional strain rate effects on soot evolution in turbulent non-premixed bluff-body flames". Under review.

- Amir Rowhani, Zhiwei Sun, Paul. R. Medwell, G. J. Nathan, Bassam. B. Dally, "Flow dynamics and soot evolution in turbulent methane flames stabilised on a bluff-body". Under review.

Appendix E: Publications associated with this thesis

Journal papers

- W. Zhang, X. Dong, C. Liu, Graham. J. Nathan, Bassam B. Dally, Amir Rowhani, Zhiwei Sun, "Generating planar distributions of soot particles from luminosity images in turbulent flames using deep learning", Applied physics B, Vol. 127 (2), 2021, 1-13.

Conference papers

- Amir Rowhani, Zhiwei Sun, Paul R. Medwell, Graham J. Nathan, Bassam B. Dally, "Experimental Investigation of Soot Evolution in Turbulent Non-premixed Bluff-body Ethylene/Nitrogen Flames", In Proceedings of the Australian Combustion Symposium, Adelaide, Australia. 4-6 December 2019.

- Amir Rowhani, Zhiwei Sun, Alfonso Chinnici, Paul R. Medwell, Graham J. Nathan, Bassam B. Dally, "Flow-field and residence time distribution in a series of turbulent non-premixed bluff-body flames", In Proceedings of the 12th Asia-Pacific Conference on Combustion, Fukuoka, Japan. 1-5 July 2019.

- Amir Rowhani, Zhiwei Sun, Zeyad T. Alwahabi, Paul R. Medwell, Graham J. Nathan, Bassam B. Dally, "Effects of Bluff-body diameter on the flow field of turbulent bluff-body ethylene/nitrogen flames", 11th Mediterranean Combustion Symposium. Tenerife, Spain. 16-20 June 2019.

- Amir Rowhani, Alfonso Chinnici, Michael J. Evans, Paul R. Medwell, Graham J. Nathan, Bassam B. Dally, "Variation of residence time in non-premixed turbulent bluff-body ethylene flames as a function of burner diameter", 21st Australian Fluid Mechanics Conference. Adelaide, Australia. 10-13 December 2018.